Insights into the origin of the Scourie Dykes from geochemistry and geochronology

by

Joshua Davies

A thesis submitted in partial fulfillment of the requirements for the degree of

Doctor of Philosophy

Department of Earth and Atmospheric Science
University of Alberta

Abstract

A multi-technique geochemical study of the Scourie dykes in the Lewisian gneiss complex (LGC) of northwest Scotland is presented. The Scourie dykes are a set of northwest-southeast trending mafic and ultramafic dykes that intrude the LGC between two periods of high-grade regional metamorphism. New U-Pb radiometric ages from zircon and baddeleyite indicate dyke emplacement occurred during two periods separated by ~400 m.y. The majority of the dykes were emplaced at ~2.4 Ga, with a minor intrusion event at ~2.0 Ga. The distribution of ages in the ~2.4 Ga event is consistent with dyke emplacement during post collisional extension after the collision of the Assynt and Rhiconich terranes in the northern LGC.

The oxygen isotopic composition ($\delta^{18}O$) of zircon from the Scourie dykes indicates that the source region of the dykes contained a low $\delta^{18}O$ component. The zircons have primary $\delta^{18}O$ values down to -3.7 ‰. $\delta^{18}O$ values below 5.5 ‰ can only be created through interaction with meteoric water at the Earth's surface. Therefore, the Scourie dyke magmas likely contain a recycled component that has previously interacted with surface waters. The magmatic low $\delta^{18}O$ signature in the zircons is obscured by post-emplacement fluid alteration during the Caledonian orogeny at ~430 Ma. A new technique involving Raman spectroscopy and trace element analysis combined with ion probe oxygen isotopic analysis is presented which distinguishes areas of zircon grains that still record primary $\delta^{18}O$ signatures from areas in grains which have been reset.

Geochemical modeling of the Scourie dykes is also presented. The modeling indicates that melting of an enriched mantle source cannot produce the dyke trace element chemistry. Melting of a Primitive Mantle source followed by assimilation

of crustal material can explain the enriched trace-element compositions found in the dykes. The geochemical model is consistent with the oxygen isotopic information from the zircons in the dykes.

An initial study investigating the possibility of oxygen isotopic analysis of baddeleyite by ion probe is also presented. In mafic rocks baddeleyite is more common than zircon and commonly records concordant or close to concordant U-Pb ages. Oxygen isotopic analysis of zircon has been instrumental in understanding U-Pb systematics and fluid-rock interactions. Unfortunately, baddeleyite oxygen isotopic analysis by ion probe is currently hindered by heterogeneous reference materials. Analysis of baddeleyite from the Duck Lake sill (DLS) in northern Canada, which has co-crystallized with zircon suggests that the baddeleyite can be in isotopic equilibrium with zircon and therefore record the oxygen isotopic composition of the parent magma. The DLS baddeleyite oxygen isotopic compositions also indicate that baddeleyite may exchange oxygen more readily than zircon with meteoric water without losing significant lead.

Preface

Some of the research conducted during this thesis forms part of an international and national research collaboration. The results presented in Chapter 3 were collected at McEwan University, University of Wisconsin - Madison and the University of Alberta. I collected the Raman data with the assistance of Dr. Erin Walton at McEwan University. Whole-rock laser fluorination oxygen isotopic results were generated at the University of Wisconsin - Madidon by Dr John Valley. Dr Richard Stern, with assistance from me, conducted all SIMS oxygen isotopic results presented in chapter 2 and chapter 4 of this thesis at the Canadian Center for Isotopic Microanalysis at the University of Alberta.

The results from chapter 2 were also part of a collaborative effort involving McEwan and Western Ontario Universities. The Raman spectra were generated by myself at McEwan University with guidance from Dr. Erin Walton and EBSD analyses were conducted at the University of Western Ontario by Dr. Desmond Moser.

Chapter 2 has been submitted to Chemical Geology for publication as Davies, J.H.F.L., Stern, R.A., Heaman, L.M., Moser, D and Walton, E.L. Evaluating the systematics of baddeleyite SIMS oxygen isotopes.

Chapter 3 from this thesis has been accepted for publication in Precambrian Research and is being published as, Davies, J.H.F.L., and Heaman, L.M., New U-Pb baddeleyite and zircon ages for the Scourie dyke swarm: A long-lived large igneous province with implications for the Paleoproterozoic evolution of NW Scotland.

A version of Chapter 4 has been submitted to Geochimica Cosmochimica Acta for

publication as Joshua H.F.L. Davies, Stern, R.J., Heaman, L.M., Rojas, X., Walton, E.L., Valley, J.V., and DuFrane, S.A., Seeing through the effects of oxygen isotopic disturbance in zircon using SIMS, Raman spectroscopy and trace element analyses: a case study from the low $\delta^{18}O$ Scourie dykes, NW Scotland.

Chapter 5 will be combined with Hf isotopes analyses from the Scourie dyke zircons, which will be conducted during the summer and then prepared for publication.

All of the ideas presented here are my own, although they have been developed through discussions with all co-authors. All of the writing and figures presented here are my own work.

Acknowledgments

I would like to thank my PhD supervisor Dr. Larry Heaman for his guidance and support over the past 4 years. He has allowed me free reign over my work and the direct my research has taken. This has enabled me to investigate new areas of research without the confines of a strict structure. While this freedom has facilitated my use of numerous analytical techniques and has allowed me to learn about things I had never previously considered, I occasionally got lost in scientific wanderings. Luckily for me, Larry has always been available for discussion, and has invariably steered me in the right direction, he has a knack for providing me with much needed motivation, by asking a question I don't know the answer to, or getting excited about new results. I am very grateful for all of his help, especially with my writing abilities, its strange to think that someone that has spoken English their whole life has such difficulties conveying a coherent message through text.

Dr. Richard Stern has also been a great help throughout my thesis, not just with SIMS work. He has been available for numerous discussions about my data, even though his lab is incredibly busy. His enthusiasm is infectious, and his drive to produce excellent data is something that I admire and aspire towards.

My thesis, and the work it contains benefited significantly from discussions and analytical help from Andrew Locock, Tom Chacko, Sergei Matveev, James LeBlanc, Ryan Ickert, Alex Wolfe, Guangcheng Chen, Andy DuFrane and my external collaborators, Erin Walton, Des Moser and John Valley.

Finally I should thank my friends; these are the people that made my time in Edmonton unforgettable. I don't have room to mention everyone here, so I'll just start by

saying thanks to Deco and Francesca – you two are truly inspiring individuals, you know what you want, and how to take it without anyone else knowing.

Other than those two, these people are thanked individually as well, Jesse – being a really great friend and showing me Americans aren't that bad, Joe – how to prepare thoroughly for a race, Ras – un-ending entertainment, Frenchman – the verb peloter, Josh T – being bad at darts so I win, Karen – being an awesome great friend, Katie – being funny and stylish, Aleks – being a blond with dark hair, Britta – wonderful moral compass and inspiring advice, Berto – epitomizing the combination of fun and science, Emily – help getting me started and helping me grow both scientifically and emotionally, Duane F – motivation to get fit and for numerous scientific discussions, Shawna – being a great friend even if I wasn't all the time, Mike – unending belief in me. Finally I would like to thank my parents and grandparents for supporting me throughout this process, and throughout life generally.

List of Symbols and Abbreviations

~	Approximately
≈	Approximately equal to
Δ	Difference
°	Degrees
ºC	Degrees centigrade
=	Equals
>	Greater than
<	Less than
±	Plus or minus
+/-	Non normally distributed error
+	Plus
%	Percent
‰	Parts per thousand or per mille
σ	Standard deviation
x or *	Times
Δm/m	Difference in masses
#	Aliquot number
χ^2/n	Reduced chi squared statistic
↔	Two directional reaction
λ	Decay constant
$\delta^{18}O$ or $\delta^{18}O_{VSMOW}$	Oxygen isotopic composition relative to the international VSMOW standard
$\alpha^{18}O_{SIMS}$	SIMS instrumental bias
$\delta^{18}O^*$	Term for oxygen isotopic composition used when evaluating reference materials before they are proven to be $\delta^{18}O_{VSMOW}$

$\delta^{18}O_{zircon}$	Zircon oxygen isotopic composition
$\delta^{18}O_{baddeleyite}$	Baddeleyite oxygen isotopic composition
100, 010 and 001	Crystal faces
< uv0>	Crystal orientation directions
a^{-1}	Years ago
α/g	Alpha particles per gram
A or α	Fractionation factor
A_g, B_g	Raman active modes in baddeleyite
AFC	Assimilation-fractional-crystallization
Ar+	Positively charges ions of argon
BGS	British geological survey
BSE	Back-scattered Electron Imaging
C_{2h}	Point group of baddeleyite
c/s	Counts per second
cU	Concentration of uranium
cTh	Concentration of thorium
Ca^{2+}	Calcium with a 2+ positive charge
Ca-Kα	The Kα line for calcium
Cameca IMS1280	Multi-collector ion microprobe
CCD	Charge coupled device
CCIM	Canadian center for isotopic microanalysis
CL	Cathodoluminescence
cm	Centimeters
$^{133}Cs^{+}$	Positively charged isotope of Cesium
DLS	Duck Lake Sill
EBSD	Electron backscatter diffraction
etc.	Etcetera

e.g.	for example
Elan6000	Model of LA-Quad-ICP-MS from Perkin Elmer
EPMA	Electron probe micro analysis
ESA	Electrostatic analyzer
F	Amount of melt remaining in AFC model
Fig.	Figure
FCA	Fractional-crystallization-assimilation
FWHM	Full width at half maximum
Γ_t	True full width at half maximum
Γ_a	Measured full width at half maximum
g/cc	Grams per cubic centimeter
Ga	Giga annum
GLITTER	LA-Quad-ICP-MS data reduction software
h	Hours
H^+	Hydrogen with a positive charge
H'2	High Faraday cup
H_2O	Water
HCl	Hydrochloric acid
HF	Hydrofluoric acid
HGB	Harris granulite belt
HNO_3	Nitric acid
HREE	Heavy rare earth elements
Hz	Hertz
i.e.	That is
ID-TIMS	Isotope dilution thermal ionization mass spectrometry
IMF	Instrumental mass fractionation
ISOPLOT	Age calculation Excel macro

J	Joules
J/cm^2	Joules per square centimeter
JEOL 8900	Model of EMPA
K-Ar	Potassium argon geochronology
kg	Kilogram
kV	Kilo-volt
L'2	Low Faraday cup
LA-Quad-ICP-MS	Laser ablation quadrupole inductively coupled plasma mass spectrometer
LA-MC-ICP-MS	Laser ablation multi collector inductively coupled plasma mass spectrometer
LF	Laser fluorination
LGC	Lewisian gneiss complex
LH94-15	In-house zircon standard
LIL	Large ion lithophile
LREE	Light rare earth elements
$M_{\#\#\#}$	Mass of ### isotope
Ma	Mega annum
MASH	Melt-assimilation-storage-homogenization
mg	Milligram
ml	Milliliters
mm	Millimeter
N-MORB	Normal mid ocean ridge basalt
E-MORB	Enriched mid ocean ridge basalt
MSWD	Mean Square of weighted deviants
mW	Milli-watts
n	Number of analysis

N	Normality of an acid
nA	Nano-amp
N_A	Avogadro's number
NAC	North Atlantic craton
NaCl	Salt
NAPI	North Assynt pull in dyke
Nd:YAG	Laser producing crystal
NIST 612	Standard Glass
nm	Nanometer
NW	North west
^{18}O ^{16}O	Isotopes of Oxygen
OH	Outer Hebrides
Olympus BX51	Model of microscope
ρ	Number of fitting parameters
^{205}Pb-^{235}U	Lead-Uranium spike isotopes
$^{206}Pb/^{238}U$	Ratio of lead to uranium isotopes, usually in reference to age
$^{207}Pb/^{235}U$	Ratio of lead to uranium isotopes, usually in reference to age
$^{207}Pb/^{206}Pb$	Ratio of lead isotopes, usually in reference to age
$^{206}Pb/^{204}Pb$	Ratio of ^{206}Pb and ^{204}Pb lead isotopes
$^{206}Pb^*$	Radiogenically produced ^{206}Pb
$P2_1/c$	Space group of baddeleyite
PDF	Probability density function
pg	Pico-grams
PMP	Polymethylpentene
ppm	Parts per million
R	r_a/r_c
r_c	Rate of crystallization

r_a	Rate of assimilation
Rb-Sr	Rubidium- strontium geochronology
^{87}Rb	One isotope of rubidium
REE	Rare earth element
Re-Os	Rhenium- osmium geochronology
RM	Reference Materials
S	Spectral resolution
s	Seconds
SEM	Scanning Electron Microscope
Si^{4+}	Silicon with a 4+ positive charge
SIMS	Secondary Ion Mass Spectrometry
SiO_n	Polymer of silicon and oxygen
SiO_2	Chemical formula for quartz
Si-Kα	The Kα line of silicon
Sm-Nd	Samarium- neodymium geochronology
T	Temperature
t	Time
TEM2	Temora zircon
Th/U	Thorium Uranium ratio
Th-Mα	The Mα line of thorium
TIMS	Thermal ionization mass spectrometry
$^{205}Tl/^{203}Tl$	Thalium isotope ratio
TTG	Tonalite-trondhjemite-granodiorite
µm	micrometers
U-Pb	Uranium – Lead, usually in reference to geochronology
U-Mβ	The Mβ line of uranium
UP 213	Model of laser from New Wave Research

UAMT1	Mudtank zircon
UP-213	Model of Laser from Merchantek
UOG	Garnet standard from Gore Mountain
ν_3 (SiO_4)	Stretching mode at ~1000 cm^{-1} from Si-O bonds in zircon
ν_1 (SiO_4)	Stretching mode at ~975 cm^{-1} from Si-O bonds in zircon
VG354	TIMS mass spectrometer
WDS	Wavelength dispersive spectrometer
WR	Whole rock
wt. %	Weight percent
Zeiss EVO MA15	Type of SEM
Zr^{4+}	Zirconium with a 4+ positive charge
ZrO_2	Baddeleyite chemical formula
$ZrSiO_4$	Zircon chemical formula
Zr-Lα	The Lα line of zirconium

Table of Contents

Chapter 1: Introduction

The field of geochronology (the absolute timing of geological events) has advanced exponentially over the past 100 years due to the development of the U-Pb system in zirconium-rich minerals zircon ($ZrSiO_4$) and more recently baddeleyite (ZrO_2). These developments have had a profound effect on the science of geology. Uranium is unique amongst elements with geochronometric capabilities, it has two long-lived radioactive isotopes, ^{238}U and ^{235}U, both of which decay through a series of daughter products to the stable isotopes of ^{206}Pb and ^{207}Pb, respectively. The two radioactive uranium isotopes allow two independent U-Pb ages to be calculated from the same sample, and when both of these agree (a concordant age) there is high degree of certainty that the age dates zircon crystallization. Zircon, and baddeleyite strongly partition uranium into their crystal structure during crystallization and reject lead. Their high U-Pb initial ratio (>1000), and very low diffusivities of Pb and U in these minerals (Cherniak and Watson, 2003) make them excellent minerals for geochronology.

The advances in U-Pb geochronology have only been possible through the development of new techniques or the improvement of old practices. For example the precision and accuracy of U-Pb zircon ages has increased drastically over the last century, mostly due to advances in instrumentation and the development of clean laboratory techniques. Work by John Strutt (Lord Rayleigh) in the early 20th century identified zircon as an excellent mineral for chemical dating because of its inertness (Strutt, 1909). However the size of typical zircon crystals (<500 μm) and problems with He loss (early dating employed a U-He total fusion technique) limited its application. Almost half a century later, Larson (1952) re-invigorated interest in zircon as a mineral for geochronology. He identified its very high U/Pb ratios and suggested dating it by measuring the Pb contents by atomic emission, and using α counting to measure

U. In this way <1 gram of zircon was needed and ages of ± 10% could be created. Pioneering work by Tilton et al. (1955) developed isotope dilution (ID) to accurately measure the U and Pb isotopic ratios of a sample relative to a spike of known isotopic composition. U and Pb were chemically separated using complex multi-acid digestion and precipitation techniques and were then measured on a thermal ionization mass spectrometer (TIMS). This measurement technique resulted in significantly better yields and sensitivity than any of the measurements made previously allowing precise measurements to be made on milligrams of material.

Further pivotal advances in the U-Pb dating technique were the introduction of the Concordia diagram (Wetherill, 1956), from which investigators could visualize U-Pb results and interpret discordant data. The use of Teflon bombs for zircon digestion in HF and trace HNO_3 combined with chemical separation and purification of the U and Pb on anion exchange columns (Krogh, 1973). Precise determinations of the ^{238}U and ^{235}U decay constants (Jaffey et al. 1971). Air abrasion techniques to remove the outer, U-rich rim of zircon that often contributed to discordance (Krogh, 1982). New techniques, pioneered by Krogh, reduced Pb blanks to the state that it was possible to measure U-Pb isotopes from single zircon crystals. The air abrasion pre-treatment of zircon significantly reduced discordance and resulted in U-Pb zircon geochronology becoming universally recognized as *the* tool for dating rocks through time.

More recent advances have made the technique even more precise, and have further reduced the effect of discordance and laboratory blanks. The chemical abrasion technique of Mattinson (2005) has essentially removed the effect of discordance in zircon by selectively dissolving discordant parts of a zircon crystal before analysis. Gravimetrically calibrated tracer solutions and quadruple isotopic spikes (^{202}Pb-^{205}Pb-^{233}U-^{235}U) have significantly reduced inter-laboratory differences and improved

the tracking of mass bias during TIMS analysis (Condon et al. submitted).

In conjunction with the analytical advances made in the ID-TIMS U-Pb community, other techniques have been simultaneously developed to obtain different information from tiny zircon grains. Secondary Ion Mass Spectrometry (SIMS) has added high spatial resolution to U-Pb dating (Anderson and Hinthorne, 1972; Compston et al. 1984) and is routinely used to date zircon in-situ. This technique is commonly applied to zircon with complex metamorphic histories and different periods of zircon growth (e.g. Whitehouse et al. 1997). Also laser ablation inductively coupled plasma mass spectrometry (LA-ICP-MS) U-Pb zircon dating has been developed (Fryer et al. 1993) which sacrifices precision and some amount of spatial resolution for increased sample throughput. LA-ICP-MS also benefits from not requiring precisely matrix-matched standards like SIMS techniques (Horstwood et al. 2003), although this may not be true for monazite.

The growth in interest in zircon was led by the development of U-Pb geochronology. Since the 90's almost all aspects of the geochemistry as well as the physical properties of zircon have been probed, and most provide new and complimentary insight into its age and history. The development of oxygen isotope analysis in zircon for example have been instrumental in understanding discordance. Valley et al. (1994) discovered that oxygen isotopic exchange due to fluid infiltration in zircon is associated with lead loss. Raman spectroscopic studies of zircon have also shown that as uranium in zircon decays it damages the crystal structure and creates pathways through which water can enter and expel lead from zircon (Nasdala et al. 1995). The elemental geochemistry of zircon has been used as a provenance tool (Heaman et al. 1990; Belasouva et al. 2002). The hafnium isotopic composition of zircon has been used to understand how the continental crust formed over time (Hawksworth

and Kemp, 2006). Titanium contents in zircon have been suggested as a magmatic thermometer (Watson and Harrison, 2005). These are only a small selection of the research that has been conducted on zircon.

This thesis reports research that expands the application of zircon and baddeleyite to the earth sciences through the use of traditional and the development of new techniques. The work attempts to build on the legacy of research that has developed over the past ~100 years. The majority of the work in this thesis is conducted on the Paleoproterozoic Scourie dykes which intrude the Lewisian gneiss complex (LGC) of northwest Scotland. This area is a classic location for geology as it has been studied for the past ~150 years and has been a testing ground for many new geochemical techniques, especially those involving isotopes (Teall, 1885; Peach et al. 1907; Sutton and Watson, 1950; O'Hara, 1961; Tarney, 1963; Evans and Tarney, 1964; Evans, 1965; Moorbath and Gale, 1969; Holland and Lambert, 1975; Chapman and Moorbath, 1977; Chapman, 1979; Hamilton et al. 1979; Heaman and Tarney, 1989; Whitehouse, 1989; Waters et al. 1990; Whitehouse 1990; Cartwright and Valley, 1991; Cohen et al. 1991; Corfu et al. 1994; Kinny and Friend, 1997; Whitehouse et al. 1997; Zhu et al. 1997; Corfu et al. 1998; Friend and Kinny, 2001; Love et al. 2004; Mason et al. 2004; Whitehouse and Kemp, 2010; Zirkler et al. 2012; Goodenough et al. 2013). With so many studies it may seem like the area is comprehensively understood, however the results of this thesis suggest that there are still many interesting discoveries that remain to be made.

The Scourie dykes are geologically interesting for a number of reasons. They intrude the LGC in between periods of high-grade metamorphism, the earlier Badcallian and Inverian metamorphisms at 2.7 and 2.5 Ga respectively and the later Laxfordian metamorphism which starts at ~1.9 Ga. The dykes were initially used as time

markers to distinguish between the older and younger metamorphic events (Peach et al. 1907; Sutton and Waton, 1950). The dykes are all in the same general orientation (NW-SE) with few obvious cross cutting relationships. Parallel orientation is often used as evidence of synchronicity in dyke swarms (e.g. Ernst and Buchan, 2009), however, high precision U-Pb dating from two of the dykes in the Scourie swarm indicated that they intruded ~400 Ma apart (Heaman and Tarney, 1989). The extremely long time span between two dykes of the same orientation, in apparently the same swarm has not been previously identified. Some of the Scourie dykes, around the hamlet of Scourie (after which the dykes are named) have extremely low $\delta^{18}O$ values of ~2 ‰ (Cartwright and Valley, 1991). Mantle-derived basaltic rocks almost invariably have $\delta^{18}O$ values of ~5.5 ‰ if they are unaltered (Eiler, 2001), and typical hydrothermal alteration or crustal contamination results in heavier isotopic compositions (see compilation of Valley et al. 2005). Cartwright and Valley (1991) suggested that the oxygen isotopic composition was the result of incorporating subducted oceanic crust that had a low $\delta^{18}O$ as a result of interaction with 0 ‰ seawater at elevated temperatures (T>300ºC) into the source of the dykes. If this explanation was correct, it would strongly support the presence of plate tectonics in the late Archean. The elemental geochemistry of the dykes indicates that they are not the products of melting from typical depleted mantle, or primitive mantle sources (Weaver and Tarney, 1981). They are enriched in trace-elements but many of the dykes are also ultramafic requiring high degrees of melting to produce their major element geochemistry. The mixture of high degrees of partial melting of the mantle combined with the enriched trace-elements lead Weaver and Tarney, (1981) to suggest that the mantle source for the dykes was anomalously enriched in trace-elements. Crustal contamination of the dyke magma was discounted due to extremely depleted Th and U contents in the gneisses of the Assynt terrane, which is not reflected in the dykes.

The intention of this thesis was to investigate many of the anomalous features in the Scourie dykes using new or updated techniques. The goals outlined at the beginning of the thesis were to: 1) understand the timing of dyke emplacement in the Scourie dykes using baddeleyite and zircon U-Pb geochronology; 2) discover if the anomalous $\delta^{18}O$ signatures shown in the dykes around Scourie are real, and if they are recorded elsewhere in the swarm; 3) create a geochemical model for the evolution of the dykes; 4) develop ion probe baddeleyite oxygen isotopic analysis and use this tool on the Scourie dykes.

The research presented in this thesis describes the progress made trying to accomplish the goals of the thesis, it is broken down into four chapters followed by a concluding chapter and each of the chapters are described briefly below.

Chapter 2

This chapter describes the systematics of Secondary ion mass spectrometry (SIMS) oxygen isotope analysis in baddeleyite. The intention for this chapter was to develop SIMS oxygen isotopic analysis of baddeleyite and apply it to the low $\delta^{18}O$ Scourie dykes. However, the technique is more complex than oxygen isotopic analysis of zircon and therefore still has some wrinkles to be ironed out. Oxygen isotopic results from two mega-crysts of baddeleyite are presented. The mass bias effects of orientation and metamictization are quantified and are shown to be very small. A case study from a 3rd sample of baddeleyite and zircon extracted from the Duck Lake sill in the North West Territories in Canada suggests that baddeleyite can record magmatic oxygen isotopic compositions and that the laser fluorination $\delta^{18}O$ value for one of the reference materials may be incorrect. Furthermore, it is shown that baddeleyite may retain U-Pb isotopic information even if the oxygen isotopic systematics have been disturbed.

Chapter 3

The chapter presents U-Pb ages from baddeleyite and zircon from the Scourie mafic dykes. Mafic rocks are traditionally very hard to date as they rarely contain zircon. Baddeleyite is more common (although still very rare) within mafic rocks, and since this mineral has many similar properties to zircon it is an ideal target for U-Pb geochronology. The dykes have a history of geochronology dating back to the 1950's when their relative ages were used to distinguish between metamorphic events pre-dating and post-dating dyke emplacement. The age results in this chapter provide new information on the tectonic history of the LGC.

Chapter 4

This chapter describes a new technique, which can be used to assess which areas of zircon retain their primary magmatic compositions. A combination of in-situ Raman spectroscopy, trace-element analysis and oxygen isotopic analysis are used to determine which areas of zircon crystals have or have not experienced post emplacement interaction with fluids. This new technique is applied to zircons from the Scourie dykes to obtain their primary oxygen isotopic composition. The Scourie dyke zircons are shown to preserve extremely low $\delta^{18}O$ values, which indicate that their magmas interacted with hydrothermally altered crust prior to emplacement.

Chapter 5

This chapter describes the geochemistry of the Scourie dykes. The dykes can be split into two broad categories, one ultramafic with fractionated rare earth elements, and one mafic with less fractionated but enriched trace-element contents relative to primitive mantle. A model of primitive mantle melting followed by an assimilation-frac-

tional-crystallization (AFC) of different crustal components is presented which can explain the geochemical signatures of the mafic and ultramafic dykes.

Conclusion.

The results from chapters 2-5 are summarized, and some broad conclusions are drawn.

Appendix A

Computer program, programed in Mathmatica, used to process the Raman Spectra.

Appendix B

Microprobe amphibole data.

Appendix C

Inventory of the Scourie samples collected and processed during this study.

References

Andersen, C.A., Hinthorne, J.R., 1972. U, Th, Pb and REE Abundances and $^{207}Pb/^{206}Pb$ Ages of Individual Minerals in Returned Lunar Material by Ion Microprobe Mass Analysis. Earth and Planetary Science Letters 14, 195–200.

Belousova, E., Griffin, W., O'Reilly, S., Fisher, N., 2002. Igneous Zircon: Trace-element Composition as an Indicator of Source Rock Type. Contributions to Mineralogy and Petrology 143, 602-622.

Cartwright, I., Valley, J.W., 1991. Low-^{18}O Scourie Dike Magmas From the Lewisian Complex, Northwestern Scotland. Geology 19, 578-581.

Chapman, H.J., 1979. 2,390 Myr Rb–Sr Whole-Rock for the Scourie Dykes of North-West Scotland. Nature 277, 642-643.

Chapman, H.J., Moorbath, S., 1977. Lead Isotope Measurements From the Oldest Recognised Lewisian Gneisses of North-West Scotland. Nature 268, 41-42.

Cherniak, DJ, and EB Watson. 2003. Diffusion in Zircon. Reviews in Mineralogy and Geochemistry 53, 113-143.

Cohen, A.S., O'Nions, R.K., O'Hara, M.J., 1991. Chronology and Mechanism of Depletion in Lewisian Granulites. Contributions to Mineralogy and Petrology 106, 142–153.

Compston, W., Williams, I.S., Meyer, C., 1984. U-Pb Geochronology of Zircons From Lunar Breccia 73217 Using a Sensitive High Mass-Resolution Ion Microprobe. Journal of Geophysical Research 89, B525-B534.

Condon, D.J., Schoene, B., Mclean, N., Bowring, S.A., Parrish, R.R., 2014. Metrology and Traceability of U-Pb Isotope Dilution Geochronology (EARTHTIME2 Tracer Calibration Part I). G-Cubed (Submitted)

Corfu, F., Crane, A., Moser, D., Rogers, G,. 1998. U-Pb Zircon Systematics at Gruinard Bay, Northwest Scotland: Implications for the Early Orogenic Evolution of the Lewisian Complex. Contributions to Mineralogy and Petrology 133, 329–345.

Corfu, F., Heaman, L.M., Rogers, G,. 1994. Polymetamorphic Evolution of the Lewisian Complex, NW Scotland, as Recorded by U-Pb Isotopic Compositions of Zircon, Titanite and Rutile. Contributions to Mineralogy and Petrology 117, 215–228.

Eiler, J. M., 2001. Oxygen isotope variations of basaltic lavas and upper mantle rocks. In: J.W. Valley, D.R. Cole (Eds.), Stable Isotope Geochemistry, Reviews in Mineralogy and Geochemistry, vol. 51, 1–81.

Ernst, R.E., Buchan, K.L., 1997. Giant radiating dyke swarms: their use in identifying pre-Mesozoic large igneous provinces and mantle plumes. In: Large igneous provinces: Continental, Oceanic and Planetary Flood Volcanism, Geophysical Monograph 100. American Geophysical Union, 297-234.

Evans, C.R., 1965. Geochronology of the Lewisian Basement Near Lochinver, Sutherland. Nature 207, 54–56.

Evans, C.R., Tarney, J., 1964. Isotopic Ages of Assynt Dykes. Nature 204, 638-641.

Friend, C., Kinny, P., 2001. A Reappraisal of the Lewisian Gneiss Complex: Geochronological Evidence for Its Tectonic Assembly From Disparate Terranes in the Proterozoic. Contributions to Mineralogy and Petrology 142, 198–218.

Fryer, B.J., Jackson, S.E., Longerich, H.P., 1993. The Application of Laser Ablation Microprobe-Inductively Coupled Plasma-Mass Spectrometry (LAM-ICP-MS) to in Situ U-Pb Geochronology. Chemical Geology 109, 1–8.

Goodenough, K.M., Crowley, Q.G., Krabbendam, M., Parry, S.F., 2013. New U-Pb age constraints for the Laxford Shear Zone, NW Scotland: Evidence for tectono-magmatic processes associated with the formation of a Paleoproterozoic supercontinent. Precambrian Research 233, 1–19.

Hamilton, P.J., Evensen, N.M., O'Nions, R.K., 1979. Sm-Nd Systematics of Lewisian Gneisses: Implications for the Origin of Granulites. Nature 277, 25–28.

Hawkesworth, C.J., Kemp, A.I.S., 2006. Evolution of the Continental Crust. Nature 443, 811–17.

Heaman, L.M., Bowins, R., Crocket, J., 1990. The Chemical Composition of Igneous Zircon Suites: Implications for Geochemical Tracer Studies. Geochimica et Cosmochimica Acta 54, 1597–1607.

Heaman, L.M., Tarney, J., 1989. U Pb Baddeleyite Ages for the Scourie Dyke Swarm, Scotland: Evidence for Two Distinct Intrusion Events. Nature 340, 705–708.

Horstwood, M.S.A., Foster, G.L., Parrish, R.R., Nobel, S.R., Nowell, G.M., 2003. Common-Pb Corrected in Situ U–Pb Accessory Mineral Geochronology by LA-MC-ICP-MS. Journal of Analytical Atomic Spectrometry 18, 837-846.

Jaffey, A.H., Flynn, K.F., Glendenin, L.E., Bentley, W.C., Essling, A.M., 1971. Precision Measurement of Half-Lives and Specific Activities of ^{235}U and ^{238}U. Physical Review C 4, 1889-1906.

Kinny, P.D., Friend, C.R.L., 1997. U-Pb Isotopic Evidence for the Accretion of Different Crustal Blocks to Form the Lewisian Complex of Northwest Scotland. Contributions to Mineralogy and Petrology 129, 326–340.

Krogh, T.E., 1973. A Low-Contamination Method for Hydrothermal Decomposition of Zircon and Extraction of U and Pb for Isotopic Age Determinations. Geochimica et Cosmochimica Acta 37, 485–494.

Krogh, T.E., 1982. Improved Accuracy of U-Pb Zircon Ages by the Creation of More Concordant Systems Using an Air Abrasion Technique. Geochimica et Cosmochimica Acta 46, 637–649.

Larsen, E.S., Keevil, N.B., Harrison, H.C., 1952. Method for Determining the Age of Igneous Rocks Using the Accessory Minerals. Bulletin of the Geological Society of America 63, 1045-1052.

Love, G.J., Kinny, P.D., Friend, C.R.L., 2004. Timing of Magmatism and Metamorphism in the Gruinard Bay Area of the Lewisian Gneiss Complex: Comparisons with the Assynt Terrane and Implications for Terrane Accretion. Contributions to Mineralogy and Petrology 146 , 620–636.

Mason, A.J., Parrish, R.R., Brewer, T.S., 2004. U–Pb Geochronology of Lewisian Orthogneisses in the Outer Hebrides, Scotland: Implications for the Tectonic Setting and Correlation of the South Harris Complex. Journal of the Geological Society, London 161, 45-54.

Mattinson, J.M., 2005. Zircon U–Pb Chemical Abrasion ('CA-TIMS') Method: Combined Annealing and Multi-Step Partial Dissolution Analysis for Improved Precision and Accuracy of Zircon Ages. Chemical Geology 220, 47–66.

Nasdala, L., Irmer, G., Wolf, D., 1995. The Degree of Metamictization in Zircons: a Raman Spectroscopic Study. European Journal of Mineralogy 7, 471–478.

O-Harah, M.J., 1961. Zoned Ultrabasic and Basic Gneiss Masses in the Early Lewisian Metamorphic Complex at Scourie, Sutherland. Journal of Petrology 2, 248–276.

Peach, B.N., Horne, J., Gunn, W., Clough, C.T., Hinxman, L.W., Teall, J.J.H., 1907. The geological structure of the North-West Highlands of Scotland. Memoir of the Geological Survey of Great Britain, published by HMSO, Glasgow.

Strutt, R.J., 1910. The Accumulation of Helium in Geological Time. III. Proceedings of the Royal Society of London. Series A 83, 298–301.

Sutton, J., Watson, J., 1950. The Pre-Torridonian Metamorphic History of the Loch Torridon and Scourie Areas in the North-West Highlands, and Its Bearing on the Chronological Classification of the Lewisian. Quarterly Journal of the Geological Society 106, 241–307.

Teall, J.J.H., 1885. The Metamorphosis of Dolerite Into Hornblende-Schist. Quarterly Journal of the Geological Society 41, 133–145.

Tilton, G.R., Patterson, C., Brown, H., Inghram, M., Hayden, R., Hess, D., Larsen, E., 1955. Isotopic Composition and Distribution of Lead, Uranium, and Thorium in a Precambrian Granite. Bulletin of the Geological Society of America 66, 1131-1148.

Valley, J.W., Chiarenzelli, J.R., McLelland, J.M., 1994. Oxygen Isotope Geochemistry of Zircon. Earth and Planetary Science Letters 126, 187–206.

Valley, J.W., Lackey, J.S., Cavosie, A.J., Clechenko, C.C., Spicuzza, M.J., Basei, M.A.S., Bindeman, I.N., Ferreira, V.P,. Sial, A.N., King, E.M., Peck, W.H., Sinha, A.K., Wei, C.S., 2005. 4.4 billion years of crustal maturation: oxygen isotope ratios of magmatic zircon. Contributions to Mineralogy and Petrology 150, 561–580.

Waters, F.G., Cohen, A.S., O'Nions, R.K., O'Hara, M.J., 1990. Development of Archaean Lithosphere Deduced From Chronology and Isotope Chemistry of Scourie Dykes. Earth and Planetary Science

Letters 97, 241–55.

Watson, E.B., Harrison, T.M., 2005. Zircon Thermometer Reveals Minimum Melting Conditions on Earliest Earth. Science 308, 841-844.

Weaver, B.L., Tarney, J., 1981. The Scourie dyke suite: petrogenesis and geochemical nature of the Proterozoic sub-continental mantle. Contributions to Mineralogy and Petrology 78, 175–188.

Wetherill, G.W., 1956. Discordant Uranium-Lead Ages, I. Transactions of the American Geophysical Union 37, 320–326.

Whitehouse, M.J., Kemp, A.I.S., 2010. On the Difficulty of Assigning Crustal Residence, Magmatic Protolith and Metamorphic Ages to Lewisian Granulites: Constraints From Combined in Situ U–Pb and Lu–Hf Isotopes. Geological Society, London Special Publications 335. Geological Society of London, 81–101.

Whitehouse, M.J., 1989. Sm-Nd Evidence for Diachronous Crustal Accretion in the Lewisian Complex of Northwest Scotland. Tectonophysics 161, 245–256.

Whitehouse, M.J., 1990. Isotopic Evolution of the Southern Outer Hebrides Lewisian Gneiss Complex: Constraints on Late Archaean Source Regions and the Generation of Transposed Pb-Pb Palaeoisochrons. Chemical Geology 86, 1–20.

Whitehouse, M.J., Claesson, S., Sunde, T., Vestin, J., 1997. Ion Microprobe U-Pb Zircon Geochronology and Correlation of Archaean Gneisses From the Lewisian Complex of Gruinard Bay, Northwestern Scotland. Geochimica et Cosmochimica Acta 61, 4429–4438.

Zhu, Z.K., O'Nions, R.K., Belshaw, N.S., Gibb, A.J., 1997. Lewisian Crustal History From in Situ SIMS Mineral Chronometry and Related Metamorphic Textures. Chemical Geology 136 205–218.

Zirkler, A., Johnson, T.E., White, R.W., Zack, T., 2012. Polymetamorphism in the Mainland Lewisian Complex, NW Scotland - Phase Equilibria and Geochronological Constraints From the Cnoc an t'Sidhean Suite. Journal of Metamorphic Geology 30, 865–885.

Chapter 2: Evaluating the systematics of baddeleyite SIMS oxygen isotopes

2.1. Introduction

Baddeleyite (ZrO_2) is a relatively uncommon mineral in rocks, occurring in trace amounts in some ultramafic, mafic, kimberlitic and carbonatitic igneous rocks, and is also produced during metamorphism in some skarns and metacarbonates (Heaman and LeCheminant, 1993 and references therein). Similar to zircon, baddeleyite preferentially incorporates the actinide elements U (up to 5000 ppm) and Th into its structure during crystallization while excluding Pb, making it an excellent mineral for U-Pb geochronology (see Heaman and LeCheminant, 1993). The use of the U-Pb baddeleyite geochronometer to date mafic rocks, especially Precambrian diabase dykes, which have previously been difficult to reliably date using other geochronometers, has increased rapidly over the past decade. This expansion has been facilitated by improved extraction techniques designed to recover micro-baddeleyite (<50 μm) crystals from solid rock (e.g., Söderlund and Johansson, 2002) coupled with recent advances in in-situ dating techniques by secondary ion mass spectrometry (Chamberlain et al., 2010; Li et al., 2010). As baddeleyite is now commonly used to date mafic rocks, other aspects of its geochemistry have been utilized to provide information on the origin and evolution of these rocks, such as trace-elements (Reischmann et al., 1995; Rodionov et al., 2012) and hafnium isotopes (Schärer et al., 1997; Xie et al., 2008).

The oxygen isotopic composition of baddeleyite has received relatively little

attention despite its potential for providing important information on the origin of mafic/ultramafic magmas and post-emplacement alteration. The oxygen isotopic composition could also be used to help understand complex U-Pb systematics, such as discordance, which are occasionally discovered when dating baddeleyite (e.g. Heaman and LeCheminant, 2000; Amelin and Zaitsev, 2002). Using oxygen isotopes in conjunction with U-Pb dating has greatly enhanced the understanding of U-Pb systematics in zircon (Valley et al., 1994; Valley, 2003). This combined approach has lead to the discovery that Pb loss in zircon is often associated with hydrothermal alteration (Valley et al. 1994).

There have been only two studies that have investigated the oxygen isotopic composition of baddeleyite, and in both the oxygen isotopic information from baddeleyite was not influential in the conclusions. Valley (2003) reported a $\delta^{18}O$ of 3.5 ± 1.5‰ for 6 fragments of megacrystic baddeleyite from the Phalaborwa carbonatite analyzed by laser fluorination (LF). Wotzlaw et al. (2012) analyzed baddeleyite from the Skaergaard intrusion by LF and reported a $\delta^{18}O$ of 2.04 ± 1.12 ‰. Since the high melting temperature of baddeleyite can reduce the oxygen yield, Wotzlaw et al. (2012) mixed garnet (UOG from Gore Mountain) with the baddeleyite to enhance the yield and used a mass balance calculation to extract the $\delta^{18}O$ value. The high error and difficulty with the analysis caused neither author to pursue the technique further.

The high spatial resolution of the SIMS technique is potentially ideal for baddeleyite oxygen isotopic analysis, as baddeleyite crystals are typically very small and their abundance in rocks is low. However, O-isotopic fractionation has been observed in SIMS analyses of other minerals that are related to both crystal chemistry and orientation of the material analyzed (Slodzian, 1975). This type of fractionation is

called instrumental mass fractionation (IMF) and has been discovered for multiple minerals analyzed for different elements/isotopes. For example, orientation effects have been found for garnet (Lyon et al., 1998), baddeleyite (Wingate and Compston, 2000), hematite and magnetite (Huberty et al., 2010), sphalerite (Kita et al., 2010), and rutile (Taylor et al., 2012). IMF has also been correlated with metamictization – the degree of radiation induced damage in zircon (White and Ireland, 2012), and crystal chemistry – typically for minerals with solid solutions, such as olivine (Eiler et al., 1997) and garnet (Vielzeuf et al., 2005). Collectively these IMF processes are referred to as matrix effects and could be potentially important processes affecting the measured oxygen isotope composition of baddeleyite. Before baddeleyite SIMS analysis can be routinely applied to natural samples, the significant matrix effects need to be understood.

Here we explore the suitability of two natural baddeleyite samples as potential reference materials (RM) for SIMS, and attempt to quantify different matrix effects (including crystal orientation and metamictization), which have been shown to cause mass bias during SIMS analysis in other minerals. We also investigate the oxygen isotope composition of co-existing zircon and baddeleyite to help further quantify the IMF.

2.2. Sample descriptions

For understanding the systematics (matrix effects and calibrations) of baddeleyite oxygen isotopic analysis we used a baddeleyite megacryst (2 cm) from the Phalaborwa carbonatite complex South Africa and a baddeleyite megacryst from the Mogok metamorphic belt Myanmar.

The 2060 Ma Phalaborwa carbonatite contains numerous mm-cm size baddeleyite phenocrysts, which are suitable for RMs used in U-Pb geochronology (see Heaman, 2009). The baddeleyite crystals from Phalaborwa have reported inclusions of apatite, carbonate, barite, celestite, feldspar, magnetite, monazite, uranothorianite, sulfide, and zircon (Forster, 1958; Reischmann et al., 1995; Heaman, 2009). However, careful backscattered electron (BSE) and cathodoluminescence (CL) imaging indicated that the baddeleyite used in this study did not contain inclusions at the micron scale. The crystal was chosen based on its euhedral morphology and lack of visible alteration/ inclusions. The selected crystal (given CCIM sample number S0045) was broken into fragments 50-250 μm in length for SIMS analysis. The only previous oxygen isotopic studies performed on the Phalaborwa carbonatite other than the data from Valley (2003) mentioned previously, were $\delta^{18}O$ values in igneous calcite and dolomite (Dawson and Hinton, 2003).

The Cenozoic Mogok metamorphic belt in Myanmar contains marbles and associated placer deposits of corundum, spinel, forsterite with accessory zircon and baddeleyite (Searle et al., 2007; Garnier et al., 2008). The Mogok baddeleyite crystal used in this study was obtained commercially. The 2 cm-long euhedral crystal (CCIM sample number S0069) was selected for analysis based on its pristine appearance, and was broken into 50-250 μm fragments for oxygen isotope analysis. BSE and CL imaging of the baddeleyite revealed oscillatory zoning features and no mineral inclusions. The $\delta^{18}O$ compositions of metamorphic calcite, dolomite and zircon from the Mogok metamorphic belt have been previously reported by Garnier et al., (2008) and Cavosie et al., (2011), both of whom discovered isotopically heavy values (19.9-27.8 ‰ in carbonates and 18-25.5 ‰ in zircon) suggesting that they both originated from metamorphism of marine carbonates.

Large (>1 cm) baddeleyite crystals are very unusual in the geological record, so to test the technique on more typical baddeleyite samples we measured the oxygen isotopic composition of ~30-70 µm bladed baddeleyite crystals from the Duck Lake sill (DLS, Bleeker and Kamo, 2003; Bleeker et al. 2007), a mafic intrusion near Yellowknife, Northwest Territories, Canada. The DLS was chosen as it is un-metamorphosed and contains both baddeleyite and zircon, which have both been dated by U-Pb isotope dilution thermal ionization mass spectrometry (ID-TIMS) techniques, and both give indistinguishable near concordant ages of 2181 ± 2 Ma ($^{207}Pb/^{206}Pb$ weighted mean age, Bleeker and Kamo, 2003). The grains used in this study were provided by Dr. Sandra Kamo at the University of Toronto and are part of the same sample used for U-Pb dating.

2.3. Analytical techniques

2.3.1 Secondary ion mass spectrometry (SIMS)

All SIMS measurements were done at the Canadian Center for Isotopic Microanalysis (CCIM) at the University of Alberta using a Cameca IMS1280 multi-collector ion microprobe. The experiments were conducted using 7 grain mounts in 9 ion probe sessions over a three year period. Epoxy grain mounts (25 mm diameter) were prepared using West System® 105 and 206 resin and hardener, respectively. The mounts contained fragments of either or both of the two potential RMs, S0045 (Phalaborwa) and S0069 (Mogok). Mechanical grinding and final polishing utilized 9, 3, and 1 µm diamond compounds, followed by ultrasonic cleaning with a soap solution, deionized H_2O, and oven dried at 50 ºC. Mounts were evaporatively- or

sputter-coated with 5 nm of Au prior to scanning electron microscopy (SEM). A Zeiss EVO MA15 SEM, equipped with panchromatic cathodoluminescence and solid-state back-scattered electron detectors was utilized with typical beam conditions of 15 kV and 3 – 5 nA. A further 25 nm of Au was subsequently deposited on the mounts prior to SIMS analysis.

SIMS analytical techniques for oxygen isotopes (^{18}O, ^{16}O) were identical for both baddeleyite and zircon, and generally follow the methods described for garnet by Ickert and Stern (2013). A $^{133}Cs^{+}$ primary beam was utilized having an impact energy of 20 keV. The ~12 μm diameter probe was rastered slightly during acquisition to form rectangular sputtered areas ~15 x18 μm across and ~1.5 μm deep. The normal incidence electron gun was utilized for charge compensation. Negative secondary ions were extracted through 10 kV into the secondary (transfer) column. Transfer conditions included a 120 μm entrance slit, 5 x 5 mm pre-ESA (field) aperture, and 100x image magnification at the field aperture. The energy window was set at full transmission. The mass-separated oxygen isotopes were detected simultaneously in Faraday cups L'2 ($^{16}O^{-}$) and H'2 ($^{18}O^{-}$) in the multi-detector array. Mass resolution ($\Delta m/m$) was typically 1950 and 2250, respectively, using 500 μm exit slits. Faraday cup baselines were measured at the start of the day, and were sufficiently stable and low that no further measurements were necessary. Secondary ion count rates for $^{16}O^{-}$ were ~1.5 − 3 x 10^{9} c/s, with zircon having about 1.3x the yield as baddeleyite. A single analysis took 4.5 minutes and typically comprised rastering the probe for 30 – 60 s over a 20 x 20 μm area to clean and implant Cs, followed by automated secondary ion tuning, and 100 s of measurement.

Prior to commencing analytical sessions for baddeleyite, we first identified, through reconnaissance analyses of many fragments, one or more from either S0045 or

S0069 with internally uniform and identical raw $^{18}O/^{16}O$ values. Repeated analyses of these grains over the course of the session provided the means to correct for any drift in instrumental mass fractionation (IMF), and to estimate minimum spot-to-spot uncertainties. These analyses of reference grains were also used to make IMF corrections of the unknowns using the following laser fluorination $\delta^{18}O_{VSMOW}$ reference values (see next section): S0045 = +4.44 and S0069 = +21.17. Analyses of the RMs were processed collectively for long-term drift and spot-to-spot statistics for the entire analytical session lasting usually several hours (see Ickert and Stern, 2013). Identical methods were followed for zircon, with IMF monitored by the same 1:4 sequence (RM: unknowns) using RMs S0022 (TEM2) zircon with $\delta^{18}O_{VSMOW}$ = +8.2 ‰ (Black et al., 2004) or S0081 (UAMT1) zircon with $\delta^{18}O_{VSMOW}$ = +4.87 ‰ (Stern R., unpublished data). Individual spot uncertainties for $\delta^{18}O$ at 95 % confidence are typically ±0.20 – 0.30‰, and include within-spot (counting) and between-spot (geometric) errors.

2.3.2 Raman

Raman microanalysis was done at MacEwan University and was used to investigate the degree of disorder (metamictization) within the baddeleyite grains. Raman spectroscopy was performed using a Bruker Senterra Raman spectrometer with a CCD detector attached to an Olympus BX51 optical microscope. The 50x objective was used to focus the excitation laser beam (532 nm line of Ar+ laser) resulting in a spot diameter of ~3 μm. The depth resolution was ~5 μm producing a spatial resolution of <10 μm^3. The spectral resolution was ~3−5 cm^{-1} and the wave number accuracy was ± 1 cm^{-1}. Data were collected over the spectral range 50 - 1500 cm^{-1}. To avoid sample deterioration and to achieve good counting statistics, a sequence of 10 s exposures were acquired using a laser power of 10 mW. These multiple exposures were then summed to achieve the final spectrum. The samples were viewed in

reflected light. Raman analyses were conducted inside SIMS ablation pits to ensure direct correlation of information between the two techniques. Repeat analyses were conducted on several pits throughout the analytical period to check reliability and detector drift. All Raman data were modeled using a Levenberg-Marquet non-linear least squares fitting routine and a Pearson VII function for band fitting using the program Fityk (Wojdyr, 2010). The probability of model fit was always better than 0.995.

In order to obtain more accurate FWHM (full width at half maximum) parameters of the band ~470 cm^{-1}, especially for metamict samples, a broad background feature at a low frequency, which was assigned to the amorphous component, was subtracted from the main spectra in a technique similar to Geisler et al. (2001). The FWHM of the ~470 cm^{-1} band was also corrected for the apparatus function which causes an apparent broadening of the bandwidth due to finite widths of the slits in the Raman detector. Since the slits are not as small as the linewidths of Raman spectra the effects of peak broadening due to the apparatus function can be quite large on narrow Raman band lines. The equation (equation 2 from Tanabe and Hiraishi, 1980)

$$\Gamma_t = \Gamma_a[1-(S/\Gamma_a)^2] \quad (1)$$

was used to correct for the apparatus function, where Γ_t is the true FWHM, Γ_a is the measured FWHM and S is the spectral resolution (2 cm^{-1} in this study).

2.3.3 Electron backscatter diffraction

Electron backscatter diffraction (EBSD) measurements were used to determine the orientation of the mounted baddeleyite grains. The EBSD measurements were done at the University of Western Ontario.

2.3.4 Imaging

BSE and CL imaging was done on all baddeleyite crystals before analysis. Imaging was conducted at the CCIM using a Zeiss EVO 15 scanning electron microscope equipped with a secondary electron and backscattered electron detectors, a Robinson wide spectrum CL detector and a Gatan Chroma CL detector.

2.3.5 Laser Fluorination

Laser Fluorination (LF) analysis was conducted at University of Oregon following the techniques described in Bindeman et al. (2008). The samples were pretreated with a gas of BrF_5 to reduce blank contributions before being heated by a 35W CO_2 laser. The extracted gas was purified by a series of cryogenic traps cooled with liquid nitrogen and a mercury diffusion pump. The oxygen gas from the sample was converted to CO_2 using graphite and the CO_2 was measured on a MAT 253 mass spectrometer.

Seven analyses of the in house standard Gore Mountain garnet UOG were analyzed during baddeleyite analysis. The variability in the oxygen isotope composition of the garnet standard ranged from +0.1 ‰ to -0.05 ‰, these uncertainties were propagated as part of the uncertainty assigned to the unknowns.

Some jumping was noticed during the laser heating of S0045, which could indicate the presence of a fluid phase within the crystal.

2.3.6 Electron microprobe

Electron microprobe analyses (EPMA) were done using a JEOL 8900 electron

microprobe with 5 wavelength dispersive spectrometers (WDS) at the University of Alberta. Fragments of S0045 and S0069 were mounted in epoxy and polished using 0.5 and 0.25 μm diamond powder to expose the grains and ensure a flat surface for analysis. During WDS analysis, the accelerating voltage was 20 kV and the beam current was 20 nA with a beam diameter of ~1 μm. Quantitative analysis was performed after calibration on well-characterized RMs (listed in Table 2.1). Major-element results for the Temora and Mudtank zircons (standard zircons for U-Pb geochronology), run at the same time are presented in Table 2.1. Count times were 30 seconds on the background and 60 seconds on the peaks.

2.3.7 LA-Quad-ICP-MS

Laser ablation quadrupole inductively coupled mass spectrometric (LA-Quad-ICP-MS) analyses were conducted for trace-element concentrations of the baddeleyite using a Perkin Elmer Elan6000 quadrupole ICP-MS attached to a UP-213 Merchantek laser ablation system at the University of Alberta. The laser was set up with a spot diameter of 50 μm with an energy density of 10 J cm^{-2}. Each analysis consisted of a 20 second measurement on the background and a 50 second period of ablation and ion acquisition. Multiple ablation spots were made on multiple grains to obtain an average composition of both Phalaborwa and Mogok baddeleyites. The NIST 612 glass standard was used as the external calibration standard since no baddeleyite trace-element standards were available. The NIST glass was analyzed throughout the data acquisition period and the average results are presented in Table 2.1 along with trace-element data for the samples. The analyses of NIST 612 were within ± 5 % of the recommended values for all elements although most elements were within ± 1 % (Table 2.1). Hafnium contents of the samples obtained by electron microprobe analysis were used as internal standards. Data were reduced using the GLITTER software (http://www.glitter-gemoc.com).

2.4. Quantification of the Technique

2.4.1. Oxygen isotopic composition of Phalaborwa and Mogok baddeleyite crystals

A well-calibrated baddeleyite standard is a prerequisite for evaluating the accuracy of SIMS $\delta^{18}O$ measurements. In this study we determined reference oxygen isotopic compositions for Phalaborwa (S0045) and Mogok (S0069) baddeleyite using laser fluorination (LF). Six LF oxygen isotope measurements of Phalaborwa yielded a weighted average $\delta^{18}O$ value of 4.47 ± 0.30 ‰ (2σ, MSWD = 8) with a median value of 4.44 +0.49/-26‰ and a range of 0.95 ‰ (Fig. 2.1a, Table 2.2). The heterogeneous $\delta^{18}O$ values for Phalaborwa indicate that the crystal has oxygen isotopic variation outside analytical error.

SIMS analyses of multiple fragments of Phalaborwa baddeleyite analyzed over five analytical sessions, were normalized to the LF median value and produce a weighted mean $\delta^{18}O$ value of 4.49 ± 0.05 ‰ (2σ, n = 125, MSWD = 7) and a total range of 1.57 ‰ (Fig. 2.1, Table 2.2), which is in good agreement with the LF data. For all subsequent SIMS baddeleyite analyses, a single homogeneous Phalaborwa crystal fragment, with a median composition, was used as the RM. This crystal was analyzed once every 4 'unknown' analyses and used to track instrument drift. The isotopic composition of this crystal was normalized to the median of the LF data and this correction was applied to the Phalaborwa 'unknowns'. Using this technique, the RM and the unknowns are exactly the same and so the large uncertainty on the absolute composition of the Phalaborwa crystal (range of 0.95 ‰) does not need to be

propagated onto the unknowns since the uncertainties should be perfectly correlated. Therefore only within spot uncertainties corrected for instrument drift are presented in Table 2.2 and Fig. 2.1.

Fig. 2.1a shows that there is good agreement between the SIMS and LF $\delta^{18}O$ results although there is slightly more dispersion in the SIMS data for certain analytical sessions (e.g., Day 1 and 2); outside of the range of values observed in the LF data. The increase in range shown by the SIMS results is most likely due to the difference in the size of material analyzed between the techniques, the LF analyses used ~1.5 mg of material effectively homogenizing any oxygen isotopic variation within that volume, whereas typical sample weights are in the picogram range for SIMS (e.g. Page et al., 2007). In heterogeneous material, SIMS analyses are expected to record a greater range than 'bulk' analyses like LF. Another potential explanation for the differences between the SIMS and LF results is matrix effects during SIMS analysis (discussed further in section 4.2) however, considering the good agreement between SIMS and LF $\delta^{18}O$ values for S0045, it is likely that matrix effects play a minor role in the $\delta^{18}O$ values produced by SIMS.

In an attempt to understand the $\delta^{18}O$ variation in the Phalaborwa crystal, each crystal fragment was analyzed up to 3 times and care was taken to analyze fragments with differences in CL zoning to qualitatively assess whether there is any correlation between $\delta^{18}O$ and CL response, similar to the observation that in some minerals there is a correlation between trace-element content and oxygen isotopic composition measured during SIMS analysis (Hanchar and Rudnick, 1995; Nasdala et al., 2002; 2003). No correlation between CL bands and oxygen isotope composition was discovered, and the low trace-element abundances (specifically rare earth elements) in Phalaborwa and Mogok baddeleyite crystals (Table 2.1) suggest that trace-

element variations are unlikely to cause oxygen isotopic fractionation. No obvious relationships between $\delta^{18}O$ and structural features observed during imaging, such as fractures etc., were discovered.

To test the internal reproducibility of SIMS oxygen isotopic measurements, an individual crystal fragment of Mogok (S0069) baddeleyite was analyzed. The LF data for Mogok produced a $\delta^{18}O$ of 20.99 ± 0.7 ‰ (2σ, n = 8, MSWD = 23) with a median of 21.17 +0.24/-0.47 ‰ and a range of 1.87 ‰. SIMS results from one randomly oriented fragment of Mogok, corrected only for instrument drift produced an average $\delta^{18}O$ composition of 21.07 ± 0.05 ‰ (2σ, n = 18, MSWD = 0.83, Fig. 2.1b). The very high precision of the SIMS oxygen isotope results is due to the homogeneity of the individual fragment chosen, individual spot precision was ~0.2 ‰. This result suggests that the SIMS technique is potentially capable of producing very high precision $\delta^{18}O$ compositions of individual baddeleyite grains, similar to that of zircon.

Neither Phalaborwa nor Mogok baddeleyite crystals have the homogeneous oxygen isotopic composition that is required to be an ideal mineral standard for SIMS, however they can still be used to help understand the systematics of baddeleyite oxygen isotopic analysis by SIMS.

2.4.2. Potential Matrix effects

The heterogeneous $\delta^{18}O$ composition of the Phalaborwa and Mogok baddeleyite crystals make it challenging to assess whether there are any systematic matrix effects that produce isotopic bias during SIMS oxygen isotope analysis. However, since crystal orientation has been shown to produce isotopic bias during U-Pb analysis

of baddeleyite (Wingate and Compston, 2000) it is important to determine if crystal orientation causes isotopic fractionation in other elements during sputtering (i.e. oxygen isotopes). Also, U-Pb isotopic bias due to metamictization has been discovered in zircon (White and Ireland, 2012), logically it is possible that this process may also cause bias during baddeleyite analysis due to the high U content of baddeleyite. Topographic effects on the sample mount have also been shown to cause isotopic bias (e.g. Kita et al., 2010). However all mounts analyzed were polished carefully and checked with secondary electron imaging and reflected light microscopy before analysis to ensure a perfectly flat surface, so topographic effects are discounted here. Below we investigate potential biases due to metamictization and orientation in oxygen isotopic analysis of baddeleyite.

2.4.2.1. Metamictization

The term 'matrix effect' refers to structural and chemical properties of minerals, which in some way bias the yield of secondary ions during ion microprobe analysis (Slodzian, 1975; Eiler et al., 1997). Matrix effects are common in minerals with complex solid solutions e.g. olivine and garnet (Eiler et al., 1997; Vielzeuf et al., 2005). Since baddeleyite does not form as part of a solid solution (apart from HfO_2 which is very rare in nature) and the chemical composition is relatively uniform based on electron microprobe results from multiple fragments of S0045 and S0069 (Table 2.1), which compare well with previously published data, it is not anticipated that there will be significant matrix effects based on the chemical composition of unknown baddeleyite. One of the reasons baddeleyite is an ideal mineral for U-Pb geochronology is the presence of trace to weight percent amounts of uranium (up to 5000 ppm), which substitutes for Zr in the crystal structure, similar to zircon (Hoskin and Schaltegger, 2003). Over time, uranium spontaneously decays to lead and during this decay process, α-particles are produced and the associated α-recoil can cause

~1000 atomic displacements (this is the case for zircon, it may be slightly different in baddeleyite, Ewing et al., 2003). The damage to the crystal structure caused by α-recoil is called metamictization and variation in the levels of metamictization between minerals can cause matrix effects; this has been documented in SIMS U-Pb analyses where high degrees of metamictization are linked to enhanced emission of Pb^+ relative to U and hence older ages (White and Ireland, 2012). To evaluate the effect of metamictization in baddeleyite on SIMS oxygen isotope measurements, Raman spectra of baddeleyite were used to assess the degree of metamictization within the analyzed crystals and determine whether metamictization could be a cause of oxygen isotopic variation during SIMS analysis.

Raman spectroscopy is a technique that identifies low frequency modes within a crystallographic system and is highly sensitive to the short-range order of the analyzed material. Raman bands are broadened and shifted towards lower wavenumbers in response to metamictization. These features can be directly correlated with α-dose in zircon (Nasdala et al., 1998; 2001; 2003) and similar behavior is anticipated for baddeleyite.

Baddeleyite has a space group of $P2_1/c$ and a point group C_{2h}, standard group theory predicts that it should have 36 modes at the Γ point (the Brillouin zone), 18 of the modes should be Raman- active ($9A_g$ and $9B_g$), the remaining modes are non-Raman-active infrared modes and frequency translational modes (Anastassakist et al., 1974). The Raman modes A_g and B_g are individual Raman tensors (Loudon, 1964), which produce frequencies that can be related to crystal orientation (Ishigame and Sakurai, 1977). For this reason we focus on the A_g Raman band which occurs at a frequency of ~470 cm^{-1} because it is a strong band in all crystal orientations and therefore easy to measure (Phillippi and Mazdiyasni, 1971; Ishigame and Sakurai, 1977), and we

use the FWHM and frequency of the peak to investigate the effect of metamictization on oxygen isotopes measured by SIMS.

The effect of metamictization on oxygen isotope analysis by SIMS was investigated by analyzing a portion of Phalaborwa S0045 grain fragments which were annealed at 1000°C for 48 hours and comparing the results to non-annealed grains (annealed grains are referred to as S0045D). The Raman spectra from the annealed fragments (Fig. 2.2a) show a narrowing of all bands, and a much flatter background characteristic of a more crystalline material. Annealed (S0045D) grains also had a much more consistent band frequency with a higher wave number and a lower FWHM than the non-annealed grains (Fig. 2.2b). They also had a FWHM of ~9 which is typical of intermediate crystalline material, whereas the FWHM of the metamict Phalaborwa S0045 was >12, which is considered metamict (Nasdala et al. 1995). The oxygen isotopic compositions of annealed and non-annealed grains are indistinguishable (Fig. 2.2c, Table 2.3) suggesting that metamictization does not have a discernable effect on the yield of oxygen isotopic compositions determined by SIMS.

2.4.2.2. Crystal orientation

U-Pb dating of baddeleyite by ion microprobe has previously indicated that grain orientation has an affect on the yield of Pb and U ions leading to imprecise and inaccurate $^{206}Pb/^{238}U$ ratios by ± 10 % (Wingate and Compston, 2000). Orientation-related matrix effects have also been discovered in isometric iron oxide minerals when analyzing oxygen isotopes by SIMS (e.g. Lyon et al., 1998; Huberty et al., 2010; Ickert and Stern unpublished data). The orientation-related fractionation is related to channeling of incident Cs^+ ions and focusing of secondary ions when the primary ion beam is parallel to the set of directions < uv0> from 110 to 100 in cubic minerals (Gnaser, 2007; Huberty et al., 2010). Orientation effects in the oxygen isotopic

system have not been reported for other oxide or silicate minerals. Orientation causes elemental fractionation during baddeleyite U-Pb analysis (Wingate and Compston, 2000) so we have investigated the possibility that crystal orientation could cause matrix effects in the SIMS oxygen measurements.

EBSD analyses were performed on grain fragments, which had previously been analyzed for oxygen isotopes by SIMS to investigate the relationship between crystal orientation and oxygen isotopic composition. Orientations of each of the crystallographic axes relative to the flat surface used for SIMS analysis were calculated using the polls of the 100, 010 and 001 planes. Comparing crystallographic orientation to $\delta^{18}O$ values produces no clear trend (Fig. 2.3a,b, Table 2.3) suggesting that there is no obvious orientation effect at the precision of the analyses achieved in this study. Oxygen isotopic compositions would be expected to vary in a sinusoidal pattern with orientation if there was a detectable effect. Another potential orientation-related feature that needs to be evaluated is the common occurrence of twinning in baddeleyite crystals. Twinned crystals produce two or more orientations of each crystallographic axis and in these cases, the dominant orientation was chosen. Choosing between the orientations in this way simplifies the relationship between crystallographic orientation and the primary ion beam, however since the range of oxygen isotopic analyses for Phalaborwa S0045 and S0045D falls within the expected range, any orientation related bias is likely to be small.

One unexpected consequence of acquiring EBSD data for baddeleyite was the discovery of the heterogeneous distribution of metamictization, providing insight into the spatial aspects of recrystallization from a metamict state. EBSD only produces orientation information when the material analyzed is crystalline at a scale of >50 nm. Phalaborwa S0045 grains produce a patchy EBSD response (white space in Fig. 2.3c,

3d) suggesting that there are heterogeneously distributed areas of amorphous material at >50 nm. The EBSD results complement the Raman data for S0045, confirming a disordered structure. However, the annealed grains (S0045D), which show a high degree of crystallinity by Raman (Fig. 2.2), show large areas of no response by EBSD (Fig. 2.3c). This is likely attributed to heterogeneous recrystallization of baddeleyite during the annealing at slightly different length scales. Nasdala et al. (2002) show that during annealing of metamict zircon, nanocrystals are the first crystalline material to form at 950 °C with lengths of <50 nm. In the baddeleyite fragments annealed at 1000 °C, nanocrystalline material is likely to have formed, and if the crystal size is <50 nm it would be too small to produce a detectable Kikuchi diffraction pattern. In the annealed crystals it is likely that the white areas with no EBSD response reflect areas where the recrystallization has produced nano-scale crystals <50 nm. The pink lines in Fig. 2.3c are possibly related to growth of large crystalline domains >50 nm, all in the same orientation, this arrangement is likely controlled by the pre-metamict orientation of the crystal.

Since the EBSD data is ambiguous regarding the relationship between oxygen isotopic composition and crystallographic orientation, one more test was conducted. In this test, a mount of S0045 was analyzed for its oxygen isotopic composition by SIMS, it was then extracted, lightly polished to remove any surface debris produced during analysis, rotated 90° and placed back into mass spectrometer and the exact same points were reanalyzed. The results of the rotation test (Fig. 2.4, Table 2.3) indicate that most of the data (21 out of 26) show no orientation effect. Five analyses however produce different $\delta^{18}O$ values after rotation, outside of analytical uncertainty. These 5 analyses (green points in Fig. 2.4) indicate that there is a slight orientation effect, and the magnitude of the effect is <0.12 ‰. However, it is also possible that since each analysis before and after rotation ablate a small portion of the sample,

the two analyses are not on the exact same material and therefore the analyses could be measuring real $\delta^{18}O$ variation within the crystal. Therefore, orientation related matrix effects may be present although their effects are likely to be subtle.

2.4.3. Calibrations/Standardization

Up to this point, all analyses presented have been analyzed such that the RM used to calibrate instrumental mass fractionation (IMF) and the unknown are the same material. For a true test of the accuracy of the SIMS oxygen isotope measurements, secondary RMs need to be used to ensure that the calibration calculated from the primary RM is applicable to other samples of the same mineral. The calculation for IMF for baddeleyite is relatively simple since it has limited solid solution (Table 2.1), and as discussed above the impact of metamictization and crystal orientation are negligible. Equation 2.1 in Kita et al. (2009) defines $\alpha^{18}O_{SIMS}$ to describe the instrumental bias of the measured oxygen isotopic composition versus the value on the VSMOW scale for a mineral of known $\delta^{18}O$ composition:

$$\alpha^{18}O_{SIMS} = \frac{1 + (\delta^{18}O_{RAW}/1000)}{1 + (\delta^{18}O_{VSMOW}/1000)} \quad (2)$$

A preliminary $\delta^{18}O^*$ value for each unknown is then calculated using $\alpha^{18}O_{SIMS}$ from the RM and equation 2.5 from Kita et al. (2009):

$$\delta^{18}O^* = \{\frac{1 + (\delta^{18}O_{RAW}/1000)}{\alpha^{18}O_{SIMS} - 1}\} * 1000 \quad (3)$$

$\delta^{18}O^*$ is equivalent to $\delta^{18}O_{VSMOW}$ if the bias is the same for both the RM and the unknown. Fig. 2.5 shows $\Delta = \delta^{18}O^* - \delta^{18}O_{VSMOW}$ for Phalaborwa S0045 and Mogok

S0069 when they are analyzed as unknowns using the $\alpha^{18}O_{SIMS}$ correction from the other mineral (i.e. S0045 is analyzed as an unknown with S0069 as the RM), and indicates that there is an unaccounted component of bias between the LF oxygen isotopic compositions and SIMS. Essentially, the difference in LF $\delta^{18}O$ values between S0045 and S0069 is ~16.55 ‰ whereas it is ~15 ‰ when measured using SIMS. The bias is different for S0045 (~1.5 ‰) and S0069 (~1 ‰), but suggests that the $\delta^{18}O_{VSMOW}$ for baddeleyite can only be determined to ± ~1 ‰, which is by far the largest source of uncertainty.

The heterogeneous $\delta^{18}O$ composition of Phalaborwa S0045 and Mogok S0069 (Fig. 2.1) could potentially be invoked to explain the bias. If just one crystal of the RM is used, there is no way to know what the exact isotopic composition of that crystal is, therefore it could have a composition anywhere within the known range. In this case, the error on the $\delta^{18}O$ value of the RM should reflect the range of isotopic composition (0.95 ‰ for S0045) and should be propagated as a component of the uncertainty to the unknown. To reduce the uncertainty associated with the heterogeneous RM, multiple fragments of each primary RM were tested prior to selecting the grain/grains for standardization to ensure that only grains with a median composition were used. These grains were then assumed to represent the median value of the crystal. After normalizing to a median-value grain, the unknowns should plot with a median value at 0Δ ‰ (Fig. 2.5, Table 2.4) and a range that reflects the isotopic heterogeneity of the sample, which is clearly not the case.

The calibration bias, identified here is at odds with most other minerals with simple chemistry analyzed by SIMS for oxygen isotopes (e.g. Kita et al., 2010). As it is unlikely that the bias is related to metamictization (Fig. 2.2), mineral chemistry (Table 2.1), or crystal orientation (Fig. 2.3 and 2.4), it could be related to some difference

in sputtering process between the two baddeleyite crystals. However, neither S0045 nor S0069 show evidence of an enlarged range of oxygen isotopic composition when analyzed on their own.

Bias could be created by a poorly understood mechanism of channeling and focusing of ions during the sputtering process, or possibly by trace-element variations between the samples. The Mogok and Phalaborwa baddeleyites however contain relatively low trace-element abundances with only Nb, Ta and U at over 500 ppm (Table 2.1) and most elements significantly lower, ~1 ppm suggesting that trace-element variations are unlikely to be the cause for SIMS bias. Potential avenues for future research into this effect could be varying the analytical parameters such as 1) varying the accelerating voltages of the primary and secondary beams, 2) changing the impact energy or 3) applying an energy offset, to see how these effect the calibration bias (e.g. Huberty et al. 2010), and looking in detail at the trace-element variation in the baddeleyite. In order to effectively answer these questions, other homogeneous baddeleyite crystals with a known oxygen isotopic composition are needed.

The final possible explanation for the calibration bias is related to the LF process. The S0045 samples sent for LF were all small (< 250 μm) multi grain aliquots since the original large crystal had already been crushed whereas the samples from S0069 were all larger single grain aliquots. A crystal size effect during LF analysis has been previously identified during analysis of SiO_2 (Fouillac and Girard, 1996) where small multi grain aliquots consistently record lower $\delta^{18}O$ values than individual larger grains. Using a defocused laser beam at full power to rapidly heat the sample significantly reduces this effect (Spicuzza et al. 1998), which is the technique used here. A crystal size effect is therefore unlikely to cause the bias seen between the LF and SIMS data, although the crystal size effect with baddeleyite has not been

specifically investigated. A bias towards lower $\delta^{18}O$ values for S0045 by ~1 ‰, would explain the difference between LF and SIMS oxygen isotopic results

Jumping of S0045 small grains was noticed during laser heating, which can be caused by the presence of fluid inclusions inside the grain reacting with the BrF_5 gas (see Trail et al. 2005). If the fluid had a low $\delta^{18}O$ composition, mixing between the baddeleyite and fluid would bias the results towards lighter isotopic compositions and explain the bias shown here, although an anonymously large mass of fluid would be required to shift the baddeleyite oxygen isotopic composition. Assuming that the fluid inclusions have a relatively constant oxygen isotopic composition, and that they are homogeneously distributed throughout the crystal, the LF results should still record the range in $\delta^{18}O$ composition of the crystal, however the absolute value could be biased.

It is unclear what the exact cause of the bias between the LF and SIMS data is caused by, at present, however, as shown below, the bias in the SIMS data appears to be consistent between samples.

2.5. A Test Case: The Duck Lake Sill

Another way to assess the calibration bias is to investigate whether the measured oxygen isotope composition of two cogenetic minerals follows the laws of high temperature stable isotopic fractionation in natural samples (Chacko et al. 2001). Rocks with both baddeleyite and zircon are ideal for this test since both minerals crystallize at high temperatures in igneous rocks, and zircon is known to be relatively robust to secondary processes that might affect its oxygen isotopic composition, e.g.

metamorphism and hydrothermal alteration (Valley 2003). If baddeleyite and zircon are in oxygen isotopic equilibrium, then their oxygen isotopic compositions should vary as a function of temperature based on the simplified equation:

$$\delta^{18}O_{zircon} - \delta^{18}O_{baddeleyite} \approx A_{zircon\text{-}baddeleyite}(10^6/T^2) \quad (4)$$

where A is the fractionation factor between zircon and baddeleyite, and T is temperature in Kelvin. The temperature coefficient of the fractionation factor, A, can be estimated in cases where it has not been determined by laboratory experiments (i.e. for zircon-baddeleyite) using bond strength methods (see Chacko et al., 2001). Assuming the minerals are in high temperature (>600 °C) equilibrium, the calculated fractionation factor can be used to compare with the $\delta^{18}O_{zircon} - \delta^{18}O_{baddeleyite}$ (equation 3) measured by SIMS and can be used as an independent tool to estimate the mass spectrometer bias (and possibly eventually as a thermometer).

Another benefit of comparing baddeleyite-zircon pairs, is that there are other independent indicators that show that baddeleyite and zircon should be in oxygen isotopic equilibrium; 1) identical U-Pb ages and 2) lack of discordance. Identical U-Pb ages prove that zircon and baddeleyite crystallized at the same time, a feature that is often assumed and not proven during stable isotopic studies on other mineral pairs. U-Pb discordance can be a useful tool to quantify the degree of secondary hydrothermal alteration in zircon (and possibly baddeleyite). Fluid alteration is a common process that can induce Pb-loss (Sinha et al., 1992; Valley et al., 1994; Geisler and Schlercher, 2000; Pidgeon et al., 2013), and also leads to disturbance in the oxygen isotopic system in zircon (and likely baddeleyite) (Valley et al. 1994). Therefore baddeleyite and zircon crystals that have concordant identical U-Pb ages are likely to be in high temperature equilibrium, and potentially retain equilibrium

oxygen isotopic fractionations.

The DLS is an excellent natural sample for testing equilibrium fractionation between a magmatic zircon-baddeleyite pair and to further investigate the bias between SIMS and LF baddeleyite oxygen isotopes. Both DLS baddeleyite and zircon have been dated by TIMS U-Pb techniques and are concordant or close to concordant (Fig. 2.6). They produce a weighted mean $^{207}Pb/^{206}Pb$ age of 2181±2 Ma (Bleeker and Kamo, 2003; Bleeker et al., 2007), which indicates that both minerals formed at the same time and are not significantly affected by secondary hydrothermal alteration or metamorphism.

The backscattered electron images of zircon from the sill (Fig. 2.7a) suggest that there has been some alteration since there are thin alteration rims on some grains, and along some cracks. This alteration could be the cause of the discordant zircon U-Pb analysis that was rejected from the age regression (Bleeker and Kamo, 2003).

Oxygen isotope analysis of fresh areas within the zircon crystals indicate that there has been very little oxygen isotopic exchange and the zircon oxygen isotope analyses plot as a simple Gaussian distribution with a mean $\delta^{18}O$ of 5.7 ± 0.1 ‰ (Fig. 2.7d, Table 2.5). Since the DLS zircons have a slightly higher $\delta^{18}O$ than average mantle derived zircons (~5.3 ‰, Valley, 2003) it is possible that the sill cannibalized some component of high $\delta^{18}O$ continental crust during emplacement and the zircons crystallized after the magma had become enriched in ^{18}O. Hydrothermal alteration could also raise the $\delta^{18}O$ composition of the zircon away from a typical mantle value, however, we do not favor this interpretation because the majority of SIMS spot analyses were selected to avoid visible alteration. There was one area of visibly altered zircon that was analyzed and it yielded a more mantle-like composition ($\delta^{18}O$

of 5.55 ± 0.21 ‰), suggesting that the hydrothermal fluid in this case could have been depleted in ^{18}O.

Baddeleyite from the DLS shows no signs of visible alteration in backscattered electron imaging, unlike the co-existing zircon, and produces no CL response, likely indicating that the grains are highly metamict (Nasdala, 2001). It is impressive that the U-Pb results for baddeleyite are so close to concordant (Fig. 2.6) despite the apparent very high degree of metamictization. The oxygen isotopic composition of the baddeleyite from the DLS show a prominent mode at ~2.1 ‰ and then a tail to lighter values, with the lightest part of the crystal have a value of -1.07 ‰ (Fig. 2.7, Table 2.5). The overall distribution of baddeleyite oxygen isotope values is quite different to the coeval zircon.

It is possible to estimate the equilibrium isotopic fractionation between baddeleyite and zircon using the site potential method (Smyth and Clayton, 1988; Smyth, 1989), where the oxygen isotopic fractionation between two minerals is proportional to the strength of the cation - anion bond in the minerals. The expected isotopic fractionation between baddeleyite and quartz can be estimated by calculating the site potential of oxygen in baddeleyite and comparing it to known oxide - quartz equilibrium fractionation values (Fig. 2.8). The calculated baddeleyite quartz equilibrium oxygen isotopic fractionation is $1000 \ln \alpha_{(quartz- baddeleyite)} = 7.3 \times 10^6/T^2$ (Fig. 2.8), which can then be combined with the quartz - zircon isotopic fractionation of $1000 \ln \alpha_{(quartz- zircon)} = 3.0 \times 10^6/T^2$ from Keiffer (1982) to produce a $1000 \ln \alpha_{(zircon-baddeleyite)} = 4.3 \times 10^6/T^2$. Zircon - baddeleyite fractionations would therefore range between 3.7 - 2.0 ‰ in the temperature range 800 - 1200 °C.

The calculated high temperature fractionation factor overlaps with the main peak of the baddeleyite DLS data (grey box in Fig. 2.7d) which suggests that the majority of the baddeleyite analyses are in isotopic equilibrium with the zircon from the DLS. The DLS baddeleyite were calibrated using the S0069 RM and there is no evidence for a ~1.5 ‰ calibration bias when using S0069 as the RM, which suggests that calibration bias could be caused by an incorrect LF $\delta^{18}O$ for S0045. If the DLS baddeleyite are in equilibrium with the zircon, and the S0069 $\delta^{18}O$ value is correct, both of which are suggested by the data, then this study would be the first to show that baddeleyite can record of magmatic oxygen isotopic compositions.

If the majority of the baddeleyite oxygen data can be explained by high-temperature crystallization from a mafic magma, another explanation is required for the few baddeleyite data that trend towards isotopically light compositions (Fig. 2.7, Table 2.5). One possible explanation is isotopic exchange with low $\delta^{18}O$ waters at low temperature. Due to the northern latitude of the Duck Lake sill, meteoric water in the area has an isotopically light composition ($\delta^{18}O$ of -15 ‰ in Yellowknife, Gibson, 2001) and is likely to have been at this composition or lower during much of the Cenozoic. The hydrothermal alteration causing the low $\delta^{18}O$ isotopic exchange between meteoric water and baddeleyite is likely to have occurred recently since minerals are much more susceptible to isotopic and elemental exchange when they have experienced volume expansion due to metamictization (Geisler and Schleicher, 2000). This process would also explain the low $\delta^{18}O$ composition seen in the altered zircon (Fig. 2.7a), although it is interesting that the zircon is much more homogeneous in its oxygen isotope composition despite experiencing the exact same conditions. If exchange with low temperature meteoric water is the cause of the light oxygen isotope tail displayed by the DLS baddeleyite, the exchange (~15 % assuming meteoric water of ~-15 ‰) would be expected to cause significant Pb-loss,

as is the case for zircon (Valley et al., 1994). The concordia diagram (Fig. 2.6) shows some lead loss for one zircon analysis, which is expected due to the alteration seen in BSE imaging (Fig. 2.7), however all the baddeleyite U-Pb analyses plot close to concordia. The baddeleyite U-Pb results do trend away from concordia, however, if the crystals experience up to 15 % exchange in oxygen isotopes, their Pb isotopic composition should be severely compromised. Two explanations can be posited to explain this; 1) baddeleyite is significantly more retentive to Pb during hydrothermal alteration than zircon, or 2) the hydrothermally altered grains of baddeleyite were not analyzed during U-Pb analysis. The second option is the preferred explanation since, the grain with the greatest $\delta^{18}O^*$ variation (Fig. 2.7b) is a small slightly fractured crystal that would unlikely be selected for ID-TIMS U-Pb analysis.

Despite the presence of the isotopically light oxygen isotopic tail in the DLS baddeleyite dataset, the dominant feature is that most of the baddeleyite oxygen isotopes (plus the calibration bias) suggest high temperature oxygen isotopic equilibrium with zircon from the same magma. The inference from the DLS data set is that the same suite of baddeleyite crystals potentially record close to concordant U-Pb age information, the original oxygen isotopic composition of the magma, and information on secondary hydrothermal alteration.

2.6. Conclusions

In this study we have investigated for the first time the feasibility of baddeleyite SIMS oxygen isotope measurements. Repeat analysis of fragments from two baddeleyite megacrysts from Phalaborwa and Mogok indicate that SIMS oxygen isotope results are in good agreement with laser fluorination results and within spot precision (±

0.1 ‰) is excellent and comparable to zircon. However, these baddeleyite crystals are not homogeneous in their oxygen isotopic composition. Matrix effects, such as degree of metamictization and crystal orientation were evaluated and found to be negligible (~0.1 ‰). The main challenge with the current SIMS analysis protocol is uncertainty regarding the true $\delta^{18}O$ values of the RM. Additional research on potential baddeleyite standard material that has a more homogeneous oxygen isotopic composition is needed.

The oxygen isotopic compositions of baddeleyite and co-crystallizing zircon from the Duck Lake sill suggest that baddeleyite is in high temperature isotopic equilibrium with zircon and that the $\delta^{18}O$ value for the Mogok (S0069) RM may be correct. The combination of oxygen isotopes, U-Pb dating and imaging of the zircon and baddeleyite from the Duck Lake sill suggest that highly metamict baddeleyite can record original oxygen isotopic compositions that are in high temperature equilibrium with zircon. Also metamict baddeleyite maybe a sensitive indicator of hydrothermal alteration yet the same crystal suite can produce near concordant U-Pb age information.

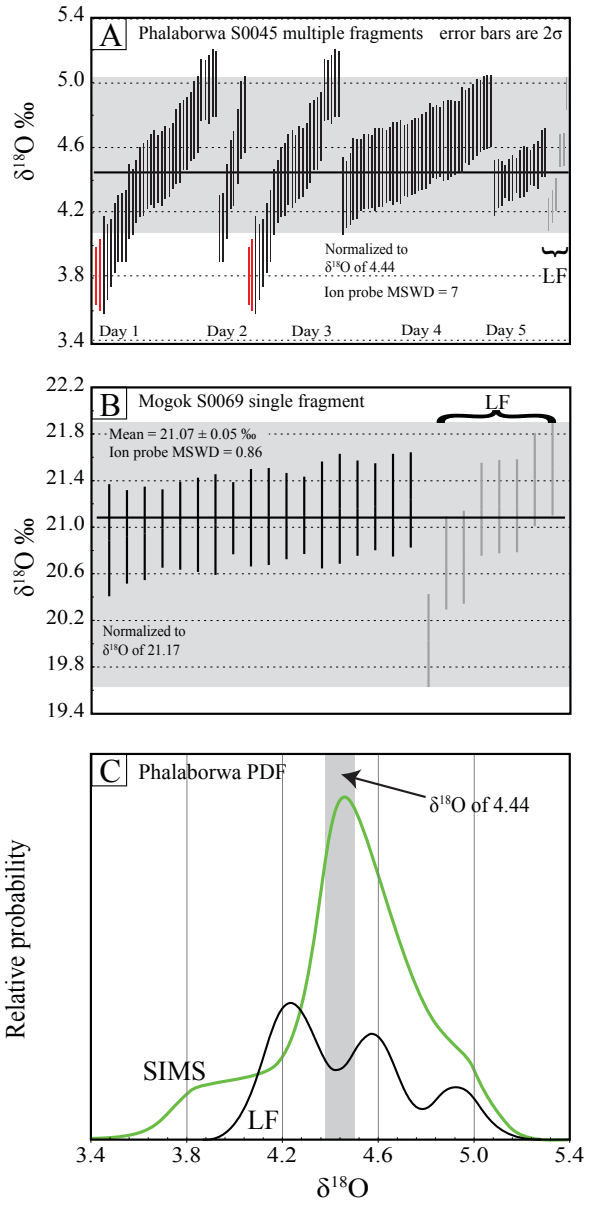

Figure 2.1. SIMS oxygen isotopes

SIMS oxygen isotope results from baddeleyite normalized to the median of the laser fluorination (LF) analyses for the same grain. A, randomly oriented fragments of Phalaborwa carbonatite baddeleyite grain S0045 analyzed over 5 analytical sessions by SIMS. The grey bar in the background is the full range including 2σ uncertainties on the LF $\delta^{18}O$, red SIMS analyses fall outside this range. B, multiple analyses of a single fragment of Mogok baddeleyite S0069. The analyses are normalized to the median of the LF analyses, the grey box in the background is the full range of S0069 $\delta^{18}O$ variation determined by LF. C, Probability density function (PDF) for the SIMS and LF analyses of S0045, the median of the LF results is marked.

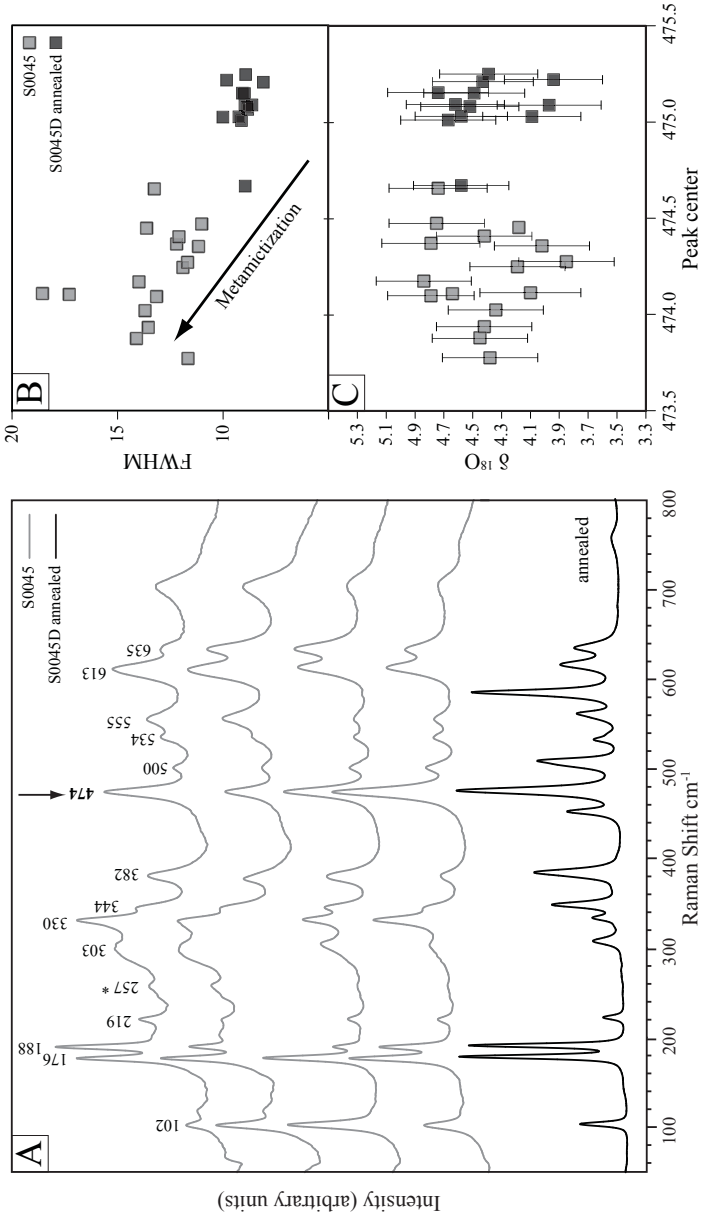

Figure 2.2. Metamictization

A, Representative Raman spectra from S0045 are shown in grey. Peaks matching those expected for monoclinic baddeleyite are numbered. Peak 474 is highlighted with an arrow, peak 257* is marked since this peak potentially corresponds with tetragonal ZrO_2 rather than monoclinic (Anastassakis et al. 1975). A representative Raman spectrum for fragments of Phalaborwa S0045 annealed at 1000°C for 48 hours is shown in black (S0045D), (S0045D spectra is almost identical to the Spectra from Mogok S0069). B, Full width at half maximum (FWHM) of peak ~474 nm is shown for annealed and un-annealed S0045 compared with the center of the peak. C, SIMS $\delta^{18}O$ values of areas analyzed by Raman spectroscopy compared with peak center ~474nm. Error bars are 2σ.

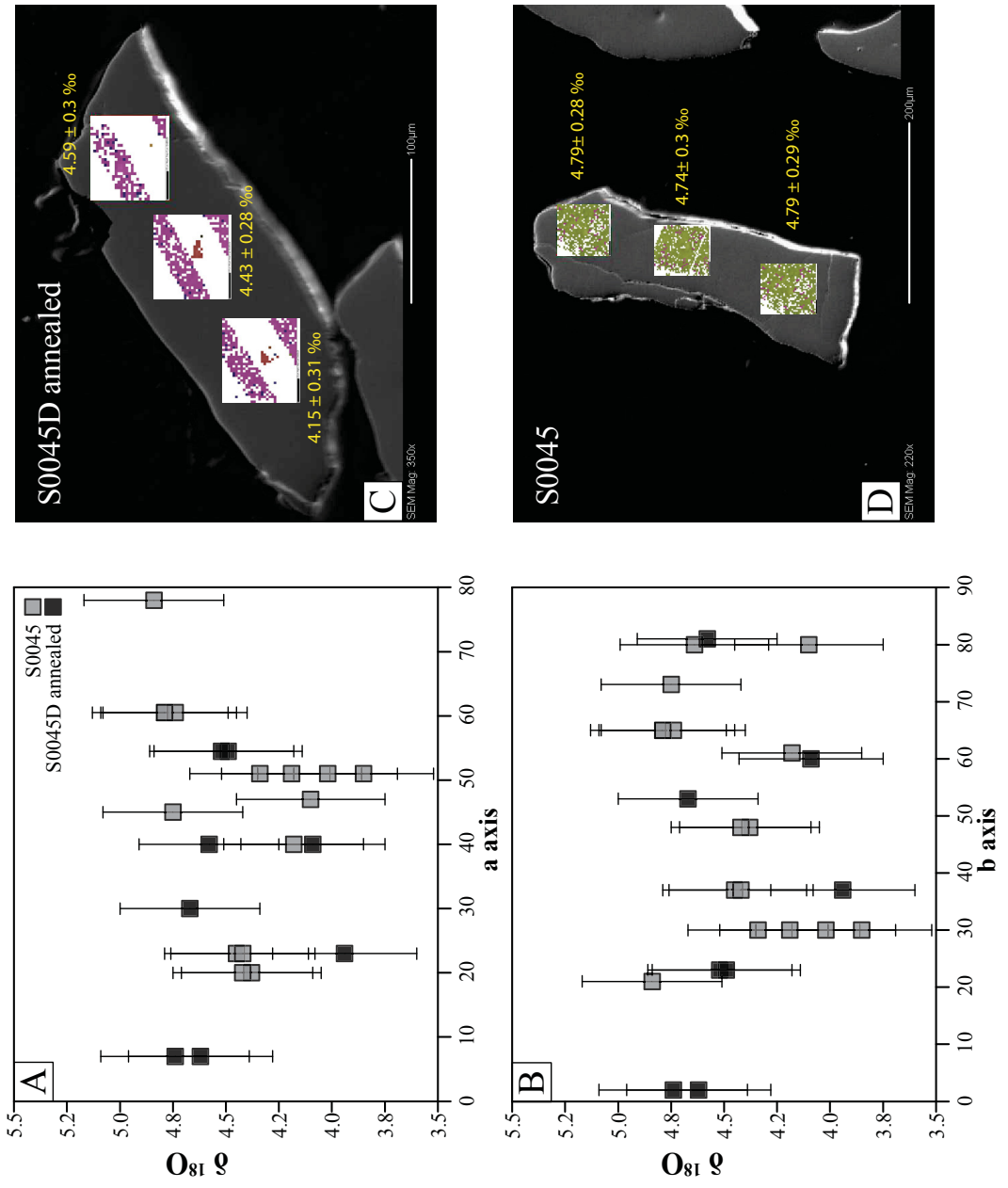

Figure 2.3. Orientation

A, orientation of (100) pole relative to the analyzed surface, compared with oxygen isotopic composition. B, oxygen isotopic composition compared with the orientation of the (110) pole. Error bars are 2σ. C, Secondary electron map of an annealed grain of S0045 with EBSD analysis in squares overlaid on the image. The color in the EBSD squares refers to a particular crystallographic orientation and is indexed to baddeleyite, white areas indicate no data. The $\delta^{18}O$ values from the same area as the EBSD analysis are shown. D, the same as C, but for a fragment of S0045 without annealing.

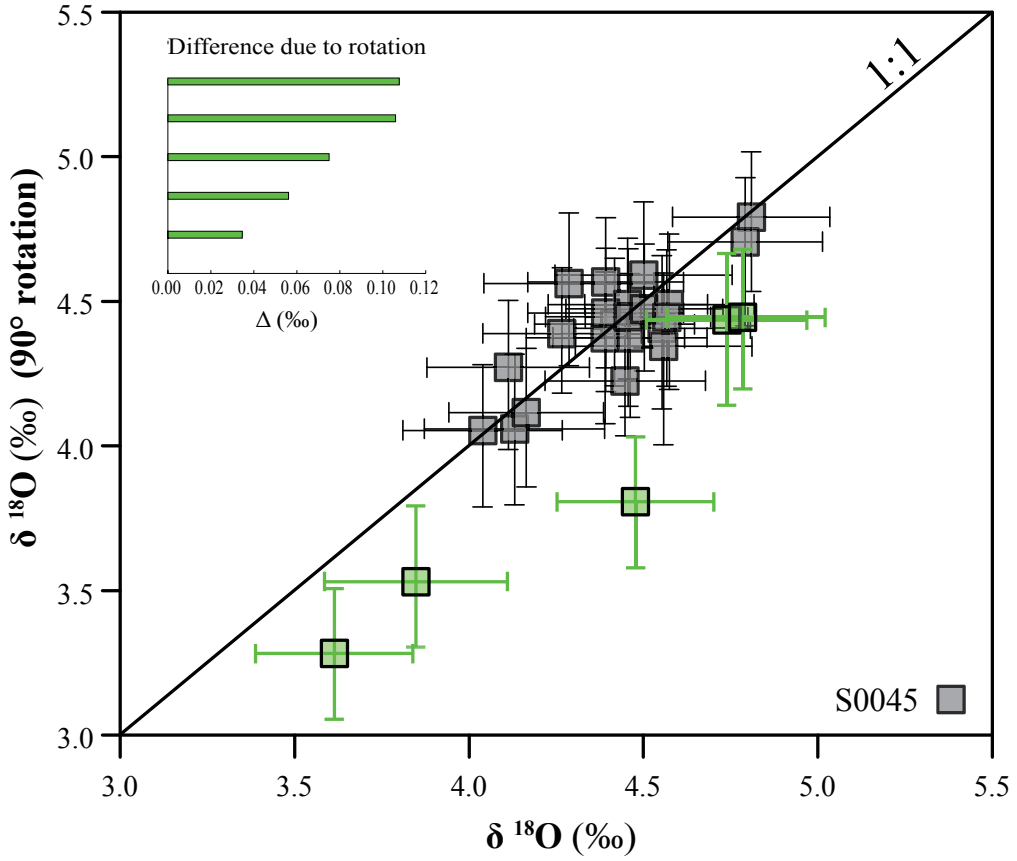

Figure 2.4. Orientation 2

$\delta^{18}O$ value for Phalaborwa S0045 verses the $\delta^{18}O$ value for the same spots reanalyzed after a 90° rotation of the mount. Black diagonal line shows the 1:1 ratio where orientation has not affected the $\delta^{18}O$ composition. Analyses highlighted in green have values that are different after rotation, outside of analytical uncertainties; the difference due to rotation (Δ) is shown for the 5 green analyses in the insert. All error bars are 2σ.

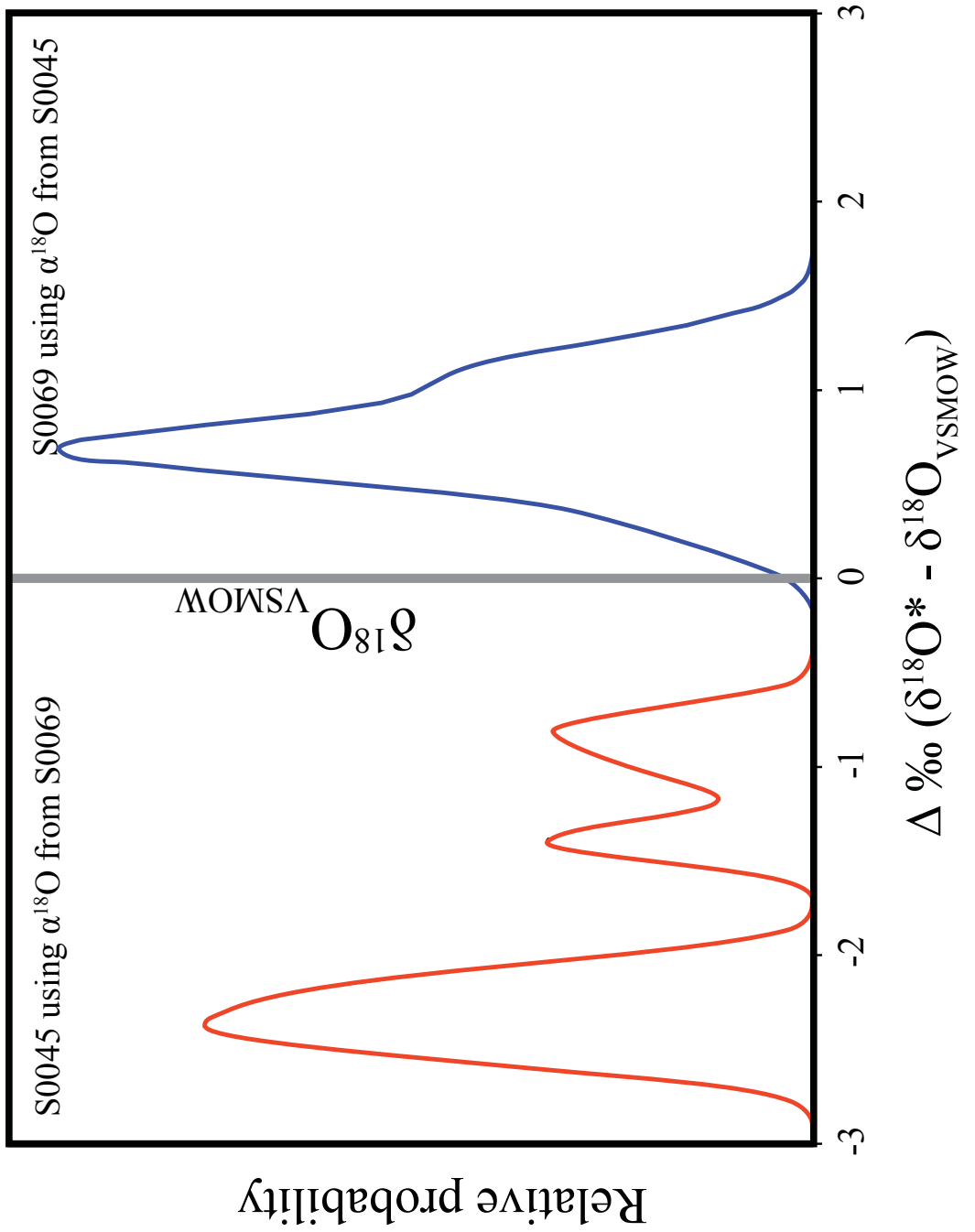

Figure 2.5. Possible calibration bias

Probability density function showing the Δ‰ ($\delta^{18}O^{*}$- $\delta^{18}O_{VSMOW}$) for Phalaborwa S0045 calculated using Mogok S0069 as the standard for calibration (Red) and Mogok S0069 using Phalaborwa S0045 as the standard (blue). The grey line at 0Δ ‰ shows the $\delta^{18}O$ value if there was no calibration bias, note that both probability density functions do not plot near 0‰.

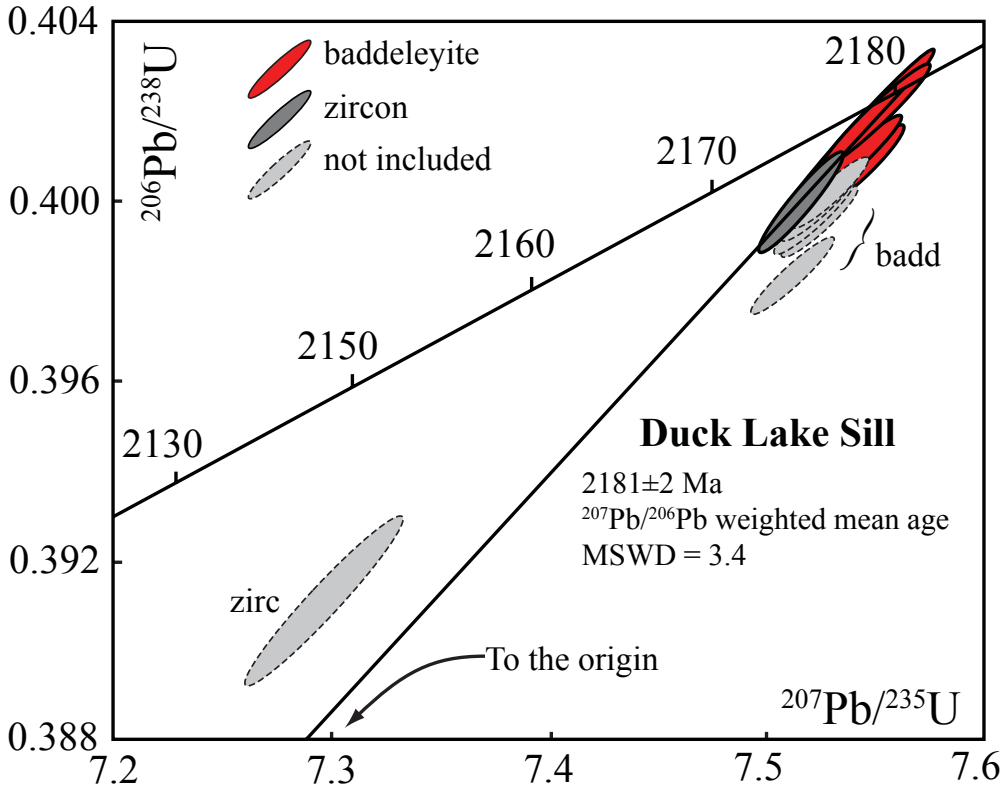

Figure 2.6. Duck Lake sill concordia diagram

Concordia diagram for the Duck Lake sill modified from Bleeker et al. (2007). 2181±2 Ma is a $^{207}Pb/^{206}Pb$ weighted mean age calculated using only the zircon and baddeleyite analyses with bold outlines.

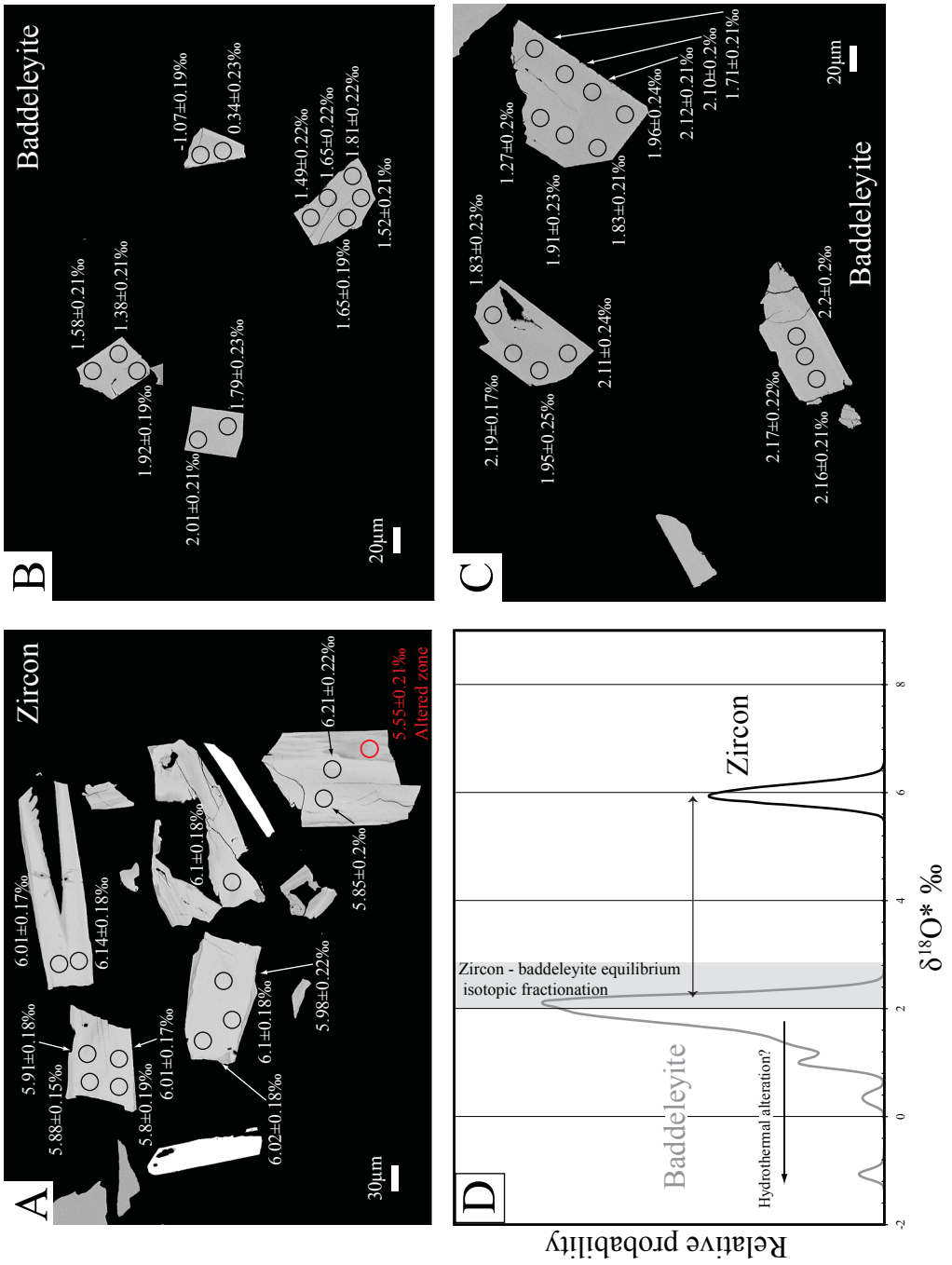

Figure 2.7. Duck Lake sill oxygen isotopic data

Oxygen isotopic data from the Duck Lake sill. A-C Representative backscatter electron images of zircon (A) and baddeleyite (B-C) before SIMS analysis. Ion probe spots are located as well as the $\delta^{18}O$ values and 2σ errors (zircon) and the $\delta^{18}O^*$ and 2σ errors (baddeleyite). D, probability density plot of oxygen isotopes from zircon (black $\delta^{18}O$) and baddeleyite (grey $\delta^{18}O^*$) including 2σ error. Grey box indicates the oxygen isotopic composition of baddeleyite in equilibrium with zircon.

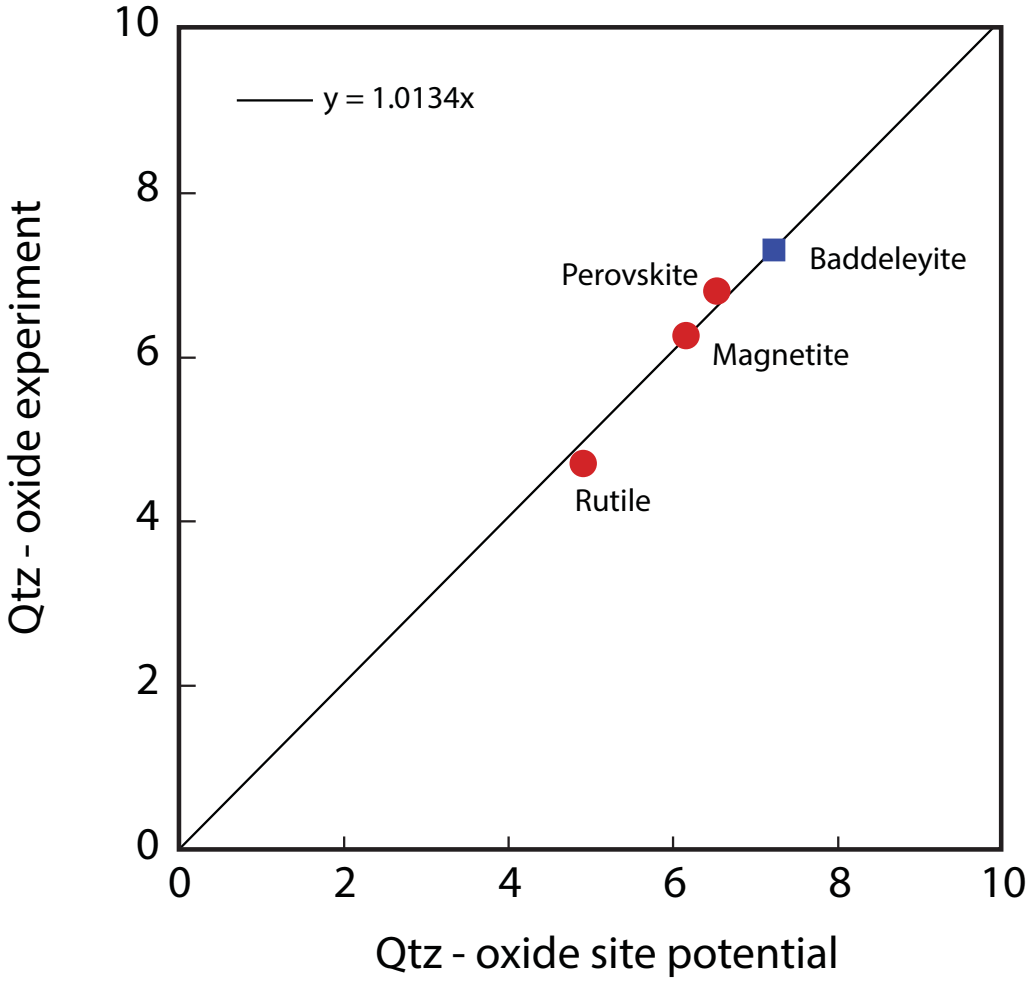

Figure 2.8 Oxygen isotopic fractionation between quartz and oxide minerals using the site potential method

Comparison of bond strength and experimental oxygen isotopic fractionation factors between oxide minerals and quartz. The regression line through the data is forced through the origin. Experimental data are from Chiba et al. (1989), Gautason et al. (1993) and Chacko et al. (1996). Site potential calculations are from Smyth (1989) and the figure is modified from Chacko et al. (2001).

	Mogok (S0069)	Phalaborwa (S0045)		Zircon Standards	
(wt.%)	averagea	averageb	Heaman, 2009c	Temorad	Mudtanke
ZrO2f	97.68 (0.35)	97.89 (0.23)	97.92	64.94 (0.27)	64.83 (0.37)
HfO2g	1.83 (0.06)	1.92 (0.05)	1.79	1.19 (0.07)	1.35 (0.06)
SiO2h	0.00 (0.00)	0.01 (0.01)	0.05	32.91 (0.08)	32.99 (0.07)
TiO2i	0.5 (0.13)	0.42 (0.09)		0.01 (0.01)	0.01 (0.01)
UO2j	0.11 (0.08)	0.01 (0.02)	0.07	0.01 (0.01)	0.00 (0.00)
Nb2O5k	0.08 (0.06)	0.06 (0.06)		0.03 (0.04)	0.02 (0.04)
Total	100.32 (0.37)	100.43 (0.25)	99.83	99.21 (0.22)	99.28 (0.4)
(ppm)	l	m	n	NIST 612o	% devation from recommended value
Sc	283 (14)	417 (35)	243	41.0	0.1
Sr	0.1 (0.1)	2 (4)		76.2	2.7
Y	6 (2)	16 (3)	12	38.2	0.4
Nb	897 (187)	354 (129)	422	38.2	4.6
Ba	0.2 (0.4)	6 (10)		37.7	4.9
Ag	83 (19)	81 (11)		21.9	0.3
La	0.4 (0.7)	0.4 (0.5)	0.6	35.7	0.3
Ce	0.1 (0.1)	6 (2)	4.1	38.3	0.4
Pr	0.2 (0.3)	0.3 (0.5)	0.23	37.1	0.1
Nd	1.4 (3.4)	1.2 (1.9)	0.99	35.4	2.1
Sm	0.2 (0.3)	0.5 (0.8)	1.3	36.6	3.9
Eu	0.1 (0.1)	0.2 (0.2)	0.35	34.4	1.9
Gd	0.2 (0.3)	0.9 (0.6)	1.7	36.8	0.6
Tb	0.05 (0.1)	0.2 (0.1)	0.36	35.9	0.5
Dy	0.2 (0.3)	2 (0.6)	2.6	35.9	0.1
Ho	0.1 (0.1)	0.5 (0.1)	0.73	37.7	0.6
Er	0.1 (0.2)	1.9 (0.5)	2.2	37.3	2.0
Tm	0.04 (0.04)	0.4 (0.1)	0.4	37.4	1.4
Yb	0.2 (0.3)	2.9 (0.8)	3.7	39.8	1.6
Lu	0.04 (0.04)	0.5 (0.1)	0.53	37.6	1.8
Ta	500 (128)	148 (69)	139	39.6	0.9
Pb	0.9 (1.4)	1.7 (2.3)		39.0	1.6
Th	0.3 (0.4)	7.9 (13.1)	8	37.1	1.9
U	2030 (393)	417 (200)	702	37.2	1.4

numbers in brackets refer to 1σ a, average of 40 WDS analyses of multipul Mogok crystals b, average of 40 WDS analyses of multipul Phalaborwa crystals c, average based on 29 laser ablation quadrupole ICP-MS anayses of a single crystal d, average based on 29 analyses e, average based on 30 analyses f, standardized using ZrO2 h, standardized using hafnon i, standardized using rutile j, standardized using UO2 k, standardized using Nb metal l, average based on 23 laser analyses m, average based on 32 laser analyses n, trace-element values of Phalaborwa reported by Heaman, (2009) o, average of 7 analyses of NIST 612 obtained during analytical session

Table 2.1. Baddeleyite chemistry

Trace-element compositions of Mogok and Phalaborwa baddeleyite

Phalaborwa (S0045)													
Laser Fluorination		Analytical Session 1		Analytical Session 2		Analytical Session 3		Analytical Session 4		Analytical Session 5		Analytical Session 6	
		aM0128		aM0039		aM0128		aM0073C		aM0120		aM0175	
		bIP12105		bIP12105		bIP10123A		bIP1101B		bIP12037		bIP13092	
δ18O	2σ (‰)	δ18O	2σ (‰)	δ18O	2σ (‰)	δ18O	2σ (‰)	δ18O	2σ (‰)	δ18O	2σ (‰)	δ18O	2σ (‰)
4.18	0.20	3.80	0.18	4.10	0.21	3.80	0.18	4.30	0.24	4.34	0.17	3.95	0.23
4.23	0.20	3.81	0.22	4.10	0.21	3.81	0.22	4.30	0.21	4.37	0.15	3.95	0.23
4.31	0.20	3.87	0.30	4.26	0.23	3.87	0.30	4.34	0.22	4.37	0.14	4.15	0.20
4.58	0.20	3.89	0.23	4.43	0.21	3.89	0.23	4.40	0.25	4.39	0.10	4.23	0.23
4.58	0.20	3.94	0.21	4.46	0.23	3.94	0.21	4.40	0.25	4.40	0.13	4.32	0.22
4.93	0.20	4.04	0.22	4.60	0.23	4.04	0.22	4.43	0.22	4.41	0.14	4.32	0.22
		4.10	0.21	4.77	0.24	4.11	0.22	4.45	0.23	4.42	0.11	4.32	0.22
		4.10	0.21	4.80	0.24	4.26	0.20	4.45	0.23	4.43	0.15	4.32	0.22
		4.11	0.22			4.33	0.19	4.45	0.22	4.45	0.15	4.37	0.25
Median for calib	4.44	4.26	0.23			4.39	0.22	4.46	0.26	4.46	0.14	4.41	0.21
		4.26	0.20			4.40	0.22	4.47	0.24	4.47	0.11	4.44	0.23
		4.33	0.19			4.46	0.22	4.47	0.24	4.49	0.13	4.44	0.23
		4.39	0.22			4.46	0.24	4.48	0.22	4.49	0.15	4.45	0.24
		4.40	0.22			4.46	0.21	4.49	0.23	4.56	0.14	4.53	0.23
		4.43	0.21			4.50	0.22	4.50	0.25	4.57	0.15	4.53	0.24
		4.46	0.22			4.51	0.21	4.50	0.25			4.54	0.20
		4.46	0.24			4.54	0.20	4.51	0.26			4.56	0.22
		4.46	0.21			4.62	0.25	4.52	0.22			4.57	0.24
		4.46	0.23			4.67	0.21	4.52	0.22			4.57	0.24
		4.50	0.22			4.69	0.22	4.53	0.23			4.64	0.22
		4.51	0.21			4.73	0.21	4.54	0.23			4.64	0.22
		4.54	0.20			4.95	0.19	4.55	0.22			4.71	0.23
		4.60	0.23			4.95	0.18	4.57	0.23				
		4.62	0.25			4.96	0.21	4.58	0.23				

		M1028		M0039		M0128		M0073C		M0120		M0175	
		IP12105		IP12105		IP10123A		IP1101B		IP12037		IP13092	
		4.67	0.21			4.99	0.21	4.62	0.25				
		4.69	0.22			4.99	0.20	4.63	0.22				
		4.73	0.21					4.63	0.23				
		4.77	0.24					4.63	0.22				
		4.80	0.24					4.64	0.24				
		4.95	0.19					4.64	0.24				
		4.95	0.18					4.65	0.24				
		4.96	0.21					4.65	0.23				
		4.99	0.21					4.66	0.22				
		4.99	0.20					4.71	0.26				
								4.73	0.22				
								4.73	0.24				
								4.76	0.23				
								4.78	0.24				
								4.79	0.22				
								4.81	0.23				
								4.82	0.23				
								4.82	0.22				

Mogok (S0069)					
Laser Fluorination		Analytical session 5		Analytical session 6	
		aM0120		aM0175	
		bIP12037		bIP13092	
δ18O	2σ (‰)	δ18O	2σ (‰)	δ18O	2σ (‰)
20.03	0.20	20.89	0.24	21.40	0.25
20.69	0.20	20.92	0.20	21.52	0.23
20.74	0.20	20.95	0.20	21.64	0.23
21.15	0.20	20.99	0.17	21.67	0.24
21.18	0.20	21.01	0.19	21.71	0.21
21.18	0.20	21.02	0.20	21.76	0.24
21.41	0.20	21.02	0.22	21.81	0.24
21.50	0.20	21.08	0.15	21.82	0.21
		21.08	0.21	21.93	0.24
Median for calib	21.17	21.09	0.21	21.97	0.23
		21.10	0.18	21.98	0.22
		21.10	0.17	22.02	0.22
		21.10	0.23	22.06	0.25
		21.16	0.24	22.08	0.22
		21.16	0.20	22.08	0.24
		21.18	0.19	22.11	0.23
		21.19	0.22	22.31	0.21
		21.23	0.20	22.31	0.26

δ18O
(‰)=((18O/16OSample)/(18O/16OVSMOW)−1)*1000 18O/16OVSMOW =0.0020052 (Baertschi, 1976).
2σ (‰) is the internal error
Phalaborwa and Mogok analyses were calibrated internally to the median values of the Laser Fluorination data
a = CCIM Mount number, b = CCIM Ion Probe number

Table 2.2. Oxygen isotope data

SIMS oxygen isotope results from Phalaborwa and Mogok baddeleyite

Phalaborwa							
S0045		S0045Da		S0045b		S0045c	
		Annealed at 1000°C		1st analysis		Rotated 90°	
δ18O	2σ (‰)	δ18O	2σ (‰)	δ18O	2σ (‰)	δ18O	2σ (‰)
3.55	0.30	3.56	0.28	3.28	0.11	3.61	0.22
3.85	0.28	3.94	0.29	3.81	0.17	4.48	0.22
3.87	0.30	3.97	0.31	3.89	0.14	3.79	0.24
3.90	0.30	4.09	0.29	4.05	0.13	4.04	0.23
3.93	0.30	4.15	0.31	4.06	0.13	4.13	0.26
3.98	0.28	4.19	0.29	4.12	0.13	4.16	0.22
4.02	0.28	4.22	0.30	4.23	0.10	4.45	0.23
4.18	0.27	4.28	0.29	4.27	0.14	4.11	0.23
4.19	0.28	4.36	0.30	4.34	0.17	4.56	0.25
4.20	0.29	4.37	0.30	4.37	0.15	4.39	0.23
4.28	0.28	4.39	0.29	4.37	0.14	4.46	0.22
4.34	0.28	4.43	0.28	4.39	0.10	4.27	0.23
4.38	0.27	4.45	0.30	4.41	0.14	4.55	0.25
4.42	0.28	4.49	0.31	4.42	0.11	4.42	0.23
4.42	0.29	4.50	0.27	4.43	0.15	4.74	0.23
4.45	0.29	4.52	0.29	4.44	0.12	4.57	0.23
4.59	0.29	4.58	0.27	4.44	0.12	4.78	0.24
4.65	0.28	4.58	0.29	4.45	0.15	4.46	0.24
4.74	0.29	4.59	0.30	4.46	0.14	4.39	0.22
4.75	0.28	4.59	0.28	4.47	0.11	4.50	0.22
4.79	0.29	4.61	0.29	4.49	0.13	4.45	0.23
4.79	0.28	4.62	0.30	4.49	0.15	4.57	0.24
4.79	0.28	4.66	0.30	4.56	0.14	4.29	0.24
4.81	0.29	4.67	0.27	4.57	0.15	4.39	0.22
4.83	0.27	4.69	0.30	4.59	0.13	4.50	0.25
4.83	0.31	4.71	0.28	4.71	0.14	4.79	0.22
4.84	0.29	4.72	0.27	4.79	0.13	4.81	0.23
		4.74	0.27				

δ18O (‰)=((18O/16OSample)/(18O/16OVSMOW)−1)*1000 18O/16OVSMOW =0.0020052
2σ (‰), is the internal error
a, Phalaborwa crystal annealed at 1000°C for 48 hours to reduce the effects of metamictization
b, first analysis of Phalaborwa crystals
c, re-analysis of the same spots as (b) after a 90° rotation of the sample mount

Table 2.3. Rotation and annealing test data

Rotation and Annealing test

Phalaborwa (S0045)			Mogok (S0069)		
α18O from S0069			α18O from S0045		
δ18O*	2σ (‰)	Difference from LF median	δ18O*	2σ (‰)	Difference from LF median
3.00	0.18	-1.44	22.26	0.29	1.09
3.10	0.20	-1.34	22.43	0.29	1.26
3.42	0.24	-1.02	22.25	0.28	1.08
3.69	0.20	-0.75	21.93	0.30	0.76
2.19	0.20	-2.25	21.90	0.31	0.73
2.04	0.20	-2.40	22.16	0.28	0.99
1.95	0.25	-2.49	21.58	0.30	0.41
2.11	0.20	-2.33	21.73	0.28	0.56
2.00	0.19	-2.44	21.41	0.29	0.24
1.86	0.18	-2.58	21.85	0.28	0.68
2.37	0.21	-2.07	21.86	0.30	0.69
2.22	0.22	-2.22	21.81	0.30	0.64
2.31	0.21	-2.13	21.87	0.30	0.70
3.58	0.23	-0.86	21.90	0.29	0.73
formula for calculation of α18O and δ18O* are avaliable in the main article 2σ (‰), is the internal error laser flourination median for phalaborwa is δ18O = 4.47‰ and δ18O = 21.17‰ for Mogok					

Table 2.4. Calibration test data

Calibration results

Duck Lake baddeleyite		Duck Lake zircon	
α18O from S0069			
δ18O*	2σ (‰)	δ18OSMOW	2σ (‰)
-1.07	0.19	5.55a	0.21
0.34	0.23	5.75	0.18
0.94	0.23	5.80	0.19
0.95	0.17	5.85	0.20
1.03	0.19	5.88	0.15
1.08	0.19	5.91	0.18
1.26	0.20	5.95	0.19
1.27	0.20	5.98	0.22
1.38	0.21	6.01	0.17
1.41	0.20	6.02	0.18
1.49	0.22	6.10	0.18
1.52	0.21	6.14	0.18
1.58	0.21	6.21	0.22
1.65	0.22		
1.65	0.19		
1.71	0.21		
1.72	0.20		
1.79	0.23		
1.81	0.24		
1.81	0.22		
1.83	0.23		
1.83	0.21		
1.83	0.22		
1.89	0.19		
1.91	0.23		
1.92	0.19		
1.95	0.25		
1.95	0.16		
1.96	0.24		
2.01	0.21		
2.01	0.20		
2.04	0.23		
2.10	0.20		
2.10	0.20		
2.11	0.20		
2.11	0.24		
2.12	0.21		
2.16	0.21		
2.16	0.23		
2.17	0.22		
2.18	0.21		

2.19	0.17		
2.20	0.20		
2.22	0.23		
2.27	0.25		
2.34	0.19		
a = altered zone 2σ (‰), is the internal error formula for calculation of α18O and δ18O* are avaliable in the main article			

Table 2.5. Duck Lake sill oxygen isotope data

Duck lake sill baddeleyite and zircon results

References

Amelin, Y., Zaitsev, A. N., 2002. Precise geochronology of phoscorites and carbonatites: the critical role of U-series disequilibrium in age interpretations. Geochimica et Cosmochimica Acta 66, 2399-2419.

Anastassakis, E., Papanicolaou, B., Asher, I. M., 1975. Lattice dynamics and light scattering in hafnia and zirconia. Journal of Physics and Chemistry of Solids 36, 667–76.

Baertschi, P., 1976. Absolute ^{18}O content of standard mean ocean water. Earth and Planetary Science Letters 31, 341-344.

Bindeman, I., Gurenko, A., Sigmarsson, O., Chaussidon, M., 2008. Oxygen isotope heterogeneity and disequilibria of olivine crystals in large volume Holocene basalts from Iceland: evidence for magmatic digestion and erosion of Pleistocene hyaloclastites. Geochimica et Cosmochimica Acta 72, 4397–4420.

Bleeker, W., Kamo, S., 2003. A precise age for the Duck Lake sill and its relevance for fitting the Slave in a global Archean context. In: 31st Yellowknife Geoscience Forum, November 19-21, C.S. Lord Northern Geoscience Center, Yellowknife, Canada, Abstract 7-8.

Bleeker, W., LeCheminant, A.N., Davis, W.J., Buchan, K., Ketchum, J.W., Sircombe, K., Snyder, D., van Breemen, O., and Ootes, L., 2007. Transect across the southwestern Slave craton: From Phanerozoic platform edge to the core of the Yellowknife supracrustal domain. Geological Association of Canada, Field Trip Guidebook (A1), 232

Cavosie, A. J., Valley, J. W., Kita, N. T., Spicuzza, M. J., Ushikubo, T., Wilde, S. A., 2011. The origin of high $\delta^{18}O$ zircons: marbles, megacrysts, and metamorphism. Contributions to Mineralogy and Petrology 162, 961–74.

Chacko, T., Hu, X., Mayeda, T.K., Clayton, R.N., Goldsmith, J.R., 1996. Oxygen isotope fractionations in muscovite, phlogopite and rutile. Geochimica Cosmochimica Acta 60, 2595-2608.

Chacko, T., Cole, D. R., Horita, J., 2001. Equilibrium oxygen, hydrogen and carbon isotopic fractionation factors applicable to geologic systems. In: J.W. Valley, D.R. Cole (Eds.), Stable Isotope Geochemistry, Reviews in Mineralogy and Geochemistry, vol. 51, 1–81

Chamberlain, K. R., Schmitt, A. K., Swapp, S. M., Harrison, T. M., Swoboda-Colberg, N., Bleeker, W., Peterson, T. D., Jefferson, C. W., Khudoley, A. K., 2010. In situ U-Pb SIMS (in-SIMS) micro-baddeleyite dating of mafic rocks: method with examples. Precambrian Research 183, 379–87.

Cherniak, D.J., Watson, E.B., 2003. Diffusion in Zircon, In: Hanchar, J.M., Hoskin, P.W.O. (Eds.), Zircon: Reviews in Mineralogy and Geochemistry, vol. 53, pp. 113-143.

Chiba, H., Chacko, T., Clayton, R.N., Goldsmith, J.R., 1989. Oxygen isotope fractionations involving diopside, forsterite, magnetite and calcite: Application to geothermometry. Geochimica Cosmochimica Acta 53, 2985-2995.

Dawson, J. B., Hinton, R. W., 2003. Trace-element content and partitioning in calcite, dolomite and apatite in carbonatite, Phalaborwa, South Africa. Mineralogical Magazine 67, 921–930.

Eiler, J. M., Graham, C., Valley, J. W., 1997. SIMS analysis of oxygen isotopes: matrix effects in complex minerals and glasses. Chemical Geology 138, 221-244.

Ewing, R.C., Meldrum, A., Wang, L.M., Weber, W.J., Corrales, L.R., 2003. Radiation effects in zircon. In: Hanchar, J.M., Hoskin, P.W.O. (Eds.), Zircon: Reviews in Mineralogy and Geochemistry, vol. 53, 387–425.

Forster, I.F., 1958. Paragenetical ore mineralogy of the Loolekop- Phalaborwa carbonatite complex, eastern Transvaal. Transactions of the Geological Society of South Africa 61, 359-365.

Fouillac, A-M., Girard, J-P., 1996. Laser oxygen isotope analysis of silicate/oxide grain separates: Evidence for a grain size effect? Chemical Geology 130, 31-54.

Garnier, V., Giuliani, G., Ohnenstetter, D., Fallick, A. E., Dubessy, J., Banks, D., Vinh, H. Q., Lhomme, T., Maluski, H., Pêcher, A., Bakhsh, K. A., Long, P. V., Trinh, P. T., Schwarz, D., 2008. Marble-hosted ruby deposits from central and southeast Asia: towards a new genetic model. Ore Geology Reviews 34, 169-191.

Gautason, B., Chacko, T., Muehlenbachs, K., 1993. Oxygen isotope partitioning among perovskite ($CaTiO_3$), Cassiterite (SnO_2) and Calcite ($CaCO_3$). Geological Association of Canada Abstract Program, Edmonton, Alberta P A34.

Geisler, T., Schleicher, H., 2000. Improved U–Th–total Pb dating of zircons by electron microprobe using a simple new background modeling procedure and Ca as a chemical criterion of fluid-induced U–Th–Pb discordance in zircon. Chemical Geology 163, 269-285.

Geisler, T., Pidgeon, R.T., Van Bronswijk, W., Pleysier, R., 2001. Kinetics of thermal recovery and recrystallization of partially metamict zircon: a Raman spectroscopic study. European Journal of Mineralogy 13, 1163-1176.

Geisler, T., Pidgeon, R. T., Kurtz, R., van Bronswijk, W., Schleicher, H., 2003. Experimental hydrothermal alteration of partially metamict zircon. American Mineralogist 88, 1496-1513.

Gibson, J. J., 2001. Forest-tundra water balance signals traced by isotopic enrichment in lakes. Journal of Hydrology 251, 1-13.

Gnaser, H., 2007. Energy and angular distributions of sputtered species. Sputtering by particle bombardment: Topics in Applied Physics. Springer-Verlag, New York, pp. 231–328.

Hanchar, J. M., Rudnick, R. L., 1995. Revealing hidden structures: the application of cathodoluminescence and back-scattered electron imaging to dating zircons from lower crustal xenoliths. Lithos 36, 289–303.

Heaman, L., LeCheminant, A., 1993. Paragenesis and U-Pb systematics of baddeleyite (ZrO_2). Chemical Geology 110, 95–126.

Heaman, L., LeCheminant, A., 2000. Anomalous U-Pb systematics in mantle-derived baddeleyite xenocrysts from Île Bizard: evidence for high temperature radon diffusion? Chemical Geology 172, 77-93.

Heaman, L., 2009. The application of U-Pb geochronology to mafic, ultramafic and alkaline rocks: an evaluation of three mineral standards. Chemical Geology 261, 43-52

Hoskin, P., Schaltegger, U., 2003. The composition of zircon and igneous and metamorphic petrogenesis In: Hanchar, J.M., Hoskin, P.W.O. (Eds.), Zircon: Reviews in Mineralogy and Geochemistry, vol. 53, pp. 27-62.

Huberty, J. M., Kita, N. T., Kozdon, R., Heck, P. R., Fournelle, J. H., Spicuzza, M. J., Xu, H., Valley, J. M., 2010. Crystal orientation effects in δ18O for magnetite and hematite by SIMS. Chemical Geology 276 269–83.

Ishigame, M., Sakurai, T., 1977. Temperature dependence of the Raman spectra of ZrO_2. Journal of the American Ceramic Society 60, 367–69.

Jamtveit, B., Hervig, R. L., 1994. Constraints on transport and kinetics in hydrothermal systems from zoned garnet crystals. Science 263, 505–507.

Kita, N. T., Ushikubo, T., Fu, B., Valley, J. W., 2009. High precision SIMS oxygen isotope analysis and the effect of sample topography. Chemical Geology 264, 43–57.

Kita, N. T., Huberty, J. M., Kozdon, R., Beard, B. L., Valley, J. W., 2010. High-precision SIMS oxygen, sulfur and iron stable isotope analyses of geological materials: accuracy, surface topography and crystal orientation. Surface and interface analysis 43, 427–431.

Li, Q. L., Li, X. H., Liu, Y., Tang, G. Q., Yang, J. H., Zhu, W. G., 2010. Precise U–Pb and Pb–Pb dating of Phanerozoic baddeleyite by SIMS with oxygen flooding technique. Journal of Analytical Atomic Spectrometry 25, 1107-1113.

Lyon, I. C., Saxton, J. M., Cornah, S. J., 1998. Isotopic fractionation during secondary ionisation mass spectrometry: crystallographic orientation effects in magnetite. International Journal of Mass Spectrometry and Ion Processes 172, 115–122.

Nasdala, L., Wenzel, M., Vavra, G., Irmer, G., Wenzel, T., Kober, B., 2001. Metamictisation of natural zircon: accumulation versus thermal annealing of radioactivity-induced damage. Contributions to Mineralogy and Petrology 141, 125–144.

Nasdala, L., Pidgeon, R. T., Wolf, D., Irmer, G., 1998. Metamictization and U-Pb isotopic discordance in single zircons: a combined Raman microprobe and SHRIMP ion probe study. Mineralogy and Petrology 62, 1–27.
Nasdala, L., Legauer, C. L., Hanchar, J. M., Kronz, A., Wirth, R., Blanc, P., Kennedy, A. K., Seydoux-Guillaume, A. M., 2002. Annealing radiation damage and the recovery of cathodoluminescence. Chemical Geology 191, 121–140.

Nasdala, L. Zhang, M., Kempe, U., Panczer, G., Gaft, M., Andrur, M., Plötze, M., 2003. Spectroscopic methods applied to zircon. In: Hanchar, J.M., Hoskin, P.W.O. (Eds.), Zircon: Reviews in Mineralogy and Geochemistry, vol. 53, pp. 427-467.

Nasdala, L., Irmer, G., Wolf, D., 1995. The degree of metamictization in zircons: a Raman spectroscopic study. European Journal of Mineralogy 7, 471–478.

Page, F. Z., Ushikubo, T., Kita, N. T., Riciputi, L. R., Valley, J. W., 2007. High-precision oxygen isotope analysis of picogram samples reveals 2µm gradients and slow diffusion in zircon. American Mineralogist 92, 1772–1775.

Pidgeon, R.T., Nemchin, A.A., Cliff, J., 2013. Interaction of weathering solutions with oxygen and U–Pb isotopic systems of radiation-damaged zircon from an Archean granite, Darling Range Batholith, Western Australia. Contributions to Mineralogy and Petrology 166, 511-523.

Reischmann, T., Brügmann, G. E., Jochum, K. P., Todt, W. A., 1995. Trace-element and isotopic composition of baddeleyite. Mineralogy and Petrology 53, 155–164.

Rodionov, N. V., Belyatsky, B. V., Antonov, A. V., Kapitonov, I. N., Sergeev, S. A., 2012. Comparative in-situ U–Th–Pb geochronology and trace-element composition of baddeleyite and low-U zircon from carbonatites of the palaeozoic Kovdor alkaline–ultramafic complex, Kola Peninsula, Russia. Gondwana Research 21, 728–44.

Rossman, G.R., Smyth, J.R., 1990. Hydroxyl contents of accessory minerals in mantle eclogites and related rocks. American Mineralogist 75, 775-780.

Schärer, U., Corfu, F., Demaiffe, D., 1997. U-Pb and Lu-Hf Isotopes in baddeleyite and zircon megacrysts from the Mbuji-Mayi kimberlite: constraints on the subcontinental mantle. Chemical

Geology 143, 1–16.

Searle, M. P., Nobel, S. R., Cottle, J. M., Waters, D. J., Mitchell, A. H. G., Hlaing, T., Horstwood, M. S. A., 2007. Tectonic evolution of the Mogok metamorphic belt, Burma (Myanmar) constrained by U-Th-Pb dating of metamorphic and magmatic rocks. Tectonics 26, doi:10.1029/2006TC002083.

Sinha, A.K., Wayne, D.M., Hewitt, D.A., 1992. The hydrothermal stability of zircon: Preliminary experimental and isotopic studies. Geochimica et Cosmochimica Acta 56, 3551-3560.

Slodzian, G., 1975. Some problems encountered in secondary ion emission applied to elementary analysis. Surface Science 48, 161–186.

Smyth, J.R., 1989. Electrostatic characterization of oxygen sites in minerals. Geochimica Cosmochimica Acta 53, 1101-1110.

Smyth, J.R., Clayton, R.N., 1988. Correlation of oxygen isotope fractionations and electrostatic site potentials in silicates. EOS Transactions of the American Geophysical Union 69, 1514.

Söderlund, U., Johansson, L., 2002. A simple way to extract baddeleyite (ZrO_2). Geochemistry Geophysics Geosystems 3, doi: 10.1029/2001GC000212.

Spicuzza, M.J., Valley, J.W., Kohn, M.J., Girard, J-P., Fouillac, A-M., 1998. The rapid heating, defocused beam technique: a CO_2–laser-based method for highly precise and accurate determination of $\delta^{18}O$ values of quartz. Chemical Geology 144, 195-203.

Tanabe, K., Hiraishi, J., 1980. Correction of finite slit width effects on Raman line widths. Spectrochimica Acta, Part A: Molecular Spectroscopy 36, 341-344.

Taylor, R., Clark, C., Reddy, S.M., 2012. The effect of grain orientation on secondary ion mass spectrometry (SIMS) analysis of rutile. Chemical Geology 300-301, 81-87.

Trail, D., Bindeman, I,N., Watson, E.B., Schmitt, A.K., 2009. Experimental calibration of oxygen isotope fractionation between quartz and zircon. Geochimica et Cosmochimica Acta 73, 7110-7126.

Valley, J. W., Chiarenzelli, J. R., McLelland, J. M., 1994. Oxygen isotope geochemistry of zircon. Earth and Planetary Science Letters 126, 187-206.

Valley, J. W., 2003. Oxygen isotopes in zircon. In: Hanchar, J.M., Hoskin, P.W.O. (Eds.), Zircon: Reviews in Mineralogy and Geochemistry, vol. 53, pp. 343-385.

White, L. T., Ireland, T. R., 2012. High-Uranium matrix effect in zircon and its implications for SHRIMP U–Pb age determinations. Chemical Geology 306-307, 78–91.

Wingate, M., Compston, W., 2000. Crystal orientation effects during ion microprobe U-Pb analysis of baddeleyite. Chemical Geology 168, 75–97.

Wojdyr, M., 2010. Fityk: a general-purpose peak fitting program. Journal of Applied Crystallography 43, 1126-1128.

Xie, L., Zhang, Y., Zhang, H., Sun, J., Wu, F., 2008. In situ simultaneous determination of trace-elements, U-Pb and Lu-Hf isotopes in zircon and baddeleyite. Chinese Science Bulletin 53, 1565–1573.

Zhao, X., Vanderbilt, D., 2002. Phonons and lattice dielectric properties of zirconia. Physical Review B 65 doi: 10.1103/PhysRevB.65.075105.

Zheng, Y. F., 1991. Calculation of oxygen isotope fractionations in metal oxides. Geochimica et Cosmochimica Acta 55, 2299-2307.

Chapter 3: New U-Pb baddeleyite and zircon ages for the Scourie dyke swarm: A long-lived large igneous province with implications for the Paleoproterozoic evolution of NW Scotland

3.1. Introduction

Precambrian mafic dyke swarms occur in all cratons and are considered to represent the eroded remnants of continental large igneous provinces. These dykes typically intrude in a radiating or parallel orientation and are often associated with major craton-wide events, such as rifting and continental break-up (Fahrig, 1987; Druecker et al., 1987; LeCheminant and Heaman, 1989; Zhao et al. 2003; Li et al. 2008; Söderlund et al. 2010). Mafic dyke swarms are therefore critical to understanding cratonic evolution.

Detailed geochronological studies of Precambrian mafic dyke swarms and associated large igneous provinces have identified three types of provinces based on the duration of magmatism; 1) short events ~1 m.y. e.g. the 780.3 ± 1.4 Ma Gunbarrel mafic event (Harlan et al., 2003), 2) moderate-duration events with magmatism lasting ~10 m.y., e.g. the 1078-1070 Ma Warakurna large igneous province (Wingate et al., 2004) and 3) long-duration events spanning ~50 m.y. e.g. the 2125-2067 Ma Marathon large igneous province proposed by Halls et al. (2008). The reasons for this variation in longevity of dyke swarm magmatism are currently poorly understood.

One location where the <50 Ma dyke swarm paradigm breaks down is the Scourie Dyke Swarm of the Lewisian Gneiss Complex (LGC) in NW Scotland. In this region there is a multitude of Proterozoic mafic dykes that have a similar orientation, a feature often used as evidence for synchronicity. However, two apparently similar Scourie dykes, dated previously using high precision U-Pb baddeleyite geochronology, indicate that the emplacement ages of similar-oriented mafic dykes in the Lewisian span 400 Ma (Heaman and Tarney, 1989).

This paper presents the results of new high precision TIMS U-Pb baddeleyite and zircon dates from the Scourie Dyke Swarm on the Scottish mainland as well on the island of Lewis. The new ages for the Scourie dykes are used to better constrain the duration of mafic magmatism, identify the main periods of dyking activity, evaluate the crustal block model proposed for the formation of the Lewisian crust (Friend and Kinny, 2001; Kinny et al., 2005), and are compared to the global inventory of similar-age dyke swarms to evaluate if the Scourie dykes can be used as a robust tectonic pin in Paleoproterozoic continental reconstructions.

3.2. Geological setting and history of geochronology.

3.2.1 The Lewisian Gneiss Complex (LGC)

The LGC of NW Scotland consists of deformed and metamorphosed amphibolite, tonalite, trondhjemite and granodiorite (Fig. 3.1). The LGC on the Scottish mainland was first described in detail in a British Geological Survey memoir (Peach et al., 1907), where it was subdivided into three units; the northern, central, and southern, based on the presence of orthopyroxene-bearing gneiss in the central unit, and strongly deformed amphibole-biotite gneiss in the southern and northern

regions. Sutton and Watson (1950) further refined this three-unit subdivision, based on the relative timing of metamorphic events. They used the Scourie Dyke Swarm to distinguish between metamorphic events with a 'Scourian event' pre-dating dyke intrusion and a 'Laxfordian event' post-dating dyke intrusion. The Laxfordian event was pervasive in the northern and southern regions of the LGC but only found in discrete shear zones in the central region. The Scourian metamorphic event was later renamed 'Badcallian' and redefined as a period of granulite-grade metamorphism only recognized the central region (Park, 1970; Zirkler et al., 2012). As a consequence the dykes in the central region are much less metamorphosed. A third metamorphic event, the Inverian, was identified by Evans (1965). The Inverian event was defined as a period of amphibolite-grade metamorphism and deformation, which occurred after the Badcallian but before the intrusion of the Scourie Dyke Swarm. Corfu et al. (1994) obtained U-Pb ages on zircon from gneisses in the central region of ~2710 and ~2490 Ma, which were interpreted to date the Badcallian and Inverian metamorphic events, respectively. Neither of these ages have yet been recognized from U-Pb zircon dating of gneisses from the Northern region (Kinny and Friend, 1997).

More recently and mainly due to of the application of in-situ ion microprobe U-Pb dating of zircon, the Lewisian has been reinterpreted to consist of multiple discrete terranes, amalgamated along major suture zones during the Proterozoic. This new model is usually referred to as the 'terrane model' (Friend and Kinny, 2001; Kinny et al., 2005). It is based on the discovery that the different blocks have distinct ages of igneous and metamorphic zircon growth and therefore may have different histories (Kinny and Friend, 1997; Whitehouse et al., 1997; Friend and Kinny, 2001; Whitehouse and Bridgewater, 2001; Love et al., 2004). The regions were also renamed to reflect that these blocks have different igneous and metamorphic histories (See Fig. 3.1). The best example of the different crustal histories is between

the Rhiconich terrane (northern region) and the Assynt terrane (northern part of the central region). The Rhiconich terrane contains gneisses with emplacement ages of ~2.84 Ga, whereas the Assynt terrane gneisses have older protolith ages of 2.96-3.03 Ga (Friend and Kinny, 1995; Kinny and Friend, 1997). These terranes were then amalgamated during the Inverian event at 2480 Ma forming the Laxford Shear Zone (Goodenough et al., 2013; Fig. 3.1).

The Laxfordian event, which has traditionally been identified as any post-Scourie dyke emplacement metamorphic event, is now interpreted to be a range of magmatic and metamorphic events over a protracted time period (Kinny et al. 2005). Large granitic sheets at the boundary between the Assynt and Rhiconich terranes have U-Pb zircon ages of 1880-1850 Ma which mark the onset of Laxfordian metamorphism (Friend and Kinny, 2001; Goodenough et al., 2013). Similar-aged Laxfordian magmatism and metamorphism is also recorded in other areas of the Lewisian, including the South Harris complex, Ness complex, and the Loch Maree Group (Fig. 3.1a; Whitehouse and Bridgewater 2001; Park, 2001; Mason et al., 2004). Granitic sheets in the Assynt and Rhiconich terranes dated at 1770-1780 Ma are also attributed to Laxfordian events (Goodenough et al., 2013). 1770 Ma ages for granitic intrusion have not been recorded elsewhere in the Lewisian, although titanite from the gneisses of the Assynt and Rhiconich terranes, and rutile from the Scourie Dyke Swarm have U-Pb ages of ~1750 Ma (Heaman and Tarney, 1989; Corfu et al. 1994; Kinny and Friend, 1997).

Despite the heterogeneous distribution of protolith and metamorphic ages throughout the LGC, there is one aspect of the U-Pb systematics that is consistent in all areas; the gneisses commonly have U-Pb zircon ages that smear along Concordia from the protolith age down to the age of the last metamorphic event the gneiss experienced. This spread of ages has led to a debate about the presence or absence of the Badcallian

metamorphic event in the Assynt terrane (Corfu et al., 1994; Friend and Kinny, 1995; Whitehouse and Kemp, 2010). Thermal ionization mass spectrometry (TIMS) U-Pb zircon and monazite ages from the Assynt terrane indicate there is evidence of Badcallian metamorphism (Corfu et al. 1994; Zhu et al. 1997). However, the Gruinard terrane (Fig. 3.1a; Love et al., 2004) was separated from the Assynt terrane based on the difficulty identifying a Badcallian event in the ion microprobe U-Pb data from the latter (Love et al., 2004; Kinny et al., 2005). More recently, a detailed investigation of the ion microprobe data suggests that the smearing along Concordia can be explained by a mix of ages between the protolith age, Badcallian and Inverian events in the Assynt (and potentially Gruinard) terranes (Whitehouse and Kemp, 2010).

Subsequent to the Precambrian metamorphism and igneous activity, the Lewisian was also involved in the Scottish section of the Caledonian orogeny, which was caused by the collision of Baltica and Laurentia during the Silurian at ~435-425 Ma (Gee, 1975; Dallmeyer et al., 2001; Goodenough et al., 2011). The Moine thrust zone, which marks the Western most extent of the Caledonian orogeny in the UK (Fig. 3.1), is the Eastern boundary of Lewisian exposure, apart from some minor basement inliers to the East of the thrust zone (Friend et al., 2008). Early TIMS U-Pb data from the Assynt terrane indicate that the Caledonian event caused Pb-loss in zircon (Pidgeon and Bowes, 1972), although Pb-loss of this age in zircons from the Lewisian gneisses is not commonly identified.

3.2.2 The Scourie Dyke Swarm

Teall (1885) first described two doleritic dykes close to the town of Scourie and noticed that they had variable levels of amphibolitization. Since this seminal work, numerous Scourie dykes have been identified and they have subsequently been divided into four

petrological groups, Mg-rich bronzite picrites, norites, olivine gabbros and Fe-rich quartz dolerites (O'Hara, 1962; Tarney and Weaver, 1987a). The doleritic dykes are by far the most abundant accounting for ~90% of documented dykes (Tarney, 1973). All dykes are 10-50 m wide and concentrated mostly within the Assynt and Gruinard terranes, although some do occur within the Tarbert, Rhiconich, and Uist terranes (Fig. 3.1). Throughout the Lewisian these dykes are variably metamorphosed and were completely converted to amphibolite in the Rhiconich and Gruinard terranes during the ~1.9-1.8 Ga Laxfordian amphibolite-grade metamorphism (Corfu et al., 1994; Kinny and Friend, 1997; Zhu et al., 1997; Goodenough et al., 2013). Within the Assynt terrane, where the Laxfordian event is mostly confined to shear zones, the mineralogy varies between dykes composed of 100% metamorphic amphibole and plagioclase, to those preserving igneous minerals and textures (Tarney, 1973; Fig. 3.2). Two main explanations have been proposed for the varied metamorphic nature of the dykes; 1) they experienced variable degrees of autometamorphism during intrusion at depth into hot Lewisian country rock (Tarney, 1963; O'Hara, 1977), or 2) the variations are related to localized alteration/metasomatism during the Laxfordian, where fluid flow through the middle crust was enhanced by the steeply dipping fabrics in the Lewisian gneisses (Tarney, 1973).

Numerous attempts have been made to date the Scourie dyke emplacement. Initial studies using the K-Ar and Rb-Sr techniques produced a large range of ages from ~2.19 Ga to 1.95 Ga with some of the oldest and youngest ages explained by open system behavior in the K-Ar system (Evans and Tarney, 1964). A more precise date was obtained by combining Rb-Sr analyses from three different dolerite dykes from the Assynt terrane (re-dated in this study) to produce an age of 2.390 ± 0.020 Ga and an $^{87}Sr/^{86}Sr$ initial of 0.7022 ± 0.0001 (Chapman, 1979), which is higher than bulk silicate Earth at the time (0.7017; DePaolo and Wasserburg, 1976), potentially

reflecting contamination with an older component in the lithosphere. Using the updated ^{87}Rb decay constant of 1.3968 x 10-11 a-1 (Rotenberg et al., 2012) this composite dyke age can be recalculated to 2.405 ± 0.020 Ga, which agrees well with the U-Pb baddeleyite age of 2,418 Ma obtained from a picritic dyke in the Assynt terrane (Heaman and Tarney, 1989). A second U-Pb baddeleyite age of 1,992 Ma was obtained from an olivine gabbro dyke (Strathan dyke) (Heaman and Tarney, 1989). The Sm-Nd technique has also been applied to dykes of the Assynt terrane, these results are more difficult to interpret as two of the same dykes used in the Chapman, (1979) Rb-Sr study produce Laxfordian Sm-Nd ages of 1.98 Ga and 1.76 Ga (Waters et al., 1990), suggesting that the Sm-Nd ages may have been reset during the Laxfordian. Two fresh dykes from the Tarbert terrane on the Isle of Lewis have been dated using Sm-Nd isochrons; one (the Cleitichean Beag dyke in this study) has a Sm-Nd age of 2.54 Ga, whereas the other has an age of 2.14 Ga (Cliff et al., 1998). Five dykes from the Inner Hebrides islands of Tiree and Coll, geochemically similar to the Scourie swarm, give Laxfordian Sm-Nd ages of 1.75 Ga (Muir et al., 1993).

3.3. Sample descriptions

The Scourie dykes have been previously described in the field by Tarney (1973), petrographically by Teall (1885), Weaver and Tarney (1981a) and Tarney and Weaver (1987a), geochemically by Weaver and Tarney (1981b), Muir et al. (1993), and Goodenough et al. (2010), and on the Outer Hebrides by Mason and Brewer (2004). Only sample specific descriptions are provided here. Previous high precision U-Pb geochronology has focused on the picritic and olivine gabbroic compositions, due to the lack of dateable minerals in the other dykes (Heaman and Tarney, 1989). However, 90% of the dykes are doleritic in composition making this group by far

the most abundant. Here we report new U-Pb dates for gabbroic/doleritic and noritic dykes.

One-to-three kg samples were collected from the coarsest grained sections of the dykes, typically close to the dyke centers. We focused on sampling areas within the dykes that preserve primary igneous textures. We tended to sample only the widest sections of exposed dykes, typically where the coarsest most evolved areas of the dyke occur, since these areas are more likely to contain zircon and baddeleyite with a grain size that can be recovered using standard mineral separation techniques. For dykes with good exposure, for example the Poll Eorna dyke, we were able to traverse the dyke and look for coarse- grained granophyric sections rich in plagioclase, which are most likely to contain zircon and baddeleyite. Granophyric domains within the dyke were not necessarily in the center, but were always away from the contact with the country rock. For dykes with poor exposure, for example the Cnoc and Leothaid dyke, where only small outcrops are exposed, areas with the coarsest, most igneous-looking textures were sampled. The contact between the dyke and the Lewisian gneisses, where exposed, was always sharp. The Graveyard dyke is well-exposed on the south portion of the Scourie inlet. It contains mineralogical heterogeneity across the dyke. The southern contact with the Lewisian gneiss contains garnet and also a small offshoot of the dyke trending south contains abundant amphibole and garnet. The northern contact is less well-exposed, and is mostly covered by the sea and so it is not clear if it too contains garnet. We sampled the center of the dyke where it is relatively fresh, containing primary igneous minerals/textures and no garnet.

The original sampling strategy for this study was to date dykes from a number of discrete terranes (e.g., Rhiconich, Assynt, Gruinard and Tarbert), however, dateable U-bearing minerals were not found in dykes from the Rhiconich or Gruinard terranes.

The minerals within the dykes (Table 3.1) include clinopyroxene, orthopyroxene, olivine and plagioclase as well as quartz, apatite and epidote group minerals (epidote and clinozoisite; Fig. 3.2). In most dykes the clinopyroxene and orthopyroxene have been partially to completely pseudomorphed by magnesiohornblende that often exhibit actinolite rims. The Poll Eorna, Graveyard, Unapool, Cleitchean Beag, and Badcall Bay dykes all have low contents of hydrous minerals relative to the other dykes and show no saussurite alteration of plagioclase.

Zircon and baddeleyite commonly occur in association with late-crystallizing phases quartz and plagioclase but are also hosted by clinopyroxene, magnesiohornblende and oxide minerals. Large (500 μm) zircon crystals were found in the Graveyard dyke associated with quartz, biotite, apatite and plagioclase (Fig. 3.2e), which represent a late-stage evolved melt from the dyke. Baddeleyite typically occurs as tabular grains 10-80μm in length and appear relatively pristine, a thin zircon rim can be seen on a baddeleyite crystal from the Cleitchean Beag dyke (Fig. 3.2f). Zircon is typically tabular or skeletal (apart from the Loch a'Choin and North Assynt dykes where it can be sub-rounded) and usually appears unaltered in thin section with no obvious core–rim structure.

3.4. Analytical techniques

Zircon and baddeleyite were extracted from whole rock samples using standard crushing and mineral separation techniques (tungsten carbide shatter box, Wilfley Table, Franz Isodynamic Separator, and methylene iodide heavy liquid), followed by selection of mineral grains using a high-powered binocular stereoscopic microscope.

The chemical abrasion technique (Mattinson, 2005) with some modifications (Schoene et al. 2010) was applied to a few zircon grains in an attempt to reduce the effect of Pb-loss. Due to high levels of metamictization present in these grains, and the consequent complete dissolution of all zircon in the first three test cases, a less aggressive acid leach technique was applied compared to that usually used on Phanerozoic zircons. The selected grains were combined in a quartz beaker and annealed at 1000°C for ~30h. They were then placed in 3ml hexatop Savillex vials with 30% HF and trace HNO3 and leached for ~16h at 160°C, cleaned in 6N HCl in the same Savillex vials, and placed back in the oven overnight. After chemical abrasion, the remaining zircon fragments were cleaned and loaded into dissolution vessels using the techniques described below.

Most of the zircon and baddeleyite separated during this study are extremely small (<40μm) and hence innovative techniques were employed to clean and dissolve the minerals ensuring they were not lost during processing. Mineral fractions separated for isotopic analysis were photographed and their mass estimated based on a volume and density (zircon 4.85 gm/cc, baddeleyite 5.75 gm/cc) calculation. The selected minerals were then cleaned by placing them sequentially into 3 drops of 7N HNO3 at room temperature located in dimples made on a sheet of Parafilm. The grains were held in each droplet for ~10 minutes before being transferred using a pipette to the next drop, and then transferred directly to Teflon bombs or Teflon microcapsules for dissolution. A mixed ^{205}Pb-^{235}U tracer solution was added to each sample before dissolution in an ~8:1 mixture of 48% HF and 7N HNO3 at 190ºC for 48 hours. After dissolution, the samples were dried down on a hotplate before being converted to chloride by redissolving the precipitate in 6N HCl at 190ºC overnight. The solutions were then dried down with 1 drop of phosphoric acid in pre-cleaned

polymethylpentene (PMP) beakers. The dissolved sample and spike mixtures were loaded directly onto outgassed Re filaments with a mixture of silica gel and phosphoric acid for isotopic analysis. Typical sample loads contained ~30 pg of Pb and ~70 pg of U.

Uranium and Pb isotope measurements were made using a VG354 mass spectrometer following the procedures outlined in Heaman et al. (2002). All samples were measured using an analog Daly photomultiplier detector in peak-hopping mode. Total analytical blanks monitored during this study were ~0.5-1 pg for Pb and ~0.5 pg for U. Model Th concentrations are used to calculate Th/U assuming all of the ^{208}Pb has been produced by the decay of ^{232}Th. All data processing was done using the equations of Schmitz and Schoene (2007), with the final age calculations made using ISOPLOT (Ludwig, 2003). Corrections for common Pb were made following the two-stage model of terrestrial Pb evolution of Stacey and Kramers (1975).

U-Pb age determinations for baddeleyite and zircon extracted from the dykes during this study, using the ^{235}U and ^{238}U decay constants of Jaffey et al. (1971) are presented in Table 3.2 and on Concordia diagrams in Figures 3 and 5 (uncertainties are shown at 2σ). The Phalaborwa baddeleyite was analyzed during this study; the results are within error of the recommended values (Heaman, 2009).

Cathodoluminescence (CL) imaging to assess zoning, alteration and degree of metamictization of the zircons was conducted in grain mounts using a Zeiss EVO 15 scanning electron microscope equipped with a Robinson wide spectrum CL detector running at 15 kV and ~3 nA.

3.5. Results

U-Pb baddeleyite and zircon data are reported from 10 ‘Scourie’ dykes that intrude the LGC (Table 3.2). Baddeleyite results are concordant or near concordant (0-2% discordant) whereas zircon data are typically discordant (0-41% discordant). Representative CL images of zircons from the dykes are displayed in Fig. 3.4

Poll Eorna dyke (LH99-51)

Approximately 30 small clear tabular zircon shards were recovered from the Poll Eorna dyke. The zircons in this sample are colorless and <100μm long with no inclusions or visible signs of metamorphic overgrowth (Fig. 3.4a). The zircons have quite low Th/U ratios of 0.32-0.50, mafic zircons typically have Th/U of 1-2 (e.g. Blackburn et al., 2013), however the dyke also contains abundant apatite, which can preferentially partition Th over U and change the Th/U of the melt (Prowatke and Klemme, 2006). Despite the clear and tabular appearance, analyses of all zircons yield discordant results ranging from 7-31%. The one recovered baddeleyite was colorless and gave a (1.9%) discordant result with a typical Th/U (for baddeleyite) of 0.07. All of the data (except #5 and #8) lie on a regression line with an upper intercept date of 2396.8 ± 4.3 Ma (MSWD = 3.8), interpreted as the age of dyke emplacement, and a lower intercept of 397 ± 24 Ma. Analysis #5 and #8 lie to the left of the regression line, and may have been affected by more than one Pb loss event.

Graveyard Dyke (LH99-46)

One large clear zircon (~500μm) and ~25 small clear skeletal grains were extracted from two coarse granophyric sections of the dyke (Fig. 3.2e shows an example of a large zircon crystal within a granophyric section of the dyke). The large zircon was extracted directly from one sample whereas the skeletal grains were recovered after full mineral processing of a second sample. The large zircon was broken into three pieces and each analyzed separately (analyses #1-3) along with 5 aliquots

of the skeletal grains (CL images of the skeletal grains are shown in Fig. 3.4b). Similar to Poll Eorna, all of the zircons from the Graveyard dyke have moderate Th/U ratios (0.21-0.46). All but two are concordant or near concordant. Two of the fractions (#2 and #8) have $^{207}Pb/^{206}Pb$ ages that are younger than other analyses without being less concordant, suggesting these grains may have experienced lead loss prior to the Caledonian orogeny. Aliquot #8 is the most concordant analysis, though less precise than aliquots #3 and #4. Analyses #7 and #8 were the only grains to receive a chemical abrasion pre-treatment, the results are surprising in that #7 is highly discordant (37%) and #8, though being most concordant, produces a young $^{207}Pb/^{206}Pb$ age. Removing fractions #2 and #8 from the regression produces an upper intercept age of 2391.7 ± 1.6 Ma (MSWD = 2.6), which is interpreted as the time of dyke crystallization. The lower intercept age is 370 ± 13 Ma, consistent with a Caledonian lead loss event.

Unapool Dyke (LH07-12)

Six fractions of baddeleyite and zircon were analyzed from the Unapool dyke, four aliquots of tan-colored baddeleyite grains and two aliquots of zircon, one brown (#3) and one clear (#6). The baddeleyite grains all have low Th/U ratios 0.01-0.03 typical of baddeleyite from mafic dykes and are all concordant or lie close to concordia. The two zircon analyses are discordant (#3=17% and #6=39%), and both have low Th/U (0.10 for #3 and 0.48 for #6). The low Th/U value for #3 is not typical of igneous mafic zircon and is more similar to metamorphic or hydrothermal zircon (Rubatto, 2002), however it could represent an intergrowth between baddeleyite and zircon. Analysis #5 is concordant and produces a concordia age of 2382.4 ± 3.9 Ma. A regression line constructed to pass through all of the baddeleyite fractions is slightly more precise but indistinguishable from the single analysis, yielding an upper intercept age of 2384.1 ± 2.2 Ma (MSWD = 2.2) with a lower intercept of 799

± 125 Ma. . This upper intercept age of 2384.1 ± 2.2 Ma is interpreted as the best estimate for the timing of Unapool dyke emplacement.

North Assynt Dyke (JD09-21)

Seventy zircon grains were recovered from a coarse-grained norite sample from the North Assynt Dyke. The zircon grains were split into two populations with one population comprising rounded clear light pink grains ranging from 50-150 μm in length and another population containing tabular/sub-rounded grain fragments that are clear and inclusion-free (Fig. 3.4c shows examples of both zircon morphologies). The tabular grains were smaller ranging from 30-60 μm in length and had no obvious signs of mottling around their edges, as would be expected due to metamorphic overgrowths. CL imaging of the grains (Fig. 3.4c) shows clear core-rim structures, possibly indicating different periods of zircon growth. The rounded pink grains are considered to be xenocrystic/metamorphic and were avoided for U-Pb analysis. Ten tabular grains were selected for U-Pb analysis yielding a range in $^{207}Pb/^{206}Pb$ ages from 2492 to 2549 Ma. Most of the analysis smear along Concordia (similar to zircons from the surrounding gneisses) although one fraction (#1) shows significant reverse discordance (-6%) and another fraction (#3) yields 20% normal discordance. The oldest $^{207}Pb/^{206}Pb$ age of 2549 Ma is produced by aliquot #7, but this fraction is slightly reversely discordant (-0.4%). A regression line constructed to pass through all the grains (excluding #5 with the younger $^{207}Pb/^{206}Pb$ age and grain #1 with the reverse discordance) produces an upper intercept age of 2540 ± 10 Ma (MSWD = 139). The zircons analyzed from this dyke are likely xenocrysts from the surrounding gneisses (discussed in detail in section 6.2).

Loch na h Dyke (JD09-14)

Approximately 20 small (30-60μm) zircons were extracted from a dioritic section

in the center of this dyke from the west end of Loch Assynt. The zircons are highly metamict, with very little response in CL (Fig. 3.4d). Eight zircon grains were selected for analysis yielding results that ranged from concordant to 33% discordant. A regression line anchored at 430 Ma, the age of movement along the Moine Thrust, which represents the front of the Caledonian orogeny (Goodenough et al., 2011), produces and upper intercept age of 2395 ± 7.6 Ma (MSWD = 17), considered to be the best estimate for the timing of dyke emplacement. A chemical abrasion treatment was applied to aliquots #2-#5 but did not result in appreciably more concordant analyses. This is potentially due to the high levels of metamictization observed in the grains with no areas unaffected by Pb loss.

Loch a' Choin Dyke (JD09-24)

A coarse-grained sample from the center of this amphibolite dyke produced ~70 colourless zircons with morphologies ranging from prismatic to rounded (CL images of the grains are shown in Fig. 3.4e). Eight tabular clear grains, which were chosen for analysis, yielded slightly discordant results and an upper intercept age of 2480 ± 17 Ma (MSWD=10.8). Samples #1 and #4 are both imprecise analyses due to their small size and low U and Pb contents, both were omitted from the regression calculation. The age from this dyke overlaps with the Inverian metamorphic event dated by Whitehouse and Kemp (2010) possibly indicating that these zircons are xenocrysts reset or grown during this event.

Lochan Fearna Dyke (JD09-17)

A coarse-grained felsic zone at the center of this gabbroic dyke yielded ~30 40-70 μm clear skeletal zircon crystals. Twelve skeletal zircon grains were selected for U-Pb analysis producing results that ranged from 7-39% discordant (the discordance is likely related to the metamict nature of the grains, Fig. 3.4f). All of the fractions have

moderate U concentrations (286-630 ppm). A regression line through all but two of the most discordant analyses (#1 and #4) yields an upper intercept age of 2375.3 ± 1.7 Ma (MSWD = 1.7), considered to be the best estimate of the emplacement age for the dyke. The lower intercept of the regression is 489 ± 27 Ma, which is broadly consistent with a Caledonian lead loss event for the zircons.

Cnoc an Leothaid Dyke (JD09-27)

Only ~12, 50 μm zircons were recovered from this metagabbro dyke. Eight grains were colourless and prismatic with no visible metamorphic coat, however they did contain tiny black inclusions. The other 4 zircons were rounded, tan and also contained inclusions indicating a likely metamorphic or xenocrystic origin. The 8 prismatic grains processed for U-Pb geochronology produced analyses ranging from 8-33% discordant. Unfortunately, the zircons were analyzed before CL imaging, and no further grains were recovered from this sample. Grain #2 had a low $^{206}Pb/^{204}Pb$ ratio of 245 and low U and Pb concentrations resulting in a large uncertainty in the analysis. A regression line through all of the fractions yields an imprecise 213 ± 320 Ma lower intercept age with a 2395 ± 56 Ma upper intercept, the MSWD is 27. The age uncertainty is improved to 2373 ± 38 Ma if the regression line is anchored at the origin, but the MSWD increased to >1000. The large errors and high MSWD reflect the poor correlation between the analyses. Although the U-Pb zircon systematics of this sample are complex, we interpret the 2395 ± 56 Ma date as the best estimate for the timing of dyke emplacement, since this age produces the lowest MSWD and has a lower intercept that is within error of the other dykes analyzed during this study.

Cleitchean Beag Dyke (Lewis) (LH99-42)

This large ultra-mafic dyke produced ~20 30-50 μm baddeleyite fragments, most with thin polycrystalline zircon overgrowths. Three baddeleyite grains without

visible zircon overgrowths were chosen for U-Pb analysis, which yielded 0.3-1% discordant analyses and an upper intercept age of 2409.6 ± 1.7 Ma (MSWD=0.018), considered the best estimate for the emplacement age of the dyke.

Badcall Bay Dyke (LH86-40)

Two previously reported zircon analyses from the Badcall Bay noritic dyke (Heaman and Tarney, 1989) have been reinterpreted using the same error propagation procedure as the other analyses in this study. Also, a single colourless skeletal grain, selected from the same mineral separate, was analyzed (images of the Badcall zircons are shown in Fig. 3.4g). A regression line through all three analyses produces an upper intercept age of 2393.6± 4.8 Ma interpreted to be the best estimate of dyke emplacement. The lower intercept of 399.6 ± 7.8 Ma is consistent with a Caledonian Pb loss event.

3.6. Discussion

New U-Pb age results presented here significantly extend the coverage of dated Scourie dykes within the Lewisian and indicate that the age distribution of the dykes is complex, with most of the dykes having ~2.4 Ga emplacement ages. All dykes show evidence of a previously unidentified Caledonian Pb-loss event, possibly related to fluid mobilization during the generation of the Moine Thrust (Goodenough et al., 2011).

The 2391.7 ± 1.6 Ma Graveyard and 2396.8 ± 4.3 Ma Poll Eorna dykes investigated in this study were previously dated using the Rb-Sr and Sm-Nd techniques (Chapman, 1979 and Waters et al. 1990, respectively). The U-Pb results, although more precise and slightly younger, are within uncertainty of the recalculated Rb-Sr age (2.405 ± 0.020 Ga, see section 2.2) indicating that the Rb-Sr whole rock system has remained

largely undisturbed in these dykes. The Sm-Nd data for the same dykes reported by Waters et al. (1990) yield younger dates of 1.76 Ga and 1.98 Ga, respectively. The younger Sm-Nd ages were calculated from mineral separates and therefore likely reflect element mobility between major mineral phases during the Laxfordian orogeny, where as the whole rock Rb-Sr systematics may have been immune to such resetting.

3.6.1. The main Scourie dyking event

A total of twelve 'Scourie' dykes have now been dated by the TIMS U-Pb technique on zircon/baddeleyite and nine have emplacement dates within the range ~2410-2375 Ma, a span of ~40 m.y. We propose that this is the main period of Scourie dyke emplacement. The North Assynt and Loch a'Choin dykes yielded older and more complex U-Pb zircon age results, these are discussed separately in the following section (Section 6.2), only the dykes from the main ~2.4 Ga emplacement period are presented in this section.

Within this main period of Scourie dyke emplacement, potentially three discrete events can be recognized: an older suite 2418-2408 Ma consisting of the ultramafic Cleitchean Beag and Beannach dykes, the main suite at ~2395-2390 Ma consisting of doleritic and noritic Cnoc an Leothaid, Loch na h, Poll Eorna, Graveyard and Badcall Bay dykes, and a late-stage event at ~2375-2385 Ma consisting of the doleritic Unapool and Lochan Fearna dykes (Fig. 3.5). The lack of additional ~2000 Ma dykes identified suggests that this period of dyke emplacement, previously identified by Heaman and Tarney (1989), is likely a minor component of magmatism within the swarm. We therefore propose that only dykes formed during the main intrusion event at ~2.4 Ga (identified here) be referred to as Scourie dykes sensu stricto, thereby

avoiding confusion with the different Paleoproterozoic dykes in the region that span an emplacement history of more than 400 m.y (a ~2.0 Ga dyke is identified by LA-ICP-MS in Chapter 4).

The new dyke ages allow an initial chronology of events to be constructed indicating how the dyke compositions vary over time (Fig. 3.5), which is an important step in understanding the origin of the dykes. Petrologically the Scourie dykes can be subdivided into 4 categories: bronzite picrite, norite, olivine gabbro and dolerite (Tarney, 1973). Weaver and Tarney (1981b) noted that these 4 petrologic classes of dykes could be separated into two geochemical groups, likely originating from different mantle sources. The ultra-mafic picritic and noritic dykes form one group with enriched trace-element contents relative to primitive mantle, and La/Sm of ~3.2 (normalized to primitive mantle; Fig. 3.6). The mafic dolerite and olivine gabbro dykes form the second group, which cannot be related to the first through crystal fractionation (Weaver and Tarney, 1981b). The second group also contains enriched trace-element compositions (relative to primitive mantle) but less fractionated rare earth element ratios (La/Sm of ~1.7-1.8, normalized to primitive mantle; Fig. 3.6). Oxygen isotopic analysis of the dolerite and olivine gabbro dykes indicate that they are not contaminated by the surrounding Lewisian gneiss (at least in the area around Scourie, Cartwright and Valley, 1991) and that the geochemistry of these samples is representative of their source. If the different geochemical groups do sample separate sources, the U-Pb data indicate that the ultramafic picrite and norite dykes were emplaced before the dolerite and olivine gabbro dykes (see Fig. 3.5).

In addition to the emplacement ages of the dykes, the U-Pb data also provide information on the timing of Pb-loss. A somewhat surprising result of this study is that most of the dykes analyzed have Caledonian lower intercept ages rather than a

disturbance related to the ~1.9-1.8 Ga Laxfordian orogeny. There are however two exceptions, the Loch na h and Cnoc and Leothaid dykes. Both of these dykes have high MSWDs (17 and 27, respectively) indicating that zircon from these samples cannot be simply explained by one Pb loss event during the Caledonian. Both of these dykes are located close to the Canisp shear zone, which could indicate they experienced Laxfordian as well as Caledonian overprinting. The Graveyard dyke also contains some complex U-Pb systematics. Aliquots #2 and #8 are both relatively concordant but produce younger ages than the main zircon population. Mineralogically, the Graveyard dyke has Laxfordian overprinting, especially at its margins where garnet has crystalized (Waters et al., 1990), these zircon analysis could reflect minor Pb disturbance during the Laxfordian orogeny.

The lack of Laxfordian Pb-loss for the majority of the dykes could indicate that the dykes were still at mid-crustal levels and at high temperature (>250°C) during this time and had not previously cooled below this temperature. Alpha tracks in zircon don't accumulate at temperatures ~>250°C (Murakami et al., 1991; Meldrum et al., 1999), and without damage to the zircon crystal lattice, Pb-loss is unlikely (Nasdala et al., 1998). Also, recently MacDonald et al. (2013) discovered that zircons from the LGC only record Laxfordian ages when they have been physically deformed by shearing during the Laxfordian orogeny. In order to study these zircons, MacDonald et al. (2013) sampled highly deformed gneiss, and discovered only ~5% of the zircons were affected by Laxfordian Pb mobility. During this study, we intentionally sampled the least deformed areas of the dykes, in an effort to avoid or at least minimize deformation-associated Pb-loss. The lack of Laxfordian Pb-loss could therefore reflect the sampling strategy utilized in this study, combined with the high temperatures associated with their storage at mid- crustal levels throughout most of the Precambrian.

Subsequent uplift and erosion of the LGC occurred during the Caledonian orogeny and the development of the Moine Thrust (Holdsworth et al., 2007; Goodenough et al., 2011). By the time of the caledonian orogeny the dykes had cooled below 250°C and the zircons had accumulated radiation damage and were therefore susceptible to Pb loss during the caledonian event. It is interesting that most of the zircons from the Lewisian gneisses show minimal evidence for a Caledonian Pb-loss event (Corfu et al. 1994; Kinny and Friend, 1997; Zhu et al. 1997; Whitehouse and Bridgewater, 2001; Love et al. 2004; Whitehouse and Kemp, 2010; Goodenough et al., 2013; Macdonald et al., 2013). Some samples do show evidence for more recent Pb loss, which can be attributed to the Caledonian (e.g. Pidgeon and Bowes, 1972; Friend and Kinny, 1995; Love et al., 2004), although this is not a dominant feature of the Lewisian zircon populations.

3.6.2. The Age of the Older Dyke Suite

Field relationships suggest that the 2.42 Ga picritic dykes, currently the oldest reliably dated dykes (Heaman and Tarney, 1989) maybe cross-cut by dolerite dykes (Tarney, 1973). The cross cutting relationships were originally supported by early K-Ar dates, which suggested two dolerite intrusion events, one before and one after intrusion of the picrite dykes (Evans and Tarney, 1964). The new U-Pb dates for the North Assynt norite and Loch a'Choin dolerite dykes (2540 ± 10 Ma and 2480 ± 17 Ma, respectively) appear to support the early intrusion theory for some dolerites since both pre-date emplacement of the 2418 +7/-4 Ma Beannach bronzite picrite dyke (Heaman and Tarney, 1989). However, there is uncertainty regarding the origin of the zircon crystals in these samples since the ages overlap with U-Pb zircon ages from the surrounding gneisses (Corfu et al. 1994; Kinny and Friend, 1997; Whitehouse et al., 1997; Whitehouse and Kemp, 2010; Zirkler et al., 2012;

Goodenough et al., 2013). The U-Pb analyses for the North Assynt dyke also smear along Concordia in a similar manner to zircons from the gneisses. While CL images of zircon fragments (Fig. 3.4c and e) show features such as separate core and rims and rounded morphologies that indicate some crystals may have a xenocrystic or metamorphic origin. The CL images also look remarkably similar to the images of zircons from the gneisses (see Kinny and Friend, 1997; Whitehouse and Kemp, 2010). Here we discuss the U-Pb, CL and petrographic properties of the zircon from the North Assynt and Loch a'Choin dykes, to elucidate their origin.

The Loch a'Choin dyke age overlaps with the age of Inverian metamorphism revealed by U-Pb dating of zircon and titanite in the gneisses (Corfu et al., 1994; Whitehouse and Kemp, 2010; Zirkler et al., 2012; Goodenough et al., 2013) and the dyke is also located within the Canisp shear zone, which is an Inverian structure (Fig. 3.1; Zirkler et al. 2012). The North Assynt dyke zircons are older than the ~2.49 Ga Inverian event and since the dyke lies outside any known Inverian shear zones and is unmetamorphosed, they may have escaped the fluid metasomatism and metamorphism associated with the event. The age of the North Assynt dyke still overlaps with zircon growth from Assynt terrane gneisses (e.g. Whitehouse and Kemp, 2010; Goodenough et al., 2013), indicating that the zircons could be xenocrystic.

Observations of zircon in thin section from both the North Assynt and Loch a'Choin dykes (Fig. 3.2c and d) provide petrographic information on the paragenesis of these zircons. Zircons from the North Assynt dyke (Fig. 3.2c) appear to have co-crystallized with ilmenite, orthopyroxene and plagioclase with later biotite altering the pyroxene. The elongated shape of the zircon is not typical of either zircons from the surrounding gneisses or metamorphic zircon. Zircon from the Loch a'Choin

dyke is sub-rounded and is hosted within a quartz grain (Fig. 3.2d). The presence of quartz could indicate a late-stage melt pocket within the dyke or evidence of assimilation of the surrounding gneiss. The sub-rounded zircon morphology is more consistent with a xenocrystic origin and therefore the assimilation hypothesis, since zircon from mafic rocks typically forms skeletal, blocky or prismatic grains with a ~4:1 length:width ratios (Heaman et al., 1990).

The Loch a'Choin U-Pb zircon data do not show the typical Lewisian smear along Concordia, although aliquots 5z and 6z, are both close to concordant and have $^{207}Pb/^{206}Pb$ ages of 2469 ± 4 and 2487 ± 4 Ma indicating a small spread along Concordia. When the U-Pb evidence is combined with the inconclusive petrographic information and the multifaceted morphologies of many of the grains in CL, it suggests that the zircons are xenocrysts.

The North Assynt dyke U-Pb data is the most complicated to interpret in this study, with analyses that smear along concordia, one discordant analysis anchoring the regression line and one with 6% reverse discordance. Complicated U-Pb systematics within a sample does not in-itself distinguish xenocrystic, metamorphic or igneous zircons but it can be used to clarify the zircon origin. If the most discordant fraction is ignored (#3 Table 3.2) and an Inverian age is used to anchor the reference chord, an upper intercept of 2664 ± 1600 Ma is produced, which is highly imprecise but similar to U-Pb ages found in the host gneisses (Corfu et al., 1994; Kinny and Friend, 1997; Whitehouse and Kemp, 2010; Goodenough et al., 2013), possibly suggesting a xenocrystic origin for the zircons. The reversely discordant fraction (#1 Table 3.2) is unusual, and even though it is not included in age regressions, it requires further discussion to understand its origin.

Reversely discordant data are relatively rare in TIMS U-Pb geochronology, although it is being more commonly reported, especially in Precambrian baddeleyite (e.g. Söderlund et al., 2005; 2010; Nilsson et al., 2010). The reverse discordance is most likely related to the low $^{206}Pb/^{204}Pb$ of 127 and high common Pb (43.34 pg) from aliquot 1 of the North Assynt dyke. When $^{206}Pb/^{204}Pb$ is lower than ~200 for Precambrian zircons and the mol % $^{206}Pb^*$ is less than 98%, the common Pb correction has a strong impact on the final isotopic composition. Incorrectly assigning the common Pb to either the blank or common Pb at the time of zircon formation can easily create artificial reverse discordance, since the true origin of the common Pb is unknown. For this reason fraction #1 (and fractions #1 and #4 from the Loch a'Choin dyke) was removed from the age regression.

In summary, both the zircons from the Loch a'Choin and North Assynt dyke analyzed in this study are likely xenocrysts and the ages produces reflect zircon growth in the surrounding gneiss rather than dyke emplacement.

3.6.3. Constraints on the existing terrane model, and a comparison between the Scourie dykes and dykes from the Outer Hebrides.

In this study, it has been shown that ~2.4 Ga dykes occur both on the mainland (Assynt terrane) as well as on the Isle of Lewis in the Outer Hebrides (northern Tarbert terrane) and could be a valuable piercing point connecting these two terranes at this time. Prior to this study, there has been debate as to whether the Outer Hebrides and the mainland Lewisian were connected prior to the Laxfordian metamorphic event. Friend and Kinny (2001) and Kinny et al. (2005) proposed that there was no connection whereas Park (2005; 2010) and Mason (2012) provided evidence for a shared history. The debate relates to U-Pb zircon ages from gneisses of the Assynt,

Rhiconich and Tarbert terranes, which all have different protolith ages and preserve different ages of metamorphism prior to ~1650 Ma (Friend and Kinny, 2001). The presence of large shear zones and faults in the Outer Hebrides and mainland terranes with unknown displacements (e.g. Outer Hebrides thrust and Inverian shear zones, Fig. 3.1) has made direct correlation of geological units between the terranes difficult (e.g. Whitehouse and Bridgewater, 2001). However a mafic dyke swarm on the Outer Hebrides (the OH dykes of Mason and Brewer, 2004) located in the Southern Gneisses of the Tarbert terrane and around the South Harris Igneous Complex (the Cleitichean Beag dyke is not obviously related to this swarm) has previously been linked to the Scourie dykes (Dearnley, 1963). If this connection were correct it would indicate the Tarbert and Assynt terranes had a shared history before the Laxfordian orogeny. Below, the Scourie dykes are compared geochemically to the OH dykes to assess their relationship followed by an assessment of the bedrock geology between the Outer Hebrides and the mainland.

A geochemical study by Mason and Brewer (2004) suggests that the Outer Hebrides dykes (OH) are geochemically distinct from Scourie dykes. The study also suggested that the OH dykes could be ~2.0 Ga based on lower intercept ages from zircons in the surrounding gneisses, although the dykes themselves have not been directly dated. The geochemistry of Scourie dykes is complex, partly due to the varied lithologies. Weaver and Tarney (1981) and Tarney and Weaver (1987b) used geochemical modeling to suggest that the dykes originated from two distinct mantle sources, with the picritic and noritic dykes being more enriched than the gabbroic and doleritic dykes. The dolerite dykes (to which the OH dykes are more geochemically similar) are thought to originate from a metasomatically enriched mantle peridotite melting at various depths beneath continental lithosphere within the spinel stability field.

The OH dykes have similar trace-element characteristics to the dolerite dykes from the Assynt terrane suggesting that they could be from the same source (Mason and Brewer, 2004; Fig. 3.6a). However, select incompatible element ratios, which vary predominantly based on source composition (Pearce and Norry, 1979) show consistently lower Zr/Nb and Zr/Y ~10 and ~3.2, respectively for OH dykes compared with ~15 and ~5 for the Assynt dolerites (Fig. 3.6b and c). An increase in the degree of partial melting of the same source could explain the Zr/Y differences between the Assynt dykes and the OH dykes, since this ratio reduces with increasing degree of melting (Fig. 3.6c). However increasing the degree of partial melting does not explain the higher Zr/Nb of the Scourie dolerites compared with the OH dykes since this ratio is independent of degree of melting. In addition, increasing the degree of melting would cause a flatter spider diagram profile for the OH dykes, which is not observed (Fig. 3.6a). Considering the differences in geochemistry and unknown age of the OH dykes, we concur with Mason and Brewer (2004) that the Scourie dykes and the OH dykes could have a different origin. Isotope geochemistry could potentially determine if the dykes are related. For example, some Scourie dykes have anomalously low $\delta^{18}O$ signatures of ~2 ‰ (Cartwight and Valley, 1991). If these signatures were present in the OH dykes it would provide good evidence that they sampled the same mantle source. Despite the inconclusive geochemical connection between the OH and the Scourie dykes, the presence of a Scourie-aged dyke within the Tarbert terrane (Cleitichean Beag dyke) suggests that the Tarbert and Assynt terranes may have been linked prior to the formation of the ~2.4 Ga dykes.

Geochemical and geochronological connections between the basement geology in the Outer Hebrides and the mainland Lewisian are debated before the Laxfordian metamorphic event (1.9-1.7 Ga), which is clearly recorded in both areas (Kinny and Friend, 1997; Friend and Kinny, 2001; Mason et al., 2004; Mason and Brewer, 2004).

The Outer Hebrides contains Archean TTG gneissic rocks to the north and south of a Proterozoic supracrustal belt (Fig. 3.1). The northern gneisses of the Tarbert terrane are genetically similar to the southern gneisses, both consist of ~2.8 Ga TTG orthogneisses containing local areas with an older (inherited) zircon core growth (3.6-3.0 Ga) and a 2.73 Ga metamorphic event (Francis, 1973; Friend and Kinny, 2001; Mason et al., 2004; Kelly et al., 2008). Both the formation of ~2.8 Ga gneisses in the Outer Hebrides and the presence of a zircon-forming metamorphic event at ~2.7 Ga is consistent with the geological history of gneisses from the Assynt and Gruinard terranes of the mainland (Corfu et al., 1994; Whitehouse et al., 1997; Zhu et al., 1997; Corfu et al., 1998; Love et al., 2004; Whitehouse and Kemp, 2010; Zirkler et al., 2012; Goodenough et al., 2013) The Outer Hebrides' Proterozoic supracrustal units are: the Harris Granulite belt, Langavat belt and the Ness complex. These supracrustal units have been linked despite slight differences in lithology, to the Loch Maree Group and Ard Gneiss within the Gruinard terrane on the mainland due to similar rock types, deformation and timing of metamorphism (Park, 2005; 2010; Mason, 2012). Despite many similarities between the Assynt and Tarbert terranes, distinct differences exist, traditionally making correlation difficult. The Assynt terrane records a ~2.5 Ga Inverian metamorphic event and contains granulite-gneisses depleted in K, Rb, Th and U; both of which are not yet known in the Tarbert terrane.

We propose that the Outer Hebrides and the mainland Lewisian terranes (with the exception of the Rhiconich terrane) were related throughout their histories due to the similar U-Pb gneiss ages, mafic dyke intrusions and supercrustal units. The differences between the Assynt terrane and the Outer Hebrides could be explained by geochemical differences in the basaltic precursor to the TTG's and also melting during granulite-grade metamorphism in the Assynt terrane (e.g. Weaver and Tarney,

1981c; Rollinson, 2012).

3.6.4. Possible tectonic setting for the Scourie dykes

Eight new TIMS U-Pb baddeleyite and zircon ages from the Scourie dykes define a period of dyke emplacement between ~2418-2375 Ma. The duration of dyke emplacement is ~40 Ma, much longer than most flood basalt events which typically last 1-5 Ma (e.g. compilation by Ernst et al., 2013). Short-duration dyking events are commonly attributed to mantle plume activity or lithospheric delamination suggesting that neither of these are the triggers for the Scourie magmatism. Examples of long-lived, uniformly oriented mafic dyking events are present in other cratons worldwide and can be attributed to persistent rifting, such as the northern Tarim block in NW China with individual rifting events lasting ~50 Ma over a ~200 Ma time period (Zhu et al., 2008), and the Adelaide geosyncline of S. Australia where individual episodes of rifting lasted 30 Ma over a total rift duration of ~130 Ma (Preiss, 2000). Small-scale rifting could explain the spread of ages within the swarm, however rift-related magmatism can contain early alkaline intrusions rather than early ultramafic intrusions, bimodal magmatism and normal faulting, none of which are currently known in the Lewisian. One possibility for the generation of extension in the Lewisian could be rifting following the collision of the Assynt and Rhiconnich terranes at 2.5 Ga (Goodenough et al., 2010). Post-orogenic extension is known to cause mafic magmatism in extensional and transpressional regimes, for example the Passamaquoddy Bay mafic dyke swarm which intruded during the accretion of terranes during the formation of the Appalachian Mountains (van Wagoner et al. 2002; van Staal et al. 2009). The Passamaquoddy dykes are potentially good analogs to the Scourie dykes since they represent Silurian and Devonian extension related to a relaxation of the Ordovician Appalachian compression. Extension in the Lewisian may have continued after 2375 Ma. A recent Re-Os study of pyrite veins cross-

cutting the gneisses and dykes in the Assynt and Gruinard terranes produced ages of 2249 ± 77 Ma (Vernon et al. in review). Sulphur isotopic compositions indicate a mantle origin for the pyrite and suggest that fluids/melts derived from the mantle continued for a long period of time after the collision. The extended extensional regime may indicate that there are ages of dykes still undiscovered in the Lewisian.

3.6.5 Comparison of the Scourie dykes with 2.4 Ga dyke swarms worldwide

Mafic dykes are often used as a tool for cratonic reconstruction since they are typically short-lived events associated with plume or rift magmatism and are commonly found on either side of rifted continents, for example the ~130 Ma Parana-Etendeka dyke swarm and magmatism in Brazil and Namibia formed during rifting of Gondwanaland and opening of the South Atlantic Ocean (Turner et al., 1994). When dyke swarms have uniform orientations and are subsequently dispersed by or during continental break up, it may be possible to reconstruct the position of the continents using the dykes as time markers. Dyke swarms commonly occur either in radial patterns (e.g. Mackenzie and Mistassini dykes in the Canadian Shield; LeCheminant and Heaman, 1989), linear arrays (e.g. Scourie dykes and Badplaas swarm from the Kaapvaal craton, Tarney, 1973; Klausen et al., 2010), or following the edges of cratons either perpendicular or parallel to their boundaries (e.g. the circum-Superior igneous event Heaman et al., 2009, and the British Tertiary igneous province, Mussett et al., 1988).

For dykes on different continents to be useful pins in paleocontinental reconstruction, certain conditions need to be met before they can be considered the same event. The dykes in different locations need to be the same age, their paleolatitude needs to be the same or close, the dyke geochemistry needs to indicate that they formed from the same mantle source, and the country rock into which they intrude also needs to

show a common crustal history. When these conditions are only partially met it is possible to make an incorrect continental reconstruction. Using a modern example based on geochronology and paleomagnetism information alone, the feeder dykes to the Mount St Helen's volcano, northwest U.S.A. could be considered correlative to feeder dykes at Mount Vesuvius, Italy.

Modern paleogeographical reconstructions of the Neoarchean crust have suggested the presence of various supercontinents, including Vaalbara (Cheney, 1996), Kenorland (Williams et al., 1991; de Kock et al., 2009), Arctica (Rogers and Santosh, 2003) and more recently Nunavutia (Pehrsson et al., 2013). Despite the small size of the LGC, the huge number of studies conducted on the area mean that its Precambrian history is relatively well known compared to most cratons worldwide. Therefore it is possible to attempt to place the Lewisian into a global context. Broadly speaking, the Lewisian shares some similarities with the newly postulated Nunavutia supercontinent. This supercontinent was conceived when problems were encountered fitting the Rae craton (western part of the Churchill Province in the Canadian Shield) into Kenorland. It is the result of the discovery that the Sask, São Francisco, NE Brazil, West Africa, Congo, Antarctic, Dharwar, Madagascar, N. China, Rae, and North Australian Cratons all contain evidence for 2.62 -2.58 Ga magmatism, and evidence for orogenesis at ~2.5 Ga and again between 2.45-2.3 Ga, followed by a further period of magmatism at ~2.1-2.2 Ga, which most of the other cratons worldwide do not (Pehrsson et al., 2013 and references therein). The Inverian metamorphic event at ~2.5 Ga, and magmatism in the Rhiconich terrane at ~2.6 Ga (Friend and Kinny, 2001) are consistent with some aspects of Nunavutia history, however the Lewisian doesn't contain evidence for an orogenic event between 2.45-2.3 Ga.

The new geochronology from the Scourie dykes provides another useful tool to aid in continental reconstruction, especially since 2.4 Ga mafic dyke swarms are relatively rare worldwide. If the Lewisian was part of Nunavutia during the Neoarchean, dyking of similar age, geochemistry and paleolatitude might be expected in its nearest neighbor in the supercontinent. Here we briefly compare the geochronology, paleomagnetic information, geochemistry and geology of similar-aged dyke swarms worldwide, with the goal of helping to constrain the location of the Lewisian during the Neoarchean and Paleoproterozoic and assess its possible nearest neighbors. It is beyond the scope of the present paper to provide an exhaustive comparison of global cratons with the Lewisian, and with the development of the IGCP 509 database system (Eglington et al., 2009), such comparisons will be readily available online in the future.

3.6.5.1. Possible paleogeography of the Lewisian during the Paleoproterozoic

~2.4 Ga dyke swarms are only known to occur on 6 cratonic blocks worldwide, the North Atlantic Craton (NAC) - 2374-2364 Ma Grædefjord dykes (Nilsson et al., 2012), Dharwar Craton – 2365-2368 Ma Bangalore Dyke Swarm (Halls et al., 2007; French and Heaman, 2010), Yilgarn Craton – 2410–2418 Ma Widgiemooltha Dykes (Doehler and Heaman, 1998; Nemchin and Pidgeon, 1998), Zimbabwe Craton – 2408.3 ± 2.0 Ma Sebanga Poort dyke (Söderlund et al., 2010), Baltic Shield - 2403 ± 3 Ma Ringvassøy mafic dykes (Kullerud et al., 2006), and the Lewisian – Scourie dykes (Fig. 3.5). All of these dyke swarms have similar emplacement dates and therefore the crustal blocks that host these dyke swarms could be potential neighbors to the Lewisian during the Paleoproterozoic. Only the Widgiemooltha, Sebanga Poort and Ringvassøy dyke ages overlap exactly with the Scourie dykes.

In terms of similar geological histories, which is a major consideration when assessing whether dyke swarms on separate terranes are part of the same event. Only the Dharwar craton and NAC are similar to the Lewisian. The Dharwar craton contains both ~2.4 Ga mafic dykes and Nunavutia-aged metamorphic and magmatic events (Pehrsson et al., 2013). The Lewisian and the NAC were joined prior to the opening of the Atlantic and their close association throughout the Proterozoic and Archean is also commonly postulated (e.g. Bridgewater et al., 1973; Wright et al., 1973; Hall et al., 1990). The Paleoproterozoic structural/metamorphic history of the Lewisian has traditionally been linked with the Nagssugtoqidian orogen of the NAC due to similarities in deformational style, including major shear zones juxtaposing reworked Archean crustal blocks at different crustal levels, 1.9 Ga juvenile arc terranes, as well as ~1.9-1.7 Ga Laxfordian metamorphism (Bridgewater et al., 1990; Kalsbeek et al., 1993; Buchan et al., 2000; Connelly and Mengel, 2000; Park et al., 2001; Friend and Kinny, 2001; Whitehouse and Bridgewater, 2001; Mason et al. 2004; Park 2005; Mason 2012). The Inverian event at ~2.5 Ga is not recorded in the NAC, although this event is only recorded between the Assynt and Rhiconich terranes in the Lewisian.

Paleomagnetically, the Lewisian and Dharwar craton are thought to be at similar latitudes during the Paleoproterozoic. A recent study on the Scourie dykes (Sampson, 2009) has indicated that the Lewisian crust was at high latitude (~60°) at 2.4 Ga. The Dharwar craton was also at similar latitude during this time (~60°; Halls et al., 2007). Unfortunately the paleolatitude of the NAC at this time is unknown.

Finally geochemical comparisons of the three potential correlated swarms are also possible and could provide evidence for an origin linked to a common large igneous province. Geochemically, the 2.37 Ga Bangalore dykes appear to be distinctive with

small peaks in Zr and Y on the spider diagram, and a steep overall slope (La/Lu = 53), possibly suggesting a garnet residue within the source (Fig. 3.6a). The Scourie and Grædefjord dykes have Zr, Y, Sr and Nb troughs and less fractionated rare earth elements (La/Lu ~32) (Fig. 3.6a). All of the dykes have similar Zr/Nb ~19 and Zr/Y which suggests that they may come from the same source, although there is much scatter in the data (Fig. 3.6b,c).

In summary, consideration of the dyke geochemistry, paleolatitudes, and regional geology, the Scourie, Grædefjord and Dharwar mafic magmas could have originated from a common large igneous province and a common mantle source. However in terms of geochronology, the Scourie dykes are older than both the Bangalore and Grædefjord dyke swarms. The regional geology is sufficiently similar between the Lewisian and NAC that they could have been part of a single craton during the Paleoproterozoic. The lack of 2.3 and ~2.2-2.1 Ga magmatism and orogenesis suggests that neither the NAC nor the Lewisian were part of the supercraton Nunavutia, at least during the late Paleoproterozoic. Currently there is insufficient evidence to suggest that the Scourie and Grædefjord dykes are coeval, especially since the ages do not overlap. More detailed geochemistry, paleomagnetic work (in the NAC) and possibly oxygen isotopic analysis on the Grædefjord dykes could help to confirm or deny that they are an extension of the Scourie dykes.

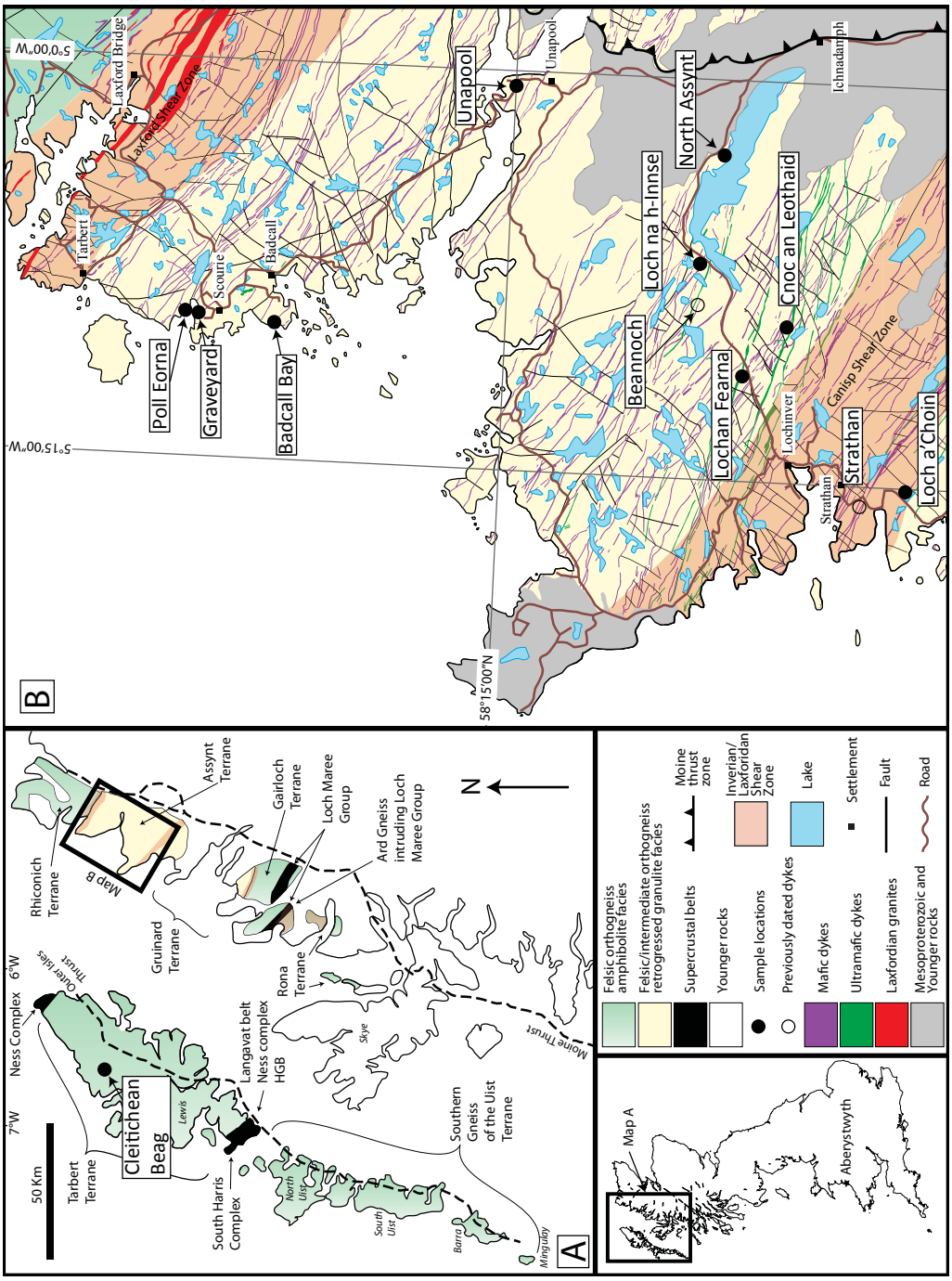

Figure 3.1. Geological Map

(A) Simplified geological map of the northwest of Scotland, and the Outer Hebrides islands of Lewis, Harris and Uist. The location of the Cleitichean Beag dyke on Lewis is shown. The South Harris Complex is a Proterozoic supracrustal belt containing the Langavat belt, Ness Complex and the Harris Granulite Belt (HGB), Modified from Mason and Brewer (2004); Wheeler et al. (2010). (B) Simplified higher resolution geological map of the Loch Assynt area on the Scottish mainland. Modified from 1:50 000 Assynt Special Sheet (Bedrock) geological map from the BGS and Fig. 3.2b from Goodenough et al. (2010).

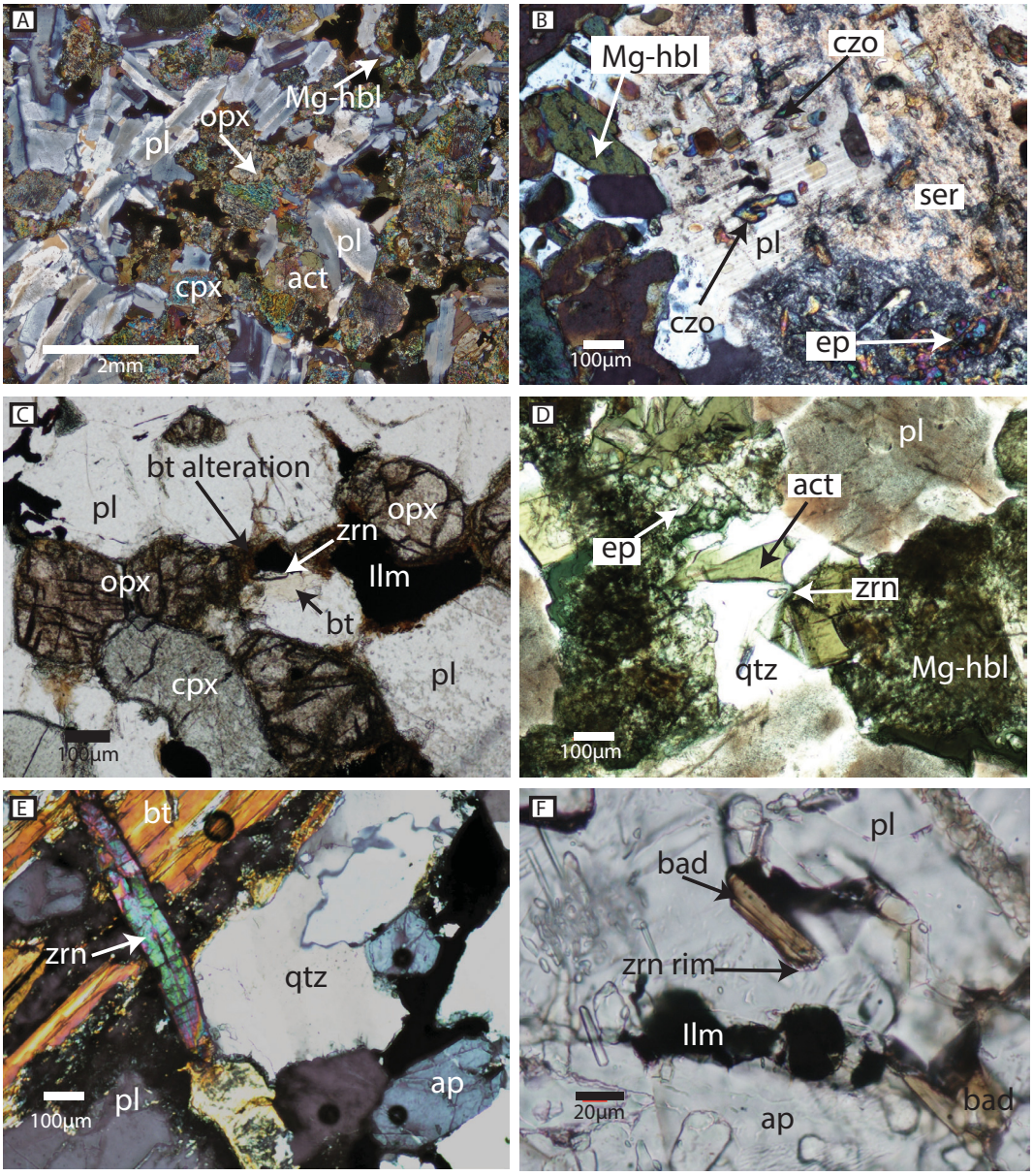

Figure 3.2. Thin Sections

Thin section evidence for igneous and metamorphic textures in the dykes. A) Poll Eorna dyke shown (in xpl) with exsolution lamellae in pyroxene and growth of actinolite and hornblende pseudomorphing pyroxene. B) Lochan Fearna dyke showing high degrees of alteration of plagioclase. C) North Assynt dyke showing elongate zircon together with with biotite, ilmenite and orthopyroxene. D) Loch a'Choin dyke showing slightly rounded zircon within a quartz crystal. E) Graveyard dyke showing large zircon crystal within late stage silica saturated melt. F) Cleitchean Beag dyke showing baddeleyite within plagioclase, apatite and magnetite, the large center baddeleyite has a thin zircon rim along its lower edge. Mineral abbreviations are from Siivola et al. (2007) except baddeleyite, which is abbreviated to bad. Mineral abbreviations are; act – actinolite, ap – apatite, bt – biotite, cpx – clinopyroxene, czo – clinozoisite, ep – epidote, ilm – ilmenite, Mg-hbl magnesiohornblende, opx – orthopyroxene, pl – plagioclase, qtz – quartz, ser – sericite, and zrn – zircon.

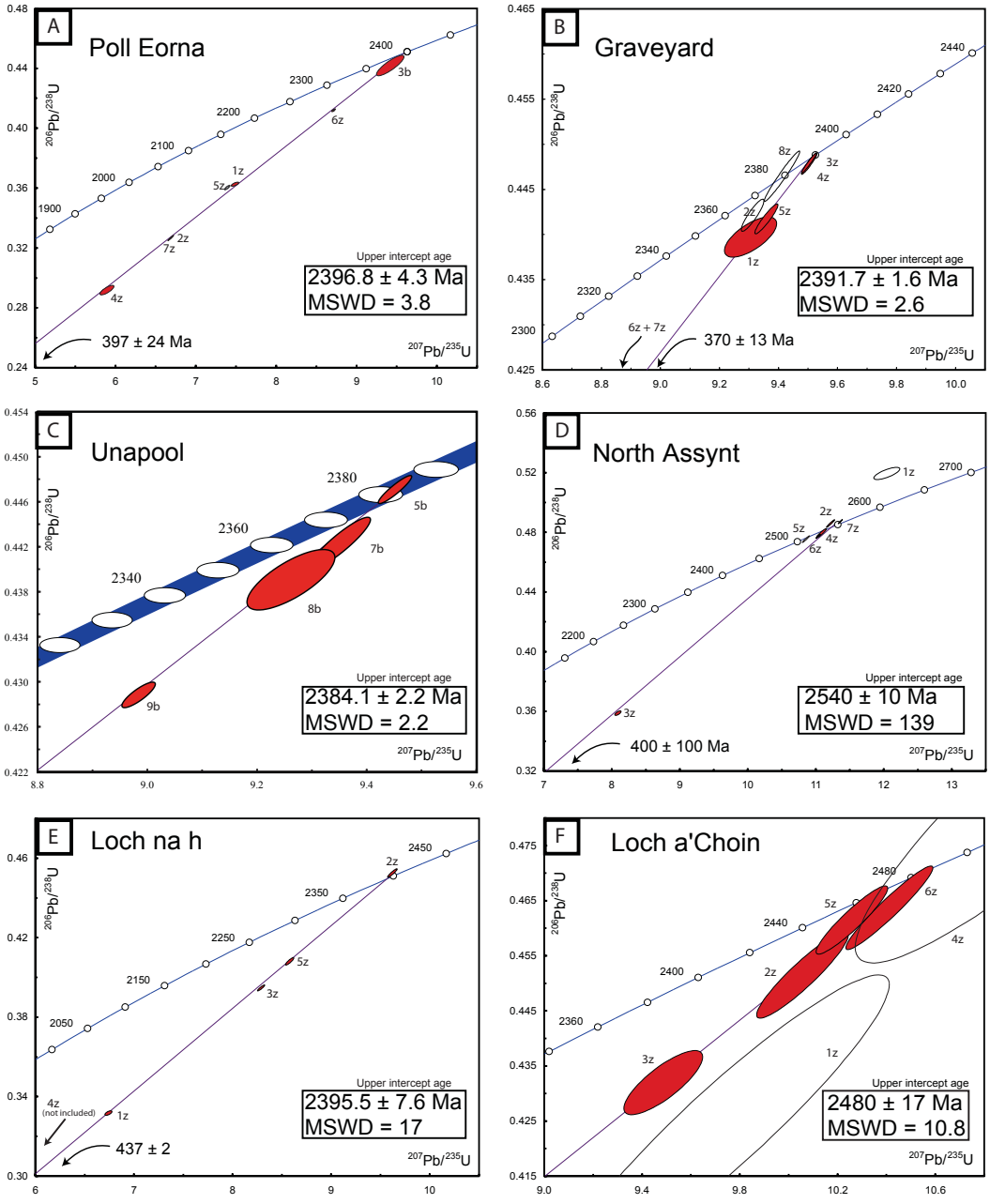
A
Poll Eorna
Upper intercept age
2396.8 ± 4.3 Ma
MSWD = 3.8
397 ± 24 Ma
B
Graveyard
Upper intercept age
2391.7 ± 1.6 Ma
MSWD = 2.6
370 ± 13 Ma
C
Unapool
Upper intercept age
2384.1 ± 2.2 Ma
MSWD = 2.2
D
North Assynt
Upper intercept age
2540 ± 10 Ma
MSWD = 139
400 ± 100 Ma
E
Loch na h
Upper intercept age
2395.5 ± 7.6 Ma
MSWD = 17
437 ± 2
F
Loch a'Choin
Upper intercept age
2480 ± 17 Ma
MSWD = 10.8
207Pb/235U
206Pb/238U

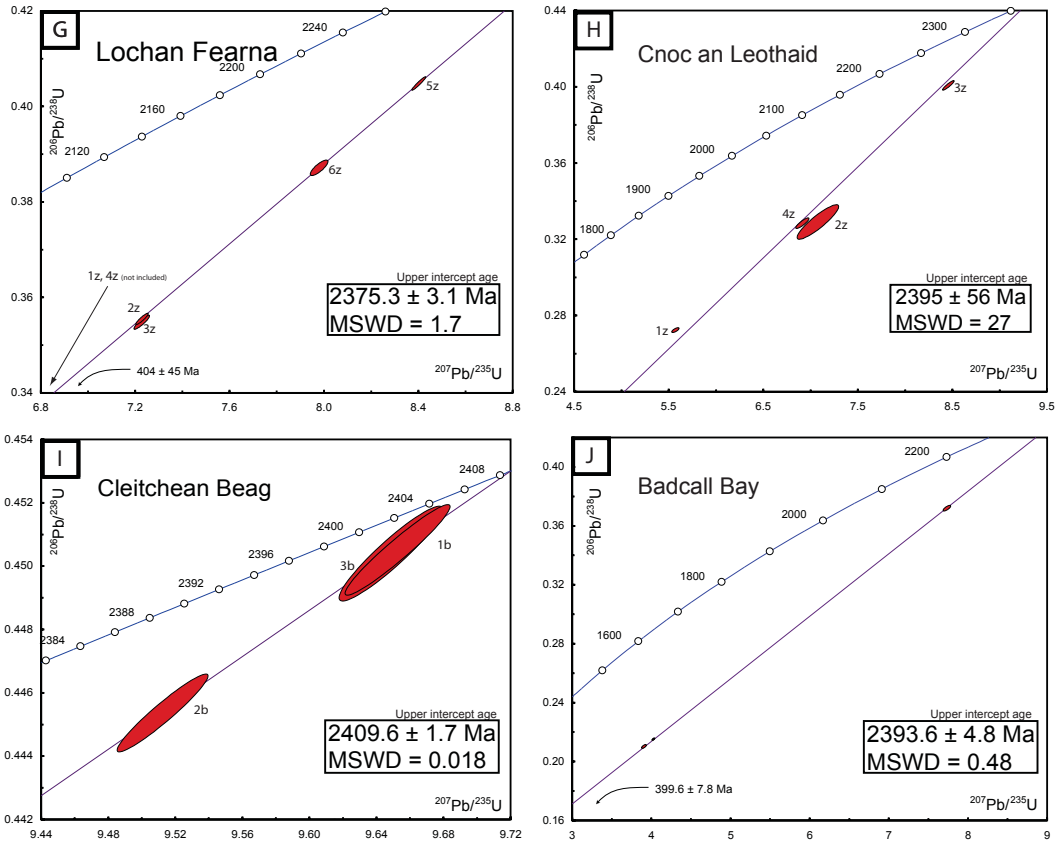

Figure 3.3. Concordia Diagrams

Concordia diagrams showing U-Pb isotopic data for the Scourie Dykes. Error ellipses are shown at the 2σ level and the labels are lined to the aliquot numbers from table 3.1. Filled ellipses are included in the regression, where as hollow ellipses are not, see text for more details.

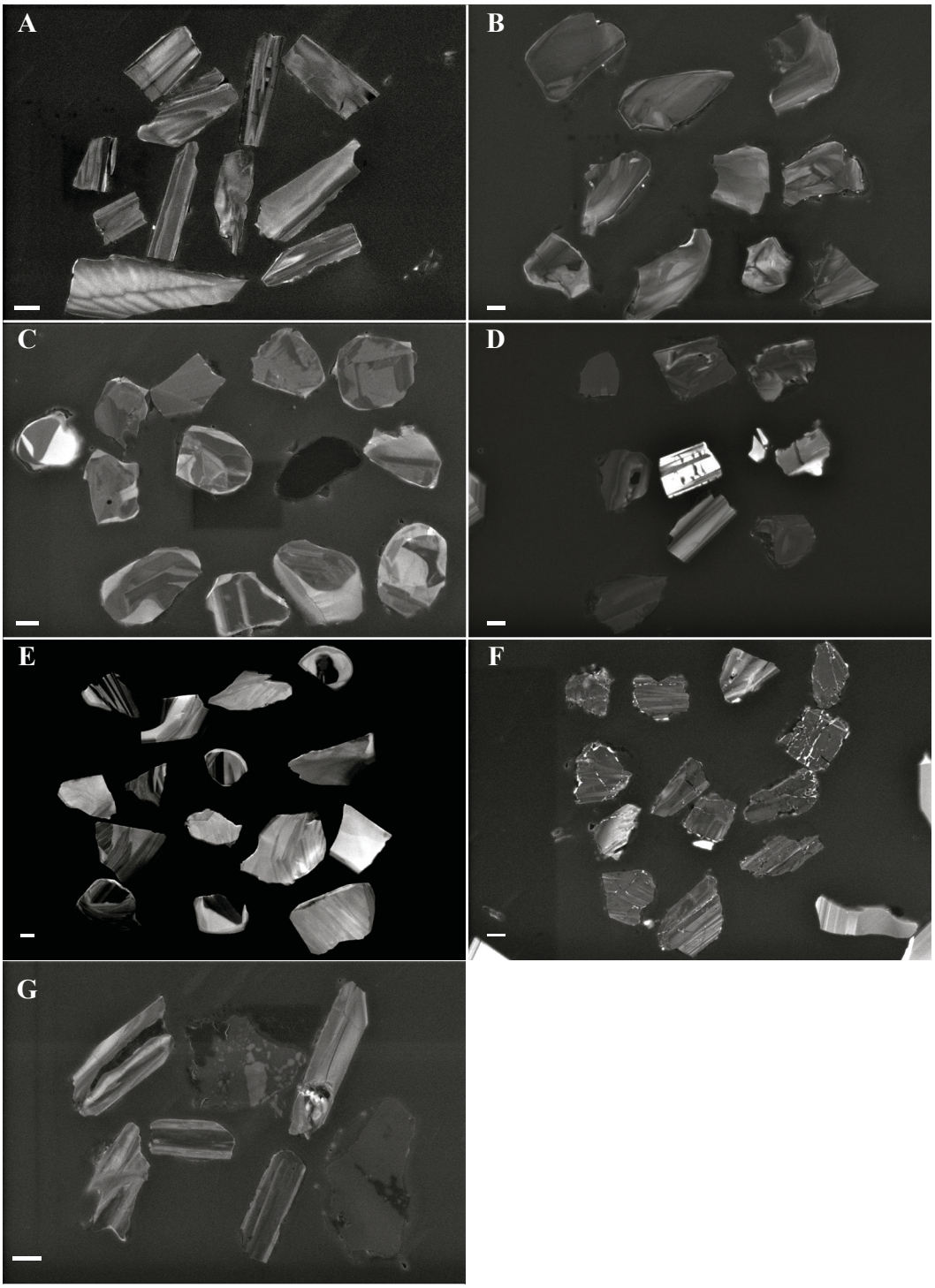

Figure 3.4. CL images

Cathodoluminescence images of zircons from the Scourie dykes: (A) Poll Eorna, (B) Graveyard, (C) North Assynt, (D) Loch na h, (E) Loch a'Choin, (F) Lochan Fearna, (G) Badcall Bay. The dull grains in C and G are apatite and plagioclase. The dull colour shown by most of the grains is due to poor CL response caused by metamictization. The white bar is 20μm.

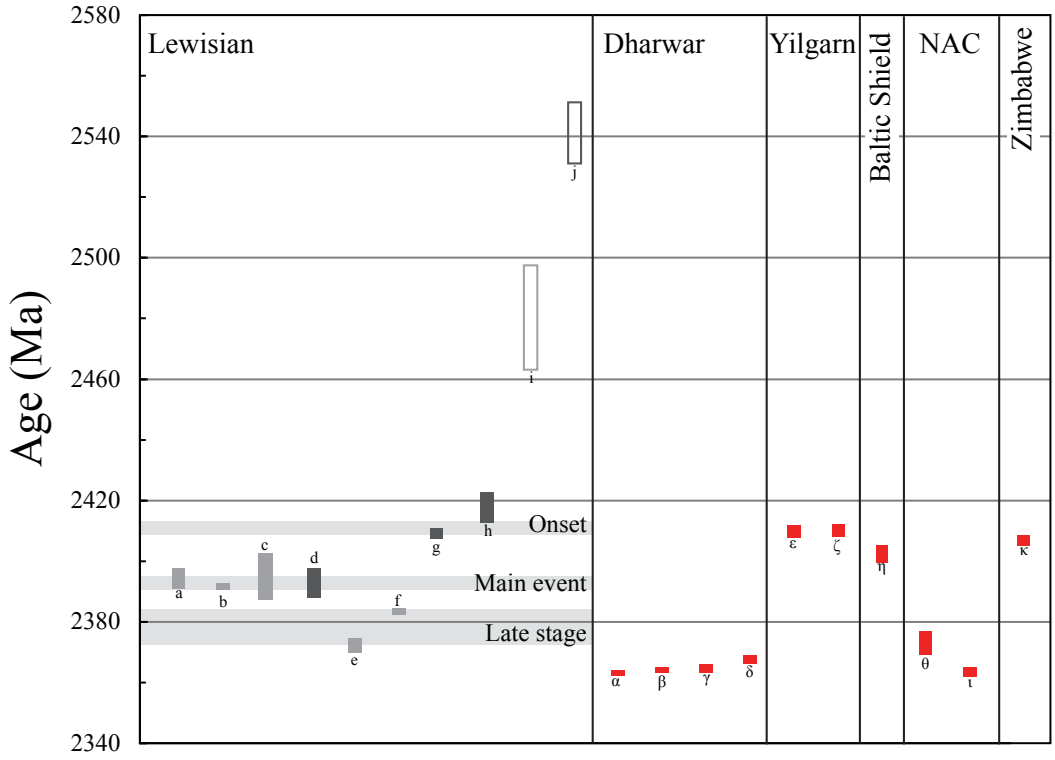

Figure 3.5. Worldwide dyke ages

Correlation chart showing the worldwide distribution of dyking events at ~2.4 Ga dated by U-Pb zircon or baddeleyite. The dykes are arranged by craton (or gneiss complex in the case of the Lewisian), all bars correspond to 2σ errors. In the Lewisian, the dark grey bars reflect picritic or olivine gabbroic dyke compositions, where as, the light grey bars reflect dolerite or norite dyke compositions, the dykes on the other cratons are not coloured by composition. The horizontal bars show the timing of the Scourie dyke emplacement events. The symbols refer to specific dykes, a) Poll Eorna dyke, b) Graveyard dyke, c) Loch na h dyke, d) Badcall Bay dyke e) Lochan Fearna dyke, f) Unapool dyke, g) Cleitchean Beag dyke, h) Beannach dyke (Heaman and Tarney, 1989), i) Loch a'Choin dyke, j) North Assynt dyke, α) Bangalore dyke (Halls et al., 2007), β) Harohalli dyke (French and Heaman, 2010), γ) Penukonda dyke (French and Heaman, 2007), δ) Chennekottapalle dyke (French and Heaman, 2010), ε) Bineringie dyke. (Doehler and Heaman, 1998), ζ) Celebration dyke (Doehler and Heaman, 1998), η) Ringvassøy dyke, (Kullerud et al., 2006), θ) Grædefjord dyke 508201 (Nilsson et al., 2012), ι) Grædefjord dyke 508214 (Nilsson et al., 2012), κ) Sebanga Poort Dyke (Söderlund et al., 2010). The North Assynt and Loch a'Choin dykes are shown as hollow rectangles since these ages are from xenocrystic zircon.

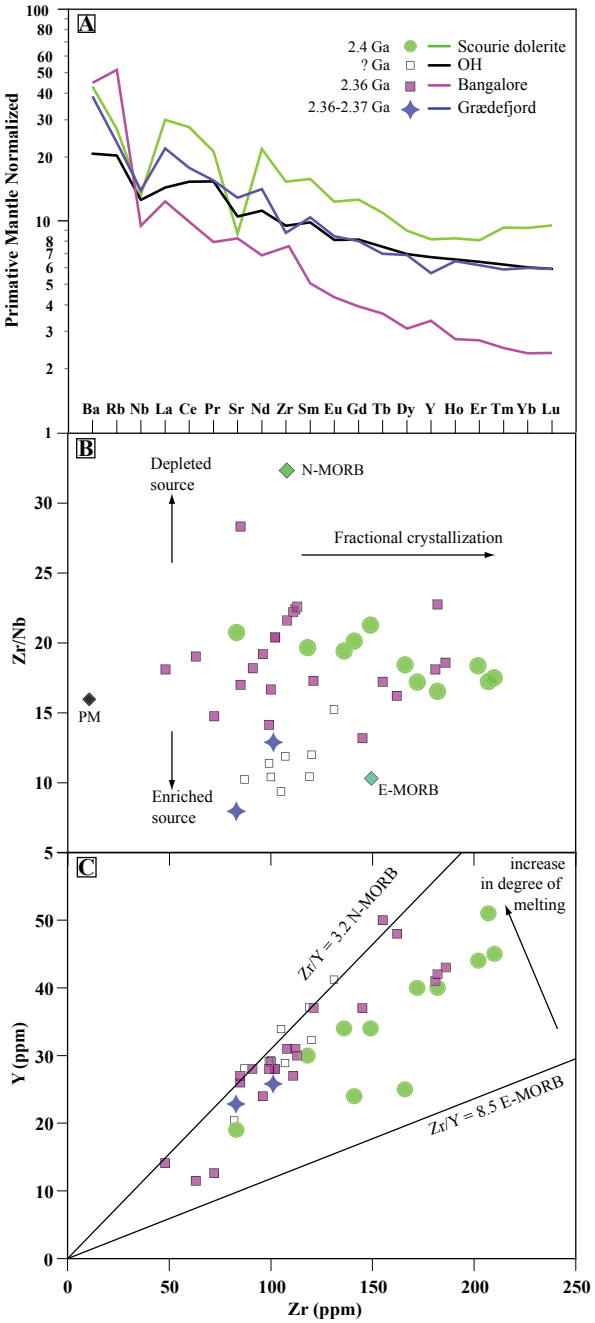

Figure 3.6. Geochemistry

Geochemical plots of worldwide ~2.4 Ga dykes. A) Primitive Mantle normalized spider diagram with average composition of the Scourie dolerites and norites (Weaver and Tarney, 1981b), OH dykes are averages of mafic dykes from the Uist and Tarbert terranes and the Langavat Belt dykes (Mason and Brewer, 2004) Bangalore dyke swarm (Halls et al., 2007; French and Heaman, 2010), Grædefjord dykes (Nillson et al., 2012), primitive mantle normalization used the values of McDonough and Sun (1995). B and C show incompatible trace-element concentrations within the dykes and the effects of fractional crystallization and degree of melting, N-MORB and E-MORB values are taken from Niu and O'Hara (2003).

Sample ID	Name	Rock Type	Minerals												
			Olivine	Orthopyroxene	Clinopyroxene	Amphibole	Plagioclase	Titanite	Calcite	Biotite	Oxide	Quartz	Epidote*	Apatite	Garnet
LH99-51	Poll Eorna	Gabbro/dolerite		5[ab]	35[ab]	10[c]	45[e]	t			5		t	t	
LH99-46	Graveyard	Gabbro/dolerite		10[ab]	25[ab]	10[c]	40[e]				13	2		t	
LH07-12	Unapool	Gabbro/dolerite		5[b]	25[ab]	15[c]	40[e]							t	
JD09-21	North Assynt	Norite	10[bf]	13	23[a]	3[d]	40[e]		5	3	2		t	t	
JD09-14	Loch na h	Gabbro/dolerite			10[b]	25[c]	48[eg]	1		1	5	5	3	2	t
JD09-24	Loch a' Choin	Amphibolite				47[c]	40[eg]		3		5	2	2	1	
JD09-17	Lochan Fearna	Gabbro/dolerite				40[c]	39[eg]				5	5	10	1	
JD09-27	Cnoc an Leothaid	Gabbro/dolerite		4[b]	19[ab]	25[c]	35[eg]			5	3		3	1	
LH99-42	Cleitchean Beag	Picrite/Norite	10[f]	59	18		12							1	
LH86-40	Badcall Bay	Norite		40[a]	15[a]		37[e]			7	1			t	

a - exsolution lamella, b - amphibole pseudomorphing pyroxene, c - magnesiohornblende, d - actinolite, e - sericite alteration, f - iddingsite alteration, g - saussurite alteration, t - trace
* includes all epidote group minerals

Table 3.1. Mineral abundances

Dyke mineralogy and mineral abundances

		Compositional Parameters								Radiogenic Isotope Ratios								Isotopic Ages						
	Wt.	U	Th	Pb	206Pb*	mol %	Pb*	Pbc	206Pb	208Pb	207Pb		207Pb		206Pb		corr.	207Pb		207Pb		206Pb		
Sample	mg	ppm	U	ppm	x10-13 mol	206Pb*	Pbc	(pg)	204Pb	206Pb	206Pb	% err	235U	% err	238U	% err	coef.	206Pb	±	235U	±	238U	±	% Dis
(a)	(b)	(c)	(d)	(c)	(e)	(e)	(e)	(e)	(f)	(g)	(g)	(h)	(g)	(h)	(g)	(h)		(i)	(h)	(i)	(h)	(i)	(h)	
Poll Eorna (58°21'35.2794"N -5°9'53.2794W, NC 14947 45614)																								
(2) col skel z -1	0.001	474	0.541	201.1	7.186	99.2%	36	5.37	1834	0.170	0.150	0.464	7.512	0.579	0.364	0.205	0.683	2343.2	7.9	2174.4	5.2	2000.1	3.5	14.6
(2) col skel z -2	0.001	511	0.389	189.7	6.978	99.1%	32	5.78	1653	0.129	0.148	0.089	6.701	0.394	0.328	0.374	0.974	2326.7	1.5	2072.8	3.5	1827.0	5.9	21.5
(1) tan b -3	0.001	88	0.072	50.6	0.818	93.1%	4	5.50	217	0.021	0.155	0.512	9.496	0.905	0.444	0.688	0.827	2404.9	8.7	2387.2	8.3	2366.4	13.6	1.6
(1) col skel z -4	0.001	163	0.497	55.7	1.989	99.1%	35	1.55	1856	0.174	0.146	0.783	5.906	1.198	0.293	0.789	0.764	2301.4	13.5	1962.1	10.4	1657.0	11.5	28.0
(1) col skel z -5	0.001	298	0.414	121.9	4.484	99.1%	33	3.58	1736	0.130	0.149	0.160	7.403	0.287	0.361	0.204	0.840	2330.4	2.7	2161.3	2.6	1987.7	3.5	14.7
(2) z col skel CA -6	0.001	467	0.343	211.9	8.091	99.6%	79	2.65	4255	0.101	0.153	0.071	8.779	0.187	0.416	0.148	0.936	2381.6	1.2	2315.3	1.7	2240.9	2.8	5.9
(2) z col skel CA -7	0.001	676	0.326	240.8	9.196	99.7%	99	2.40	5359	0.109	0.148	0.071	6.670	0.156	0.326	0.107	0.922	2326.8	1.2	2068.7	1.4	1819.7	1.7	21.8
(2) z col skel CA -8	0.003	676	0.346	277.3	31.706	99.7%	107	7.70	5576	0.108	0.152	0.065	7.874	0.184	0.375	0.149	0.946	2372.7	1.1	2216.7	1.7	2051.9	2.6	13.5
Graveyard (58°21'8.7762N -5°9'59.994W, NC 14799 44800)																								
(1) col frag z -1	0.006	247	0.40	122.4	27.300	99.2%	35	20.35	1832	0.114	0.154	0.067	9.388	0.284	0.443	0.266	0.973	2389.2	1.1	2376.6	2.6	2362.0	5.3	1.1
(1) col frag z -2	0.003	209	0.46	103.4	11.576	99.6%	78	3.91	4339	0.130	0.153	0.083	9.355	0.251	0.444	0.222	0.945	2379.3	1.4	2373.4	2.3	2366.7	4.4	0.5
(1) z col frag -3	0.001	699	0.46	350.8	13.064	99.6%	76	4.54	3947	0.131	0.154	0.079	9.524	0.156	0.448	0.098	0.903	2391.6	1.4	2389.9	1.4	2387.8	2.0	0.2
(1) z col skel -4	0.002	349	0.46	175.4	13.065	99.6%	75	4.64	3856	0.131	0.154	0.068	9.523	0.136	0.448	0.078	0.941	2391.2	1.2	2389.8	1.3	2388.2	1.6	0.1
(2) z col skel -5	0.001	502	0.449	248.9	9.214	99.4%	46	5.27	2393	0.128	0.154	0.629	9.328	0.815	0.440	0.357	0.682	2386.9	10.7	2370.8	7.5	2352.1	7.0	1.5
(2) z col skel -6	0.001	130	0.211	31.9	1.198	98.3%	17	1.76	983	0.083	0.138	0.267	4.196	0.428	0.221	0.279	0.793	2201.9	4.6	1673.2	3.5	1284.9	3.3	41.6
(2) z col skel CA -7	0.001	164	0.284	49.0	1.807	98.5%	19	2.47	1038	0.105	0.144	0.193	5.222	0.339	0.264	0.241	0.830	2272.4	3.3	1856.2	2.9	1508.0	3.2	33.6
(2) z col skel CA -8	0.001	199	0.258	95.6	3.717	99.5%	57	1.66	3219	0.073	0.153	0.091	9.432	0.441	0.447	0.421	0.979	2380.3	1.5	2380.9	4.1	2381.7	8.4	-0.1

		Compositional Parameters								Radiogenic Isotope Ratios								Isotopic Ages						
	Wt.	U	Th	Pb	206Pb*	mol %	Pb*	Pbc	206Pb	208Pb	207Pb		207Pb		206Pb		corr.	207Pb		207Pb		206Pb		
Sample	mg	ppm	U	ppm	x10-13 mol	206Pb*	Pbc	(pg)	204Pb	206Pb	206Pb	% err	235U	% err	238U	% err	coef.	206Pb	±	235U	±	238U	±	% Dis
(a)	(b)	(c)	(d)	(c)	(e)	(e)	(e)	(e)	(f)	(g)	(g)	(h)	(g)	(h)	(g)	(h)		(i)	(h)	(i)	(h)	(i)	(h)	
Unapool (58°15'0.5502"N -5°0'39.3264"W, NC 23400 33000)																								
(2) z br frag -3	0.001	917	0.103	325.0	13.208	99.7%	79	4.05	4480	0.033	0.146	0.183	6.938	0.304	0.345	0.205	0.808	2296.3	3.1	2103.6	2.7	1912.2	3.4	16.7
(1) b with silicate rim -5	0.001	326	0.011	149.7	3.037	99.1%	29	2.47	1731	0.003	0.153	0.108	9.448	0.272	0.447	0.228	0.922	2383.0	1.8	2382.5	2.5	2382.1	4.5	0.0
(2) z col skel -6	0.001	571	0.481	156.8	2.730	98.5%	19	3.84	989	0.186	0.138	0.157	4.351	0.268	0.229	0.178	0.825	2199.2	2.7	1703.1	2.2	1329.7	2.1	39.5
(1) b tan frag -7	0.001	78	0.026	37.7	1.443	97.4%	11	3.22	698	0.007	0.153	0.210	9.346	0.498	0.442	0.426	0.908	2382.7	3.6	2372.6	4.6	2360.8	8.4	0.9
(1) b tan frag -8	0.001	61	0.028	37.9	1.126	89.4%	2	10.94	175	0.008	0.153	0.489	9.255	0.722	0.439	0.500	0.737	2378.6	8.3	2363.6	6.6	2346.1	9.8	1.4
(2) b tan frag -9	0.001	473	0.012	222.9	8.455	97.0%	9	21.54	616	0.003	0.152	0.154	8.971	0.284	0.429	0.215	0.843	2365.8	2.6	2335.1	2.6	2300.1	4.2	2.8
North Assynt Dyke (5°°10'70"N -5°02'72"W, NC 21020 25099)																								
(1) z col frag -1	0.001	342	0.506	286.1	3.706	88.9%	2	43.34	127	0.135	0.169	0.327	12.086	0.395	0.520	0.307	0.591	2543.2	5.5	2611.1	3.7	2699.5	6.8	-6.1
(1) z col frag -2	0.001	717	0.353	384.7	7.271	99.6%	75	2.54	3985	0.098	0.168	0.070	11.237	0.366	0.486	0.349	0.982	2533.4	1.2	2543.0	3.4	2555.0	7.4	-0.9
(1) z col frag -3	0.002	351	0.502	163.7	7.891	96.2%	7	29.25	372	0.165	0.164	0.154	8.101	0.269	0.359	0.205	0.821	2492.5	2.6	2242.4	2.4	1978.8	3.5	20.6
(1) z col frag -4	0.000	585	0.390	329.6	2.342	98.1%	15	4.22	770	0.109	0.168	0.126	11.102	0.319	0.480	0.272	0.921	2535.5	2.1	2531.8	3.0	2527.1	5.7	0.3
(2) z col frag CA -5	0.004	653	0.475	350.5	52.088	99.9%	268	5.21	13526	0.133	0.167	0.061	10.982	0.230	0.478	0.204	0.967	2524.8	1.0	2521.6	2.1	2517.7	4.3	0.3
(2) z col frag CA -6	0.001	837	0.445	447.4	16.678	99.8%	173	2.57	9023	0.125	0.168	0.063	11.053	0.156	0.478	0.115	0.939	2535.5	1.0	2527.6	1.5	2517.7	2.4	0.7
(2) z col frag CA -7	0.002	570	0.478	313.6	23.178	99.8%	142	4.40	7176	0.133	0.169	0.063	11.377	0.174	0.488	0.137	0.944	2549.5	1.1	2554.5	1.6	2560.8	2.9	-0.4

		Compositional Parameters								Radiogenic Isotope Ratios								Isotopic Ages						
	Wt.	U	Th	Pb	206Pb*	mol %	Pb*	Pbc	206Pb	208Pb	207Pb		207Pb		206Pb		corr.	207Pb		207Pb		206Pb		
Sample	mg	ppm	U	ppm	x10-13 mol	206Pb*	Pbc	(pg)	204Pb	206Pb	206Pb	% err	235U	% err	238U	% err	coef.	206Pb	±	235U	±	238U	±	% Dis
(a)	(b)	(c)	(d)	(c)	(e)	(e)	(e)	(e)	(f)	(g)	(g)	(h)	(g)	(h)	(g)	(h)		(i)	(h)	(i)	(h)	(i)	(h)	
Loch na h (58°11'7.1982"N -5°6'47.397"W, NC 17068 26060)																								
(2) z col frag -1	0.005	718	0.659	299.5	49.858	98.0%	15	94.90	715	0.216	0.147	0.289	6.752	0.395	0.333	0.204	0.709	2312.9	5.0	2079.5	3.5	1852.0	3.3	19.9
(1) z br core z rim CA -2	0.001	345	0.656	185.7	3.260	99.0%	32	2.84	1605	0.184	0.154	0.112	9.635	0.273	0.453	0.227	0.917	2393.9	1.9	2400.5	2.5	2408.2	4.6	-0.6
(1) z col frag CA -3	0.001	565	0.542	258.0	4.659	99.4%	50	2.53	2584	0.164	0.152	0.098	8.302	0.257	0.395	0.218	0.928	2371.5	1.7	2264.5	2.3	2148.0	4.0	9.4
(2) z col skel CA -4	0.001	713	0.385	227.9	8.220	98.9%	26	8.51	1318	0.142	0.152	0.085	5.791	0.201	0.276	0.156	0.916	2368.9	1.5	1945.1	1.7	1572.6	2.2	33.6
(2) z col skel CA -5	0.001	389	0.471	187.8	3.315	98.2%	16	5.56	826	0.140	0.153	0.125	8.596	0.270	0.409	0.217	0.892	2374.2	2.1	2296.1	2.5	2209.5	4.1	6.9
Loch a' Choin Dyke (58°6'50.997"N -5°14'59.3982"W, NC 08655 18521)																								
(1) z col frag -1	0.000	104	0.666	81.5	0.184	84.7%	2	2.97	101	0.201	0.167	1.215	9.753	2.954	0.424	2.591	0.912	2525.9	20.4	2411.7	27.2	2278.7	49.7	9.8
(1) z col frag -2	0.000	412	0.735	238.7	0.778	97.3%	12	1.85	612	0.210	0.162	0.418	10.080	0.984	0.452	0.853	0.906	2473.4	7.1	2442.1	9.1	2404.7	17.1	2.8
(1) z col frag -3	0.000	608	0.639	365.7	1.097	94.3%	5	6.09	258	0.187	0.160	0.689	9.522	1.082	0.433	0.745	0.776	2450.6	11.7	2389.7	9.9	2318.9	14.5	5.4
(1) z col frag -4	0.000	88	0.860	90.4	0.180	81.1%	1	3.80	80	0.237	0.167	1.894	11.286	3.711	0.490	2.996	0.862	2528.4	31.8	2547.1	34.6	2570.6	63.5	-1.7
(2) z col frag CA -5	0.001	53	0.817	31.9	1.017	97.1%	11	2.70	537	0.230	0.161	0.273	10.303	0.668	0.463	0.583	0.913	2469.5	4.6	2462.4	6.2	2453.7	11.9	0.6
(2) z col frag CA -6	0.001	47	0.892	27.9	0.915	98.5%	23	1.18	1156	0.252	0.163	0.258	10.432	0.946	0.464	0.891	0.962	2486.9	4.3	2473.9	8.8	2458.2	18.2	1.2
Lochan Fearna Dyke (58°10'11.3982"N -5°10'59.397"W, NC 12873 24528)																								
(2) z col skel -1	0.005	484	0.751	143.9	22.996	98.0%	16	42.42	739	0.290	0.136	0.110	4.291	0.236	0.228	0.186	0.891	2183.1	1.9	1691.7	1.9	1324.1	2.2	39.3
(2) z col skel -2	0.001	324	0.693	143.7	4.810	98.2%	17	8.00	828	0.220	0.148	0.106	7.239	0.283	0.356	0.244	0.930	2319.3	1.8	2141.3	2.5	1960.8	4.1	15.5
(2) z col skel -3	0.001	355	0.727	154.9	5.271	99.0%	30	5.04	1440	0.230	0.147	0.092	7.240	0.201	0.356	0.150	0.902	2316.4	1.6	2141.4	1.8	1963.8	2.5	15.2
(2) z col skel -4	0.002	630	0.786	243.9	16.364	99.1%	35	13.39	1659	0.263	0.142	0.200	6.078	0.302	0.311	0.179	0.770	2247.8	3.5	1987.1	2.6	1746.4	2.7	22.3
(2) z col skel CA -5	0.001	429	0.670	204.8	7.256	99.6%	72	2.82	3592	0.198	0.151	0.074	8.416	0.219	0.405	0.186	0.946	2353.3	1.3	2276.9	2.0	2192.8	3.4	6.8
(2) z col skel CA -6	0.001	286	0.656	139.9	4.618	97.4%	11	11.41	560	0.199	0.150	0.125	7.994	0.267	0.388	0.216	0.888	2341.0	2.1	2230.4	2.4	2111.9	3.9	9.8

		Compositional Parameters								Radiogenic Isotope Ratios								Isotopic Ages						
	Wt.	U	Th	Pb	206Pb*	mol %	Pb*	Pbc	206Pb	208Pb	207Pb		207Pb		206Pb		corr.	207Pb		207Pb		206Pb		
Sample	mg	ppm	U	ppm	x10-13 mol	206Pb*	Pbc	(pg)	204Pb	206Pb	206Pb	% err	235U	% err	238U	% err	coef.	206Pb	±	235U	±	238U	±	% Dis
(a)	(b)	(c)	(d)	(c)	(e)	(e)	(e)	(e)	(f)	(g)	(g)	(h)	(g)	(h)	(g)	(h)		(i)	(h)	(i)	(h)	(i)	(h)	
Cnoc an Leothaid (58°9'21.24"N -5°9'2.3394"W, NC 14712 22888)																								
(1) z col frag inc CA -1	0.001	219	0.469	72.8	2.495	97.9%	14	4.78	727	0.172	0.148	0.328	5.578	0.463	0.273	0.260	0.726	2327.2	5.6	1912.7	4.0	1554.3	3.6	33.2
(1) z col frag inc CA -2	0.000	62	0.639	29.2	0.339	93.4%	5	2.08	245	0.216	0.156	0.731	7.094	1.438	0.329	1.156	0.863	2414.8	12.4	2123.3	12.8	1835.5	18.5	24.0
(2) z col frag inc CA -3	0.000	391	0.601	189.1	1.963	98.5%	20	2.70	1024	0.181	0.153	0.160	8.472	0.348	0.401	0.281	0.892	2381.9	2.7	2283.0	3.2	2174.1	5.2	8.7
(2) z col frag inc CA -4	0.000	828	0.238	318.7	1.136	97.1%	10	2.99	542	0.080	0.153	0.283	6.925	0.496	0.329	0.359	0.828	2376.8	4.8	2101.8	4.4	1832.6	5.7	22.9
Cleitchean Beag Lewis Dyke (58°14'1.827"N -6°39'0.6978"W, NB 27150 36660)																								
(2) b tan frag -1	0.001	453	0.020	207.4	8.516	99.5%	57	3.57	3294	0.006	0.156	0.074	9.670	0.191	0.451	0.151	0.932	2407.4	1.3	2403.9	1.8	2399.7	3.0	0.3
(2) b tan frag -2	0.001	545	0.022	245.2	10.129	99.7%	89	2.74	5154	0.006	0.155	0.074	9.532	0.155	0.446	0.103	0.915	2402.1	1.3	2390.6	1.4	2377.1	2.0	1.0
(1) b tan frag -3	0.001	626	0.020	284.5	11.771	99.7%	100	2.83	5790	0.006	0.155	0.069	9.668	0.216	0.451	0.186	0.952	2407.2	1.2	2403.6	2.0	2399.4	3.7	0.3
Badcall Bay (58°19'31.6194"N -5°10'3.597"W, NC 14599 41800)																								
(1) z col skel CA -1	0.001	173	0.150	75.2	2.695	96.6%	8	8.72	431	0.047	0.151	0.220	7.753	0.348	0.373	0.232	0.785	2355.5	3.8	2202.8	3.1	2042.4	4.1	13.3
(7) z col ab 8†	0.002	377	0.425	99.0	6.610	95.9%	7	25.81	364	0.128	0.135	0.273	3.928	0.479	0.210	0.368	0.823	2168.8	4.8	1619.5	3.9	1231.3	4.1	43.23
z col ab 9⊠	0.002	763	0.349	190.5	13.703	97.6%	12	30.18	631	0.105	0.136	0.158	4.046	0.301	0.215	0.240	0.853	2181.0	2.7	1643.5	2.5	1256.8	2.7	42.38
Phalaborwa baddeleyite																								
IN-1	0.002	94	0.016	35.9	2.944	98.80%	22	3.14	1334	0.005	0.127	0.261	6.606	0.385	0.377	0.245	0.740	2059.8	4.6	2060.1	3.4	2060.3	4.3	-0.03
IN-1	0.001	84	0.008	32.0	0.658	98.71%	22	0.71	1413	0.002	0.127	0.164	6.597	0.367	0.377	0.314	0.897	2057.5	2.9	2058.9	3.2	2060.2	5.6	-0.13

(a) z - zircon, b - baddeleyite, number in parenthesis denotes number of grains analyzed, CA - Chemical Abrasion treatement given after Mattinson (2005), final number is the aliqot number - also used on concordia diagrams (Figure 3). (b) Nominal fraction weights estimated from photomicrographic grain dimensions, adjusted for partial dissolution during chemical abrasion. (c) Nominal U and total Pb concentrations subject to uncertainty in photomicrographic estimation of weight and partial dissolution during chemical abrasion. (d) Model Th/U ratio calculated from radiogenic 208Pb/206Pb ratio and 207Pb/235U age. (e) Pb* and Pbc represent radiogenic and common Pb, respectively; mol % 206Pb* with respect to radiogenic, blank and initial common Pb. (f) Measured ratio corrected for spike and fractionation only. Daly analyses, based on analysis of NBS-981 and NBS-982. Daly fractionation factors used are 0.26615 for Pb and 0.11921 for U (g) Corrected for fractionation, spike, and common Pb; up to 1 pg of common Pb was assumed to be procedural blank: 206Pb/204Pb = 18.60 ± 0.80%; 207Pb/204Pb = 15.69 ± 0.32%; 208Pb/204Pb = 38.51 ± 0.74% (all uncertainties 1-sigma). Excess over blank was assigned to initial common Pb. (h) Errors are 2-sigma, propagated using the algorithms of Schmitz and Schoene (2007) and Crowley et al. (2007). (i) Calculations are based on the decay constants of Jaffey et al. (1971). 206Pb/238U and 207Pb/206Pb ages corrected for initial disequilibrium in 230Th/238U using Th/U [magma] = 2. (j) Corrected for fractionation, spike, and blank Pb only. † analysis #8 of the badcall bay dyke, Heaman and Tarney, (1989), ⊠ analysis #9 of the badcall bay dyke, Heaman and Tarney, (1989)

Table 3.2. Scourie U-Pb data

U-Th-Pb data from zircon and baddeleyite extracted from the Scourie dykes.

References

Blackburn, T.J., Olsen, P.E., Bowring, S.A., McLean, N.M., Kent, D.V., Puffer, J., McHone, G., Rasbury, E.T., Et-Touhami, M., 2013. Zircon U-Pb Geochronology links the end-Triassic extinction with the Central Atlantic Magmatic Province. Science 340, 941-945. DOI: 10.1126/science.1234204

Bridgwater, D., Austrheim, H., Hansen, B.T., Mengel, F., Pedersen, S., Winter, J,. 1990. The Proterozoic Nagssugtoqidian Mobile Belt of Southeast Greenland: a Link Between the Eastern Canadian and Baltic Shields. Geoscience Canada 17, 305-310.

Bridgwater, D,. Watson, J., Windley. B.F., 1973. The Archaean Craton of the North Atlantic Region. Philosophical Transactions of the Royal Society of London. Series a, Mathematical and Physical Sciences 273, 493–512.

Buchan, K.L., Mertanen, S., Park, R.G., Pesonen, L.J., Elming, S.Å., Abrahamsen, N., Bylund, G., 2000. Comparing the Drift of Laurentia and Baltica in the Proterozoic: the Importance of Key Palaeomagnetic Poles. Tectonophysics 319, 167–198.

Cartwright I. Valley, J.W., 1991. Low 18O Scourie dike magmas from the Lewisian complex northwestern Scotland. Geology 19, 578-581.

Chapman, H.J., 1979. 2,390 Myr Rb–Sr Whole-Rock for the Scourie Dykes of North-West Scotland. Nature 277, 642-643.

Cheney, E.S., 1996. Sequence stratigraphy and plate tectonic significance of the Transvaal succession of southern Africa and its equivalent in Western Australia. Precambrian Research 79, 3-24.

Cliff, R.D.R., Guise, P., 1998. Geochronological Studies of Proterozoic Crustal Evolution in the Northern Outer Hebrides. Precambrian Research 91, 1–18.

Connelly, J.N., Mengel, F.C., 2000. Evolution of Archean components in the Nagssugtoqidian Orogen, West Greenland. Geological Society of America Bulletin 112, 747–763.

Connelly, J.N., van Gool, J.A.M., Mengel. F.C., 2000. Temporal Evolution of a Deeply Eroded Orogen: the Nagssugtoqidian Orogen, West Greenland. Canadian Journal of Earth Sciences 37 (8), 1121–1142.

Corfu, F., Crane, A., Moser, D., Rogers, G., 1998. U-Pb Zircon Systematics at Gruinard Bay, Northwest Scotland: Implications for the Early Orogenic Evolution of the Lewisian Complex. Contributions to Mineralogy and Petrology 133, 329–345.

Corfu, F., Heaman, L.M., Rogers, G., 1994. Polymetamorphic Evolution of the Lewisian Complex, NW

Scotland, as Recorded by U-Pb Isotopic Compositions of Zircon, Titanite and Rutile. Contributions to Mineralogy and Petrology 117, 215–228.

Crowley, J.L., Schoene, B., Bowring, S.A., 2007. U–Pb dating of zircon in the Bishop Tuff at the millennial scale. Geology 35, 1123–1126.

Dallmeyer, R.D., Strachan, R.A., Rogers, G., Watt. G.R., Friend, C.R.L., 2001. Dating deformation and cooling in the Caledonian thrust nappes of north Sutherland Scotland: insights from $^{40}Ar/^{39}Ar$ and Rb-Sr chronology. Journal of the Geological Society, London 158, 501-512.

Dearnley, R., 1963. The Lewisian complex of South Harris; with some observations on the metamorphosed basic intrusions of the Outer Hebrides, Scotland. Quarterly Journal Geological Society of London 119, 243-312.

DePaolo, D.J. Wasserburg, G. J., 1976. Inferences about magma sources and mantle structure from variations of 143Nd/144Nd. Geophysical Research Letters 3 (12), 743-746.

Doehler, J.S., Heaman, L.M., 1998. 2.41 Ga U–Pb Baddeleyite ages for two gabbroic dykes from the Widgiemooltha swarm, Western Australia: a Yilgarn–Lewisian connection? In: GSA Annual Meeting, Toronto Ontario, p. A-291.

Druecker, M.D., Gay Jr, S.P., 1987. Mafic Dyke Swarms Associated with Mesozoic Rifting in Eastern Paraguay, South America. Geological Association of Canada Special Publication 34, 187–193.

Eglington, B.M., Reddy, S.M., Evans, D.A.D., 2009. The IGCP 509 database system: design and application of a tool to capture and illustrate litho- and chrono- stratigraphic information for Palaeoproterozoic tectonic domains, large igneous provinces and ore deposits; with examples from southern Africa. Geological Society of London Special Publication 323, 27–48.

Ernst, R.E., Bleeker, W., Söderlund, U., and Kerr, A.C., 2013. Large Igneous Provinces and Supercontinents: Toward Completing the Plate Tectonic Revolution. Lithos, http://dx.doi.org/10.1016/j.lithos.2013.02.017

Evans, C.R., 1965. Geochronology of the Lewisian Basement Near Lochinver, Sutherland. Nature 207, 54–56.

Evans, C.R., Tarney, J., 1964. Isotopic Ages of Assynt Dykes. Nature 204, 638-641.

Fahrig, W.F., 1987. The tectonic settings of continental mafic dyke swarms: failed arm and early passive margin. In: Halls, H.C., Fahrig, W.F. (Eds.), Mafic Dyke Swarms. Geological Association of Canada Special Paper, vol. 34, pp. 331–348.

Francis, P.W., 1973. Scourian-Laxfordian Relationships in the Barra Isles. Journal of the Geological

Society of London 129, 161-189.

Friend, C., Kinny, P., 1995. New evidence for protolith ages of Lewisian granulites, northwest Scotland. Geology 23, 1027-1030.

Friend, C., Kinny, P., 2001. A Reappraisal of the Lewisian Gneiss Complex: Geochronological Evidence for Its Tectonic Assembly From Disparate Terranes in the Proterozoic. Contributions to Mineralogy and Petrology 142, 198–218.

Friend, C.R.L., Strachan, R.A., Kinny, P.D., 2008. U-Pb zircon dating of basement inliers within the Moine Supergroup, Scottish Caledonides: implications of Archean protolith ages. Journal of the Geological Society, London 165, 807-815.

Gee, D.G., 1975. A Tectonic model for the central part of the Scandinavian caledonides. American Journal of Science 275, 468-515.

Goodenough, K., Millar, I., Strachan, R. A., Krabbendam, M., Evans, J.A., 2011. Timing of regional deformation and development of the Moine Thrust Zone in the Scottish Caledonides: constraints from the U-Pb geochronology of alkaline intrusions. Journal of the Geological Society, London 168, 99-113.

Goodenough, K.M., Park, R.G., Krabbendam, M., Myers, J.S., Wheeler, J., Loughlin, S.C., Crowley, Q.G., Friend, C.R.L., Beach, A., Kinny, P.D., Graham, R.H., 2010. The Laxford Shear Zone: an End-Archaean Terrane Boundary?. Geological Society London Special Publications 335, 103–120. doi:10.1144/SP335.6.

Goodenough, K.M., Crowley, Q.G., Krabbendam, M., Parry, S.F.. 2013. New U-Pb Age Constraints for the Laxford Shear Zone, NW Scotland: Evidence for Tectono-Magmatic Processes Associated with the Formation of a Paleoproterozoic Supercontinent. Precambrian Research, 1–47. doi:10.1016/j.precamres.2013.04.010.

Hall, R.P., Hughes, D.J., Tarney, J., 1990. Early Precambrian rocks of Greenland and Scotland, Early Precambrian Basic Magmatism, Mantle evolution, In: Parker, A.J., Rickwood, P.C., Tucker, D.H. (Eds.), Mafic Dykes and Emplacement Mechanism. A.A. Balkema, Rotterdam, pp 111–135..

Halls, H.C., Kumar, A., Srinivasan, R., Hamilton, M.A., 2007. Paleomagnetism and U–Pb geochronology of easterly trending dykes in the Dharwar craton, India: feldspar clouding, radiating dyke swarms and the position of India at 2.37 Ga. Precambrian Research 155, 47–68.

Halls, H.C., Davis, D.W., Stott, G.M., Ernst, R.E., Hamilton, M.A., 2008. The Paleoproterozoic Marathon large igneous province: New evidence for a 2.1 Ga long-lived mantle plume event alon the southern margin of the North American Superior Province. Precambrian Research 162, 327-353.

Harlan, S.S., Heaman, L.M., LeCheminant, A.N., Premo, W.R., 2003. Gunbarrel mafic magmatic event: A key 780 Ma time marker for Rodinia plate reconstructions. Geology 31, 1053-1056.

Heaman, L.M., Tarney, J., 1989. U Pb Baddeleyite Ages for the Scourie Dyke Swarm, Scotland: Evidence for Two Distinct Intrusion Events. Nature 340, 705–708.

Heaman, L.M., Bowins, R., Crocket, J., 1990. The chemical composition of igneous zircon suites: Implications for geochemical tracer studies. Geochimica et Cosmochimica Acta 54, 1579-1607.

Heaman, L.M., Erdmer, P., Owen, J.V., 2002. U–Pb geochronologic constraints on the crustal evolution of the Long Range Inlier, Newfoundland. Canadian Journal of Earth Sciences 39, 845–865.

Heaman, L.M., 2009. The application of U–Pb geochronology to mafic, ultramafic and alkaline rocks: An evaluation of three mineral standards. Chemical Geology 261, 43-52.

Heaman, L.M., Peck, D., Toope, K., 2009. Timing and geochemistry of 1.88 Ga Molson Igneous Events, Manitoba: insights into the formation of a craton-scale magmatic and metallogenic province. Precambrian Research 172, 143-162.

Holdsworth, R.E., Alsop, G.I., Strachan, S.A., 2007. Tectonic Stratigraphy and Structural Continuity of the Northernmost Moine Thrust Zone and Moine Nappe, Scottish Caledonides. Geological Society London Special Publications 272, 121–142. doi:10.1144/GSL.SP.2007.272.01.08.

Jaffey, A.H., Flynn, K.F., Glendenin, L.E., Bentley, W.C., Essling. A.M., 1971. Precision Measurement of Half-Lives and Specific Activities of 235 U and 238 U. Physical Review C 4 (5), 1889-1906.

Kalsbeek, F., Austrheim, H., Bridgwater, D., Pedersen, S., Taylor, P.N., 1993. Geochronology of Archaean and Proterozoic Events in the Ammassalik Area, South-East Greenland, and Comparisons with the Lewisian of Scotland and the Nagssugtoqidian of West Greenland. Precambrian Research 62, 239–270.

Kelly, N.M., Hinton, R.W., Harley, S.L., Appleby, S.K., 2008. New SIMS U-Pb Zircon Ages From the Langavat Belt, South Harris, NW Scotland: Implications for the Lewisian Terrane Model. Journal of the Geological Society 165 (5), 967–981. doi:10.1144/0016-76492007-116.

Kinny, P.D., Friend, C.R.L., Love, G.J., 2005. Proposal for a Terrane-Based Nomenclature for the Lewisian Gneiss Complex of NW Scotland. Journal of the Geological Society, London 162, 175–186. doi:10.1144/0016-764903-149.

Kinny, P.D., Friend, C.R.L., 1997. U-Pb Isotopic Evidence for the Accretion of Different Crustal Blocks to Form the Lewisian Complex of Northwest Scotland. Contributions to Mineralogy and Petrology 129, 326–340.

Klausen, M.B., Söderlund, U., Olsson, J.R., Ernst, R.E., Armoogam, M., Mkhize, S.W., Petzer, G., 2010. Petrological discrimination among Precambrian dyke swarms: Eastern Kaapvaal craton (South Africa). Precambrian Research 183, 501-522.

Kravchinsky, V.A., Sampson, J. Davies, J.H.F.L., Heaman, L.M. A Reappraisal of the Paleomagnetism of the Lewisian Foreland, NW Scotland: the occurrence of primary magnetizations and their implication for Proterozoic location of the Lewisian. In Prep

De Kock, M.O., Evans, D.A.D., Beukes, N.J., 2009. Validating the existence of Vaalbara in the Neoarchean. Precambrian Research 174, 145-154.

Kullerud, K., Skjerlie, K.P., Corfu, F., de la Rosa, J.D., 2006. The 2.40 Ga Ringvassøy Mafic Dykes, West Troms Basement Complex, Norway: the Concluding Act of Early Palaeoproterozoic Continental Breakup. Precambrian Research 150, 183–200. doi:10.1016/j.precamres.2006.08.003.

LeCheminant, A.N., Heaman, L.M., 1989. Mackenzie Igneous Events, Canada: Middle Proterozoic Hotspot Magmatism Associated with Ocean Opening. Earth and Planetary Science Letters 96, 38–48.

Li, Z.X., Bogdanova, S.V., Collins, A.S., Davidson, A., Waele, B.De., Ernst, R.E., Fitzsimons, I.C.W., Fuck, R.A., Gladkochub, D.P., Jacobs, J., Karlstrom, K.E., Lu, S., Natapov, L.M., Pease, V., Pisarevsky, S.A., Thrane, K., Vernikovsky, V., 2008. Assembly, configuration and break-up history of Rodinia: A synthesis. Precambrian Research 160, 179-210.

Ludwig, K.R., 2003. Isoplot 3.00: a geochronological toolkit for Microsoft Excel. Berkeley Geochronology Center Special Publication 4, 0–71.

Love, G.J., Kinny, P.D., Friend, C.R.L., 2004. Timing of Magmatism and Metamorphism in the Gruinard Bay Area of the Lewisian Gneiss Complex: Comparisons with the Assynt Terrane and Implications for Terrane Accretion. Contributions to Mineralogy and Petrology 146, 620–636.

MacDonald, J.M., Wheeler, J., Harley, S.L., Mariani, E., Goodenough, K.M., Crowley, Q., Tatham, D., 2013. Lattice distortion in a zircon population and its effecs on trace-element mobility and U-Th-Pb isotope systematics: examples from the Lewisian Gneiss Complex, northwest Scotland. Contributions to Mineralogy and Petrology 166, 21-41.

Mason, A.J., 2012. Major Early Thrusting as a Control on the Palaeoproterozoic Evolution of the Lewisian Complex: Evidence From the Outer Hebrides, NW Scotland. Journal of the Geological Society, London 169, 201–212. doi:10.1144/0016-76492011-099.

Mason, A.J., Parrish, R.R., Brewer, T.S., 2004. U–Pb Geochronology of Lewisian Orthogneisses in the Outer Hebrides, Scotland: Implications for the Tectonic Setting and Correlation of the South Harris Complex. Journal of the Geological Society, London 161, 45-54.

Mason, A.J., Brewer, T.S., 2004. Mafic Dyke Remnants in the Lewisian Complex of the Outer Hebrides, NW Scotland: a Geochemical Record of Continental Break-Up and Re-Assembly. Precambrian Research 133, 121–141.

Mattinson, J.M., 2005. Zircon U–Pb Chemical Abrasion ('CA-TIMS') Method: Combined Annealing and Multi-Step Partial Dissolution Analysis for Improved Precision and Accuracy of Zircon Ages. Chemical Geology 220, 47–66.

McDonough, W.F., Sun, S.S., 1995. The composition of the Earth. Chemical Geology 120, 223–253.

Meldrum, A., Boatner, L.A., Zinkle, S.J., Wang, S.X., Wang, L.M., Ewing, R.C., 1999. Effects of dose rate and temperature on the crystalline-to-metamict transformation in the ABO_4 orthosilicates. Canadian Mineralogist 37, 207-221.

Muir, R.J., Evans, J.A., Fitches, W.R., 1993. Mafic Dykes Within the Lewisian Complex on Tiree and Coll, Inner Hebrides. Scottish Journal of Geology 29, 167–176. doi:10.1144/sjg29020167.

Murakami, T., Chakoumakos, B.C., Ewing, R.C., Lumpkin, G.R., Weber, W.J., 1991. Alpha-decay event damage in zircon. American Mineralogist 76, 1-23.

Mussett, A.E., Dagley, P., Skelhorn, R.R., 1988. Time and duration of activity in the British Tertiary Igneous Province. Geological Society, London, Special Publications 39, 337-348.

Nasdala, L., Pidgeon, R.T., Wolf, D., Irmer, G., 1998. Metamictization and U-Pb isotopic discordance in single zircons: a combined Raman microprobe and SHRIMP ion probe study. Mineralogy and Petrology 62, 1-27.

Nemchin, A.A., Pidgeon, R.T., 1998. Precise conventional and SHRIMP baddeleyite U–Pb age for the Binneringie dyke near Narrogin, Western Australia. Australian Journal of Earth Science 45, 673–675.

Nilsson, M.K.M., Klausen, M.B., Söderlund, U., Ernst, R.E., 2012. Precise U–Pb Ages and Geochemistry of Palaeoproterozoic Mafic Dykes From Southern West Greenland: Linking the North Atlantic and the Dharwar Cratons. Lithos 1–16. doi:10.1016/j.lithos.2012.07.021.

Nilsson, M.K.M., Söderlund, U., Ernst, R.E., Hamilton, M.A., Scherstén, A., Armitage, P.E.B., 2010. Precise U-Pb Baddeleyite Ages of Mafic Dykes and Intrusions in Southern West Greenland and Implications for a Possible Reconstruction with the Superior Craton. Precambrian Research 183, 399–415. doi:10.1016/j.precamres.2010.07.010.

Niu, Y., O'Hara, M.J., 2003. The origin of ocean island basalts (OIB): A new perspective from petrology,
geochemistry and mineral physics considerations, Journal of Geophysical Research B4 108, 10.1029/2002JB002048,

Nutman, A.P., Hagiya, H., Maruyama, S., 1995. SHRIMP U–Pb single zircon geochronology of a Proterozoic mafic dyke, Isukasia, southern West Greenland. Bulletin of the Geological Society of Denmark 42, 17–22.

Nutman, A.P., Kalsbeek, F., Friend, C.R.L., 2008. The Nagssugtoqidian Orogen in South-East Greenland: Evidence for Paleoproterozoic Collision and Plate Assembly. American Journal of Science 308, 529–572. doi:10.2475/04.2008.06.

Nutman, A.P., Kalsbeek, F., Marker, M., van Gool, J.A.M., Bridgwater, D., 1999. U–Pb Zircon Ages of Kangâmiut Dykes and Detrital Zircons in Metasediments in the Palaeoproterozoic Nagssugtoqidian Orogen (West Greenland): Clues to the Pre-Collisional History of the Orogen. Precambrian Research 93, 87–104.

O'Hara, M.J., 1962. Some intrusions in the Lewisian Complex near Badcall, Sutherland. Transctions of the Edinburgh Geological Society 19, 201-207.

O'Hara, M.J. 1977. Thermal History of Excavation of Archaean Gneisses From the Base of the Continental Crust. Journal of the Geological Society, London 134, 185–200. doi:10.1144/gsjgs.134.2.0185.

Park, R.G., 1970. Observations on Lewisian Chronology. Scottish Journal of Geology 6, 379–399. doi:10.1144/sjg06040379.

Park, R.G., 2005. The Lewisian Terrane Model: a Review." Scottish Journal of Geology 41, 105–118. doi:10.1144/sjg41020105.

Park, R.G., 2010. Structure and Evolution of the Lewisian Gairloch Shear Zone: Variable Movement Directions in a Strike-Slip Regime. Scottish Journal of Geology, 46, 31-45. Doi: 10.1144/0036-9276/01-405

Park, R.G., Tarney, J., Connelly, J.N., 2001. The Loch Maree Group: Palaeoproterozoic Subduction-Accretion Complex in the Lewisian of NW Scotland. Precambrian Research 105, 205–226.

Peach, B.N., Horne, J., Gunn, W., Clough, C.T., Hinxman, L.W., Teall, J.J.H., 1907. The geological structure of the North-West Highlands of Scotland, Memoir of the Geological Survey of Great Britain HMSO, Glasgow.

Pearce, J.A., Norry, M.J., 1979. Petrogenetic implications of Ti, Zr, Y, and Nb variations in volcanic rocks. Contributions to Mineralogy and Petrology 69, 33–47

Pehrsson, S.J., Berman, R.G., Eglington, B., Rainbirs, R., 2013. Two Neoarchean supercontinents revisited: The case for a Ray family of cratons. Precambrian Research 232, 27-43.

Pidgeon, R.T., Bowes, D.R., 1972. Zircon U–Pb ages of granulites from the Central Region of the Lewisian, northwestern Scotland. Geological Magazine 109, 247-258.

Preiss, W.V., 2000. The Adelaide Geosyncline of South Australia and Its Significance in Neoproterozoic Continental Reconstruction. Precambrian Research 100, 21–63.

Prowatke, S., Klemme, S., 2006. Trace-element partitioning between apatite and silicate melts. Geochimica et Cosmochimica Acta 70, 4513-4527.

Rogers, J.J.W., Santosh, M., 2003. Supercontinents in earth history. In: Santosh, M. (Ed.), Special Issue in Honour of Prof. John J.W. Rogers on Supercontinents and Crustal Evolution. Gondwana Research 6, 357–368.

Rollinson, H.R., 2012. Geochemical constraints on the composition of Archaean lower continental crust: partial melting in the Lewisian granulites. Earth Planetary Science Letters 351–352, 1–12

Rotenberg, E., Davis, D.W., Amelin, Y., Ghosh, S., Bergquist, B.A., 2012. Determination of the Decay-Constant of ^{87}Rb by Laboratory Accumulation of ^{87}Sr. Geochimica et Cosmochimica Acta 85, 41–57. doi:10.1016/j.gca.2012.01.016.

Rubatto, D., 2002. Zircon Trace-element Geochemistry: Partitioning with Garnet and the Link Between U–Pb Ages and Metamorphism. Chemical Geology 184, 123–138.

Sampson, J.P., 2009. A reappraisal oft he Paleomagnetism oft he Lewisian Foreland, NW Scotland: the occurrence of primary magnetizations and their implication for a Baltica-Lewisian fit at 2.0 Ga. Msc Thesis, University of Alberta.

Schaltegger, U, Fanning, C.M., Günther, D., Maurin, J.C., Schulmann, K., Gebauer, D., 1999. Growth, Annealing and Recrystallization of Zircon and Preservation of Monazite in High-Grade Metamorphism: Conventional and in-Situ U-Pb Isotope, Cathodoluminescence and Microchemical Evidence. Contributions to Mineralogy and Petrology 134, 186–201.

Schmitz M.D., Schoene B., 2007, Derivation of isotope ratios, errors and error correlations for U-Pb geochronology using 205Pb-235U-(233U)-spike isotope dilution thermal ionization mass spectrometric data. Geochemistry Geophysics Geosystems, 8, Q08006, doi: 10.1029/2006GC001492

Schoene, B., Latkoczy, C., Schaltegger, U., Günther. D., 2010. A New Method Integrating High-Precision U–Pb Geochronology with Zircon Trace-element Analysis (U–Pb TIMS-TEA). Geochimica et Cosmochimica Acta 74, 7144–7159. doi:10.1016/j.gca.2010.09.016.

Siivola, J., Schmid, R., 2007. Recommendations by the IUGS Subcommission on the Systematics of Metamorphic Rocks: List of Mineral Abbreviations. IUGS Commission on the Systematics in

Petrology. Web Http://Www. Bgs. Ac. Uk/Scmr/Docs/Papers/Paper_12. Pdf.

Söderlund, U., Hofmann, A., Klausen, M.B., Olsson, J.R., Ernst, R.E., Persson. P.O., 2010. Towards a Complete Magmatic Barcode for the Zimbabwe Craton: Baddeleyite U-Pb Dating of Regional Dolerite Dyke Swarms and Sill Complexes. Precambrian Research 183, 388–398. doi:10.1016/j.precamres.2009.11.001.

Söderlund, U., Isachsen, C.E., Bylund, G., Heaman, L.M., Patchett, P.J., Vervoort, J.D., Andersson, U.B., 2005. U–Pb Baddeleyite Ages and Hf, Nd Isotope Chemistry Constraining Repeated Mafic Magmatism in the Fennoscandian Shield From 1.6 to 0.9 Ga. Contributions to Mineralogy and Petrology 150, 174–194. doi:10.1007/s00410-005-0011-1.

Stacey, J.S., and JD Kramers. 1975. Approximation of Terrestrial Lead Isotope Evolution by a Two-Stage Model. Earth and Planetary Science Letters 26, 207–221.

Sutton, J., Watson, J., 1950. The Pre-Torridonian Metamorphic History of the Loch Torridon and Scourie Areas in the North-West Highlands, and Its Bearing on the Chronological Classification of the Lewisian. Quarterly Journal of the Geological Society 106, 241–307. doi:10.1144/GSL.JGS.1950.106.01-04.16.

Tarney, J., 1963. Assynt Dykes and Their Metamorphism. Nature 199, 672–674.

Tarney, J., 1973. The Scourie dyke suite and the nature of the Inverian event in Assynt, in: The Early Precambrian of Scotland and Related Rocks of Greenland, Park, R.G., and Tarney, J., eds. pp. 105-118, 1973.

Tarney, J., Weaver, B.L., 1987a. Mineralogy, Petrology and Geochemistry of the Scourie Dykes: Petrogenesis and Crystallization Processes in Dykes Intruded at Depth. Geological Society London Special Publications 27, 217-233.

Tarney, J., Weaver, B.L., 1987b. Geochemistry of the Scourian Complex: Petrogenesis and Tectonic Models. Geological Society London Special Publications 27, 45–56. doi:10.1144/GSL.SP.1987.027.01.05.

Teall, J.J.H., 1885. The metamorphosis of dolerite into hornblende- schist. Quarterly Journal of the Geological Society, London 41, 132-145.

Turner, S., Regelous, M., Kelley, S., Hawksworth, C., Mantovani, M., 1994. Magmatism and continental break-up in the South Atlantic: high precision ^{40}Ar-^{39}Ar geochronology. Earth and Planetary Science Letters 121, 333-348.

Vernon, R., Holdsworth, R.E., Selby, D., Dempsey, E.D., Finlay, A., Fallick, T., 2014. Structural characteristics and Re-Os dating of quartz-pyrite veins in the Lewisian GneissComplex, NW Scotland: evidence of an Early Paleoproterozoic hydrothermal regime during terrane amalgamation. In review,

Precambrian Research.

Waters, F.G., Cohen, A.S., O'Nions, R.K., O'Hara, M.J., 1990. Development of Archaean Lithosphere Deduced From Chronology and Isotope Chemistry of Scourie Dykes. Earth and Planetary Science Letters 97, 241–255.

Weaver, B.L., Tarney, J., 1981a. Chemical Changes During Dyke Metamorphism in High-Grade Basement Terranes. Nature 289, 47-49.

Weaver, B.L., Tarney, J., 1981b. The Scourie Dyke Suite: Petrogenesis and Geochemical Nature of the Proterozoic Sub-Continental Mantle. Contributions to Mineralogy and Petrology 78, 175–188.

Weaver, B.L., Tarney, J., 1981c. Lewisian Gneiss geochemistry and Archaean crustal development models. Earth and Planetary Science Letters 55, 171–180.

Wheeler, J., Park, R.G., Rollinson, H.R., Beach, A., 2010. The Lewisian Complex: Insights Into Deep Crustal Evolution. Geological Society London Special Publications 335, 51–79. doi:10.1144/SP335.4.

Whitehouse, M.J., Kemp, A.I.S., 2010. On the Difficulty of Assigning Crustal Residence, Magmatic Protolith and Metamorphic Ages to Lewisian Granulites: Constraints From Combined in Situ U–Pb and Lu–Hf Isotopes. Geological Society London Special Publications 335, 81–101. doi:10.1144/SP335.5.

Whitehouse, M.J, Bridgwater, D., 2001. Geochronological Constraints on Paleoproterozoic Crustal Evolution and Regional Correlations of the Northern Outer Hebridean Lewisian Complex, Scotland. Precambrian Research 105, 227–245.

Whitehouse, M.J., Claesson, S., Sunde, T., Vestin, J., 1997. Ion Microprobe U-Pb Zircon Geochronology and Correlation of Archaean Gneisses From the Lewisian Complex of Gruinard Bay, Northwestern Scotland. Geochimica et Cosmochimica Acta 61, 4429–4438.

Williams, H., Hoffman, P.F., Lewry, J.F., Monger, J.W.H., Rivers, T., 1991. Anatomy of North America: thematic geologic portrayals of the continent. Tectonophysics 187, 117-134.

Wingate, M.T.D., Pirajno, F., Morris, P.A., 2004. Warakurna large igneous province: A new Mesoproterozoic large igneous province in west-central Australia. Geology 32, 105-108.

Wright, A.E., Tarney, J., Palmer, K.F., Moorlock, B.S.P., Skinner, A.C., 1973. The geology of the Angmalssalik area, East Greenland and possible relationships with the Lewisian of Scotland, in: The Early Precambrian of Scotland and Related Rocks of Greenland, R.G. Park and J. Tarney, eds., pp. 105-118, 1973.

Zhao, G., Sun, M., Wilde, S.A., Li, S., 2003. Assembly, accretion and breakup of the Paleo-

Mesoproterozoic Columbia Supercontinent: Records in the North China Craton. Gondwana Research 6, 417-434.

Zhu, W., Zhang, Z., Shu, L., Lu, H., Su, J., Yang, W., 2008. SHRIMP U-Pb Zircon Geochronology of Neoproterozoic Korla Mafic Dykes in the Northern Tarim Block, NW China: Implications for the Long-Lasting Breakup Process of Rodinia. Journal of the Geological Society London 165, 887–890. doi:10.1144/0016-76492007-174.

Zhu, Z.K., O'Nions, R.K., Belshaw, N.S., Gibb, A.J., 1997. Lewisian Crustal History From in Situ SIMS Mineral Chronometry and Related Metamorphic Textures. Chemical Geology 136, 205–218. doi:10.1016/S0009-2541(96)00143-X.

Zirkler, A., Johnson, T.E., White, R.W., Zack, T., 2012. Polymetamorphism in the Mainland Lewisian Complex, NW Scotland - Phase Equilibria and Geochronological Constraints From the Cnoc an T'Sidhean Suite. Journal of Metamorphic Geology 30, 865–885. doi:10.1111/j.1525-1314.2012.01003.x.

Chapter 4: Seeing through the effects of oxygen isotopic disturbance in zircon using SIMS, Raman spectroscopy and trace-element analyses: a case study from the low $\delta^{18}O$ Scourie dykes, NW Scotland

4.1. Introduction

In magmatic systems, oxygen isotopes are used to probe the origin of magmas, determine which phases are in equilibrium, and calculate the temperatures of mineral growth (Taylor and Sheppard, 1986; Valley and Cole, 2003). The oxygen isotopic composition of a rock can be altered through geological processes, such as metamorphism, where increased temperatures and fluid-rock interaction enhance isotopic diffusion between minerals (see Baumgartner and Valley, 2001). Also, hydrothermal alteration can significantly alter the oxygen isotopic composition of a rock through exchange between the minerals and the fluid, thereby reducing the ability to obtain meaningful geological information about its origin.

Zircon is one of the most robust recorders of the oxygen isotopic composition of a magmatic rock because it can retain its original isotopic signature through high-grade metamorphism and even anatexis (see Valley, 2003). Both experimental and natural examples suggest that oxygen isotopic diffusion in zircon is extremely slow even at high temperatures (Muehlenbachs and Kushiro, 1975; Cherniak and Watson, 2003; Page et al., 2007). However, damage to the zircon crystal structure can occur

through several processes, including radiation damage due to the presence of elevated concentrations of radioactive elements U and Th. Enhanced radiation damage can create amorphous domains and a porous structure that is susceptible to fluid infiltration and oxygen isotopic exchange (Valley et al., 1994; Geisler et al., 2003a).

Zircon that has experienced fluid exchange can be indirectly identified because the exchanging fluid causes disturbance in most of the geochemical properties of the crystal, not just in oxygen isotopes (e.g. Booth et al. 2005). Zircons that have interacted with fluids typically have disturbance in their U-Pb isotopic systematics, recognized by discordance in their $^{206}Pb/^{238}U$ and $^{207}Pb/^{235}U$ dates (e.g. Krogh, 1982; Valley et al., 1994; Geisler et al., 2003b; 2003c; Breeding et al., 2004), altered cathodoluminescence (CL) and back-scattered electron properties (Corfu et al., 2003; Geisler et al., 2007), elevated trace-element contents (Geisler et al., 2002; 2003b; Rayner et al., 2005), and oxygen isotopic disturbance (Valley et al., 1994; Booth et al., 2005).

Populations of fluid-altered zircon can produce highly variable U-Pb ages and oxygen isotopic compositions that are difficult to interpret and cloud the true geologic history (e.g. Nemchin and Pidgeon, 1997; Pidgeon et al. 2013). In these cases, numerous analyses, and often multiple techniques are required to "see through" the effects of the fluid alteration and determine the original age and oxygen isotopic composition of the zircon and host rock (e.g. Liu and Zhang, 2013). Even after multiple analyses have been conducted, the original magmatic composition of a fluid-altered zircon may still be unclear.

Here we show that recognizing the oxygen isotopic disturbance in zircon can be better evaluated through a combination of Raman spectroscopy and trace-element

analyses, as well as indirectly through U-Pb dating and CL imaging. We describe a technique that can be used to determine which zircon grains or areas of grains record the original, or near-original oxygen isotopic composition of a zircon population. This is especially useful in scenarios where the whole rock (WR) oxygen isotopic composition has been modified by secondary processes.

Firstly, we provide a brief introduction to the metamictization process in zircon and explain how this facilitates isotopic exchange between zircon and the fluid. Secondly, we show how Raman spectroscopy and trace-element abundances can be used to document this process. The technique is used on complex zircon populations from nine mafic Paleoproterozoic Scourie dykes from NW Scotland, and confirms that these zircons originated from low-$\delta^{18}O$ magmas as previously shown by Cartwright and Valley, (1991). We identify the areas in the zircon that have experienced the least amount of fluid exchange and therefore record near-original magmatic composition.

4.1.1. Metamictization and structural recovery

Zircon ($ZrSiO_4$) is the most common U- and Th-bearing accessory mineral in upper crustal rocks and therefore, the primary target for U-Pb geochronology (see Hanchar and Hoskin, 2003). Over time, U and Th decay to different isotopes of Pb via a sequence of decay reactions ejecting either an alpha particle or a combination of a beta and an antineutrino particle from the nucleus. The prolonged accumulation of alpha fission track and alpha recoil (radiation) damage can cause zircon to change from a crystalline to metamict state, with alpha recoil being the dominant cause of the radiation damage (Holland and Gottfried, 1955; Weber et al. 1994; Ewing et al. 2003). Alpha fission tracks cause the displacement of 100s of atoms in the crystal lattice generating Frenkle defect pairs (Ewing et al. 1987). During alpha recoil, the heavy nucleus (daughter isotope) expends its energy in short-range elastic collisions

causing ~1000 atomic displacements creating a completely amorphous domain with a diameter of ~5 nm (Ewing et al. 1987; 2003; Geisler et al. 2003a). The amorphous domains caused by alpha recoil have a unique structure with a matter-depleted core surrounded by a SiO_n polymerized high-density rim (Trachenko et al. 2001; 2002; 2004; Geisler et al. 2003a). Accumulation of these amorphous domains over time within the zircon causes shear deformation (Ríos and Salje, 1999), swelling, and volume expansion (Murakami et al. 1991; Weber et al. 1994), all of which result in a reduction in density (Holland and Gottfried, 1955).

Once the zircon crystal has undergone a sufficient amount of metamictization such that the amorphous domains overlap and create an interconnected network (the percolation point from Salje et al. 1999), its low density and porous nature result in an increase in the diffusivity of water by ~10 orders of magnitude from the original crystalline state (Geisler et al. 2003a). Interestingly, experimental and natural evidence suggests that highly metamict zircon can be partially recrystallized in the presence of ~200-400 °C fluids diffusing into the crystal (Geisler et al., 2003b; 2003c). Geisler et al. (2003b) suggest that the partial structural recovery (recrystallization) of zircon is catalyzed by the diffusion of hydrous species into the grain, which also bring with them non-formula solvent cations e.g. Ca and Al (Geisler et al. 2002; Hoskin et al., 2003; Ryner et al. 2005), and expel non compatible radiogenic Pb which builds up in metamict areas resulting in Pb loss (Pidgeon, 1992; Geisler et al. 2003c; Rayner et al. 2005).

Recovery from a metamict state via diffusion of the hydrous species into the grain is not favored in all studies. Putnis (2002); Tomaschek et al. (2003); Putnis et al. (2005) and Hay et al. (2009) suggest that metamict zircon can be dissolved during interaction with fluids and new zircon re-precipitated epitaxially in its place. This mod-

el results in crystalline but highly porous new zircon growth, pseudomorphing the parent crystal. The newly grown zircon is devoid of radiogenic or common Pb; has very low contents of solvent cations (U, Th, Ca etc); has completely reset isotopic systematics; and often contains mineral inclusions. Geisler et al. (2007) suggest that both the diffusion reaction and dissolution re-precipitation models are end members of the structural recovery process, and although both models require the involvement of a hydrous phase, each model produces distinct features in the zircon.

Radiation damage and structural recovery is further complicated by the overall temperature of the hydrothermal system since structural damage due to a radiation can only be retained in zircon at temperatures below ~250 °C (Murakami et al. 1991; Meldrum et al. 1999; Geisler et al. 2001; Davis and Krogh, 2000; Moser et al. 2011; Pidgeon 2013).

During both methods of hydrous recovery from metamictization, zircon exchanges oxygen isotopes with the fluid, resulting in oxygen isotopic compositions out of equilibrium with the parent rock (e.g. Valley et al., 1994; Valley, 2003; Booth et al. 2005). Diffusional structural recovery is likely to result in a mixed oxygen isotopic composition between the fluid and the magmatic value because the diffusing fluid catalyzes new crystal growth in the metamict domains of the crystal leaving the crystalline domains unaffected. Dissolution-precipitation structural recovery is likely to result in complete resetting of the oxygen isotopic composition and should create a distinct boundary between the original oxygen isotopic composition and that of the newly precipitated zircon.

In addition to the chemical differences described above, structural recovery through diffusion or dissolution re-precipitation produces very distinctive Raman spectro-

scopic responses (Geisler et al., 2001; 2003b; 2003c, Fig. 4.1). However, the connection between hydrous recovery, Raman spectroscopy and oxygen isotopic disturbance has not previously been established. In this contribution, we investigate the Raman spectra of zircon that has experienced oxygen isotopic disturbance, and attempt to show that Raman spectra and geochemistry can indicate which zircons, or areas of zircon retain an oxygen isotopic composition that is closest to their magmatic composition.

4.1.2. Raman response to metamictization and structural recovery

Detailed discussions of the Raman response to metamictization in zircon (Nasdala et al. 1995; 1998a; 2001; Zhang et al. 2000a), along with thermal annealing of metamict zircon (Zhang et al. 2000b; Geisler et al. 2001a; 2002; Nasdala et al. 2002) and hydrothermal alteration of zircon (Geisler et al. 2001a; 2003b; 2003c; 2007) have been previously provided, and only the most relevant features are reviewed here.

Raman spectrometry measures the phonon frequency of a molecular vibration in a crystal. Phonon modes in perfectly crystalline solids have frequencies that relate to the short range angle and length of a particular bond, whereas the linewidth (full width at half max – FWHM) is related to long range order (e.g. Dillon et al. 1984). Therefore the Raman properties of zircon are perfectly suited to studying metamictization since both short range bond damage (e.g. Frenkle defect pairs) and long range damage (fully amorphous domains) build up over time.

The line width and frequency of the of the Raman ν_3 (SiO_4) band at ~1000 cm^{-1} are one of the best indicators of the degree of metamictization in zircon (Nasdala et al. 1995; 1998a,b; 2001; Zhang et al. 2000a). This particular Raman mode measures the degree of order, or crystallinity in one particular stretching mode of the

silica tetrahedra. It retains a degree of order (producing a measureable peak) even in extremely metamict zircon when all of the other Raman active modes have been reduced to background. During metamictization, the peak of the ν_3 (SiO_4) band becomes broader, changing from a linewidth of ~3 cm^{-1} for fully crystalline zircon to >30 for extremely metamict grains (Fig. 4.1). At the same time, the band becomes less intense and reduces in frequency from ~1008 cm^{-1} for fully crystalline zircon, to ~995 cm^{-1} for the most metamict grains (Nasdala et al. 1995; Wopenka et al. 1996; Nasdala et al. 1998a; 2001; Zheng et al. 2000, Geisler et al. 2003c). The change in parameters follows a linear trend, which has been referred to as the radiation damage trend (Geisler et al. 2003c, Fig. 4.1). When the zircon becomes highly metamict, the phonon frequency for the ν_3 (SiO_4) band reaches a minimum value but the linewidth continues to increase as the zircon moves towards a completely amorphous state (Fig. 4.1).

Even though the ν_3 (SiO_4) Raman band appears to be a good recorder of metamictization, there are other processes that could affect the linewidth and frequency of the band. Elemental substitution has been shown to cause band broadening in rare-earth phosphates (Podor, 1995), and therefore could create band broadening in zircon. However, both Nasdala et al. (1995) and Zhang et al. (2000b) reported ν_3 (SiO_4) band parameters for zircon with up to wt. % U and Th and found no perceptible effect on the linewidth associated with high trace-element abundances. The most common impurity in zircon is Hf, and the Zr-Hf substitution causes only a small increase in the frequency of Si-O stretching modes when the Hf content exceeds 2 wt. % (Nicola and Rutt 1974; Hoskin and Rogers, 1996). It should be noted that >2 wt. % Hf is unlikely in zircon crystallizing from mafic magmas (Hoskin et al. 2003) and therefore this effect should be minimal for the zircon investigated in this study.

The most important process (for this study) that affects the parameters of the ν_3 (SiO_4) band is recrystallization, either thermal, or catalyzed by fluids. Numerous experiments have documented how metamict zircon responds to thermal annealing. The process is complex, involving both defect annealing (Colombo and Crosch, 1998) and epitaxial recrystallization (Capitani et al. 2000). During experimental annealing of highly metamict zircon, Zhang et al. (2000b) also noticed a ZrO_2 phase, both monoclinic and tetragonal, as well as some unidentified Si-O bonds, which they referred to as an intermediate phase. Thermal annealing is an important process over geological time, and was studied experimentally by Geisler et al. (2001a; 2002) who calculated the expected change in the ν_3 (SiO_4) band in highly metamict zircon after prolonged periods (1 Ma) at temperatures between 100-400 °C (red arrow in Fig. 4.1). They showed that the recovery (or recrystallization) from a metamict state occurs in two stages. The first stage occurs at relatively low temperatures (<~700 °C) and is due to defect annealing and the recovery of short-range disordered crystalline domains (Colombo and Crosch, 1998; Zhang et al. 2000b), and results in the recovery of the phonon frequency. The second stage recrystallizes completely amorphous domains within the crystal structure (long range defects), and requires higher temperatures (>~700 °C) and efficient diffusion of matrix atoms to facilitate recovery (Capitani et al. 2000). During this higher temperature structural recovery the linewidth and frequency both shift towards the radiation damage trend, or towards fully crystalline zircon (Geisler et al. 2001a; 2002; Fig. 4.1).

Both these types of structural recovery are likely to produce distinct Raman signatures and will be described below.

1.) Diffusional structural recovery in metamict zircon has been investigated experimentally (Geisler et al 2003b) and found to occur in natural zircon samples (Schalteg-

ger et al. 1999; Hoskin and Black, 2002; Geisler et al. 2003c); the general disorder trends observed are shown by the thick blue band in Fig. 4.1. A highly metamict zircon (position B in Fig. 4.1) will experience a recovery of short range disorder (e.g. Frenkel defects) after exposure to low temperature fluids (~200 °C), and this results in the recovery of the frequency of the ν_3 (SiO_4) phonon mode with little recovery in the linewidth (Geisler et al, 2002). Diffusional recovery follows a similar path to thermal annealing (Fig. 4.1) although it can easily be distinguished through geochemical analysis of the grains, since thermal annealing is unlikely to reset any isotopic/geochemical signatures in the zircon. The linewidth of the ν_3 (SiO_4) band can be recovered through exposure to higher-temperature fluids, which have faster crystallization kinetics enabling recovery of amorphous domains. Once a zircon has experienced partial recovery of its radiation damage through a diffusional process, the Raman band parameters are likely to significantly deviate from the radiation damage trend (see blue arrow in Fig. 4.1), under these conditions, it is not clear how the Raman band parameters will respond to further metamictization. Since radiation damage accumulates both short-range and long-range disorder in the crystal and these cause predictable changes in the band parameters, it is likely that the zircon will follow a trajectory parallel with the radiation damage trend over time (dashed grey arrow Fig. 4.1).

2.) Zircon that recrystallizes through a dissolution-precipitation process (e.g. Putnis, 2002; Putnis et al. 2005) should also produce a distinct Raman signature. The dissolution reaction is thought to be controlled by a dissolution front possibly characterized by a thin film of fluid that progresses into metamict areas in the crystal (Geisler et al. 2003b). The new zircon that crystallizes has micron-scale pores and mineral inclusions but the crystalline sections of the grains should be perfectly crystalline as the new zircon is typically devoid of solvent cations (Geisler et al. 2007). New

zircon that crystallizes from metamict zircon (B in Fig. 4.1) through dissolution-precipitation reactions should have a Raman response similar to crystalline zircon (A in Fig. 4.1). This leaves the parent grain with a distinct boundary between the newly crystallized sections and the old metamict areas. Over time the newly crystallized zircon should accumulate radiation damage along the radiation damage trend (move to D in Fig. 4.1), although the U content of the new zircon is typically low and so it is unlikely to accumulate damage quickly.

4.2. Geological history of the samples

The zircon in this study were extracted from nine quartz dolerite and norite dykes from the Scourie dyke swarm, Lewisian gneiss complex, NW Scotland (Fig. 4.2). The dykes intrude Lewisian granulite-facies tonalite-trondhjemite-granodiorite (TTG) gneiss, which have protolith ages of between 3040 and 2960 Ma (Kinney et al. 1997) and experienced high-grade metamorphism during the Badcaullian metamorphic event at ~2760 Ma and the Inverian metamorphic event at 2490 Ma (Corfu et al. 1994; Zhu et al. 1997; Whitehouse and Kemp, 2010).

The Scourie dyke swarm can be divided into four petrological groups; quartz dolerites, norites, olivine gabbros, bronzites and picrites with the dolerites being by far the most abundant (Tarney, 1973). Zircons were extracted from norite and quartz dolerite dykes because the ultra-mafic dykes (picrites and olivine gabbros) contain baddeleyite rather than zircon as their Zr-bearing accessory phase (Heaman and Tarney, 1989). All but two of the dykes have been previously dated by the U-Pb TIMS technique (Davies and Heaman, 2014, the ages are shown in Fig. 4.2) with the remaining two dykes, the NAPI and JD09-2 dykes dated by U-Pb laser ablation in-

ductively coupled plasma mass spectrometry (LA-ICP-MS) during this study (Table 4.1, Fig. 4.3). The zircons fall broadly into three age categories 1.) Zircons from the North Assynt and Loch a'Choin dykes yeild ages of ~2.5 Ga and are thought to be xenocrysts rather than primary igneous zircons, 2.) ~2.4 Ga, zircons from JD09-2, Poll Eorna, Badcall Bay, Graveyard, Loch na h, and Lochan Fearna dykes and 3.) ~2 Ga zircons from the NAPI dyke (Fig. 4.2, 4.3).

All of the dykes experienced a major Pb-loss event at ~430 Ma, which is thought to be related to movement along the Moine thrust belt during the Caledonian orogeny (Goodenough et al. 2011; Davies and Heaman, 2014; Fig. 4.2, 4.3). Basement rocks bounding the fault zone contain metamorphic actinolite replacing hornblende and recrystallization of feldspar phenocrysts, both of which suggest syntectonic temperatures of 350-400 °C (upper greenschist) (Holdsworth et al. 2007).

Previous oxygen isotopic studies of the Scourie dykes have indicated that the dykes around the town of Scourie are anomalously low in $\delta^{18}O$ with WR values of ~2 ‰ (Cartwright and Valley, 1991). The isotopically light signature is thought to be primary and not related to contamination by the Lewisian gneisses since the minerals retain high-temperature equilibrium $\delta^{18}O$ fractionation, and the surrounding gneisses have $\delta^{18}O$ values of >6 ‰ (Cartwright and Valley, 1991; 1992). Dykes with a high amphibole content have $\delta^{18}O$ values of 5-6 ‰ which was thought to indicate that these dykes interacted with crustal fluids during the Laxfordian metamorphic event between 1950-1800 Ma (Cartwright and Valley, 1991). However U-Pb lower intercept ages of ~430 Ma (Davies and Heaman, 2014) from the dykes suggest that fluid alteration and Pb loss could be much younger.

4.3. Analytical techniques

4.3.1. Secondary ion mass spectrometry (SIMS)

SIMS measurements were conducted using a Cameca IMS1280 multicollector ion microprobe at the Canadian Center for Isotopic Microanalysis (CCIM), University of Alberta. An epoxy grain mount containing ~120 Scourie dyke zircons, along with two aliquots of Mudtank and Temora reference zircons was prepared using West System® 105 and 206 resin and hardener, respectively. After mechanical grinding and polishing of the mount to ensure a perfectly flat surface, the mount was evaporatively- or sputter-coated with 5 nm of Au prior to imaging with a scanning electron microscopy (SEM). A further 25 nm of Au was subsequently deposited on the mounts prior to SIMS analyses.

The SIMS analytical techniques used in this study followed those described by Ickert and Stern (2013) for garnet. Details of the specific instrument conditions for the analytical session IP13048 are briefly described here. A $^{133}Cs^{+}$ primary beam was used, which had an impact energy of 20 keV. The ~12 µm diameter probe was rastered slightly during acquisition forming rectangular shaped sputtered areas ~15 x 18 µm across and ~1.5 µm deep. For charge compensation, the normal incidence electron gun was used. The transfer conditions for the negative ions from the sample included a 120 µm entrance slit, 5 x 5 mm pre-ESA (field) aperture, and 100x image magnification at the field aperture with the energy window set at full transmission. Faraday cups were used to simultaneously measure the oxygen isotopes. Mass resolution ($\Delta m/m$) was typically 1950 and 2250, for ^{16}O and ^{18}O respectively. The stability of the Faraday cup baselines was checked at the beginning of the day and the baseline was found to be sufficiently stable and low that no further corrections or analysis was necessary. Secondary ion count rates for $^{16}O^{-}$ were ~1.5 − 3 x 10^{9} c/s. A single

analysis took 4.5 minutes and comprised rastering the probe for 30 – 60 s over a 20 x 20 µm area to clean and implant Cs^+, followed by automated secondary ion tuning, and 100 s of measurement.

Analyses of the reference materials (RM) were processed collectively for long-term drift and spot-to-spot statistics for the entire analytical session (see Ickert and Stern, 2013). Instrumental mass fractionation (IMF) was monitored by repeat analyses of the reference materials in a 1:4 sequence (RM: unknowns) using RMs S0022 (TEM2 Temora) zircon with $\delta^{18}O_{VSMOW}$ = +8.2 ‰ (Black et al., 2004) or S0081 (UAMT1 Mudtank) zircon with $\delta^{18}O_{VSMOW}$ = +4.87 ‰ (Stern R., unpublished data). Individual spot uncertainties for $\delta^{18}O$ at 95 % confidence are typically ± 0.20 – 0.30 ‰, and include within-spot (counting) and between-spot (geometric) errors.

4.3.2. Laser fluorination whole rock oxygen isotope analyses

Whole-rock laser fluorination analysis was done at the University of Wisconsin, Madison following the techniques of Weichert et al. (2001). The UWG-2 garnet standard was analyzed a total of 6 times before and after the dyke WR powders. The garnet standard results were very reproducible giving an oxygen isotopic composition of 5.70 ± 0.12 ‰ 2σ, which is within the accepted range for the standard (Valley et al. 1995).

4.3.3. Imaging

CL and back-scattered electron (BSE) imaging was conducted on all zircons prior to analysis to investigate the internal structures of the grains. Imaging was conducted at the CCIM using a Zeiss EVO 15 scanning electron microscope equipped with a Robinson wide spectrum CL detector, secondary electron and BSE detector. Typical

beam conditions were 15 kV and 3 – 5 nA.

4.3.4. Laser ablation multi collector inductively coupled plasma mass spectrometry (LA-MC-ICP-MS)

U-Pb geochronology of zircon crystals from NAPI and JD09-2 was conducted at the Radiogenic Isotope Facility (RIF) at the University of Alberta. A detailed description of the analytical techniques is provided by Simonetti et al. (2005), so only an overview is provided here. Data were collected using a Nu Plasma I MC-ICP-MS coupled to a New Wave Research™ UP 213 Nd:YAG laser ablation system operating with a wavelength of 213 nm. We ablated the zircon using a 30 mm diameter laser beam with an energy density of 2-3 J/cm^2 and a repetition rate of 4 Hz. The vaporized material was simultaneously mixed with a Tl solution using a desolvating nebulization system and transported in a He carrier gas to the torch of the MC-ICP-MS where all of the material was ionized in an Ar plasma. A total analytical sequence consisted of a 4 second laser warm up, a pre-ablation pass plus 3 second magnet settling time, and 30*1 second integrations of data collection plus additional delays between each integration for a total duty cycle of approximately 70 seconds. Between each analysis we allowed 15-20 seconds of washout to clear the laser cell. Lead isotope ratios were corrected for mass bias using an exponential law and assuming a $^{205}Tl/^{203}Tl$ of 2.3871, while U-Pb fractionation and instrument drift was accounted for using a sample standard bracketing technique. An in-house zircon standard (LH94-15, Ashton et al. 1999) was analyzed 3 times per decade of unknowns along with a secondary standard (OG1-1, Stern et al. 2009) to assess data quality. The average $^{207}Pb/^{206}Pb$ of LH94-15 over the analytical period was 0.11193 ± 0.00092 2s (n=10 MSWD = 23) which is in excellent agreement with the published ID-TIMS value of 0.11187 ± 0.00004 (Ashton et al. 1999). OG1 produced a weighted average $^{207}Pb/^{206}Pb$ age of 3458.0 ± 7.1 Ma (n= 6, MSWD = 0.1) which is a slightly younger, but within error

of the published TIMS and SIMS age for this standard of 3465.4 ± 0.6 Ma (Stern et al. 2009; Table 4.1). The ^{204}(Hg+Pb) acid+gas blank was found to be consistent before and after ablation, which enabled the effects of ^{204}Pb background and ^{204}Hg interference to be subtracted from each analysis. Any excess on mass 204 after blank subtraction is attributed to a common Pb component within the zircon crystal. Samples NAPI and OG1 both had low ^{204}Pb counts, however, JD09-2 contained more common ^{204}Pb (100-1000 cps ^{204}Pb). High ^{206}Pb/^{204}Pb values for JD09-2 (>1000) indicate that the common Pb component was minor relative to the radiogenic Pb, and so no common Pb correction was performed. Despite the high ^{204}Pb in JD09-2, the main source of uncertainty for this analysis is the external reproducibility which is estimated at ~2.5 % for U/Pb and ~1 % for ^{207}Pb/^{206}Pb for this analytical session.

4.3.5. Electron probe micro-analysis (EPMA)

EPMA analyses of the zircons were conducted using a JEOL 8900 instrument at the University of Alberta. Three wavelength dispersive spectrometers were used, with each spectrometer assigned to two elements. Counting times of 600 seconds on the U-Mβ and Th-Mα peaks and 300s on the background were used along with 60 seconds on the Zr-Lα, Si-Kα and Ca-Kα peaks and 30 seconds on the background. The accelerating voltage was 15 kV and a 200 nA beam current was used with a 2 mm beam diameter. Counting statistics yielded lower limits of determination of 21 ppm for Ca, 82 ppm for U and 106 ppm for Th (concentration associated with a signal at the peak position that is 6σ above the mean background signal; calculated using the formula of Potts, 1992 with the ZAF modification by John Fournelle from the University of Wisconsin, Madison). Two secondary standards (the Mud Tank and Temora zircons) were analyzed 9 times throughout the analytical session to check for machine drift. Averaged secondary standard values are presented in Table 4.2. Measured U content for the Temora zircon (260 ± 70 ppm) is in good agreement with the

published values of 228 ± 56 ppm (Black et al. 2004). The published Th abundance is ~100 ppm (Black et al. 2004) which is at the limit of determination in this study.

The U content of the Mud Tank zircon is ~30-80 ppm (Yuan et al. 2008) which is at the lower limit of determination for U in this study. The Th content of Mudtank is ~7 ppm (Yuan et al. 2008), which is significantly below the limit of determination obtained here. The U content obtained for Mud Tank zircon during this study is 146 ± 30 ppm, which is a little above the U content measured in the study of Yuan et al. (2008).

EPMA analyses was conducted after SIMS oxygen isotopic analyses and care was taken to analyze within ~10 μm of the SIMS spots (and Raman spots) to ensure that there was good spatial correlation between the techniques.

4.3.6. Raman spectroscopy

Laser Raman spectra were collected at the MacEwan University using the 532 nm line of an Ar^{+} laser and a Bruker Senterra Raman spectrometer. The scattered Raman light was analyzed by a charge-coupled device (CCD) detector after being disbursed by a grating of 1800 groves per mm. A 50x objective lens was used to focus the laser beam resulting in a spot diameter of 2.5 mm, a depth resolution of 5 mm and a spatial resolution of <10 mm^3. The spectral resolution was ~3 cm^{-1} with a wave-number accuracy of ± ~0.5 cm^{-1}, which was determined by analyzing the same spot at multiple times throughout the analytical session. A laser power of 10 mW was used, which has been shown to occasionally cause color changes in some strong light adsorbing zircons (typically black and brown colored grains) at the location of the spot, and melting of the surrounding epoxy due to heating of the zircons (Nasdala et al. 1998a). However, since the zircons in this study were all transparent, no light ad-

sorbed temperature increases were observed. Also, analysis of the same spot at multiple times during the analytical session indicated that the 10 mW laser was causing no detectable structural changes. Detector drift was also monitored in by analyzing the same sample location multiple times throughout the session and was determined to be negligible. Spectral data were collected over a range of 50-1500 cm^{-1}, to ensure good counting statistics for the data, a sequence of 10 second exposures were collected over a 2 minute period and summed to achieve the final spectrum. A background noise measurement was conducted prior to every analysis and was subtracted from the spectrum for each sample. Also each sample was carefully checked to see if there was any interference from the surrounding epoxy grain mount, since the small size of the zircons resulted in phonons from the epoxy occasionally interfering with the sample phonons. The interference was monitored by observing the presence of the characteristic epoxy peak at ~821 cm^{-1}. SIMS analytical pits have been shown to cause no detectable damage to the crystal structure (Nasdala et al. 1998a), and to ensure direct correlation between the Raman spectra and the oxygen isotopic composition, all of the Raman analyses were conducted inside SIMS spots.

All Raman data was corrected for the effects of the finite slit width on the measured linewidth. The equation

$$\Gamma = \Gamma_m[1-(S/\Gamma_m)^2] \qquad (1)$$

was used to correct the peak broadening associated with the finite slit width (Tanabe and Hiraishi, 1980). Where Γ, Γ_m, and S are the corrected line width, measured line width, and spectral slit width respectively.

4.3.6.1. Raman band fitting

The line width (full width at half maximum - FWHM) and the frequency (peak center) of the asymmetrical $\nu_3(SiO_4)$ stretching band was used to determine the degree of metamictization within the zircons (Nasdala et al. 1995), and also to determine the age of a-dose retention (e.g. Nasdala et al. 2001; 2004). Estimating the band parameters accurately and quantifying the uncertainty in the fit is essential to interpreting Raman spectra, and comparing results between studies. Raman bands in minerals are often nonsymmetrical in profile due to interferences between bands. In the case of metamict zircon, the $\nu_3(SiO_4)$ band is overlapped by the $\nu_1(SiO_4)$ band, making extraction of the peak parameters for the $\nu_3(SiO_4)$ band more difficult. To obtain the relevant parameters of the $\nu_3(SiO_4)$ band (linewidth and peak center), the contribution from the $\nu_1(SiO_4)$ stretching mode at ~975 cm^{-1} (A_{1g} symmetry; Dawson et al. 1971) and the broad band associated with the amorphous component of metamict zircon (Geisler et al. 2001a; Zhang et al. 2000a) need to be subtracted.

When fitting a model to the data there are numerous parameters to consider, e.g. the type of model (Gaussian, Lorentzian etc.); the number of functions; the goodness of fit (chi square, reduced chi square, etc.). The type of model used to fit the data officially implies a physical characteristic of the phonon frequency that is being modeled. For example, phonons produced in a perfectly crystalline material have a long lifetime and their peak can be perfectly modeled by a Lorentzian function. As disorder is introduced to the crystal structure (though elemental substitutions, metamictization, Frenkel defects etc.), phonons have a shorter lifetime and the subsequent phonon peak becomes broader. Broader peaks may be modeled more accurately with a Gaussian or Voigt function, both of which can account for the disorder in the crystal. The samples in this study represent a continuum from crystalline material to metamict, we therefore analyzed all of the data using Lorentzian, Voigt and Gaussian functions and chose the model which best fits the data. Also, because of the large

number of Raman spectra to analyze (>100) we developed an automated procedure for fitting the data, the details of which are described below.

The region of interest in the Raman spectra is between 850 and 1150 cm^{-1} containing both $\nu_1(SiO_4)$ and $\nu_3(SiO_4)$ modes. Before any fitting, the Raman background is subtracted, but since there is no simple model to fit the background, we use a third order polynomial function to fit the spectra in the region preceding and following the phonon peaks, therefore only removing the background (and the amorphous component) of the Raman spectra over the region of interest. After background subtraction we fit the $\nu_1(SiO_4)$ and $\nu_3(SiO_4)$ modes with two different peaks.

In order to assess the accuracy of the different fitting functions, we calculated a reduced chi squared statistic (c^2/n) for each fit, where n = n-p-1, n is the number of observations and p is the number of fitting parameters (Fig. 4.3). The reduced chi squared statistic assesses the goodness of fit, and produces a value of 1 if the measurement error is perfectly accounted for by the model, values greater than or less than one indicate that the measurement error is too small or two large, respectively to perfectly fit the model.

All of the models produce relatively consistent peak centers for the $\nu_3(SiO_4)$ band (Fig. 4.4a) although the Voigt and Gaussian models differ from the Lorentzian model occasionally. The FWHM (Fig. 4.4b) for the $\nu_3(SiO_4)$ bands are a little more divergent between the models, with the Gaussian frequently producing a different result to the Voigt and Lorentzian. The Voigt model is a combination of the Gaussian and Lorentzian functions and Fig. 4.4b indicates that the Voigt model preferentially takes the Lorentzian form most of the time, even in highly metamict samples.

The low reduced chi squared statistic indicates that all of the models fit the data well when the degree of metamictization is high (i.e. low wavenumbers for the peak center) (Fig. 4.4c). The accuracy of the fit at low wavenumbers is expected - as the peak becomes broader, more data points define the peak and it is easier for the model to fit. As the wavenumber for the ν_3 (SiO_4) band increases, the Gaussian models diverge significantly from the Raman spectra. The Gaussian model is expected to fail at high degrees of crystallinity (high wavenumbers) because phonons in crystalline materials show homogeneous broadening (where the interdeterminacy of the phonons under consideration is the same) and produce a Lorentzian profile. The Lorentzian and Voigt models fit the data equally well, although at higher degrees of crystallinity, the functions have difficulty resolving the apex of a very intense peak, and also struggle with the slight asymmetry of the shoulders of the ν_3 (SiO_4) band.

All uncertainties reported at the 2s confidence level unless stated otherwise.

4.4. Results

4.4.1. Techniques for identifying isotopic disturbance in zircon

Fluid alteration of zircon can be identified by many different techniques. Here we use CL imaging, SIMS oxygen isotopic analysis, U-Pb dating, and elemental composition to indicate the degree of interaction between zircon and secondary fluids. We then report the new Raman spectroscopy results and demonstrate how this technique provides complimentary information quickly and in a non-destructive manner. All the elemental, isotopic and Raman band parameter data are provided in Table 4.2.

4.4.2. Oxygen isotopes and CL images

CL images have previously been used to identify oxygen isotopic variations in zircon (e.g. Booth et al. 2005). In our study there is a broad agreement between CL response and oxygen isotopic disturbance, the grains with convoluted and variable zoning display the most variability in oxygen isotopes. CL images of representative zircon samples with the $\delta^{18}O$ isotopic compositions and SIMS spot locations are shown in Fig. 4.5.

All grains show a weak CL response with some grains darker than the epoxy, indicating that they have a high degree of metamictization (Koshek, 1993; Nasdala et al. 2006). The zircons can be divided into three broad groups based on their CL properties: 1.) zircon showing some igneous oscillatory zoning – Poll Eorna, Graveyard, Badcall Bay and NAPI; 2.) zircon with core and rim type zoning – Loch a'Choin, North Assynt and JD09-2; and 3.) highly altered/metamict zircon – Loch na h, and Lochan Fearna.

The group 1 grains, with normal grain morphologies (~4:1 length-width ratio; Heaman et al. 1990), show divergent patterns of oxygen isotopic variation with highly consistent intergrain values obtained for Graveyard and NAPI dyke zircons, while the other samples contain inter grain differences (Fig. 4.5, 4.6). The grains typically show oscillatory CL zoning along the c-axis of the grain, suggestive of igneous growth, although there are some more complexly zoned grains (highlighted with a star in Fig. 4.5). The complex CL zoning could be the result of recrystallization of the zircon along anastomosing cracks (e.g. Ashwal et al. 1999) or possibly diffusional re-crystallization associated with fluid exchange (Geisler et al. 2002; 2003b; 2007; Rayner et al. 2005). The recrystallization features in the Poll Eorna zircons correspond to the maximum ($\delta^{18}O$ = 4.93 ‰) and minimum ($\delta^{18}O$ = 3.41 ‰) values in the sample, suggesting the features may be related to fluid exchange. For the Group

1 zircons, those from the Poll Eorna dyke are the most out of equilibrium with the WR oxygen isotopic composition (Fig. 4.6), consistent with the more complex CL response when compared with the Graveyard and NAPI zircons.

Group 2 zircons have core-rim type textures that suggest they have experienced some degree of re-crystallization (e.g. Corfu et al. 2003). Zircons from JD09-2 show convoluted zones at the center of the grains, with rims of more homogeneous material, whereas Loch a'Choin and North Assynt both show similar patterns of dark (metamict) cores with lighter (less metamict) rims. The JD09-2 zircons are out of equilibrium with the WR oxygen isotopic composition by up to -3 ‰ and have variable $\delta^{18}O$ values between grains (Fig. 4.5, 4.6). It is difficult to distinguish whether the different zones seen in CL in JD09-2 have distinct $\delta^{18}O$ compositions since the zones are typically thinner than the diameter of the SIMS spots. However, the darker, more metamict zones appear to have $\delta^{18}O$ values of ~1 ‰, whereas the lighter, more crystalline zones have lower $\delta^{18}O$ values of <0 ‰ (Fig. 4.5). The darker CL zones in JD09-2 also contain quartz inclusions, whereas the lighter areas do not. Loch a'Choin zircons show some evidence for recrystallization along cracks similar to Poll Eorna (see stars, Fig. 4.5f) however the oxygen isotope data show no evidence of disturbance (Fig. 4.6, Table 4.2). The North Assynt zircons appear very similar to the Loch a'Choin zircons in CL images (see Davies and Heaman, 2014), however they show more oxygen isotopic disturbance (Fig. 4.6), which is further evidence that CL images alone can not be used to identify oxygen isotopic disturbance.

The zircons from Loch na h and Lochan Fearna, are the most metamict, the most out of equilibrium with the WR (with JD09-2), and have highly variable oxygen isotopic compositions (Fig. 4.5, 4.6). The CL images for these grains are very dark, contain abundant cracks (Lochan Fearna) and only faint evidence of igneous oscillatory zon-

ing. There doesn't appear to be a relationship between the CL zoning and the SIMS $d^{18}O$ values, however all of the oxygen isotopic values are out of equilibrium with the WR. None of the zircons show the reaction rim type characteristics or evidence of copious inclusions, which are thought to indicate interaction with hydrous fluids. Loch na h zircons do show evidence of convoluted zoning (star in Fig. 4.5I).

4.4.3. U-Pb dating

LA-MC-ICP-MS U-Pb zircon ages produced in this study are from the NAPI and JD09-2 dykes (Table 4.1, Fig. 4.3). The NAPI U-Pb zircon results are concordant or close to concordant with all analyses plotting along a discordia chord with an upper intercept of 2043.8 ± 6.2 Ma and a lower intercept of 324 ± 81 Ma. The upper intercept age is not in agreement with the ~2400 Ma ages for other dykes in the Lewisian Gneiss Complex (Heaman and Tarney, 1989; Davies and Heaman, 2014), however the age is relatively close to a U-Pb baddeleyite age of 1992 +3/-2 Ma for an olivine gabbro dyke in the area (Heaman and Tarney, 1989). The lower intercept of 324 ± 81 Ma is in agreement with a Caledonian Pb-loss event, which was shown to have affected most zircons isolated from Scourie dykes (Davies and Heaman 2014).

The U-Pb zircon results from the JD09-2 dyke are much more complex. These zircons are all discordant (up to 50 %) with high common Pb contents (up to 2000 cps). The data broadly define a linear array with an upper intercept of 2344 ± 80 Ma with an anchored lower intercept at 400 Ma. Without the anchored lower intercept the crystallization age (upper intercept) stays the same, however the error increases by a factor of 10. The high common Pb for the JD09-2 zircons, and the uncertainty on the composition of this common Pb, mean that producing an accurate crystallization age is difficult. A general agreement with the ~2400 Ma ages from other dykes (Heaman and Tarney, 1989; Davies and Heaman, 2014) suggests that the JD09-2 zircons likely

formed around this time, and similar to other zircon populations from Scourie dykes, may have experienced a Caledonian Pb-loss event.

In summary, both the dykes dated here, and the dykes dated previously (Heaman and Tarney, 1989; Davies and Heaman, 2014), produce ages in three broad categories: ~2.5 Ga from xenocrystic zircon and dyke emplacement ages of ~2.4 Ga and ~2.0 Ga. All the dykes were affected by a Pb- loss event during the Caledonian at ~400 Ma.

4.4.4. Elemental composition of the zircon, constraining the alpha dose

The chemical compositions of the Scourie zircons have been analyzed by electron microprobe techniques (Table 4.2). They have close to stoichiometric Zr and Si ratios with the more altered grains from Lochan Fearna, Loch na h and some Poll Eorna zircons being depleted in SiO_2 and ZrO_2 (Fig. 4.7a). The grains with Zr and Si depletions are also anomalously rich in U and Ca, with values reaching up to 5000 ppm for Ca and 1500 ppm for U. These trace-element enriched samples also display a dull CL response and more intense alpha dose, indicating a high degree of radiation damage (Fig. 4.7b,c). Low elemental totals for all of the samples, apart from the Loch a'Choin zircons, suggests enrichment in non-formula cations that were not analyzed (Al, Fe, HREE) and potentially enrichment in hydrous species.

Alpha doses for each of the grains were calculated assuming that radiation damage has been accumulating since the formation of the zircon (Fig. 4.7b). The alpha dose shows a positive correlation with the linewidth of the ν_3 (SiO_4) band, although the alpha dose amounts are very high. Nasdala et al. (2001) report alpha doses of ~1.5 $x10^{18}$ α/g linewidths of 20, where as we calculate alpha doses of ~10 $x10^{18}$ α/g for the same linewidth.

There is a clear relationship between alpha dose and Ca content (Fig. 4.7d). After the alpha dose reaches a threshold dose of ~7 x10^{18} α/g, the Ca (and U content) dramatically increase, whereas below this dose the Ca and U contents are always low. There is no obvious relationship between the CL patterns, trace-element contents and oxygen isotope compositions. In sample JD09-2, the high Ca content samples seem to be mostly associated with darker CL zones and heavier $\delta^{18}O$ values (~1 - 1.8 ‰), although this trend is clouded by the small-scale CL zoning. Correlating the results is also difficult because the trace-element, Raman and $\delta^{18}O$ measurements were all conducted on slightly different regions of the grain.

4.4.5. Raman spectra

Most of the Scourie dyke zircons have ν_3 (SiO_4) band parameters that follow the radiation damage trend (Fig. 4.8). The Loch a'Choin samples have the most crystalline zircons with the lowest linewidth and highest frequency, which is consistent with the low alpha dose, low trace-element (U, Th and Ca) contents, relatively bright CL response and equilibrium oxygen isotopic compositions (Figs. 4.5-7). All other zircons have linewidths and frequencies that classify them as either metamict or highly metamict (see Fig. 4.1).

The Raman results were split into two groups based on their Ca contents. The dominant group from the low-Ca grains are metamict, but at relatively low degrees, with linewidths of ~10-15 cm^{-1} and frequencies around 1000 cm^{-1}. All of the grains in the low-Ca group are either overlapping with the radiation damage trend, or are close to overlapping. Since the trend is only a guide based on published and unpublished Raman measurements of various zircons (Nasdala et al. 1998b; 2001; Zheng et al. 2000a; Geisler et al. 2003b,c), analyses that lie very close to the line are considered

to conform to the radiation damage trend.

The high-Ca grains have much greater degree of within-sample spread in Raman spectral line widths and frequencies than the low-Ca grains. For example, the Poll Eorna grains have linewidths and frequencies that range between ~15-32 cm^{-1} and ~998–1002 cm^{-1}, respectively, a wider range than any other sample. The most prominent feature of the high-Ca zircons is their movement away from the radiation damage trend with highly metamict zircons showing higher frequencies for the ν_3 (SiO_4) band than the linewidth suggests. The high frequencies and high linewidth are very similar to the patterns of structural recovery of short-range disorder shown by Geisler et al. (2003b,c).

4.5. Discussion

4.5.1. Evidence for fluid exchange

There is clear evidence for oxygen isotope disequilibrium between the WR and zircon in Poll Eorna, Lochan Fearna, JD09-2, Loch na h, North Assynt and to some extent the NAPI dykes (Fig. 4.6). The oxygen isotopic disequilibria is coupled with U-Pb discordance (Fig. 4.3, Davies and Heaman, 2014) and high Ca contents, all of which point towards hydrothermal alteration of the zircon. Also, the altered dykes contain abundant epidote- group minerals, characteristic of fluid alteration (Davies and Heaman, 2014). However, CL imaging of the zircon does not show the distinctive reaction rim patterns or copious mineral inclusions, which are typically associated with hydrothermal alteration of zircon (Geisler et al. 2000; 2001; 2003b; 2007; Putnis 2002; Putnis et al. 2005; Tomaschek et al. 2003).

It is possible that the zircon could have obtained its seemingly altered composition through magmatic processes. For example, contamination of the dyke magmas by continental crust or the entrainment of xenocrystic zircon could create the apparent disequilibria between the WR and zircon oxygen isotopic compositions. Concentrations of the large ion lithophile (LIL) trace-elements Rb, Th, U and K are up to 50 times higher in the dykes than in the gneisses, whereas the gneisses contain enrichments in Ti and Sr relative to the dykes (Weaver and Tarney, 1981, Rollinson, 2012). Bulk contamination of the dykes by the gneisses would significantly reduce the LIL contents of the dykes while increasing Ti and Sr, which is not observed (Tarney and Weaver, 1987; Rollinson, 2012). Entrained xenocrystic zircons (presumably from the surrounding gneisses) are likely to be distinctive in CL images, either as a core within magmatic grains or as discrete crystals. Zircons from Loch a'Choin, North Assynt and JD09-2 all have core and rim type zoning that could reflect the presence of xenocrystic zircon. However, there is no evidence for a distinctly different $\delta^{18}O$ composition of the core relative to the rim in these samples. Zircon from tonalitic gneiss surrounding the dykes should have a $\delta^{18}O$ of ~9 ‰ (Cartwright and Valley, 1992), which is much higher than observed in any of the zircons from this study. The range of values seen in the North Assynt and JD09-2 zircons could theoretically reflect diffusion of oxygen between a core and rim in highly metamict grains (Geisler et al. 2002), since metamictization causes volume expansion and areas of low atomic density (Trachenko et al. 2002). However, if the two end-members for diffusion were a core at ~9 ‰ and a rim at a lighter value reflecting the magma (~4 ‰), a range between the two would be expected with heavier values in the center, which is not observed. This study is not ideal to test this theory since the grains are not large enough for multiple spot analyses on each grain. The diffusion explanation for oxygen isotopic disequilibria does not explain the presence of Ca within the zircons, and is also not consistent with the lack of core – rim type zoning shown by the

zircon from Poll Eorna, Graveyard, Lochan Fearna, NAPI and Badcall Bay dykes.

The high Ca content of some of the Scourie zircons suggests that hydrothermal fluids have altered the grains. Ca is not partitioned into zircon during growth (see Hoskin et al. 2003) due, in part to the Goldschmidt rule, which indicates that substitution of Ca^{2+} for Zr^{4+} or Si^{4+} ions in zircon would only take place if the ionic radius of Ca^{2+} was within 15 % of Zr^{4+} or Si^{4+}; it is ~40 % larger than Zr^{4+}, the larger of the two ions (Shannon 1976). A coupled substitution mechanism has been suggested for Ca in zircon, through the hydrogrossular substitution $[Ca^{2+} + 2H^{+}] \leftrightarrow [Zr^{4+}]$ (Geisler et al. 2001), indicating that Ca may only partition into zircon in the presence of fluids. We therefore reject the hypothesis that the oxygen isotopic features are related to magmatic processes and concentrate on constraining the nature of fluid alteration.

4.5.2. Mechanism for fluid alteration

Experimental studies, outlined below, investigating the interaction between metamict zircon and hydrothermal fluids have shown that the main parameters controlling the levels of exchange between the fluid and zircon are: composition of the fluid, temperature of the fluid, and degree of metamictization.

Pidgeon et al. (1995) investigated the X-ray diffraction properties of amorphous zircon under different hydrothermal conditions. They discovered that pure water had very little effect on the structure of the zircon even after 11 hours at 500 °C, whereas experiments under the same conditions using 2M NaCl and HCl solutions revealed significant recovery of crystallinity, and also loss of Pb. Interestingly, during experiments investigating the effect of sodium carbonate solution at 400 °C on metamict zircon, Rizvanova et al. (2000) found that the structurally recovered metamict zircon,

similar to zircon in the present study, did not contain a reaction rim. However, during the reaction with sodium carbonate solution, some of the zircon dissolved and was replaced by baddeleyite and a Zr-Na phase, which is not seen in the Scourie zircons. In experiments using natural brines, Hansen and Friderichsen (1989), discovered that the presence of cations like Ca^{2+} in the water in small amounts has a significant effect on the leaching of Pb from metamict zircon, as well as structural recovery.

Detailed experimental studies by Geisler et al. (2001; 2002; 2003b) revealed that the relationships between structural recovery, temperature and composition of the fluid are complicated. They concluded that the amount of metamictization has a strong impact on the structural recovery, with temperature of the fluid playing a more important role than composition of the fluid (as long as it is not pure H_2O). Experiments at low temperature (175-350 °C) caused small degrees of structural recovery, and did not anneal amorphous domains within the crystals, however the fluids did leach trace-elements. The low temperature recovery was attributed to repairing of Frenkel defects and short range disorder in the crystal structure. As the temperature of the fluid increased, the fluids diffused further into the crystal and caused recrystallization of longer range disorder and amorphous domains. This increased penetration by higher-temperature fluids was attributed to the kinetics of fluid diffusion, and the relationship between the kinetics of diffusion, and the kinetics of recrystallization. Geisler et al. (2003c; 2007) also demonstrated that the first percolation point (Salje, et al. 1999), where the amorphous domains form infinite clusters in the crystal, is the critical point where extensive fluid alteration and recrystallization can occur.

The Raman signature of diffusion recrystallization is very distinctive (Fig. 4.1), and the Raman results from the Scourie zircons appear to indicate they have undergone this process (Fig. 4.8). The geochemical data (Fig. 4.7) also are in agreement with

the 4.critical point model of Geisler et al. (2003c; 2007), as the Ca content clearly shows a distinct increase after a critical alpha dose concentration has been reached. There are a couple of anomalies, for example, the two zircons from the North Assynt and NAPI dykes have slightly elevated Ca contents at low alpha doses. These grains plot in the metamict/highly metamict area on the radiation damage trend in Fig. 4.7 and therefore appear to not have experienced significant structural recovery. Geisler and Schleicher (2000) showed that in highly metamict areas of grains, fluid alteration could remove U from the zircon and still deposit Ca, which could explain the elevated Ca at low U in the zircons. If the fluid interacting with the Scourie zircons was not hot enough, and the grains were too metamict, it may not have been able to catalyze recovery, and therefore the grains would plot on the radiation damage trend.

There is a general relationship between distance from the radiation damage trend, linewidth, and Ca content in the zircon (Fig. 4.9). This trend suggests that the most metamict zircons experienced the greatest degree of fluid exchange, and also experienced the most recrystallization. It is apparent that small degrees of fluid interaction, which increase the Ca content to <~100 ppm in zircon have not caused significant recrystallization. This finding is in agreement with the experimental and natural sample results of Geisler et al. (2001; 2002; 2003b; 2003c; 2007). Geological data suggest that the mylonitization along the Moine thrust nappe reached temperatures of 300-400 °C (Holdsworth et al. 2007), and movement along the fault likely initiated hydrothermal fluid circulation (e.g. Travé et al. 1997). Since the high-Ca zircons also have high U (Fig. 4.7), they have experienced ~400 Ma of damage since recrystallization, if it is assumed that the recrystallization occurred at the time of the Caledonian, coinciding with the timing of Pb-loss. We suggest that the levels of recrystallization shown by the present-day Raman properties include radiation damage after the Caledonian-age alteration and recrystallization of zircon. The fluid

event the degree of structural recovery experienced by the high-Ca zircons during the Caledonian fluid event was probably much higher.

4.5.3. Timing of radiation damage accumulation

Two main properties control the accumulation of radiation damage in zircon. Firstly, the amount of time the zircon has spent at a temperature low enough to allow radiation damage to accumulate and not be thermally annealed (~150-250 °C; Meldrum et al. 1999; Davis and Krogh, 2000; Moser et al. 2011; Pidgeon 2014); and, secondly, the abundance of the radioactive elements in the crystal, essentially U and Th in zircon.

The amount of alpha decay events per gram of sample (alpha dose per gram) is a measure of radiation damage and can be calculated using the equation:

$$D\alpha = 8 \cdot \frac{cU \cdot N_A \cdot 0.9928}{M_{238} \cdot 10^6} \cdot (e^{\lambda 238t} - 1) + 7 \cdot \frac{cU \cdot N_A \cdot 0.0072}{M_{235} \cdot 10^6} \cdot (e^{\lambda 235t} - 1) + 6 \cdot \frac{cTh \cdot N_A}{M_{232} \cdot 10^6} \cdot (e^{\lambda 232t} - 1) \quad (2)$$

where cU and cTh are the concentrations of U and Th in ppm, N_A is Avogadro's number, M_{238}, M_{235} and M_{232} are the molecular weights, λ_{238}, λ_{235} and λ_{232} are the decay constants for each parent isotope and t is the amount of time radiation damage has been accumulating (Holland and Gottfried, 1953; Murakami et al. 1991). t is not necessarily known, especially with old grains that have a complex history like the Scourie zircons. However, t can be estimated by comparing the alpha dose with the FWHM of the ν_3 (SiO_4) band and iteratively changing t until the samples plot along the same trajectory as zircons with known thermal histories (e.g. Nasdala et al. 2001; Palenik et al. 2003; Pigeon 2014, Fig. 4.10). The Scourie zircons have clearly not been accumulating radiation damage since their formation (Fig. 4.6b). The alpha

doses, when calculated at the emplacement age, are too high compared with the expected FWHM of the ν_3 (SiO_4) band (Fig. 4.6b). Alpha doses at these high levels (>5 $x10^{18}$ α/g^{-1}) would also result in completely aperiodic and amorphous zircon (Ríos et al. 2000; Pidgeon, 2014).

To estimate the amount of time that the Scourie zircons have been accumulating damage, we varied the t parameter in equation (2) and compared the results to zircons from the Saxonian rhyolite (Nasdala et al. 1998b) and lunar zircon (Wopenka et al. 1996). The Saxonian rhyolite and lunar zircon are good models for how zircon should accumulate radiation damage over time, since they are thought to have stored all of their radiation damage since crystallization and have not undergone any thermal or fluid annealing. . Since the Scourie dyke zircons have a complicated history involving diffusional annealing, only the grains that haven't been annealed can be used to constrain the time of damage accumulation. Linear regression lines for different ages are plotted through the zircon analyses that have the lowest Ca, Th and U contents, and are compared to zircon from the Saxonian and lunar samples (Fig. 4.10). It is apparent that the Scourie dyke zircons have not been accumulating radiation damage since their formation in the Paleoproterozoic. The high degree of scatter in the Saxonian and lunar samples (and also the Scourie zircons) makes determining a precise age of damage accumulation difficult. An age of ~520 Ma fits the Saxonian and lunar zircons the best, although the calculations allow any age between 440 and 620 Ma. If the ~520 Ma age is approximately correct, it would mean that the dykes cooled below ~250 °C at this time, the zircon then began to accumulate radiation damage for ~100 Ma before coming into contact with fluids causing Pb-loss and Ca-gain possibly during the emplacement of the Moine thrust at 430.7 Ma (Goodenough et al. 2011).

4.5.4. What can we say about the oxygen isotopic composition of the rock?

The main benefit of combining trace-element and Raman analyses to study the fluid history of a zircon population is that together they can identify which zircons/areas of zircons are not affected by fluid alteration. Separating the oxygen isotope analyses into those which have experienced fluid alteration, and those that are unaltered provides information about the isotopic composition of the fluid, as well as the original oxygen isotopic composition of the zircon. Fig. 4.11 shows that the fluid altered zircon is isotopically heavier than the fresh zircon and therefore indicates oxygen isotopic exchange with a secondary fluid. An exception is the one high-Ca analysis from JD09-2, which is isotopically lighter than the low-Ca analyses in this sample, and is inconsistent with a high $\delta^{18}O$ signature from the other fluid altered zircons. One explaination for this could be the temperature of the hydrothermal fluid. Using the Kieffer (1982) calculations, zircon - water $\delta^{18}O$ fractionation should be > 5.7 ‰ at <100 ºC and smaller at higher temperatures. If the JD09-2 zircons experienced hotter hydrothermal fluids than the other zircons, they would be less enriched in ^{18}O. Alternatively, the U-Pb analyses for JD09-2 were completed after the SIMS oxygen study but before the microprobe and Raman analyses. This meant that the microprobe and Raman spots for both JD09-2 and NAPI samples are slightly further away from the SIMS spots than for all of the other grains. The spatial difference could result in uncorrelated Ca and $\delta^{18}O$ values especially since the JD09-2 zircons are strongly zoned. It is therefore possible that the low $\delta^{18}O$ of -1.34 ‰ is actually from a relatively undisturbed area of the grain and records a value close to the magmatic isotopic composition of the grain whereas the Raman and electron microprobe spots are from a highly disturbed area of the grain.

Even more interesting than investigating the $\delta^{18}O$ value of the fluid, this technique

allows the opportunity to find regions of the zircon that were unaffected by fluid alteration and obtain the original $\delta^{18}O$ value of the zircon before alteration. Since the fluid alteration has caused the zircons to obtain higher $\delta^{18}O$ values, the lowest $\delta^{18}O$ values recorded by the zircon are likely to be the least altered and therefore closest to the magmatic value. Poll Eorna and North Assynt zircons appear to corroborate this hypothesis since the low-Ca zircons are closest to high temperature isotopic equilibrium with the WR (Fig. 4.11). The low-Ca zircons from Loch na h, Lochan Fearna and to some extent NAPI dykes, are all far out of equilibrium from the WR, which appears at first glance to disprove the hypothesis. However, the Loch na h, and Lochan Fearna zircons are highly altered, therefore it is very likely that the WR $\delta^{18}O$ isotopic composition has been affected by fluid alteration as well. These rocks contain epidote group minerals, and highly saussuritized plagioclase, visible in thin section (not shown). In these examples, the zircons are much lighter in $\delta^{18}O$ than the WR. Fluid-rock exchange is kinetically easier than fluid-zircon exchange (Valley, 2003), therefore the isotopically heavy WR values have likely been overprinted by the fluid. In these cases, the lowest $\delta^{18}O$ and least altered zircon values can be used to estimate the original $\delta^{18}O$ composition of the rock assuming equilibrium zircon-magma fractionation. Calculated in this way, the unaltered $\delta^{18}O$ Scourie dyke WR values are as follows: NAPI (~5 ‰), Lochan Fearna (~2.3 ‰), JD09-2 (~0.5 ‰), and Loch na h (~ -3.7 ‰). The implication of this result is that all the ~2.4 Ga Scourie dykes have $\delta^{18}O$ values much lower than the mantle value of 5.5 ± 0.5 ‰ (Valley, 2003). These zircons have some of the lowest oxygen isotopic compositions ever recorded (see Valley et al. 2005), and this study provides evidence that these low compositions are reflective of original low-$\delta^{18}O$ magmatic compositions. Cartwright and Valley (1991) first identified that some Scourie dykes had low $\delta^{18}O$ compositions, although their data indicated relatively consistent WR values of ~2 ‰. These new low-$\delta^{18}O$ zircon data indicate that the low-$\delta^{18}O$ signature for Scourie magmas is variable, and

is potentially as low as -3.7 ‰.

The origin of this low-$\delta^{18}O$ signature will be discussed in detail in a subsequent study. However, the negative $\delta^{18}O$ values indicate that rocks in the source region of the dykes must have at some point experienced hydrothermal alteration from low-$\delta^{18}O$ surface waters. These waters must have been meteoric since the $\delta^{18}O$ composition of seawater (0 ‰ throughout time) is not low enough to cause the isotopic anomalies seen in the dykes. A model involving the emplacement of hydrothermally altered crustal material into the mid to lower crust where it was variably incorporated into the mafic magmas of the Scourie dykes at ~2.4 Ga is consistent with the oxygen isotopic data. Emplacement of the hydrothermally altered crust likely occurred during ~2.5 Ga high-grade metamorphism, which is ubiquitously recorded by the zircons in the Lewisian gneiss surrounding the dykes (Corfu et al 1994; Kinny and Friend 1997; Zhu et al. 1997; Whitehouse and Kemp, 2010).

4.6. Summary and Implications

This study documents how a combination of in-situ non-destructive Raman spectroscopy, electron microprobe and CL imaging can be used to understand complex altered zircon populations, and identify zircons, or areas of zircon grains, that retain their original isotopic composition. These techniques are recommended for zircon populations that may have experienced fluid alteration and may be particularly useful in detrital zircon studies where unidentified fluid alteration causes Pb loss and complicates the interpretation of U-Pb ages (e.g. Liu and Zhang, 2013).

Zircons from the ~2.4 Ga Scourie dykes have very low $\delta^{18}O$ values, as low as -3.8

‰. These low values are most representative of the magmatic value and have rarely been found on Earth especially in the Precambrian outside of Karelia, Russia (Bindeman et al. 2010; Bindeman and Serebryakov, 2011). These new data require a new interpretation of the geological history of the Lewisian high-grade gneiss terrain of NW Scotland. The source for the Scourie dykes must have contained a very low $\delta^{18}O$ component, which obtained its oxygen isotopic composition though hydrothermal alteration by highly depleted meteoric water. The low $\delta^{18}O$ component must be more depleted than oceanic crust hydrothermally altered by 0‰ seawater.

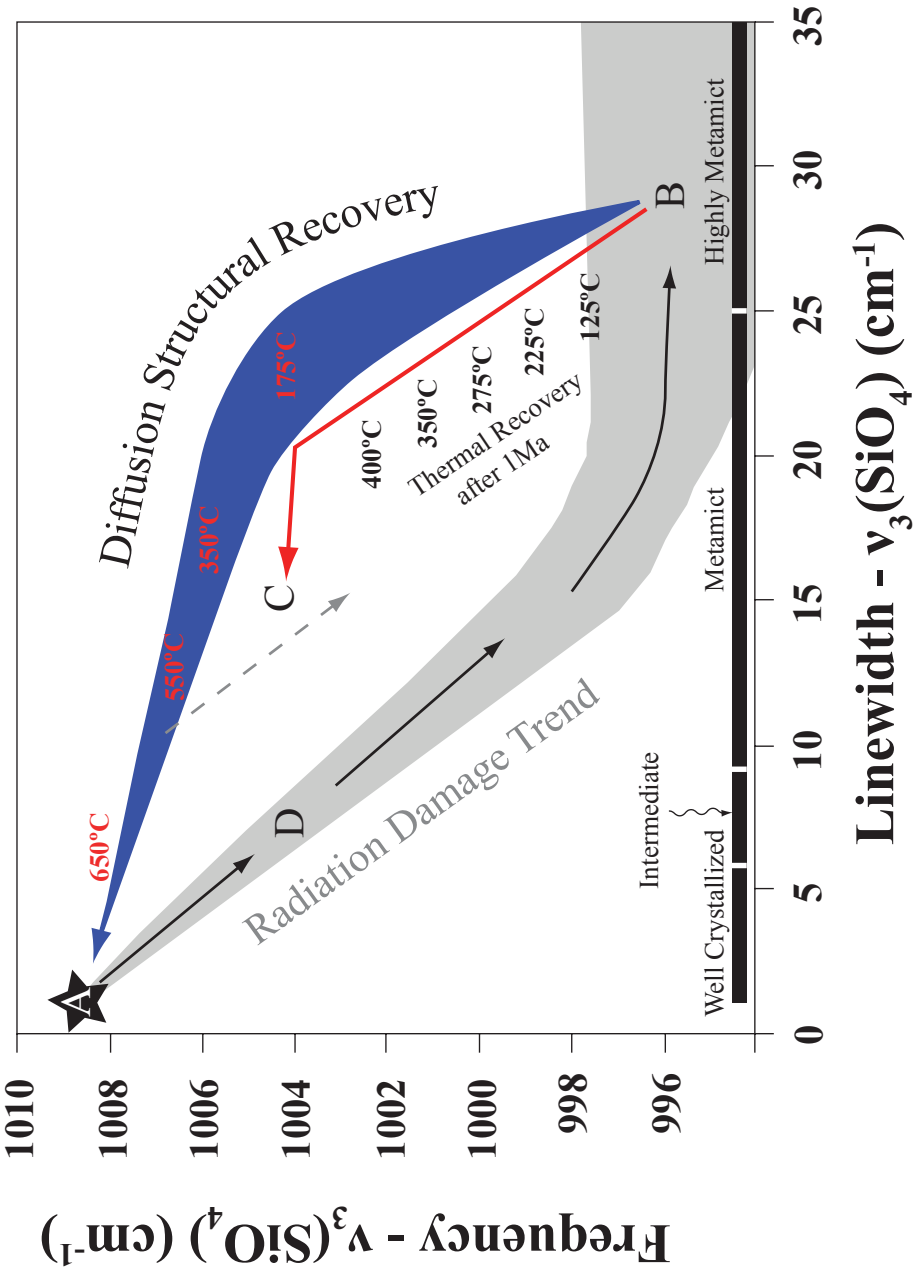

Figure 4.1. Raman model

Zircon Raman model showing how the linewidth and frequency of the v3 (SiO4) band respond to the accumulation of radiation damage, and how annealing of radiation damage either thermally, or catalyzed by fluids influences these parameters. For an explanation of the numbers and arrows see the text. The radiation damage trend is mainly based on data from Sri Lankan zircons and zircons from a Saxonian rhyolite which encompassed data from Nasdala et al. (1998b; 2001); Zheng et al. (2000a); Geisler et al. (2003b,c); Geisler unpublished. The Thermal annealing trend shown by the red arrow is from Geisler et al. 2001a, and the diffusional recovery trend is based on experimental and natural data from Geisler et al. (2003b,c).

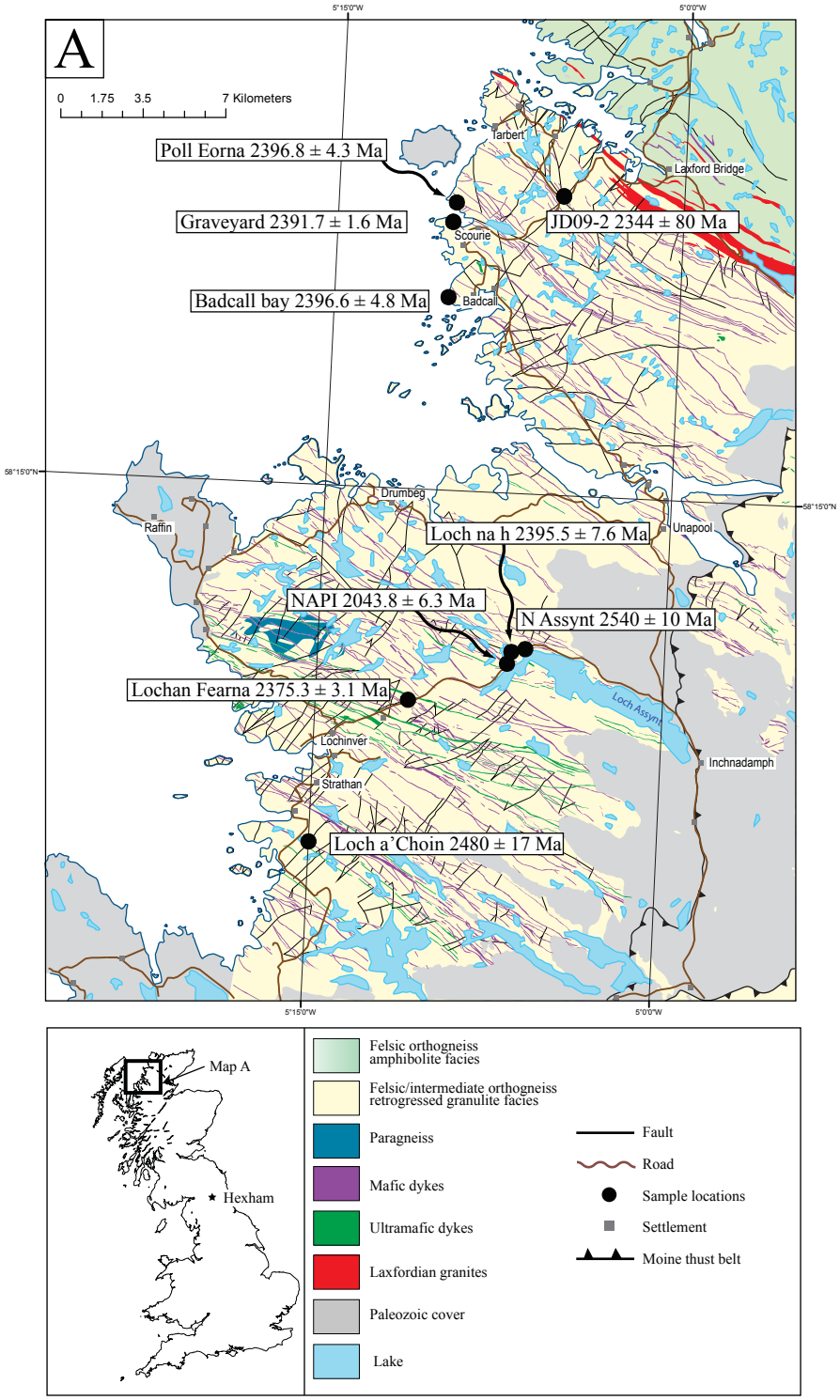

Figure 4.2. Geological map

Simplified high-resolution geological map of the Loch Assynt area on the Scottish mainland. The map is modified from a 1:25,000 scale geological map from the BGS and figure 2b from Goodenough et al. (2010). The dyke samples are located along with their emplacement age and 2σ error (Davies and Heaman, 2014).

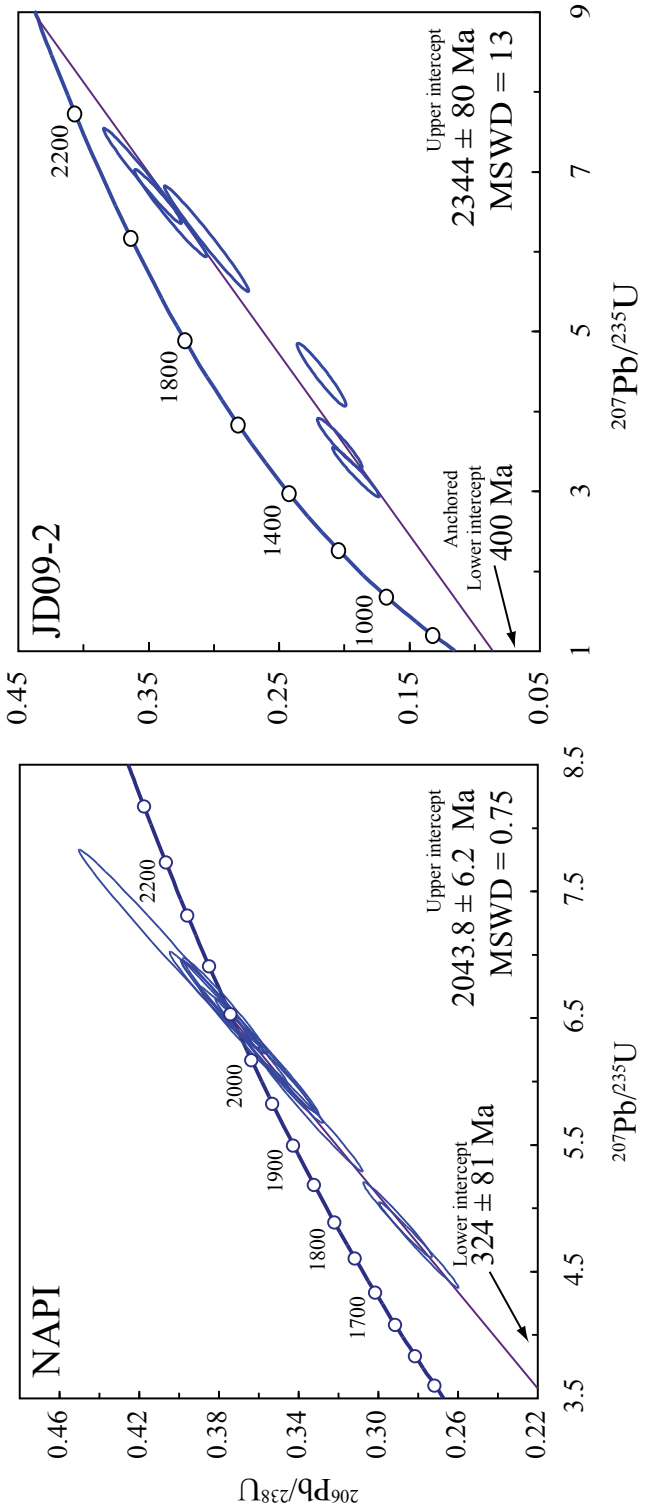

Figure 4.3. Concordia diagram

Concordia diagrams of the LA-ICP-MS U-Pb data from the NAPI and JD09-2 samples. The ages are upper and lower intercept ages with 2σ errors. The error elipses are also at 2σ.

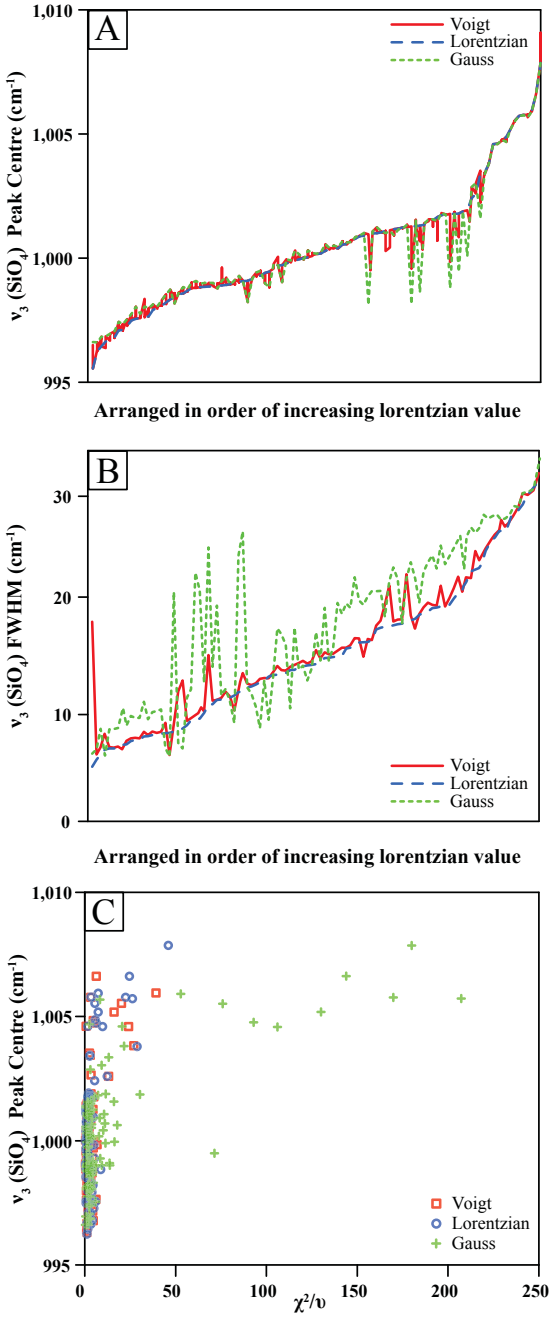

Figure 4.4. Raman fitting

Different numerical models for fitting the Raman spectra. A) peak center for the ν3 (SiO4) band plotted for all of the samples using each model, the data are in order of increasing peak center produced by the Lorentzian model. B) FWHM for the ν3 (SiO4) band plotted in the same way as A) in order of increasing Lorentzian value. C) reduced Chi squared statistic ($\chi 2/\nu$) plotted vs peak center showing that peaks with high wavenumbers are most difficult for the Gaussian and Voigt distributions to model accurately. The Lorentzian model fits the data the best, accurately modeling the position of the ν1 (SiO4) and ν3 (SiO4) bands whereas the Gaussian and Voigt models produce low wavenumbers for the peak center, and also overestimate the FWHM (see A and B as well).

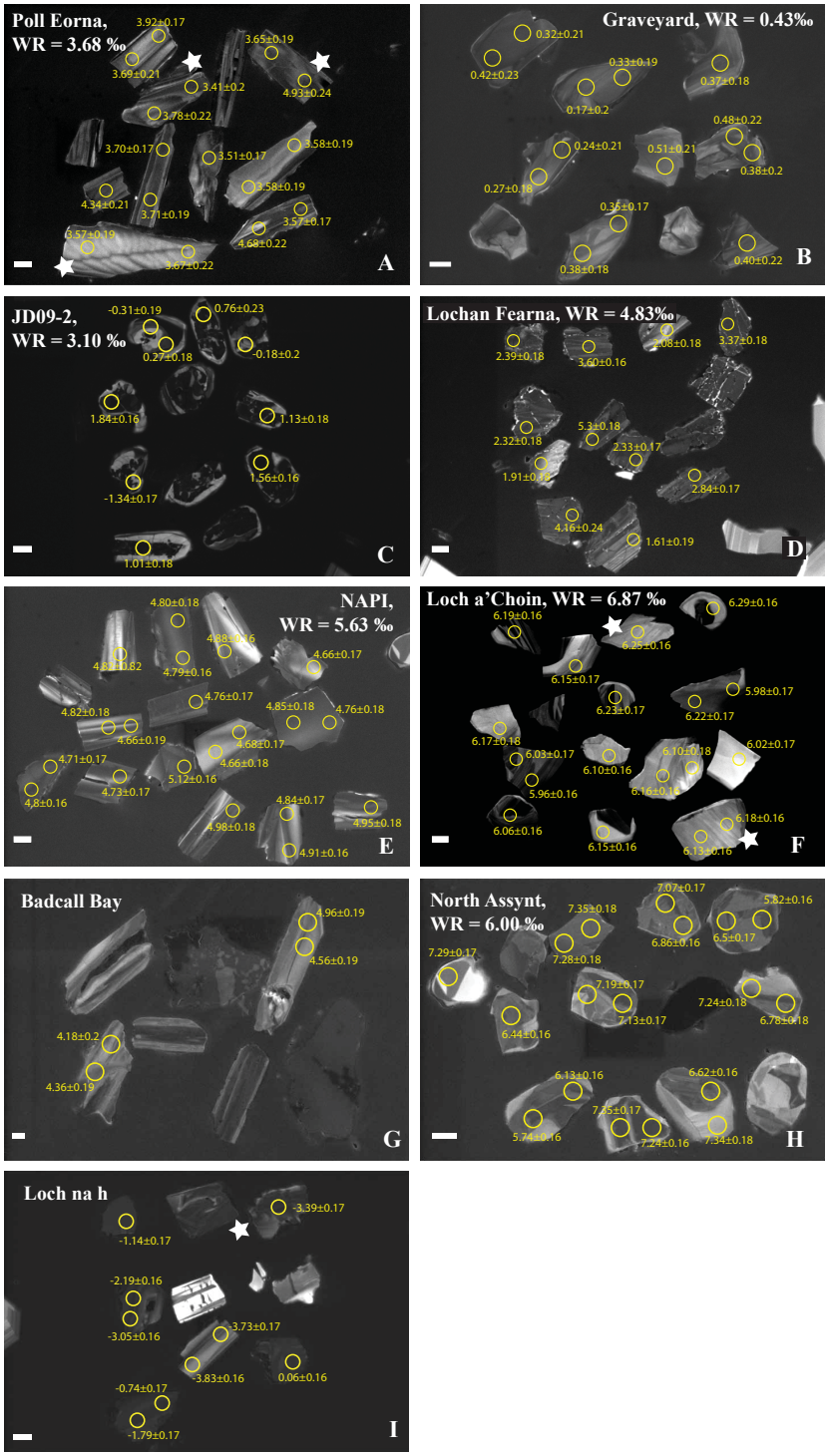

Figure 4.5. CL images

CL images of zircons from the Scourie dykes with SIMS analysis spots and the oxygen isotope values located. Oxygen isotopes are all $\delta^{18}O$ values with 2σ uncertainties. Th WR oxygen isotopic composition of each sample is also given, these are also $\delta^{18}O$ values with 2σ uncertainties. The white bar in the bottom left of each image is a 20 μm scale bar. The white stars indicate grains with a complicated CL structure within a zircon population of typical igneous oscillatory zoning.

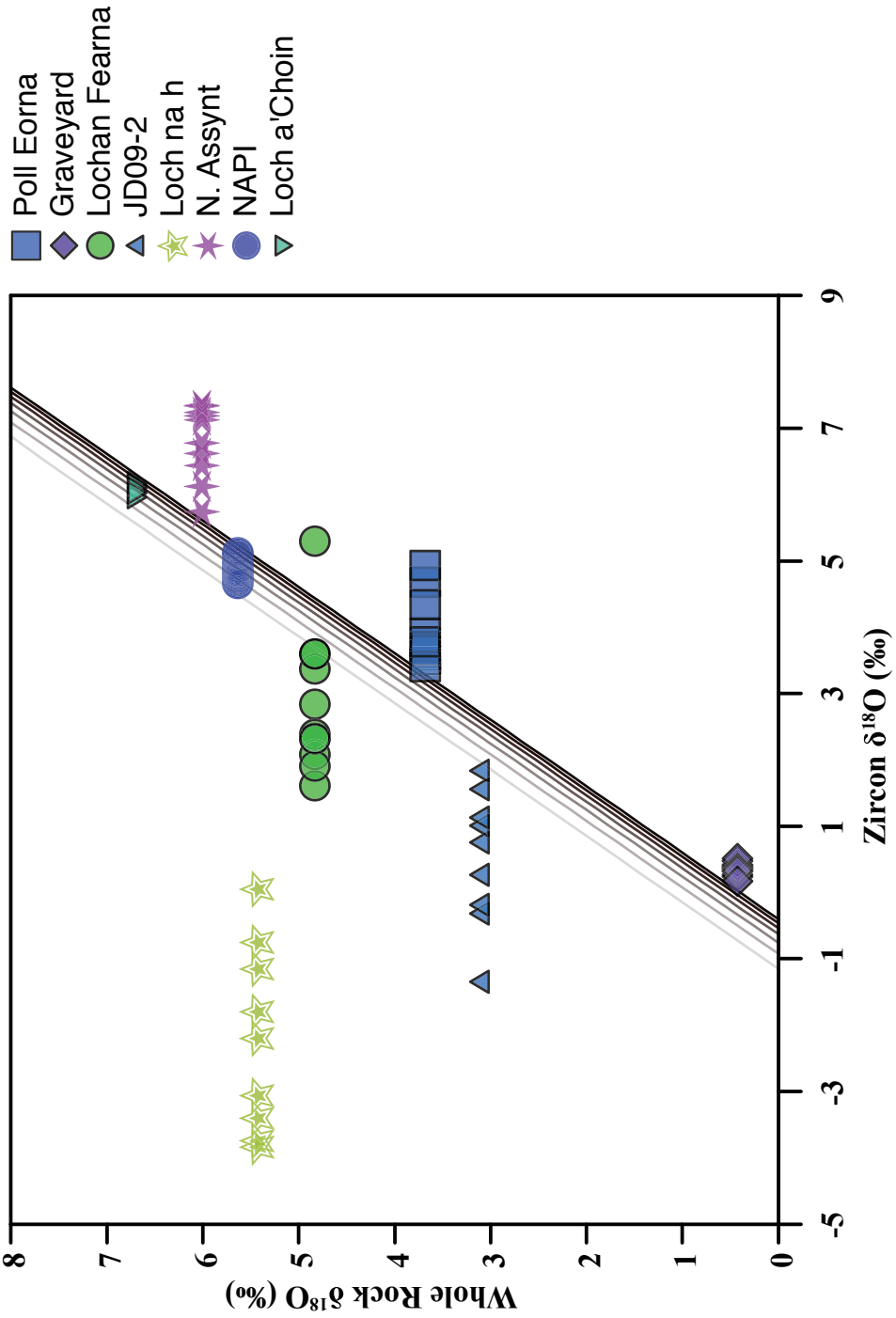

Figure 4.6. Whole rock and zircon oxygen isotopes

$\delta^{18}O$ Zircon vs $\delta^{18}O$ whole rock (WR) for the Scourie dykes. The lines represent equilibrium fractionation between zircon and WR with a fractionation factor (α) of 0.88 (explained in text). The darkest line, represents equilibrium fractionation at 1200 °C, each lighter colored line represent the larger fractionations associated with lower temperatures, each lighter line represents a 100 °C drop in temperature down to the lightest grey line which represents equilibrium fractionation at 600°C. The symbols are bigger than the 2σ errors for each analysis.

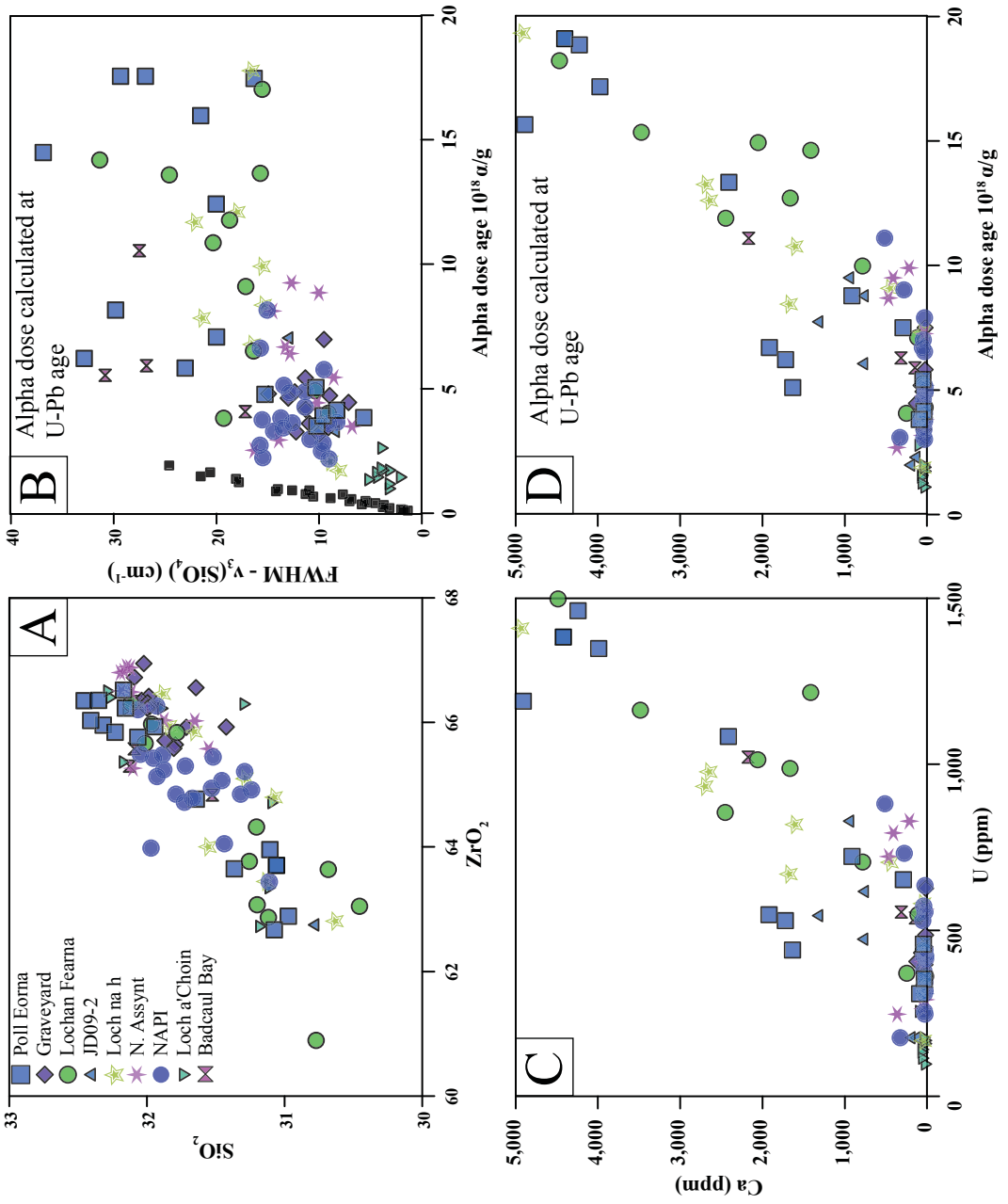

Figure 4.7. Zircon trace-elements

Geochemistry of the Scourie zircons. A) SiO_2 vs ZrO_2 all values are in percentage B) Alpha dose accumulation since zircon formation age vs the linewidth of the v3 (SiO_4) band, note the black squares close to the y-axis, these represent the expected relationship between linewidth and alpha dose, and are from the Saxonian rhyolits and lunar zircons (Nasdala 1998b; Wopenka et al. 1996). C) Ca and U elemental compositions of the Scourie zircons in ppm. D) The relationship between Ca content and the apha dose, note the abrupt change in Ca content once a threshold alpha dose has been reached, this threshold is interpreted as the first percolation point in the crystalline-amorphous transition, see discussion for details. All 2σ errors are smaller than the symbol sizes.

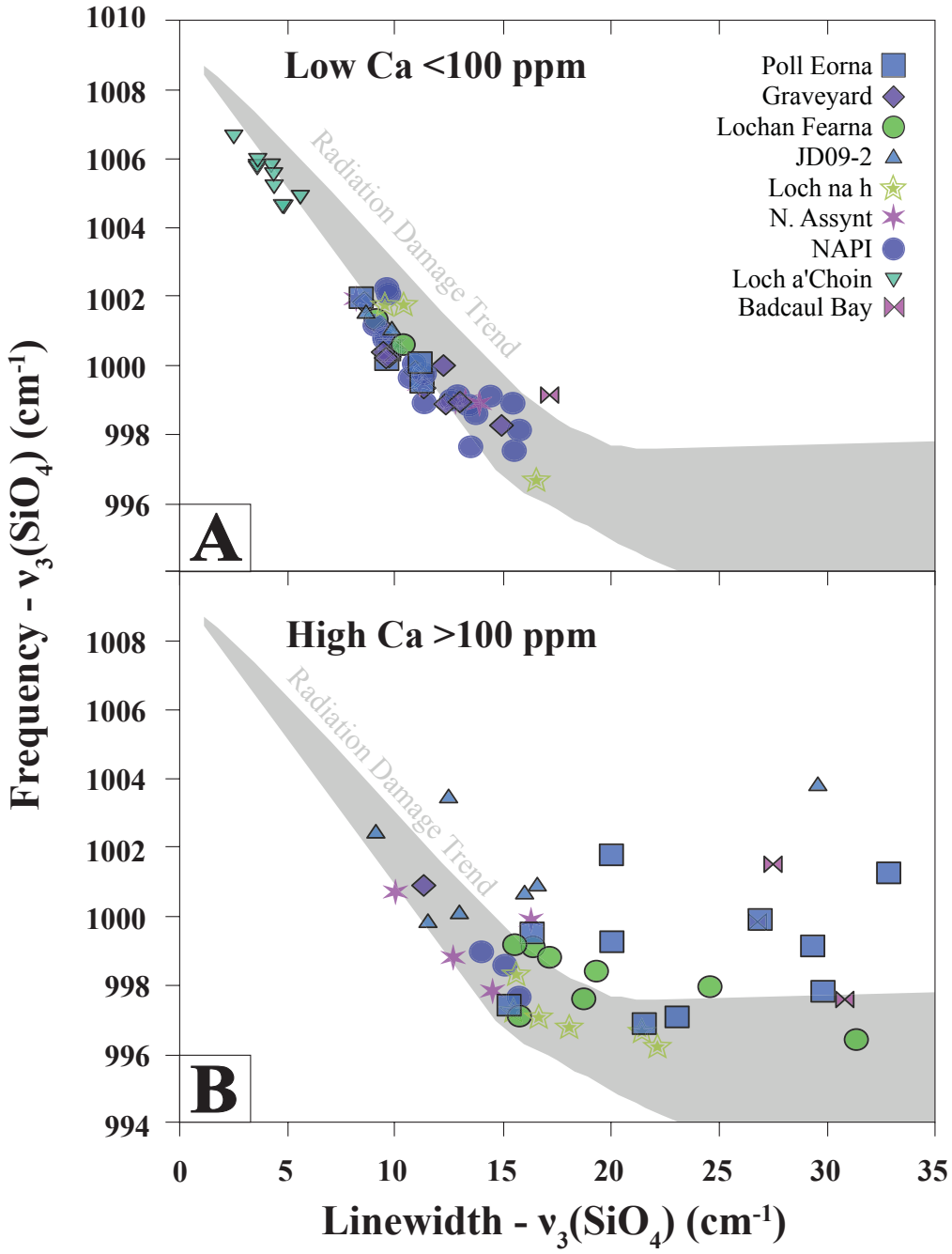

Figure 4.8. Linewidth vs frequency

Linewidth for the ν3 (SiO_4) band vs frequency. The upper graph contains raman results from zircon spots with less than 100 ppm Ca. The lower graph contains raman results for the zircons spots with higher than 100 ppm Ca. The Grey shaded field is the Radiation Damage trend from Geisler et al. 2003c which encompassed data from Nasdala et al. 1998b; 2001; Zheng et al. 2000b; Geisler et al. 2003c; Geisler unpublished)

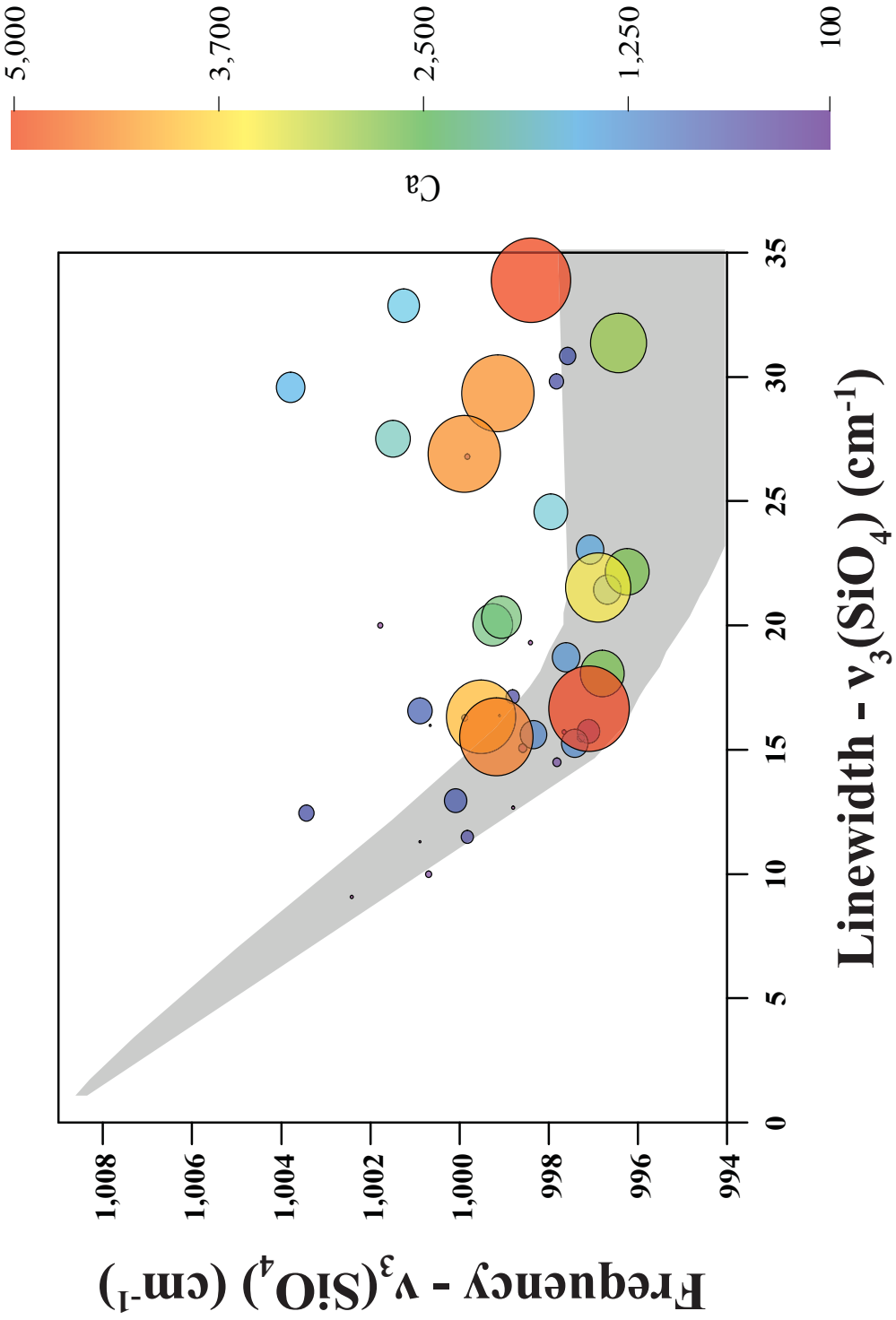

Figure 4.9. Raman band vs Ca content

A comparison of the Raman spectra of the v3 (SiO_4) band and Ca content. The figure is the same as the high Ca portion of Fig. 4.8, however the data points are colored according to their Ca content, the size of the symbol is also proportional to the Ca content.

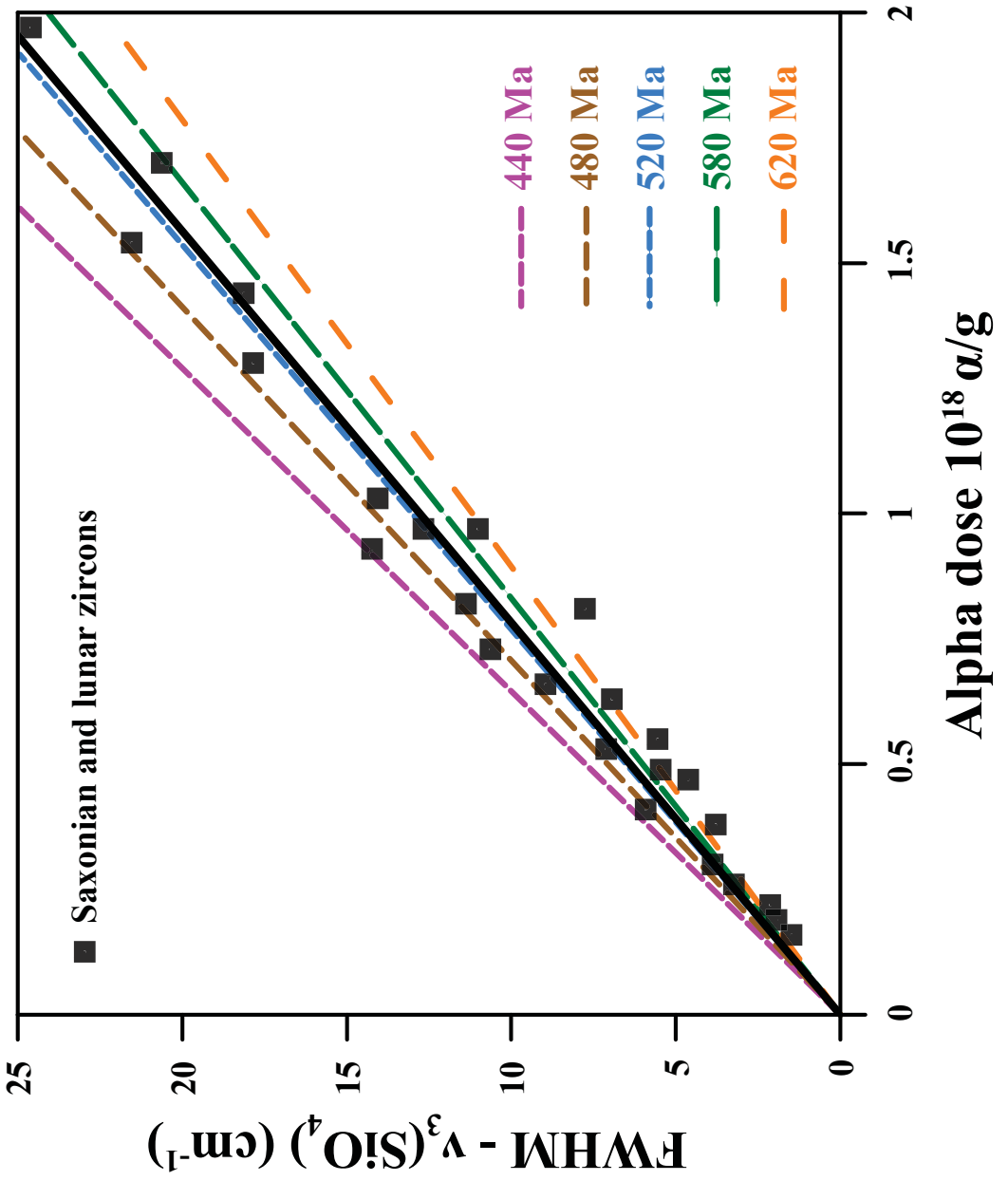

Figure 4.10. Raman radiation damage accumulation age

Different models for the radiation damage accumulation age of the low Ca zircons calculated at different ages using the measured Uranium and Thorium contents. The models are compared to the expected relationship between linewidth and frequency of the v3 (SiO_4) band and age which is represented by the Saxonian rhyolite and lunar zircons (Black squares, Nasdala et al. 1998b, Wopenka et al. 1996) The zircon models are represented as different dashed lines plotted through the Scourie zircon data (not shown for clarity) at different ages, all of the lines are forced through the origin. The black line represents a robust linear regression through the Saxonian rhyolite and lunar zircon data.

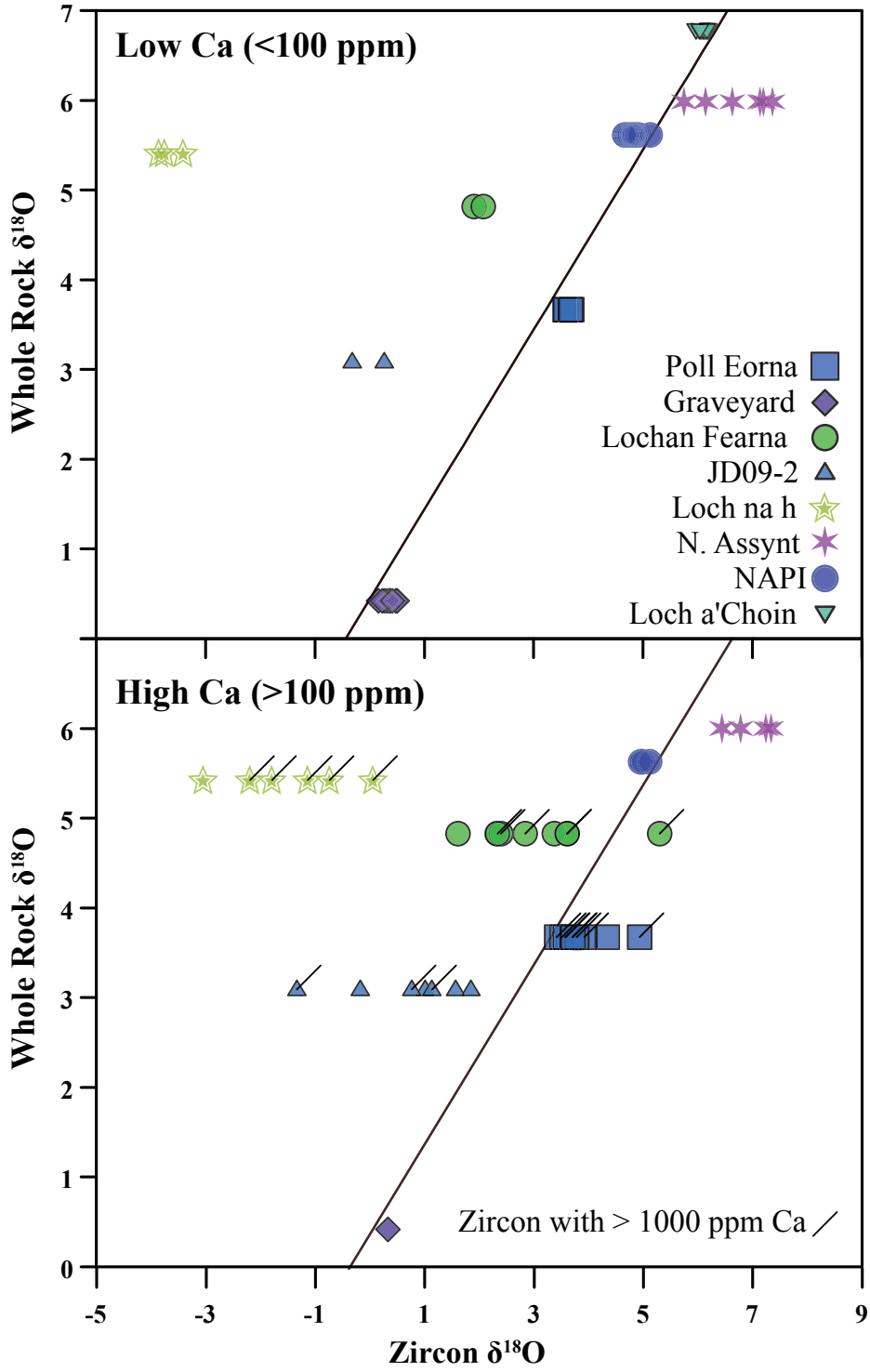

Figure 4.11. Oxygen data filtered by Raman and Ca

$\delta^{18}O$ Zircon vs $\delta^{18}O$ whole rock (WR) for the Scourie dykes separated by Ca abundance in the zircon. The large diagonal lines through both of the graphs represent high temperature (1200 °C) equilibrium between zircon and mafic melt. The small lines attached to individual analyses in the High Ca graph represent Ca analyses >1000 ppm.

Sample Name	206Pb (cps)	204Pb (cps)	206Pb(cps)/204Pb(cps)	Ratiosa							Age (Ma)						% discordance
				207Pb/206Pb	2 σ	207Pb/235U	2 σ	206Pb/238U	2 σ	ρ	207Pb/206Pb	2 σ	207Pb/235U	2 σ	206Pb/238U	2 σ	
NAPI-1	1149603	404	2845	0.127	0.002	6.727	0.469	0.385	0.026	0.984	2055	21	2076	60	2098	122	-2.5
NAPI-2	1955477	99	19674	0.126	0.001	6.322	0.501	0.363	0.028	0.989	2047	21	2021	67	1997	133	2.8
NAPI-3	930119	102	9121	0.126	0.001	6.740	0.452	0.387	0.026	0.986	2048	20	2078	58	2108	118	-3.4
NAPI-5	1482726	146	10139	0.123	0.002	5.006	0.358	0.296	0.021	0.985	1994	22	1820	59	1672	103	18.3
NAPI-6	1169267	76	15420	0.126	0.001	6.792	0.463	0.392	0.026	0.986	2039	20	2085	59	2132	121	-5.4
NAPI-7	1350373	51	26289	0.126	0.001	6.721	0.463	0.386	0.026	0.986	2047	20	2075	59	2104	121	-3.3
NAPI-8	1122240	46	24198	0.125	0.001	6.487	0.467	0.375	0.027	0.987	2035	20	2044	61	2053	124	-1.1
NAPI-9	2382003	26	90211	0.126	0.001	6.144	0.432	0.355	0.025	0.987	2037	20	1996	60	1957	116	4.5
NAPI-10	1219203	35	35267	0.126	0.001	6.267	0.448	0.361	0.025	0.987	2042	20	2014	61	1987	120	3.1
NAPI-11	988410	37	26570	0.122	0.001	4.802	0.376	0.285	0.022	0.989	1987	21	1785	64	1618	110	20.9
NAPI-12	1184477	35	34125	0.125	0.001	5.826	0.465	0.339	0.027	0.990	2024	20	1950	67	1882	128	8.1
JD09-2-1	1347042	1131	1191	0.127	0.003	3.531	0.260	0.201	0.014	0.948	2061	41	1534	57	1182	75	46.6
JD09-2-4	1174607	244	4822	0.142	0.002	6.468	0.452	0.331	0.023	0.980	2248	24	2042	60	1843	109	20.7
JD09-2-5	2459258	266	9233	0.147	0.002	6.149	0.550	0.304	0.027	0.986	2307	26	1997	75	1712	131	29.3
JD09-2-6	2557670	2533	1010	0.142	0.003	4.099	0.340	0.210	0.017	0.971	2246	34	1654	66	1229	90	49.6
JD09-2-7	1872974	145	12944	0.143	0.002	6.942	0.492	0.353	0.025	0.984	2258	22	2104	61	1950	116	15.8
JD09-2-8	1142181	585	1951	0.122	0.002	3.158	0.258	0.188	0.015	0.970	1980	35	1447	61	1112	80	47.6
SSOG1-1	1269769	45	28155	0.298	0.003	31.019	2.085	0.754	0.050	0.986	3462	18	3520	64	3622	181	-6.1
SSOG1-2	1324023	50	26647	0.298	0.003	30.769	2.083	0.749	0.050	0.986	3459	17	3512	64	3605	182	-5.5
SSOG1-3	878346	25	35489	0.298	0.003	31.199	2.112	0.759	0.051	0.986	3460	17	3525	64	3642	183	-6.9
SSOG1-4	1266580	0		0.298	0.003	29.123	1.980	0.710	0.048	0.986	3458	17	3458	65	3458	177	0.0
SSOG1-5	1366975	0		0.297	0.003	29.599	1.981	0.723	0.048	0.986	3454	17	3474	64	3507	176	-2.0
SSOG1-6	1291632	0		0.297	0.003	29.666	1.960	0.724	0.047	0.985	3455	17	3476	63	3511	174	-2.1

a = ratios not common Pb corrected
SS = Secondary standard

Table 4.1. U-Pb data

U-Pb data for NAPI and JD09-2 zircons

Dyke name	Spot ID	U-Pb age	Oxygen isotopes (‰)				Chemistry					v3 SiO4 parameters (cm^{-1})			Alpha dose $1018g^{-1}$
			δ18O whole rock	2σ[a]	δ18O zircon	2σ	SiO_2[b]	ZrO_2[b]	U[c]	Th[c]	Ca[c]	Frequency	Linewidth	χ2/v (reduced χ2)	Dyke age
Badcall Bay	3-1	2396.6 ±4.8 Ma[d]			4.18	0.20	32.07	66.34	555	-	314	999.83	26.80	2.80	5.93
	4-1				4.96	0.19	32.09	65.58	537	-	1042	997.58	30.83	4.54	5.54
	4-2				4.56	0.19	32.13	65.30	396	-	64	999.09	17.18	1.77	4.09
	3-2				4.36	0.19	31.52	64.84	1022	-	2172	1001.50	27.50	5.94	10.54
Graveyard	10-1	2391.7 ±1.6 Ma[d]	0.43	0.12	0.32	0.21	31.79	65.64	449	123	28	998.83	12.35	3.44	4.87
	10-2				0.42	0.23	31.72	65.92	431	175	71	998.22	14.94	4.48	4.8
	3-1				0.35	0.17	31.65	66.56	308	-	35	1000.39	10.00	1.45	3.18
	3-2				0.38	0.18	31.99	66.42	317	-	-	999.96	12.24	0.89	3.27
	5-1				0.38	0.2	32.02	66.95	484	219	21	999.30	11.32	5.27	5.43
	6-1				0.51	0.21	32.04	66.35	326	140	35	1000.19	9.70	1.07	3.64
	7-1				0.24	0.21	31.81	65.58	423	131	50	998.90	12.99	3.33	4.62
	7-2				0.27	0.18	32.00	66.32	431	140	35	1000.34	8.97	1.27	4.73
	8-1				0.37	0.18	31.98	66.25	625	263	21	1000.99	9.52	1.40	6.97
	9-1				0.33	0.19	32.00	66.23	405	-	128	1000.88	11.30	3.54	4.18
	9-2				0.17	0.2	31.87	65.71	334	-	42	1000.17	9.10	0.82	3.45
	1-1				0.4	0.22	31.42	65.93	396	184	28	1001.79	7.14	1.85	4.45
	5-2				0.48	0.22	32.09	66.72	326	123	28	999.79	10.94	3.26	3.6
JD09-2	10-1	2344 ± 80 Ma	3.10	0.12	0.76	0.23	30.78	62.75	543	729	1322	1000.09	12.96	1.13	7.04
	11-1				0.27	0.18	31.36	64.58	299	105	50	1001.48	7.24	2.14	3.3
	11-2				-0.31	0.19	31.32	64.54	299	105	50	1001.00	8.43	2.61	3.3
	2-1				1.01	0.18	31.31	63.55	473	363	1771	1003.79	29.57	28.77	5.59
	3-1				1.56	0.16	31.11	62.37	176	131	135	1000.66	15.97	2.64	2.08
	5-1				-1.34	0.17	31.64	64.07	-	131	1450	1000.89	16.57	12.24	
	6-1				1.13	0.18	31.79	63.59	828	210	943	1003.44	12.46	2.86	8.95
	8-1				1.84	0.16	31.74	64.50	617	834	764	999.83	11.49	4.99	8
	9-1				-0.18	0.20	31.66	62.47	176	-	200	1002.42	9.07	5.31	1.82
Loch a'Choin	1-1	2480 ± 17 Ma[d]	6.80	0.12	6.18	0.16	31.11	63.35	167	-	-	1005.72	3.11	26.14	1.73
	1-2				6.13	0.16	32.17	65.37	96	-	21	1005.77	3.12	22.49	1
	2-1				6.15	0.16	31.29	66.29	141	-	64	1004.61	4.30	1.66	1.45
	3-1				6.06	0.16	32.07	66.30	158	-	21	1004.60	4.36	9.76	1.64
	4-1				6.02	0.17	31.09	64.71	141	-	57	1006.62	2.03	24.48	1.45
	5-1				6.1	0.18	31.18	62.73	167	-	21	1005.78	3.77	3.45	1.73
	5-2				6.16	0.16	32.27	66.40	132	-	64	1004.87	5.13	5.70	1.36
	6-1				6.1	0.16	32.28	66.50	114	-	57	1005.94	3.14	7.34	1.18
	7-1				5.96	0.16	32.14	66.22	176	-	35	1005.18	3.91	7.30	1.82
	7-2				6.03	0.17	31.89	66.23	255	-	92	1005.53	3.87	5.47	2.63

Loch na-h	2-1	2395 ± 7.6 Ma[d]	5.43	0.12	-0.74	0.17	31.29	65.10	669	474	1686	996.68	21.44	1.16	7.84
	3-1				-3.73	0.17	31.29	65.10	202	-	-	1001.74	8.99	4.36	2.09
	3-1				-3.83	0.16	31.89	66.46	167	-	57	1001.73	8.11	1.80	1.73
	6-1				-3.05	0.16	31.66	65.86	705	562	457	997.28	15.47	4.98	8.37
	6-2				-2.19	0.16	31.14	63.45	1410	1643	4938	997.10	16.65	3.10	17.76
	7-1				-3.39	0.17	31.85	65.95	581	404	64	996.65	16.57	3.25	6.79
	9-1				-1.14	0.17	30.64	62.81	934	1256	2708	996.80	18.06	4.10	12.1
	1-1				0.06	0.16	31.08	64.80	819	746	1615	998.34	15.61	3.42	9.92
	2-2				-1.79	0.17	31.56	64.01	978	817	2658	996.24	22.16	1.15	11.69
Lochan Fearna	1-1	2367.7 ± 8.6 Ma[d]	4.83	0.12	1.61	0.19	32.12	66.30	370		250	998.41	19.30	3.26	3.82
	10-1				3.37	0.18	31.20	63.08	705	931	786	998.81	17.13	3.90	9.1
	11-1				2.08	0.18	32.01	65.66	440	193	50	1000.55	10.36	0.85	4.92
	12-1				3.6	0.16	30.68	63.64	855	1036	2451	99.06	20.33	1.72	10.85
	13-1				2.39	0.18	30.77	60.89	1216	562	1415	997.11	15.73	1.96	13.64
	3-1				2.84	0.17	31.12	62.87	1498	790	4481	999.17	15.53	2.12	17
	5-1				2.33	0.17	31.21	64.32	987	808	1665	997.61	18.72	2.22	11.76
	6-1				1.91	0.18	31.97	65.97	361	149	21	1001.29	9.10	2.00	4.02
	7-1				5.3	0.18	31.26	63.77	1163	1107	3480	996.43	31.35	3.85	14.17
	8-1				2.32	0.18	31.78	65.84	546	448	114	999.11	16.37	0.98	6.51
	9-1				3.6	0.17	30.46	63.05	1013	1590	2058	997.96	24.57	1.62	13.57
North Assynt	2-1	2540 ± 10 Ma[d]	6.00	0.12	6.62	0.16	32.15	66.90	264	114	50	998.84	13.91	8.68	2.95
	2-2				7.34	0.18	31.55	65.58	793	342	407	1000.69	9.99	0.59	8.85
	3-2				7.35	0.17	32.18	66.51	564	439	28	998.92	13.26	2.20	6.68
	4-1				6.13	0.16	32.12	66.88	405	131	35	999.41	10.20	1.55	4.44
	4-2				5.74	0.16	32.19	66.80	590	166	-	998.89	12.81	1.42	6.41
	5-1				6.78	0.18	31.65	66.03	722	342	464	997.82	14.50	1.55	8.12
	5-2				7.24	0.18	32.10	65.27	246	-	364	999.88	16.28	1.54	2.54
	6-1				7.13	0.17	32.16	66.82	476	281	-	1000.56	8.55	2.16	5.46
	6-2				7.19	0.17	32.11	66.49	290	254	21	1001.88	6.77	2.74	3.5
	7-1				6.44	0.16	31.88	66.03	828	360	214	998.80	12.66	2.44	9.25

NAPI	1-1	2043.8 ± 6.3 Ma	5.63	0.12	4.95	0.18	31.73	64.72	731	430	278	997.66	15.71	3.96	6.63
	10-1				4.76	0.17	31.72	65.30	528	369	57	999.70	11.34	0.74	4.88
	11-1				4.66	0.17	31.52	65.45	379	131	42	999.06	14.42	0.59	3.29
	11-2				4.82	0.18	31.67	64.79	423	-	42	997.59	13.49	0.71	3.43
	12-1				4.88	0.16	31.95	65.43	484	210	-	998.87	11.35	0.62	4.27
	13-1				4.79	0.16	31.89	65.48	343	114	28	1000.00	10.88	0.31	2.97
	13-2				4.8	0.18	31.11	63.44	555	210	28	999.08	12.88	0.40	4.84
	14-1				4.82	0.16	31.29	65.21	255	105	35	998.86	15.46	0.72	2.24
	2-1				4.91	0.16	31.97	63.98	634	386	28	1000.72	9.52	0.82	5.77
	2-2				4.84	0.17	32.05	65.49	246	114	28	1000.78	9.03	0.89	2.19
	3-1				5.11	0.16	31.44	64.05	881	623	514	998.58	15.06	1.36	8.16
	3-2				4.98	0.18	33.04	54.91	176	456	330	998.97	13.97	0.58	2.17
	4-1				4.76	0.18	31.93	65.13	414	158	21	1001.12	9.05	0.58	3.61
	4-2				4.85	0.18	31.32	64.85	317	149	28	1002.19	9.61	1.02	2.81
	5-1				4.68	0.17	31.24	64.92	423	140	21	1002.03	8.28	0.81	3.66
	5-2				4.66	0.18	31.53	64.94	308	-	35	999.60	9.76	0.76	2.5
	6-1				5.12	0.16	31.79	64.85	317	-	28	998.09	15.76	3.17	2.74
	7-1				4.73	0.17	31.46	65.07	572	307	42	998.80	13.41	1.84	5.14
	8-1				4.71	0.17	31.88	65.24	440	158	28	998.55	13.74	0.50	3.83
	8-2				4.8	0.16	32.07	66.20	423	202	21	997.49	15.53	0.69	3.76
	9-1				4.66	0.19	31.93	66.26	414	166		998.95	12.61	0.54	3.63
Poll Eorna	1-1	2396.8 ± 4.3 Ma[d]	3.68	0.12	3.57	0.17	31.06	63.70	1348	1045	3988	996.89	21.53	1.43	15.95
	10-1				3.92	0.17	30.97	62.89	1383	1660	4416	999.14	29.34	1.05	17.52
	10-2				3.69	0.21	32.07	65.76	458	166	50	999.46	10.30	1.82	5.05
	4-1				3.51	0.17	32.46	66.35	1084	623	2415	999.26	20.02	1.15	12.4
	5-1				3.7	0.17	31.64	64.77	1463	1203	4238	999.52	16.32	2.04	17.44
	5-2				3.71	0.19	31.37	63.65	1190	1124	4902	998.40	33.88	2.40	14.47
	6-1				4.34	0.21	31.08	62.67	652	175	293	1001.78	20.00	1.63	7.07
	7-2				3.65	0.19	32.16	66.23	722	360	914	997.83	29.81	0.60	8.16
	9-1				3.41	0.2	31.11	63.96	546	298	1922	1001.25	32.87	0.69	6.22
	9-2				3.78	0.22	31.94	65.93	1383	1660	4416	999.90	26.90	1.01	17.52
	1-2				4.68	0.22	31.06	63.70	352	105	35	1001.92	5.65	1.99	3.84
	2-1				3.67	0.22	32.32	65.95	308	166	92	1000.04	10.21	2.42	3.51
	2-2				3.57	0.19	32.41	66.03	334	237	-	1000.12	9.61	1.50	3.92
	3-1				3.58	0.19	32.17	66.52	440	123	1636	997.42	15.26	0.89	4.78
	3-2				3.58	0.19	32.35	66.36	370	166	-	1000.40	8.27	0.53	4.14
	7-1				4.93	0.24	32.23	65.84	528	193	1722	997.08	23.04	1.09	5.83
TEMORA[e]							32.18	66.35	262	-	-				
MUD TANK[e]							32.17	66.55	146	-	-				

a, 2σ uncertanty on the whole rock δ18O composition is based on the reproducibility of the standard garnets run during the same analytical session (UWG-2 δ18O 5.70 ± 0.12 ‰ 2σ, n=6)
b, values in weight %
c, values in ppm
d, ages from Davies and Heaman, (2014)
e, seondary standards for microprobe analysis, values are an average of 9 spots run during analytical session
-, below detection limit

Table 4.2. Raman and trace element data

Oxygen isotopes, trace elements and Raman band parameters from the Scourie zircons.

References

Ashton, K.E., Heaman, L.M., Lewry, J.F., Hartlaub, R.P., Shi, R., 1999. Age and origin of the Jan Lake Complex: a glimpse at the buried Archean craton of the Trans-Hudson Orogen. Canadian Journal of Earth Sciences 36, 185–208.

Ashwal, L.D,, Tucker, R.D., Zinner, E.K., 1999. Slow cooling of deep crustal granulites and Pb-loss in zircon. Geochimica et Cosmochimica Acta 63, 2839–2851. doi:10.1016/S0016-7037(99)00166-0.

Baumgartner, L.P., Valley, J.W., 2001. Stable Isotope Transport and Contact Metamorphic Fluid Flow. Reviews in Mineralogy and Geochemistry 43, pp 415-467.

Bindeman, I.N., Schmitt, A.K., Evans, D.A.D. 2010. Limits of hydrosphere-lithosphere interaction: origin of the lowest-known ^{18}O silicate rock on Earth in the Paleoproterozoic Karelian rift. Geology 38, 631–34. doi:10.1130/G30968.1.

Bindeman, I.N., Serebryakov, N.S., 2011. Geology, Petrology and O and H isotope geochemistry of remarkably ^{18}O depleted Paleoproterozoic rocks of the Belomorian Belt, Karelia, Russia, attributed to global glaciation 2.4 Ga. Earth and Planetary Science Letters 306, 163-174. doi:10.1016/j.epsl.2011.03.031.

Black, L.P., Kamo, S.L., Allen, C.M., Davis, D.W., Aleinikoff, J.N., Valley, J.W., Mundil, R., Campbell, I.H., Korsch, R.J., Williams, I.S., Fondoulis, C., 2004. Improved $^{206}Pb/^{238}U$ microprobe geochronology by the monitoring of a trace-element-related matrix fffect; SHRIMP, ID–TIMS, ELA–ICP–MS and oxygen isotope documentation for a series of zircon standards. Chemical Geology 205, 115–40.

Booth, A.L., Kolodny, Y., Chamberlain, C.P., McWilliams, M., Schmitt, A.K., Wooden, J,. 2005. Oxygen isotopic composition and U-Pb discordance in zircon. Geochimica et Cosmochimica Acta 69, 4895–4905.

Breeding, C.M., Ague, J.J., Grove, M., Rupke, A.L., 2004. Isotopic and chemical alteration of zircon by metamorphic fluids: U-Pb age depth-profiling of zircon crystals from Barrow's garnet zone, Northeast Scotland. American Mineralogist 89, 1067–1077.

Capitani, G.C., Leroux, H., Doukhan, J.C., Ríos, S,. Zhang, M., Salje, E.K.H., 2000. A TEM investigation of natural metamict zircons: structure and recovery of amorphous domains. Physics and Chemistry of Materials 27, 545-556.

Cartwright, I., Valley, J.W., 1991. Low-^{18}O Scourie dike magmas from the Lewisian Complex, Northwestern Scotland. Geology 19, 578-581.

Cartwright, I., Valley, J.W., 1992. Oxygen-isotope geochemistry of the scourian complex, Northwest Scotland. Journal of Geological Society 149, 115-125.

Cherniak, D.J., Watson, E.B., 2003. Diffusion in zircon. Reviews in Mineralogy and Geochemistry 53, pp 113-143.

Colombo, M., Chrosch, J., 1998. Annealing of natural metamict zircons. I low degree of radiation damage. Radiation Physics and Chemistry 55, 555-561.

Corfu, F., Hanchar, J.M., Hoskin, P.W.O., Kinny, P., 2003. Atlas of Zircon Textures. Reviews in Mineralogy and Geochemistry 53, pp 469-500.

Corfu, F., Heaman, L.M., Rogers, G., 1994. Polymetamorphic evolution of the Lewisian Complex, NW Scotland, as recorded by U-Pb isotopic compositions of zircon, titanite and rutile. Contributions to Mineralogy and Petrology 117, 215–28.

Davis, D.W., Krogh, T.E., 2001. Preferential dissolution of ^{234}U and radiogenic Pb from α-recoil-damaged lattice sites in zircon: implications for thermal histories and Pb isotopic fractionation in the near surface environment. Chemical Geology 172, 41-58.

Dawson, P., Hargreave, M.M., Wilkinson, G.R., 1971. The vibrational spectrum of zircon ($ZrSiO_4$). Journal of Physics C: Solid State Physics 4, 240-256.

Dillon, R., Woollam, J., Katkanant, V., 1984. Use of raman scattering to investigate disorder and crystallite formation in as-deposited and annealed carbon films. Physical Review B 29, 3482–3489. doi:10.1103/PhysRevB.29.3482.

Ewing, R.C., Chakoumakos, B.C., Lumpkin, G.R., 1987. The metamict state. Materials Research Society Bulletin 12, 58–66.

Ewing, R.C., Meldrum, A., Wang, L.M., Weber, W.J., Corrales, L.R., 2003. Radiation effects in zircon. Reviews in Mineralogy and Geochemistry 53, pp 387-425.

Geisler, T., Schleicher, H., 2000. Improved U–Th–Total Pb dating of zircons by electron microprobe using a simple new background modeling procedure and Ca as a chemical criterion of fluid-induced U-Th-Pb discordance in zircon. Chemical Geology 163, 269-285.

Geisler, T., Pidgeon, R.T., van Bronswijk, W., Pleysier, R., 2001a. Kinetics of thermal recovery and recrystallization of partially metamict zircon: a Raman spectroscopic study. European Journal of Mineralogy 13, 1163–1176. doi:10.1127/0935-1221/2001/0013-1163.

Geisler, T., Ulonska, M., Schleicher, H., Pidgeon, R.T., van Bronswijk, W., 2001b. Leaching and differential recrystallization of metamict zircon under experimental hydrothermal conditions.

Contributions to Mineralogy and Petrology 141 53–65. doi:10.1007/s004100000202.

Geisler, T., 2002. Isothermal annealing of partially metamict zircon: evidence for a three-stage recovery process. Physics and Chemistry of Minerals 29, 420–429. doi:10.1007/s00269-002-0249-3.

Geisler, T., Pidgeon, R., van Bronswijk, W., Kurtz, R., 2002. Transport of uranium, thorium, and lead in metamict zircon under low-temperature hydrothermal conditions. Chemical Geology 191, 141–154. doi:10.1016/S0009-2541(02)00153-5.

Geisler, T., Trachenko, K., Ríos, S., Dove, M.T., Salje, E.K.H., 2003a. Impact of self-irradiation damage on the aqueous durability of zircon ($ZrSiO_4$): implications for its suitability as a nuclear waste form. Journal of Physics: Condensed Matter 15, 597–605. doi:10.1088/0953-8984/15/37/L07.

Geisler, T., Pidgeon, R.T., Kurtz, R., van Bronswijk, W., Schleicher, H., 2003b. Experimental hydrothermal alteration of partially metamict zircon. American Mineralogist 88, 1496–1513.

Geisler, T., Rashwan, A.A., Rahn, M.K.W., Poller, U., Zwingmann, H., Pidgeon, R.T., Schleicher, H., Tomaschek, F., 2003c. Low-hemperature hydrothermal alteration of natural metamict zircons from the Eastern desert, Egypt. Mineralogical Magazine 67, 485–508. doi:10.1180/0026461036730112.

Geisler, T., Schaltegger, U., Tomaschek, F., 2007. Re-equilibration of zircon in aqueous fluids and melts. Elements 3, 43–50.

Goodenough, K.M., Millar, I., Strachan, R.A., Krabbendam, M., Evans, J.A., 2011. Timing of regional deformation and development of the Moine Thrust zone in the Scottish Caledonides: constraints from the U-Pb geochronology of alkaline intrusions. Journal of the Geological Society 168, 99–114. doi:10.1144/0016-76492010-020.

Hansen, B.T., Friderichsen, J.D., 1989. The influence of recent lead loss on the interpretation of disturbed U-Pb systems in zircons from igneous rocks in East Greenland. Lithos 23, 209-223.

Hay, D.C., Dempster, T.J., Lee, M.R., Brown, D.J., 2009. Anatomy of a low temperature zircon outgrowth. Contributions to Mineralogy and Petrology 159, 81–92. doi:10.1007/s00410-009-0417-2.

Heaman, L.M., Tarney, J., 1989. U-Pb baddeleyite ages for the Scourie dyke swarm, Scotland: evidence for two distinct intrusion events. Nature 340, 705–708.

Heaman, L.M., Bowins, R., Crocket, J., 1990. The chemical composition of igneous zircon suites: implications for geochemical tracer studies. Geochimica et Cosmochimica Acta 54, 1597–1607.

Holdsworth, R.E., Alsop, G.I., Strachan, R.A., 2007. Tectonic stratigraphy and structural continuity of the northernmost Moine Thrust zone and Moine nappe, Scottish Caledonides. Geological Society London Special Publications 272, 121–142. doi:10.1144/GSL.SP.2007.272.01.08.

Holland, H.D., Gottfried, D., 1955. The effect of nuclear radiation on the structure of zircon. Acta Crystallographica 8, 291–300. doi:10.1107/S0365110X55000947

Hoskin, P.W.O., Rodgers, K.A., 1996. Raman spectral shift in the isomorphous series (Zr1-xHfx) SiO_4. European Journal of Solid State Inorganic Chemistry 33, 1111-1121.

Hoskin, P.W.O., 2000. Identifying accessory mineral saturation during differentiation in granitoid magmas: an integrated approach. Journal of Petrology 41, 1365–1396.

Hoskin, P.W.O., Black, L.P., 2002. Metamorphic zircon formation by solid-state recrystallization of protolith igneous zircon. Journal of Metamorphic Geology 18, 423–439.

Hoskin, P.W.O., Schaltegger, U., 2003. The composition of zircon and igneous and metamorphic petrogenesis. Reviews in Mineralogy and Geochemistry 53, pp 27-62.

Ickert, R.B., Stern, R.A., 2013. Matrix corrections and error analysis in high-precision SIMS $^{18}O/^{16}O$ measurements of Ca-Mg-Fe garnet. Geostandards and Geoanalytical Research 1-20

Kieffer, S.W., 1982. Thermodynamics and lattice vibrations of minerals: Applications to phase equilibria, isotopic fractionation, and high-pressure thermodynamic properties. Reviews of geophysics and space physics 20: 827-849.

Kinny, P.D., Friend, C.R.L., 1997. U-Pb isotopic evidence for the accretion of different crustal blocks to form the Lewisian complex of northwest Scotland. Contributions to Mineralogy and Petrology 129, 326–340.

Krogh, T.E., 1982. Improved accuracy of U-Pb zircon ages by the creation of more concordant systems using an air abrasion technique. Geochimica et Cosmochimica Acta 46, 637–649.

Liu, J., Zhang, L., 2013. Neoproterozoic low to negative $\delta^{18}O$ volcanic and intrusive rocks in the Qinling mountains and their geological significance. Precambrian Research 230, 138–167. doi:10.1016/j.precamres.2013.02.006.

Meldrum, A., Boatner, L.A., Zinkle, S.J., Wang, S., Wang, L., Ewing, R.C., 1999. Effects of dose rate and temperature on the crystalline-to-metamict transformatton in the ABO_4 orthosilicates. The Canadian Mineralogist 37, 207–221.

Moser, D.E., Cupelli, C.L., Barker, I.R., Flowers, R.M., Bowman, J.R., Wooden, J., Hart, J.R., 2011. New zircon shock phenomena and their use for dating and reconstruction of large impact structures revealed by electron nanobeam (EBSD, CL, EDS) and isotopic U-Pb and (U-Th)/He analysis of the Vredefort Dome . Canadian Journal of Earth Sciences 48, 117–139.

Muehlenbachs, K, Kushiro, I., 1975. Measurements of oxygen diffusion in silicates. EOS Transaction of the American Geophysical Union 56, 549.

Murakami, T., Chakoumakos, B.C., Ewing, R.C., Lumpkin, G.R., Weber, W.J., 1991. Alpha-decay event damage in zircon. American Mineralogist 76, 1–23.

Nasdala, L., Irmer, G., Wolf, D., 1995. The degree of metamictization in zircons: a Raman spectroscopic study. European Journal of Mineralogy 7, 471–478.

Nasdala, L., Pidgeon, R.T., Wolf, D., Irmer, G., 1998a. Metamictization and U-Pb isotopic discordance in single zircons: a combined Raman microprobe and SHRIMP ion probe study. Mineralogy and Petrology 62, 1–27. doi:10.1007/BF01173760.

Nasdala, L., Götze, J., Pidgeon, R.T., Kempe, U., Seifert, T., 1998b. Constraining a SHRIMP U-Pb age: micro-scale characterization of zircons from Saxonian Rotliegend rhyolites. Contributions to Mineralogy and Petrology 132, 300–306.

Nasdala, L., Wenzel, T., Pidgeon, R.T., Kronz, A., 1999. Internal structures and dating of complex zircons from Meissen Massif monzonites, Saxony. Chemical Geology 156, 331-341.

Nasdala, L, Wenzel, M., Vavra, G., Irmer, G., Wenzel, T., Kober, B., 2001. Metamictisation of natural zircon: accumulation versus thermal annealing of radioactivity-induced damage. Contributions to Mineralogy and Petrology 141, 125–144. doi:10.1007/s004100000235.

Nasdala, L., Lengauer, C.L., Hanchar, J.M., Kronz, A., Wirth, R., Blanc, P., Kennedy, A.K., and Seydoux-Guillaume, A-M., 2002. Annealing radiation damage and the recovery of cathodoluminescence. Chemical Geology 191, 121–40. doi:10.1016/S0009-2541(02)00152-3.

Nasdala, L., Reiners, P.W., Garver, J.I., Kennedy, A.K., Stern, R.A., Balan, E., Wirth, R., 2004. Incomplete retention of radiation damage in zircon from Sri Lanka. American Mineralogist 89: 219–231.

Nasdala, L., Kronz, A., Hanchar, J.M., Tichomirowa, M., Davies, D.W., Hofmeister, W., 2006. Effects of natural radiation damage on back-scattered electron images of single crystals of minerals. American Mineralogist 91: 1739-1746.

Nemchin, A.A., Pidgeon, R.T., 1997. Evolution of the Darling range batholith, Yilgarn craton, western Australia: a SHRIMP zircon study. Journal of Petrology 38, 625–649.

Nicola, J.H., Rutt, H.N., 1974. A comparative study of zircon ($ZrSiO_4$) and hafnon ($HfSiO_4$) Raman spectra. Journal of Physics C: Solid State Physics 7, 1381-1386.

Page, F.Z., Ushikubo, T., Kita, N.T., Riciputi, L.R., Valley, J.W., 2007. High-precision oxygen

isotope analysis of picogram samples reveals 2μm gradients and slow diffusion in zircon. American Mineralogist 92, 1772–1775. doi:10.2138/am.2007.2697.

Palenik, C.S., Nasdala, L., Ewing, R.C., 2003. Radiation damage in zircon. American Mineralogist 88, 770-781.

Pidgeon, R.T., 1992. Recrystallisation of oscillatory zoned zircon: some geochronological and petrological implications. Contributions to Mineralogy and Petrology 110, 463–472.

Pidgeon, R.T., O'Neil, J.R., Silver, R.T. 1995. The interdependence of U-Pb stability, crystallinity and external conditions in natural zircons ± an early experimental study. Leon T Silver 70th Birthday Symposium and Celebration. Extended abstracts, pp 225-231

Pidgeon, R.T., Nemchin, A.A., Cliff, J., 2013. Interaction of weathering solutions with oxygen and U–Pb isotopic systems of radiation-damaged zircon from an Archean granite, Darling Range batholith, western Australia. Contributions to Mineralogy and Petrology 166, 511–523. doi:10.1007/s00410-013-0888-z.

Pidgeon, R.T., 2014. Radiation damage ages. Chemical Geology 367, 13-33. doi:10.1016/j.chemgeo.2013.12.010.
Podor, Renaud. 1995. Raman Spectra of the Actinide-Bearing Monazites.

Putnis, A., 2002. Mineral replacement reactions: from macroscopic observations to microscopic mechanisms. Mineralogical Magazine 66, 689–708. doi:10.1180/0026461026650056.

Putnis, C.V., Tsukamoto, K., Nishimura, Y,. 2005. Direct observations of pseudomorphism: compositional and textural evolution at a fluid-solid interface. American Mineralogist 90, 1909–1912. doi:10.2138/am.2005.1990.

Rayner, N., Stern, R.A., Carr, S.D., 2005. Grain-scale variations in trace-element composition of fluid-altered zircon, Acasta gneiss complex, northwestern Canada. Contributions to Mineralogy and Petrology 148, 721–734. doi:10.1007/s00410-004-0633-8.

Ríos, S., Salje, E.K.H., Zhang, M., Ewing, R.C., 2000. Amorphization in zircon: evidence for direct impact damage. Journal of Physics: Condensed Matter 12, 2401–2412. doi:10.1088/0953-8984/12/11/306.

Rizvanova, N.G., Levchenkov, O.A., Belous, A.E., 2000. Zircon reaction and stability of the U-Pb isotope system during interaction with carbonate fluid: experimental hydrothermal study. Contributions To Mineralogy and Petrology 139, 101-114.

Rollinson, H., 2012. Geochemical constraints on the composition of Archaean lower continental crust partial melting in the Lewisian granulites. Earth and Planetary Science Letters 351-352, 1–12.

doi:10.1016/j.epsl.2012.07.018.

Salje, E.K.H., Chrosch, J., Ewing, R.C., 1999. Is 'metamictization' of zircon a phase transition? American Mineralogist 84, 1107–1116.

Schaltegger, U., Fanning, C.M., Günther, D., Maurin, J.C., Schulmann, K., Gebauer, D., 1999. Growth, annealing and recrystallization of zircon and preservation of monazite in high-grade metamorphism: conventional and in-situ U-Pb isotope, cathodoluminescence and microchemical evidence. Contributions to Mineralogy and Petrology 134, 186–201.

Shannon, R., 1976. Revised effective ionic radii and systematic studies of interatomic distances in halides and chalcogenides. Acta Crystallographica Section a: Crystal Physics 32, 751-767.

Simonetti, A., Heaman, L.M., Hartlaub, R.P., Creaser, R.A., MacHattie, T.G., Böhm, C., 2005. U–Pb zircon dating by laser ablation-MC-ICP-MS using a new multiple ion counting Faraday collector array. Journal of Analytical Atomic Spectrometry 20, 677–686. doi:10.1039/b504465k.

Stern, R.A., Bodorkos, S., Kamo, S.L., Hickman, A.H., Corfu, F., 2009. Measurement of SIMS instrumental mass fractionation of Pb isotopes during zircon dating. Geostandards and Geoanalytical Research 33, 145–168.

Tanabe, K., Hiraishi, Jiro., 1980. Correction of finite slit width effects on Raman line widths. Spectrochimica Acta Part a: Molecular Spectroscopy 36, 341–344.

Tarney, J., 1973. The Scourie dyke suite and the nature of the Inverian event in Assynt, in: The Early Precambrian of Scotland and Related Rocks of Greenland, Park, R.G., and Tarney, J., eds. pp. 105-118, 1973.

Tarney, J., Weaver, B.L., 1987. Mineralogy, petrology and geochemistry of the Scourie dykes: petrogenesis and crystallization processes in dykes intruded at depth. Geological Society London Special Publications 27, 217-233.

Taylor, H.P., Sheppard, S.M.F., 1986. Igneous rocks 1: processes of isotopic fractionation and isotopic systematics. in: Valley, J.W., Taylor, H.P., and O'Neill, J.R., (eds) Stable isotopes in High Temperature Geological Processes, Reviews in Mineralogy 16. Washington, D.C.: Mineralogical Society of America, 227-271.

Tomaschek, F., Kennedy, A.K., Villa, I.M., Lagos, M., Ballhaus, C., 2003. Zircons from Syros, Cyclades, Greece—recrystallization and mobilization of zircon during high-pressure metamorphism. Journal of Petrology 44, 1977–2002. doi:10.1093/petrology/egg067.

Trachenko, K.O., 2004. Understanding resistance to amorphization by radiation damage Journal of Physics: Condensed Matter 16, 1491-1515.

Trachenko, K.O., Dove, M.T., Salje, E.K.H., 2001. Atomistic modelling of radiation damage in zircon. Journal of Physics: Condensed Matter 13, 1947–1959. doi:10.1088/0953-8984/13/9/317.

Trachenko, K.O., Dove, M.T., Salje, E.K.H., 2002. Structural changes in zircon under α-decay irradiation. Physical Review B 65, 180102R. doi:10.1103/PhysRevB.65.180102.

Valley, J.W., Lackey, J.S., Cavosie, A.J., Clechenko, C.C., Spicuzza, M.J., Basei, M.A.S., Bindeman, I.N., Ferreira, V.P,. Sial, A.N., King, E.M., Peck, W.H., Sinha, A.K., Wei, C.S., 2005. 4.4 billion years of crustal maturation: oxygen isotope ratios of magmatic zircon. Contributions to Mineralogy and Petrology 150, 561–580. doi:10.1007/s00410-005-0025-8.

Valley, J.W., 2001. Stable isotope thermometry at high temperatures. Reviews in Mineralogy and Geochemistry 43, pp 365-413

Valley, J.W., 2003. Oxygen isotopes in zircon. Reviews in Mineralogy and Geochemistry 53, pp 343-385.

Valley, J.W., Chiarenzelli, J.R., McLelland, J.M., 1994. Oxygen isotope geochemistry of zircon. Earth and Planetary Science Letters 126, 187–206.

Valley, J.W., Kitchen, N., Kohn, M.J., Niendorf, C.R., Spicuzza, M.J., UWG-2, a garnet standard for oxygen isotope ratios: Strategies for high precision and accuracy with laser heating. Geochimich et Cosmochimica Acta 59, 5223-5231.

Valley, J.W., Cole, D.R., 2003. Stable isotope geochemistry (eds), Reviews in Mineralogy and geochemistry, Vol 43.

Weaver, B.L., Tarney, J., 1981. The Scourie dyke suite: petrogenesis and geochemical nature of the Proterozoic sub-continental mantle. Contributions to Mineralogy and Petrology 78, 175–188.

Weber, W.J., Ewing, R.C., Wang, L-M., 1994. The radiation-induced crystalline-to-amorphous transition in zircon. Journal of Materials Research 9, 688–698.

Whitehouse, M.J., Kemp, A.I.S., 2010. On the difficulty of assigning crustal residence, magmatic protolith and metamorphic ages to Lewisian granulites: constraints from combined in situ U–Pb and Lu–Hf isotopes. Geological Society London Special Publications 335, 81–101. doi:10.1144/SP335.5.

Wiechert, U., Halliday, A.N., Lee, D.C., Snyder, G.A., Taylor, L.A., Rumble, D., 2001. Oxygen isotopes and the moon-forming giant impact. Science 294, 345-348.

Wopenka, B, Jolliff, B.L., Zinner, E., Kremser, D.T., 1996. Trace-element zoning and incipient metamictization in a lunar zircon: application of three microprobe techniques. American Mineralogist

81, 902–912.

Yuan, H.L., Gao, S., Dai, M.N., Zong, C.L., Günther, D., 2008. Simultaneous determinations of U–Pb age, Hf isotopes and trace-element compositions of zircon by Excimer laser-ablation quadrupole and multiple-collector ICP-MS. Chemical Geology 247, 100-118.

Zhang, M., Salje, E.K.H., Farnan, I., Graeme-Barber, A., Daniel, P., Ewing, R.C., Clark, A.M., Leroux, Hugues., 2000a. Metamictization of zircon: Raman spectroscopic study. Journal of Physics: Condensed Matter 12, 1915-1925.

Zhang, M., Salje, E.K.H., Capitani, G.C., Leroux, H., Clark, A.M., Schlüter, J., Ewing, R.C., 2000b. Annealing of alpha-decay damage in zircon: a Raman spectroscopic study. Journal of Physics: Condensed Matter 12, 3131-3148. doi:10.1088/0953-8984/12/8/333.

Zhu, Z.K., O'Nions, R.K., Belshaw, N.S., Gibb, A.J. 1997. Lewisian crustal history from in situ SIMS mineral chronometry and related metamorphic textures. Chemical Geology 136, 205

Chapter 5: Geochemical insights into the origin of the Scourie dykes from trace-element modeling.

5.1. Introduction

The Scourie dykes are found throughout the Lewisian Gneiss Complex (LGC) of northwest Scotland. They have been extensively studied in the area around the town of Scourie in the Assynt terrane, mostly due to minimal metamorphic overprinting in this area. However, the dykes also occur in the Rhiconnic, Gruinard, Gairloch, Tarbert and Uist terranes, as well as the islands of Tiree and Coll (Tarney, 1973; Kinny et al, 2005; Goodenough et al. 2010; Chapter 3,4)

The Scourie dykes have traditionally been split both petrologically and geochemically into two broad groups, one containing picritic and noritic dykes, and the other containing dykes of doleritic and olivine gabbro compositions (Tarney, 1973; Weaver and Tarney, 1981a). Most of the dykes in the Scourie swarm are doleritic, the other compositions are relatively rare with the olivine gabbro dykes only identified in a small area around the town of Strathan (Tarney, 1973; Weaver and Tarney, 1981a; Chapter 3). Both groups have enriched (relative to Primitive Mantle) trace element contents although the ultramafic dykes (picrite and norite) have more fractionated trace element patterns and lower heavy rare earth element (HREE) concentrations (Weaver and Tarney, 1981a; Tarney and Weaver, 1987a). Trace-element ratios from the dykes have been used as evidence that the two groups originated from different magmas, rather than one magma that underwent fractional crystallization. For example, the mafic dykes (dolerites and olivine gabbros) have La/Nb and Zr/Nb ratios of ~15 and ~1 respectively, whereas the ultramafic dykes have ratios of ~25 and ~4

(Weaver and Tarney, 1981a). Both of these ratios are thought to vary due to source composition rather than fractionation processes and therefore suggests that the two dyke groups originated from separate magmas.

The geochemical signatures in the dykes could potentially be obscured by crustal contamination. However, field observations from the dykes indicate that they all have sharp margins (where visible) with the surrounding tonalite-trondhjemite-granodiorite (TTG) gneissic rocks of the LGC. Also, no crustal xenoliths have been observed in any of the dykes. The TTGs in the Assynt terrane of the LGC (see Chapter 3) also have distinctive geochemical signatures with extreme depletions in Th and U (Weaver and Tarney, 1981b, Tarney and Weaver, 1987b; Rollinson, 1996; 2012). Trace element modeling has indicated that the compositions of the dykes cannot be recreated by assimilation of Assynt terrane TTGs however, assimilation of rocks from other terranes or from crustal rocks at depth has not been considered (Weaver and Tarney, 1981a; Tarney and Weaver, 1987a).

In fresh dykes where the contact with the LGC is exposed, the minerals at the contact are relatively coarse which suggests that dykes intruded hot country rock and the present levels of erosion have exposed mid (most of the LGC) to lower crust (Assynt terrane, O'Hara, 1961; 1962; Tarney, 1963; Coward and Park, 1987). Equilibrium oxygen isotopic fractionation from the minerals in the dykes around the town of Scourie suggest crystallization temperatures of ~600 °C (Cartwight and Valley, 1991). Also, amphibole-plagioclase thermometry conducted during this study from the dykes (using the equations from Holland and Blundy, 1994) suggests that these minerals equilibrated at ~800-600 °C (Table 5.1; Appendix B).

After the intrusion of the dykes (between ~2.4 and ~2 Ga, Heaman and Tarney, 1989;

Chapter 3;4), the dykes experienced a number of metamorphic events. The first was the Laxfordian amphibolite grade metamorphic event at 1.9-1.7 Ga (Corfu et al. 1994). The effects of the Laxfordian were quite variable throughout the LGC, most of the mainland experienced pervasive amphibolite grade reworking, although the Assynt terrane only experienced high degrees of fluid flow and amphibolite grade metamorphism in discrete shear zones. The Laxfordian event caused isotopic disturbance in the dykes with many of the dykes recording young Sm-Nd ages (Waters et al. 1990). After the Laxfordian event, the LGC was involved in the Caledonian orogeny, which caused hydrous alteration of the Scourie dykes and high degrees of lead loss in the Scourie dyke zircons (Chapter 3; Chapter 4). Fluids associated with the Caledonian orogeny have had less of an impact on the TTG gneisses as the zircons from these rocks typically record concordant U-Pb ages (e.g. Whitehouse and Kemp, 2010). U-Pb discordance in the zircons from the TTGs is often related to Laxfordian lead loss rather than Caledonian (Kinny and Friend, 1997; Friend and Kinny, 2001). The history of tectonic activity that the dykes have experienced has resulted in many of the dykes being completely metamorphosed, with little to no igneous minerals present (see Chapter 3).

New geochemical data for the Scourie dykes is presented using updated analysis techniques involving multi acid digestions, and Quad-ICP-MS trace element analysis. Major elements were measured by X-ray fluorescence on Li-Borate fused pucks. Typical detection limits were ~0.01 ppm for most trace elements, with results from standard analysis typically ± 5% from the recommended value (Table 5.1). Dykes are sampled from three of the terranes in the LGC, the Assynt and Gruninard terranes from the mainland, and the Tarbert terrane in the Outer Hebredies (See Chapter 3 for locations of the terranes), with 36 samples analyzed (Table 5.1).

5.2. Results

The geochemical data for 28 dykes from the Scourie dyke swarm are presented in Table 5.1. The dykes investigated in this study have been subdivided into two geochemical groups; one called 'ultramafic' containing the picrite and olivine gabbroic dykes of Tarney and Weaver (1973), the other group is called 'mafic', containing the dolerite and noritic dykes. The two groups are used rather than splitting the samples into the four petrographic groups defined previously partly for simplicity, and partly due to difficulties identifying the original mineralogy of metamorphosed dykes.

The metamorphic overprinting that many of the dykes have experienced can cause element mobility and this needs to be assessed before the geochemical data can be interpreted. Elemental mobility is especially important to characterize given the isotopic disturbances shown by the dykes in Sm-Nd isochrons (Waters et al. 1990) and zircon Pb loss (Chapter 3; 4). The elements typically considered robust or immobile during alteration are the high field strength elements (HFSE), Zr, Nd, Ti, U, Th, Hf and rare earth elements (REE), whereas large ion lithophile (LILE), elements Cs, Rb, K, Ba are most likely to be mobilized (Cann, 1970; Floyd and Winchester, 1978). The chemical index of alteration (CIA) and loss on ignition (LOI) are indicators of the degree of element mobility and alteration (Nesbitt and Young, 1982; Babechuk and Kamber, 2011). These indicators roughly co-vary in the Scourie dykes indicating that there has been some element mobility (Fig. 5.1). All samples have LOI <5 wt. % and CIA < 60 which generally reflects of low degree of alteration in rocks of such antiquity (Babechuk and Kamber, 2011). There is a poorly defined inverse correlation between LOI and CaO, which likely is related to the breakdown of plagioclase, however there is no systematic relationship between LOI and the HFSE ratios used to determine the origin of the dykes (Fig. 5.1). The lack of relationship

between the HFSE and LOI or CIA, suggests that these elements may have remained undisturbed during the alteration/metamorphism the dykes experienced.

Total alkalis verses silica (TAS) classification of the dykes (Fig. 5.2; Le Bas et al., 1986) shows that the ultramafic dykes are low in $Na_2O + K_2O$ (~2 wt.%) but unusually high in SiO_2 up to 50% with some samples falling into the field of basalt. The mafic dykes have higher alkali contents, up to ~6%, and trend towards more alkaline compositions with 3 samples falling into the trachy-basalt field, although most fall within the basalt field.

Multi-element variation diagrams for the different dyke groups highlight the geochemical differences between them (Fig. 5.3). The mafic dykes have moderately fractionated REE profiles with La/Yb of between 1.74 and 10 (Fig. 5.3b). These dykes also have variably negative anomalies in the HFSE Zr, Hf and Ti relative to primitive mantle (McDonough and Sun, 1995), and a small negative anomaly in Nb. The ultramafic dykes have similar HFSE anomalies with the most pronounced being large negative Nb and Ti anomalies with no corresponding Zr and Hf anomaly. Sr is also depleted in the ultramafic dykes and they are more fractionated than the mafic dykes, notably more light rare earth element (LREE) enriched, with La/Yb ratios between 4.18 and 16.3.

Trace element variation diagrams (Fig. 5.4) also highlight the differences between the two dyke suites. Trace element ratios are plotted relative to Nb and Th, these elements are chosen since they are relatively immobile moderately incompatible elements (Larson and Gottfried, 1960; Hoffman et al. 1986). Nb and Th are also relatively immobile during metamorphism and hydrothermal alteration (Rubin et al., 1993) and are therefore likely to provide insights into the original magmatic compo-

sition. Thorium also can be used as an indicator of the degree of fractional crystallization (Larson and Gottfried, 1960).

The Zr/Nb ratios of the two groups are distinctly different (~24 for ultramafic, and ~15 for mafic), as are the Zr/Y and Ti/Zr ratios. The Sr/Y ratios for the two dyke groups overlap, although the ultramafic samples trend towards higher values. Rare earth element (REE) ratios are also different between the two groups, with the ultramafics typically producing higher values at lower Nb and Th contents.

The trace element variation diagrams also indicate that there are no systematic differences between the dyke compositions on the different terranes. Also the exact ages of all of the dykes are not known, the results from Chapter 3 suggest that the majority of the dykes are ~2.4 Ga. Only two dykes currently have ages ~2.0 Ga, the geochemistry for one of these dykes (the NAPI dyke from Chapter 4) is highlighted with a circle (Fig. 5.4) and is not significantly different in chemistry from the other mafic dykes. Therefore, it appears that elemental chemistry may not be useful in estimating dyke age.

5.3. Discussion

5.3.1 Geochemical model

The Scourie dykes have geochemical signatures, which indicate that they did not originate from a typical mantle source like depleted mantle or primitive mantle. They are enriched in trace elements and depleted in some HFSE but require a moderate to high degree of partial melting of their source to obtain their basaltic and ultramafic SiO_2 and MgO contents. Here we attempt to generate the trace element composition

of the dykes through modeling the composition of melts produced from the mantle, and then crystalizing those melts in the crust and simultaneously assimilating crustal material from the LGC. Attempting to recreate the trace element characteristics of the dykes in this way can lead to insights into the origin and evolution of the dyke magmas. The geochemical model can then be coupled with the oxygen isotopic data from the dykes (Chapter 4) and the geochronology (Chapter 3) to fully constrain the geological history of the dykes.

Normalized multi-element variation diagrams (Fig. 5.3) and element variation diagrams (Fig. 5.4), both indicate that the compositions of the two dyke groups are distinctly different. Both geochemical groups (mafic and ultramafic) show differences in trace element ratios plotted against Th and Nb suggesting that the magmas are compositionally different rather than reflecting fractionation of a single magma.

The idea that the Scourie dykes originated from two different magmas was first proposed by Weaver and Tarney (1981a; 1987a). These authors used differences in Zr/Nb and La/Nb trace element ratios to argue that the two dyke groups were from different mantle sources. They used the negative Th and U anomalies characteristic of the TTG gneisses of the Assynt terrane (Weaver and Tarney, 1981b; Tarney and Weaver, 1987b) as evidence that the dykes did not assimilate crustal material during their ascent, as the dykes are enriched in these elements, however they only considered contamination with TTGs from the Assynt terrane. The trace element compositions of the dykes were therefore thought to reflect two anomalously enriched mantle sources, each sampled by individual dyke groups.

Recent geochemistry from the TTG gneisses of the Gruinard terrane (Rollinson, 1996; 2010) has indicated that these gneisses do not have depletions in Th and U

and therefore may be a better candidate for the geochemical nature of the local crust during assimilation. Broadly speaking, the incompatible element data presented here suggests that there is no difference between the dykes emplaced within the Assynt, Gruinard or Tarbert terranes (Fig. 5.4). Therefore suggesting that assimilation of the TTGs cannot occur during the emplacement of the dykes based only on the composition of the TTGs in the Assynt terrane may be incorrect. We explore this possibility through geochemical modeling of the dykes assuming that both dyke types originated from the same geochemical source but assimilated different crustal material. Using the same geochemical source for the dykes represents the opposite end member to the petrogenetic model of Weaver and Tarney (1981a) and Tarney and Weaver (1987a), as their models employed different mantle source compositions and no crustal assimilation.

The model used here involves melting of an asthenospheric or primitive mantle (McDonough and Sun, 1995) source, then contamination of the melt through an assimilation-fractional-crystallization (AFC) process (DePaolo, 1981). The AFC model assumes a constant ratio between the rate of crystallization (r_c) and the rate of assimilation (r_a), which may not always be the case, especially in MASH (melting-assimilation-storage-homogenization) zones at the base of the crust (Cribb and Barton, 1996; Dufek and Bergantz, 2005). However, the element ratios used here are relatively immune to the effects of decoupling the r_a/r_c and there is very little difference between AFC and the FCA model of Cribb and Barton (1996), which takes variations in r_a/r_c into account. Therefore, only AFC models are presented for clarity. The mafic melts are modeled using primitive mantle (McDonough and Sun, 1995) as a starting composition and olivine (40%), orthopyroxene (30%), clinopyroxene (20%), amphibole (5%), and plagioclase (5%) as the crystallizing/fractionating phases. An R value (r_a/r_c) of 0.3 was used and F values (relative amount of magma remaining) range from 1

to 0.46. The assimilated component was high- (and low-) titanium amphibolite from the Gruinard terrane (Rollinson, 1996). The ultramafic magmas are also modeled using primitive mantle as the starting material with olivine (65%), orthopyroxene (20%) and clinopyroxene (15%) as the fractionating phases. An R value of 0.3 and F from 1 to 0.6 were used to represent the large degree of partial melt experienced by these dykes. The assimilant used was tonalite from the Gruinard terrane (Rollinson, 1996). The partition coefficients from McKenzie and O'Nions (1991), Fujimaki et al., (1994), Foley et al., (1996), Green et al., (2000), and Zanetti et al., (2004) were used for olivine, orthopyroxene, clinopyroxene, garnet, plagioclase and amphibole. The numerical computations were conducted using the model from Ersoy and Helvacı (2010).

Many different assimilants were tested, but the amphibolites from the Gruinard terrane are preferred in the mafic model due to their slight enrichement in trace elements relative to the mafic dykes and very similar incompatible element ratios. Therefore assimilation of this material by a melt from primitive mantle easily produces geochemical patterns similar to the dykes. Tonalites are the preferred assimilant for the ultramafic dykes because of their higher SiO_2 contents, which explains the high SiO_2 in the picritic dykes, and also their highly fractionated trace element profiles which matches well with the ultramafic dykes. Neither the ultramafic or mafic dyke trace element signatures could be recreated by assimilating other crustal material from the Lewisian.

The results from the AFC modeling are shown in Figs. 5.3 and 5.4. It is clear from Fig. 5.3 that the general trace element characteristics for both the mafic and ultramafic dykes can be modeled successfully using this method. The troughs in Zr and Ti in the mafic dykes can easily be achieved by assimilating low Ti and Zr amphibolites

from the Gruinard terrane, whereas most of the other trace elements match perfectly. The model for the ultramafic dykes fits relatively well although the model does not replicate the large trough in Nb seen in the dykes. The AFC model also produces a positive Sr anomaly, which is not present in the dykes. REE trends in the dykes are reproduced well by both models.

Trace element variation diagrams (Fig. 5.4) also show some good correlations between the data and the proposed petrogenetic model. The fits between the modeled AFC trends and the dyke data are not perfect, but mostly follow the same general trends. There is likely to be excessive scatter in the dyke data sets due to some elemental redistribution during metamorphism (discussed above; Fig. 5.1). The trace element ratios chosen were designed to minimize this effect however some excessive scatter is clearly observed.

The worst model fit is shown by the Zr/Nb vs Nb graph, which reproduces the mafic data relatively well, but can not reproduce the high Zr/Nb of the ultramafic dykes. The Zr/Nb ratio should vary mostly due to source composition (Ketchum, et al., 2013), which suggests that the chosen primitive mantle composition may not be the perfect source for the ultramafic dykes. The mafic trend is also not recreated well in the Zr/Y vs Nb plot where as the model fits the ultramafic data well.

The modeling presented here indicates that the trace element geochemistry of the dykes can be explained by melting of a primitive mantle source and an AFC process involving assimilation of two different crustal components. Both of the components used are present in the LGC, but neither is present at surface in the Assynt terrane.

5.3.2 Isotopic constraints on the petrogenesis of the dykes

New geochemical data for the Scourie dykes presented in Chapter 4 indicates that the ~2.4 Ga mafic dykes have variable oxygen isotopic compositions, all of which are well below the mantle $\delta^{18}O$ of ~5.5 ‰ (Mattey et al., 1994), down to ~ -3 ‰. The oxygen isotopic composition of the ultramafic dykes is currently unknown as these dykes do not contain zircon. The ultramafic dykes contain baddeleyite but baddeleyite oxygen isotopic analysis by SIMS is in its infancy (see Chapter 2). Therefore, this section of the discussion concentrates on the mafic dykes.

The low $\delta^{18}O$ values found in the mafic dykes can only be produced two ways; 1) through subsolidus interaction with very low $\delta^{18}O$ meteoric water, or 2) through assimilation of low $\delta^{18}O$ material that previously interacted with low $\delta^{18}O$ meteoric water (Bindeman et al., 2010). The first explanation can be discounted because the dykes have emplacement textures (coarse grained margins) and amphibole crystallization temperatures (Table 5.1; Appendix, B) that indicate that they intruded hot country rock at depth. Therefore, it is unlikely that they encountered meteoric water close to the time of their emplacement. Basalt that has been hydrothermally altered by low $\delta^{18}O$ meteoric water has been discovered at ~3 km depth in Iceland (Hattori and Muehlenbachs, 1982) indicating that meteoric water can penetrate deep into the crust. However, the $\delta^{18}O$ of the surrounding TTG gneisses in the Assynt terrane is high, up to 12 ‰ (Cartwright and Valley, 1991), suggesting that low $\delta^{18}O$ meteoric water has not pervasively altered the Lewisian crust. Zircon oxygen isotopic compositions from the dykes indicate that they have experienced fluid alteration, although it was argued above that this was from a high-$\delta^{18}O$ hydrothermal alteration during the Caledonian orogeny (Chapter 4). If interaction with meteoric water is discounted, the only explanation for the low $\delta^{18}O$ composition of the dykes is due to assimilation of previously hydrothermally altered material.

The modeling above indicates that the geochemistry of the dykes can be explained by assimilation of LGC crustal material. Oxygen isotopic studies of the Lewisian TTG's from the Assynt terrane have shown that these rocks contain high $\delta^{18}O$ values, up to ~12 ‰ (Cartwright and Valley, 1992) although no rocks from the Gruinard terrane have been analyzed. If the source of the low $\delta^{18}O$ values in the dykes was the assimilated amphibolites, these rocks must have had extremely low $\delta^{18}O$ values. An R value of 0.3 was used for the mixing model, and simple mass balance calculations indicate that the amphibolite would have to have a $\delta^{18}O$ value of ~ -15 ‰ to create a dyke with a $\delta^{18}O$ of 0 ‰, assuming that the primitive mantle source of the dykes had a normal $\delta^{18}O$ of ~5 ‰. The $\delta^{18}O$ of the amphibolite would have to be lower, or the amount of assimilation slightly higher for the dykes with $\delta^{18}O$ of ~ -3 ‰, and vice versa for the dykes with higher $\delta^{18}O$. An additional complication is that the dykes intrude sections of the middle and lower crust in the LGC and Assynt terrane, respectively (Coward and Park, 1987) and the assimilation process may have been even deeper. It is difficult to envisage how amphibolites from the Gruinard terrane that have been hydrothermally altered close to the surface by meteoric water could be present in the lower crust to assimilate into dyke magmas.

Goodenough et al. (2010) concluded that the boundary between the Assynt terrane and the Rhiconich terrane to the north, is a tectonic boundary, and that these two crustal blocks were amalgamated during the Inverian metamorphic event at ~2.48 Ga (Corfu et al., 1994). It is possible that during the amalgamation event, and coincident metamorphism, hydrothermally altered low $\delta^{18}O$ amphibolite was subducted or tectonically emplaced into the source region of the Scourie dykes. The amphibolite was then assimilated into the mafic dykes, while tonalite, potentially emplaced at the same time, was assimilated into the ultramafic dykes. If the assimilated material was subducted into the source region of the Scourie dykes, the Gruinard terrane amphib-

olite and tonalite may be regarded as a proxy for this material rather than exact correlatives. Nevertheless, the trace element geochemistry and isotopic compositions of the dykes can be reproduced through melting of primitive mantle then assimilation of hydrothermally altered amphibolite or tonalite. More testing is needed to ascertain if the modeling works for the major elements as well as the trace elements.

This model of dyke emplacement following terrane amalgamation is consistent with the geochronology of the dykes (Chapter 3) and has been reported in other areas (without the low $\delta^{18}O$ complexity). The extended timing of emplacement seen in the Scourie dykes is similar to the Passamaquoddy Bay mafic dykes in southeastern New Brunswick, which were emplaced over an extended period of time in response to post collisional extension after the Appalachian orogeny (Van Wagoner et al., 2001).

The low $\delta^{18}O$ value of the assimilated material required for the model could be explained by the high latitude of the Lewisian at ~2.4 Ga (Sampson, 2009). In the modern Earth, negative $\delta^{18}O$ values only occur due to the Raleigh evaporation-precipitation cycle, with the lowest values recorded at the polar regions, or in the center of large landmasses (Criss and Taylor, 1986). Paleo-latitudes reconstructed from the dykes in the Assynt terrane suggest that the Lewisian had a latitude of ~60° ± 18° at ~2.4 Ga (Sampson, 2009). During the amalgamation of the Assynt and Rhiconich terranes, amphibolite crust, which had been at the surface and exposed to low $\delta^{18}O$ meteoric water could have been emplaced into the source region of the dykes. During post collisional extension, melting of the mantle produced magma, which assimilated the hydrothermally altered amphibolite creating the geochronological, isotopic and geochemical signatures of the mafic Scourie dykes.

5.4. Summary

Presented is a trace element geochemical model, which explains the elemental composition of the two main types of ~2.4 Ga Scourie dyke, the mafic and ultramafic dykes. Both dyke types can be explained by partial melting of primitive mantle followed by an assimilation-fractional-crystallization (AFC) process primarily involving two different crustal assimilants; amphibolite for the mafic dykes and tonalite for the ultramafic dykes. The assimilants used in the model are from the Gruinard terrane of the LGC and are considered proxies for the assimilated material.

Oxygen isotopic constraints on the composition of the assimilated material indicate that it must have had a $\delta^{18}O$ composition of ~ -15 ‰. The extremely negative $\delta^{18}O$ composition must have been obtained through interaction with very low $\delta^{18}O$ meteoric water, which obtained its low value through a Raleigh precipitation-evaporation process (Criss and Taylor, 1986). The only areas currently on Earth where meteoric water has an extremely low $\delta^{18}O$ composition are in the polar regions and in the interiors of continents (Criss and Taylor, 1986). Paleomagnetic data from the Scourie dykes at the time of emplacement (~2.4 Ga, Chapter 3; Heaman and Tarney, 1989) suggests that they were at a polar latitude of ~ 60° ± 18° at this time (Sampson, 2009), which provides an explanation for the low $\delta^{18}O$ hydrothermal alteration. Amalgamation of the Rhiconich and Assynt terranes during the Inverian metamorphic event at ~ 2.48 Ga potentially emplaced the hydrothermally altered crust into the source of the Scourie dykes, where they could be assimilated during dyke magmatism associated with post-collisional extension.

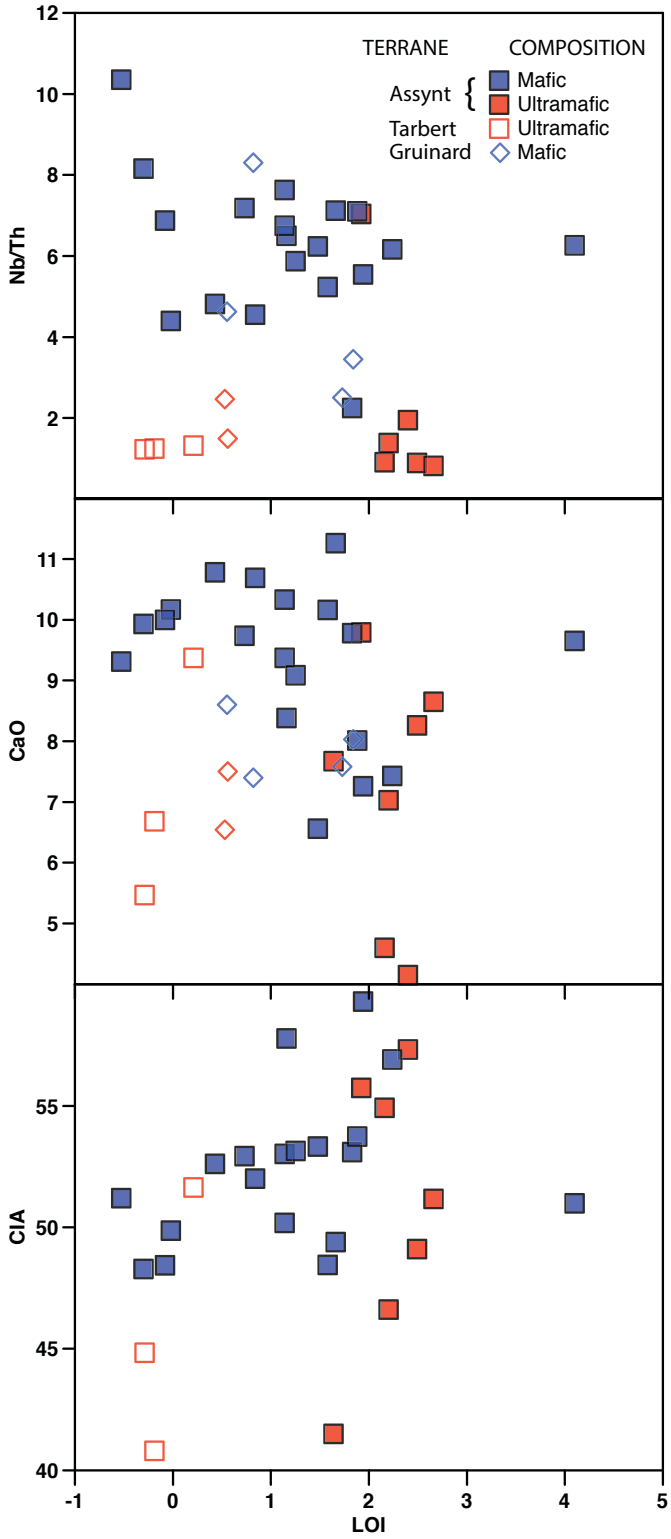

Figure 5.1. Assessment of degree of alteration

LOI against CAI, CaO and Nb/Th. A poor positive relationship between LOI and CAI is observed, an inverse relationship between LOI and CaO is observed, and no relationship between LOI and Nb/Th is seen. See text for more details.

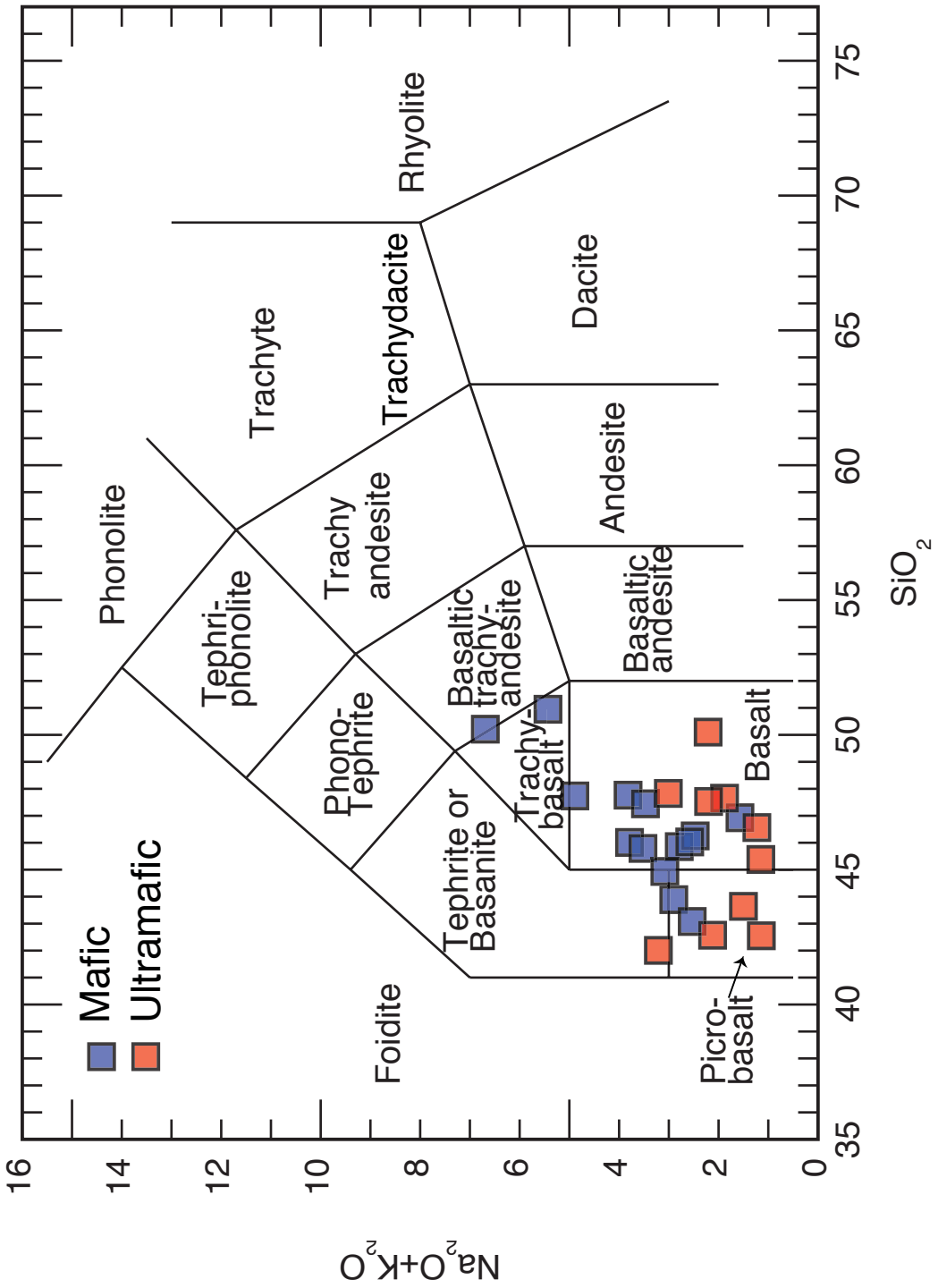

Figure 5.2. TAS diagram

TAS diagram showing the classifications of the mafic and ultramafic dykes after Le Bas et al. (1986). Note that some of the ultramafic dykes have high SiO_2

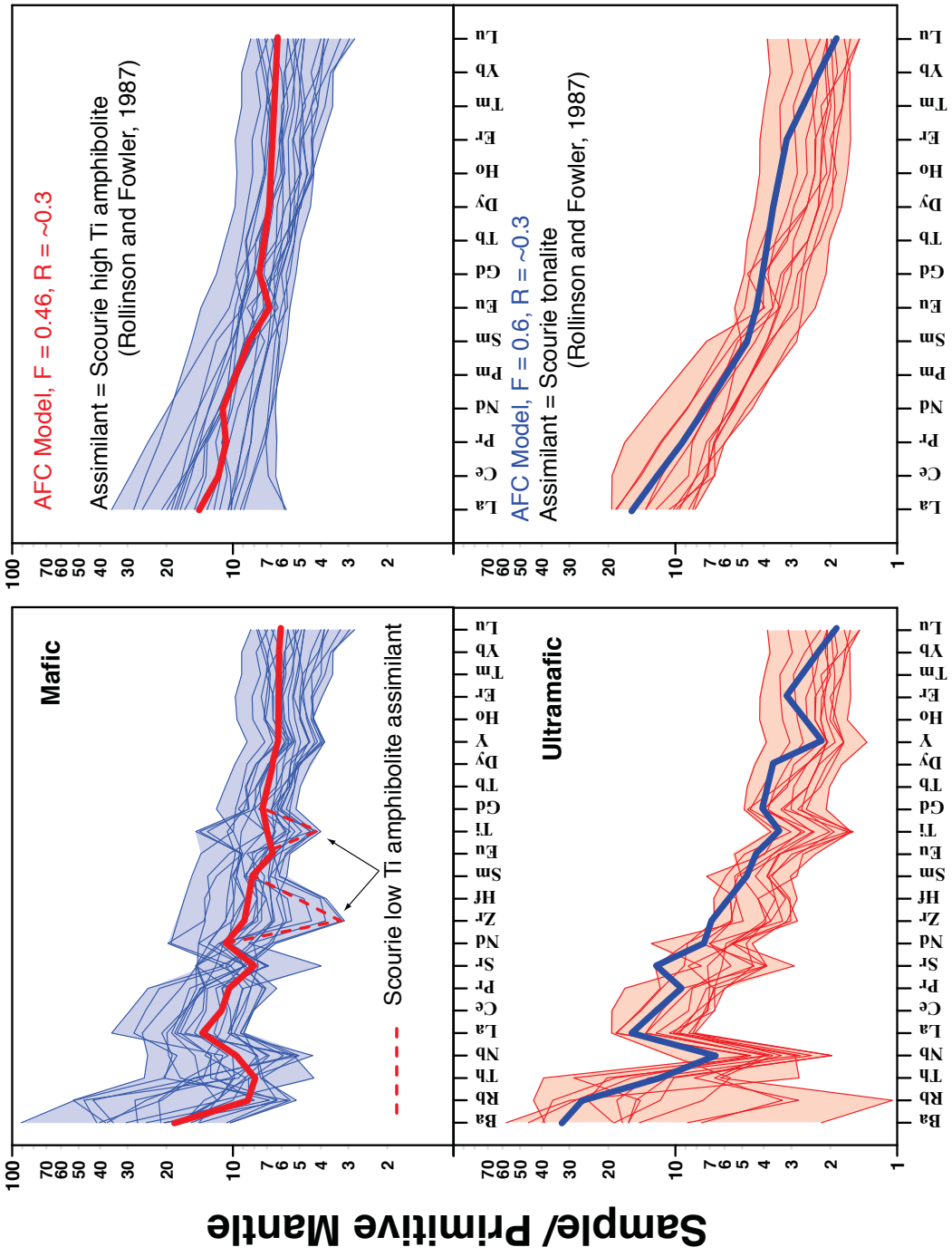

Figure 5.3. Multi element variation diagram

Multi element variation diagram for the mafic and ultramafic dykes. The thin blue and red lines represent individual samples, and the shaded area represents the full spread of data. All elements are normalized to the primitive mantle values from McDonough and Sun (1995). The AFC models for the mafic and ultramafic dykes are superimposed onto the dyke values, see text for model details. The dotted model line in the upper figure represents a low Ti amphibolite assimilant from the Gruinard terrane (Rollinson, 1996).

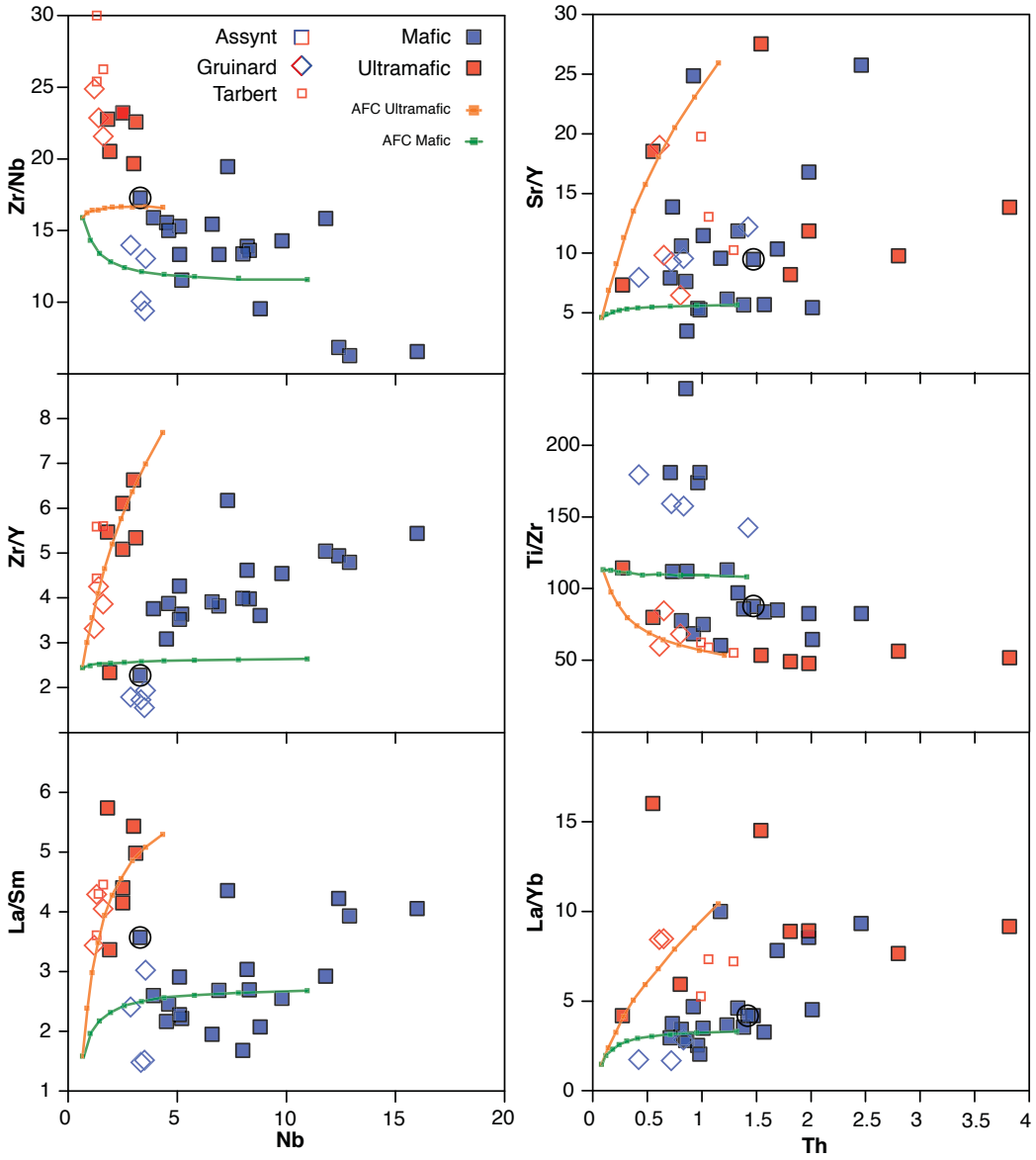

Figure 5.4. Element variation diagram

Element variation diagrams for the mafic and ultramafic dykes. AFC trajectories are also shown, these start at the composition of primitive mantle, and evolve as minerals crystalize and crust is assimilated. The mafic AFC trends end after ~ 60 % crystallization, and ultramafic trends end after ~ 40 % crystallization. The open symbols (small square and diamond) refer to samples from the Tarbert terrane on the Outer Hebrides, and samples from the Gruinard terrane respectively, square filled symbols refer to samples from the Assynt terrane. All blue symbols refer to mafic samples, and red symbols refer to ultramafic samples. The closed square with a circle around it refers to a mafic dyke that has been dated to ~2.0 Ga.

	Sample ID	Dyke name	Temperature (°C)	δ18O-zirc (‰)	Age (Ma)	wt.%										
						SiO2	Al2O3	FeO (t)	CaO	MgO	Na2O	K2O	TiO2	MnO	P2O5	LOI
MAFIC	JD09-04a					54.95	13.70	10.49	6.56	4.41	4.79	0.64	1.44	0.19	0.19	1.48
	JD09-10a	Achmelvic Bay 1	696			49.71	14.01	9.39	9.65	6.54	2.67	1.15	1.18	0.23	0.15	4.10
	JD09-14b	Loch na h		-3.83	2396	52.36	20.32	7.45	7.26	1.56	5.54	1.15	0.90	0.14	0.15	1.94
	JD09-3	Loch a'Bhagh				48.93	11.55	14.94	10.16	6.87	1.57	0.56	1.32	0.26	0.10	1.58
	JD09-17h	Lochan Fearna	631	1.91	2375	47.72	15.89	12.29	7.43	5.36	3.55	1.05	1.86	0.20	0.23	2.24
	JD09-20	NAPI	689	4.68	2043	49.24	15.36	10.79	9.78	6.11	2.60	1.19	0.84	0.20	0.12	1.83
	JD09-29	Allt an Tiachaich				49.77	14.61	11.16	10.69	7.22	1.95	0.84	0.87	0.20	0.07	0.84
	JD09-10c	Achmelvic Bay 3	696			50.25	12.89	11.19	10.33	8.82	2.02	0.45	1.16	0.19	0.15	1.14
	JD09-11a	W Achmelvich	399			50.03	13.39	13.36	8.01	5.15	3.01	0.51	2.02	0.25	0.17	1.88
	JD09-17b	Lochan Fearna	631	1.91	2375	47.38	13.36	15.21	9.37	6.52	1.99	0.48	2.15	0.25	0.23	1.14
	JD09-1e	Lochan Fearna	631	1.91	2375	48.82	13.60	14.24	9.09	5.75	2.39	0.51	2.03	0.25	0.31	1.25
	LH99-46	Graveyard1	818	0.37	2392	46.33	12.98	17.83	9.31	5.04	2.71	0.35	3.38	0.26	0.35	-0.53
	JD09-01b	Loch a' Bhadaidh	694			50.36	14.83	11.50	10.78	6.77	2.18	0.40	0.81	0.21	0.07	0.43
	JD09-8	Canisp	456			50.56	12.52	11.29	11.26	7.82	1.22	0.35	1.13	0.20	0.10	1.66
	JD09-27	Cnoc an Leothaid				46.98	13.79	14.98	9.74	6.23	2.21	0.31	2.07	0.22	0.16	0.73
	LH09-15	Graveyard2	818	0.37	2392	49.94	13.18	13.66	10.17	5.80	2.62	0.46	1.30	0.22	0.13	-0.02
	LH99-51	Poll Eorna	818		2397	45.38	11.63	18.03	9.93	6.09	2.17	0.36	3.26	0.27	0.17	-0.30
	JD10-20b					46.34	11.83	10.72	8.03	5.10	1.89	0.53	1.06	0.15	0.10	1.74
	JD10-21					48.78	11.61	9.91	7.58	5.25	1.69	0.97	1.11	0.15	0.15	1.56
	JD10-25A					48.67	12.00	9.52	8.60	5.75	1.67	0.41	0.90	0.18	0.09	0.87
	JD10-28A	Nedd				48.32	11.26	10.54	7.40	6.23	1.78	0.76	0.99	0.17	0.09	0.96

Table 5.1. Dyke geochemistry

Dyke geochemistry

	Sample ID	Dyke name	Tem-pera-ture (°C)	δ18O-zirc (‰)	Age (Ma)	wt.%										
						SiO2	Al2O3	FeO (t)	CaO	MgO	Na2O	K2O	TiO2	MnO	P2O5	LOI
Ultramafic	JD09-15	Loch Leitir Easaidh	615			53.04	10.10	9.31	8.26	12.83	1.78	0.43	0.55	0.18	0.07	2.49
	JD09-16d	Loch Torr				46.27	7.43	10.72	4.60	24.24	1.04	0.46	0.33	0.17	0.05	2.16
	JD09-23	Loch an Arbhair				45.36	16.37	11.31	9.79	9.62	1.73	1.48	0.75	0.20	0.06	1.92
	JD09-25b					50.61	12.22	9.64	8.65	11.18	1.98	1.03	0.61	0.18	0.08	2.66
	JD09-26a	Loch an Leothaid				45.41	8.42	11.01	4.15	23.76	1.45	0.67	0.53	0.17	0.09	2.40
	LH99-41a	Cleitchean Beag			2410	50.46	12.01	8.76	9.37	14.00	1.54	0.34	0.41	0.16	0.08	0.21
	LH99-42	Cleitchean Beag2			2410	49.98	5.45	9.98	6.68	23.44	0.87	0.36	0.39	0.17	0.04	-0.19
	LH99-42b	Cleitchean Beag3			2410	49.61	5.38	10.93	5.47	25.29	0.83	0.32	0.33	0.18	0.05	-0.29
	JD09-28	Poll a' Gharbh				50.59	8.06	10.14	7.03	17.56	1.33	0.87	0.48	0.17	0.07	2.20
	JD09-21	N Assynt	1304	6.00		47.10	6.25	14.68	7.67	18.21	0.80	0.34	0.70	0.24	0.02	1.64
	JD09-9	North Achmelvich				46.78	4.44	7.78	5.32	21.70	0.98	0.10	0.32	0.13	0.04	1.54
	JD10-26a					47.67	5.54	8.26	7.50	15.40	0.87	0.18	0.34	0.11	0.05	1.37
	JD10-29	Ardvar				47.32	8.90	7.82	6.54	15.77	0.99	0.21	0.49	0.13	0.08	1.87
Assimilants	Scourie Amphibolites (High Ti)					50.64	11.46	13.28	10.17	6.33	2.04	0.68	1.55	0.23	0.16	
	Scourie Amphibolites (Low Ti)					50.88	11.53	10.91	11.10	8.53	2.57	0.56	0.55	0.24	0.03	
	Tonalite Gneiss 123					68.04	15.05	3.41	4.54	1.47	3.99	1.23	0.41	0.05	0.08	
	Tonalite Gneiss 135					65.06	15.01	3.70	6.51	2.16	3.58	1.64	0.29	0.05	0.04	
AFC	F=0.4, R=0.3 ultramafic															
	F=0.6, R=0.3 mafic															
STD	W2-a (n=4)					51.9	15.46	9.85	11.1	6.37	2.17	0.62	1.1	0.18	0.12	
	W2-a recommended					52.68	15.45	9.74	10.86	6.37	2.2	0.62	1.06	0.17		

	Sample ID	Dyke name	ppm													
			V	Cr	Ni	Cu	Co	Ga	Zn	Rb	Sr	Y	Zr	Nb	Cs	Ba
MAFIC	JD09-04a		194.0	100.0	55.0	99.0	37.9	19.6	104.0	4.8	220.0	23.0	142.0	7.3	0.2	163
	JD09-10a	Achmelvic Bay 1	306.0	160.0	97.0	96.0	36.3	16.2	91.0	31.2	289.0	17.2	85.0	12.4	0.9	601
	JD09-14b	Loch na h	123.0	-	12.0	74.0	23.1	21.2	77.0	28.4	455.0	18.3	78.0	5.1	0.4	273
	JD09-3	Loch a'Bhagh	421.0	130.0	72.0	169.0	61.1	18.0	138.0	7.1	79.1	22.7	70.0	4.5	0.4	118
	JD09-17h	Lochan Fearna	376.0	90.0	58.0	201.0	41.9	20.6	125.0	14.8	293.0	24.7	114.0	8.2	0.3	245
	JD09-20	NAPI	241.0	130.0	61.0	17.0	47.3	18.0	118.0	12.6	238.0	25.1	57.0	3.3	-	266
	JD09-29	Allt an Tiachaich	259.0	170.0	113.0	134.0	57.5	16.5	94.0	16.7	204.0	17.8	69.0	4.6	0.2	179
	JD09-10c	Achmelvic Bay 3	303.0	410.0	172.0	148.0	47.3	16.4	124.0	4.1	175.0	16.9	81.0	12.9	0.0	134
	JD09-11a	W Achmelvich	367.0	90.0	50.0	410.0	49.5	18.3	142.0	7.1	175.0	30.8	140.0	9.8	0.1	94
	JD09-17b	Lochan Fearna	440.0	140.0	77.0	140.0	54.6	20.8	155.0	3.8	174.5	28.4	113.0	8.3	0.3	93
	JD09-1e	Lochan Fearna	387.0	130.0	74.0	144.0	50.8	22.0	164.0	3.4	202.0	37.1	187.0	11.8	-	136
	LH99-46	Graveyard1	454.0	30.0	60.0	50.0	46.0	21.0	160.0	6.0	178.0	23.3	84.0	8.8	0.1	122
	JD09-01b	Loch a' Bhadaidh	268.0	70.0	91.0	155.0	60.0	17.3	97.0	8.1	175.0	16.5	62.0	3.9	0.3	111
	JD09-8	Canisp	372.0	230.0	124.0	133.0	52.2	17.5	104.0	3.1	229.0	16.5	60.0	5.2	0.0	68
	JD09-27	Cnoc an Leothaid	531.0	120.0	82.0	166.0	61.5	20.4	138.0	3.3	153.0	19.3	68.0	5.1	0.0	68
	LH09-15	Graveyard2	343.0	80.0	70.0	190.0	52.0	16.0	100.0	13.0	137.0	24.1	92.0	6.9	0.3	140
	LH99-51	Poll Eorna	589.0	60.0	80.0	60.0	56.0	21.0	150.0	7.0	141.0	26.8	107.0	8.0	-	114
	JD10-20b		318.0	65.0	92.0	40.6	58.2	19.5	102.0	5.1	214.0	22.4	40.0	2.9	-	102
	JD10-21		330.0	105.0	93.0	40.2	66.2	19.3	126.0	25.8	293.0	24.0	46.3	3.6	-	230
	JD10-25A		338.0	177.0	85.0	23.3	62.0	18.0	121.0	3.8	181.0	19.5	33.6	3.3	0.1	70
	JD10-28A	Nedd	327.0	118.0	94.0	31.3	61.1	17.2	111.0	6.7	169.0	21.2	32.8	3.5	0.2	201

	Sample ID	Dyke name	ppm													
			V	Cr	Ni	Cu	Co	Ga	Zn	Rb	Sr	Y	Zr	Nb	Cs	Ba
Ultramafic	JD09-15	Loch Leitir Easaidh	160.0	1240.0	307.0	79.0	62.9	12.4	83.0	8.6	111.5	11.4	58.0	2.5	0.2	107
	JD09-16d	Loch Torr	70.0	2620.0	1300.0	56.0	101.5	9.0	86.0	14.9	89.0	7.5	41.0	1.8	0.3	126
	JD09-23	Loch an Arbhair	229.0	340.0	221.0	25.0	61.8	16.2	132.0	17.9	122.5	16.7	39.0	1.9	0.2	381
	JD09-25b		161.0	1080.0	280.0	84.0	64.0	14.8	87.0	26.1	181.5	13.1	70.0	3.1	0.4	255
	JD09-26a	Loch an Leothaid	69.0	2190.0	1375.0	55.0	102.0	11.2	92.0	16.9	245.0	8.9	59.0	3.0	0.4	302
	LH99-41a	Cleitchean Beag	184.0	1320.0	410.0	60.0	62.0	12.0	60.0	7.0	174.0	8.8	39.0	1.3	0.1	124
	LH99-42	Cleitchean Beag2	160.0	3200.0	850.0	30.0	91.0	8.0	70.0	11.0	77.0	7.5	42.0	1.6	0.3	114
	LH99-42b	Cleitchean Beag3	140.0	3280.0	960.0	30.0	98.0	7.0	70.0	9.0	77.0	5.9	33.0	1.3	0.2	107
	JD09-28	Poll a' Gharbh	151.0	2550.0	774.0	10.0	81.2	11.9	87.0	21.4	78.0	9.5	58.0	2.5	0.4	261
	JD09-21	N Assynt	97.0	1610.0	1155.0	23.0	106.0	12.4	174.0	4.5	152.0	8.2	52.0	6.9	0.1	96
	JD09-9	North Achmelvich	122.1	2582.8	900.0	37.6	86.3	7.9	94.9	0.6	142.3	7.5	31.8	1.4	-	15
	JD10-26a		176.0	2564.0	950.0	22.6	77.8	10.6	84.6	1.7	57.8	8.9	29.6	1.2	-	58
	JD10-29	Ardvar	150.0	1711.0	1130.0	23.2	70.8	11.9	81.8	2.0	87.8	8.9	34.5	1.6	0.2	50
Assimilants	Scourie Amphibolites (High Ti)				81.0	48.0		21.0	114.0	6.0	184.0	31.0	114.0	8.0		174
	Scourie Amphibolites (Low Ti)				146.0	36.0		13.0	82.0	5.0	110.0	12.0	29.0	1.0		196
	Tonalite Gneiss 123				12.0	67.0		21.0	35.0	31.0	403.0	1.0	92.0	4.0		733
	Tonalite Gneiss 135				19.0	40.0		20.0	38.0	38.0	333.0	5.0	75.0	5.0		504
AFC	F=0.4, R=0.3 ultramafic									15.8	242.8	9.4	72.0	4.3		214.8
	F=0.6, R=0.3 mafic									8.7	273.1	48.1	126.9	11.0		215.0
STD	W2-a (n=4)		286	100	74		46.7	19.4	91	21.3	204.0	21.3	102.0	7.9	0.86	179.5
	W2-a recommended		260	92	70		43	17	80	21.0	190.0	23.0	100.0	7.9	0.99	170

	Sample ID																		
		Pb	La	Ce	Pr	Nd	Sm	Eu	Gd	Tb	Dy	Ho	Er	Tm	Yb	Lu	Hf	Ta	Th	U
Mafic	JD09-04a	-	23.00	49.00	6.16	24.60	5.28	1.60	5.14	0.77	4.57	0.87	2.60	0.37	2.30	0.33	3.60	0.40	1.17	0.22
	JD09-10a	-	13.60	28.00	3.37	14.00	3.22	1.26	3.64	0.59	3.40	0.66	1.90	0.26	1.59	0.19	2.20	0.70	1.98	0.45
	JD09-14b	-	8.50	19.20	2.64	11.90	2.92	1.33	3.43	0.59	3.31	0.69	2.09	0.33	1.81	0.25	2.10	0.30	0.92	0.21
	JD09-3	7	6.80	16.30	2.28	10.60	3.14	1.09	3.62	0.63	4.26	0.87	2.61	0.41	2.35	0.38	2.00	0.30	0.86	0.34
	JD09-17h	6	11.90	27.30	3.71	16.00	3.92	1.44	4.42	0.74	4.58	0.90	2.71	0.40	2.58	0.34	2.80	0.60	1.33	0.39
	JD09-20	9	11.60	26.70	3.45	13.80	3.25	0.96	3.93	0.69	4.43	0.98	2.86	0.48	2.77	0.42	1.60	0.40	1.47	0.16
	JD09-29	-	6.80	15.40	2.10	10.00	2.77	0.87	3.12	0.52	3.50	0.68	2.14	0.28	1.95	0.27	1.90	0.30	1.01	0.21
	JD09-10c	-	12.90	27.40	3.54	14.40	3.28	1.11	3.64	0.55	3.40	0.64	1.91	0.30	1.65	0.22	2.20	0.70	1.69	0.40
	JD09-11a	-	12.30	28.50	3.98	17.90	4.82	1.39	5.28	0.90	5.82	1.21	3.59	0.51	3.46	0.47	3.80	0.70	1.38	0.32
	JD09-17b	11	11.20	25.90	3.59	16.10	4.16	1.50	4.85	0.82	5.17	1.06	3.26	0.48	3.05	0.44	3.00	0.60	1.23	0.45
	JD09-1e	10	18.20	41.60	5.47	23.90	6.23	2.15	6.46	1.07	6.59	1.43	4.27	0.62	4.02	0.56	4.70	0.80	2.01	0.81
	LH99-46	-	7.44	17.80	2.85	12.60	3.59	1.42	4.33	0.78	4.64	0.95	2.67	0.40	2.66	0.45	2.00	0.56	0.85	0.19
	JD09-01b	-	6.00	13.70	1.87	8.30	2.31	0.85	2.82	0.49	3.00	0.64	1.94	0.28	1.75	0.26	1.80	0.30	0.81	0.20
	JD09-8	-	5.80	13.50	1.81	8.60	2.62	0.93	3.00	0.52	3.36	0.65	1.73	0.24	1.55	0.20	1.70	0.30	0.73	0.22
	JD09-27	-	6.40	14.80	2.11	10.10	2.81	1.03	3.38	0.56	3.70	0.73	2.33	0.29	2.17	0.32	1.90	0.30	0.71	0.14
	LH09-15	-	9.69	22.20	3.32	13.60	3.61	1.12	4.02	0.75	4.67	0.98	2.90	0.43	2.96	0.48	2.20	0.43	1.57	0.34
	LH99-51	-	6.58	17.20	2.84	12.90	3.91	1.41	4.65	0.87	5.30	1.08	3.09	0.47	3.22	0.53	2.50	0.50	0.98	0.22
	JD10-20b	3	6.62	16.00	2.30	10.40	2.75	0.99	3.54	0.55	3.70	0.83	2.46	0.30	2.34	0.35	1.14	0.90	0.83	0.24
	JD10-21	5	10.70	22.90	3.40	14.50	3.54	1.20	4.16	0.60	3.99	0.89	2.64	0.31	2.56	0.38	1.35	1.17	1.42	0.62
	JD10-25A	6	3.72	11.60	1.80	8.36	2.51	0.89	3.28	0.54	3.45	0.74	2.18	0.24	2.22	0.36	1.10	1.37	0.72	0.33
	JD10-28A	2	3.78	10.70	1.61	8.04	2.49	1.01	3.32	0.54	3.55	0.78	2.35	0.25	2.17	0.32	1.07	1.51	0.42	0.11

	Sample ID																		
		Pb	La	Ce	Pr	Nd	Sm	Eu	Gd	Tb	Dy	Ho	Er	Tm	Yb	Lu	Hf	Ta	Th	U
Ultramafic	JD09-15	5	8.80	18.00	2.16	8.70	2.12	0.56	2.08	0.35	2.10	0.42	1.26	0.20	1.15	0.15	1.60	0.20	2.80	0.59
	JD09-16d	5	6.60	13.30	1.51	6.00	1.15	0.41	1.40	0.23	1.40	0.28	0.88	0.12	0.74	0.10	1.20	0.10	1.98	0.58
	JD09-23	6	6.90	11.10	1.69	7.40	2.05	0.83	2.66	0.47	2.95	0.62	1.82	0.27	1.65	0.26	1.20	0.10	0.27	0.22
	JD09-25b	7	12.00	23.90	2.93	11.00	2.41	0.75	2.50	0.40	2.38	0.49	1.47	0.23	1.31	0.21	1.90	0.20	3.82	0.84
	JD09-26a	7	11.90	24.30	2.97	11.10	2.19	0.62	2.17	0.32	1.72	0.35	1.03	0.14	0.82	0.13	1.50	0.20	1.54	0.28
	LH99-41a	-	5.63	12.10	1.70	6.78	1.56	0.52	1.64	0.29	1.72	0.35	1.02	0.16	1.07	0.18	0.90	0.02	0.99	0.18
	LH99-42	-	6.20	13.40	1.84	6.93	1.53	0.43	1.47	0.25	1.52	0.30	0.85	0.13	0.86	0.13	1.00	0.05	1.29	0.28
	LH99-42b	-	5.28	11.20	1.52	5.63	1.23	0.36	1.14	0.20	1.20	0.25	0.71	0.11	0.72	0.12	0.80	0.03	1.06	0.23
	JD09-28	-	8.80	19.30	2.36	9.60	2.00	0.52	2.17	0.31	1.97	0.38	1.13	0.16	0.99	0.14	1.60	0.10	1.81	0.33
	JD09-21	-	12.50	32.30	4.28	16.00	2.93	0.61	2.57	0.34	1.74	0.31	0.94	0.15	0.78	0.10	1.50	0.50	0.55	0.10
	JD09-9	5	6.41	11.93	1.78	7.02	1.49	0.46	1.53	0.22	1.32	0.29	0.82	0.10	0.76	0.11	0.86	0.52	0.61	0.19
	JD10-26a	3	5.40	12.40	1.68	6.83	1.57	0.53	1.76	0.25	1.53	0.33	0.94	0.07	0.91	0.14	0.88	0.96	0.80	0.23
	JD10-29	3	7.89	14.60	2.13	8.81	1.77	0.56	1.82	0.25	1.53	0.33	0.96	0.08	0.93	0.14	1.00	0.78	0.65	0.13
Assimilants	SA (High Ti)	2	12.16	24.60	3.39	17.60	4.01	1.21	4.69		5.02				2.92	0.43			0.71	
	SA (Low Ti)	7	17.55	33.45	3.67	13.26	2.23	0.73	2.41		2.91				2.03	0.31			0.87	
	TG 123	8	21.26	28.64	2.92	9.79	1.31	0.83	0.83		0.37				0.04	0.04			1.00	
	TG 135	8	12.06	20.66	2.49	11.50	2.24	0.66	0.66		1.61				0.12	0.12			1.00	
AFC	F=0.4, R=0.3 ultra-mafic	4.4	10.22	20.40	2.38	9.26	1.93	0.66	2.19	9.26	2.44	0.66	1.38		0.98	0.13	1.38		1.15	0.13
	F=0.6, R=0.3 mafic	2.7	15.70	33.07	4.64	23.83	5.86	1.78	7.09	23.83	7.91	1.78	7.09		4.76	0.71			1.32	0.71
STD	W2-a (n=4)	8	11.10	23.80	3.08	14.00	3.56	1.20	4.05	0.64	4.10	0.84	2.49	0.33	2.25	0.31	2.8	0.5	2.41	0.5
	W2-a recommended	9.3	10.00	23.00		13.00	3.30	1.00		0.63	3.60	0.76	2.50	0.38	2.10	0.33	2.6	0.5	2.40	0.53

References

Babechuk, M.G., Kamber, B.S., 2011. An estimate of 1.9 Ga mantle depletion using the high-field-strength elements and Nd-Pb isotopes of ocean floor basalts, Flin Flon Belt, Canada. Precambrian Research 189, 114-139.

Bindeman, I.N., Schmitt, A.K., Evans, D.A.D., 2010. Limits of Hydrosphere-Lithosphere Interaction: Origin of the Lowest-Known ^{18}O Silicate Rock on Earth in the Paleoproterozoic Karelian Rift. Geology 38, 631–634.

Cann, J.R., 1970. Rb, Sr, Y, Zr and Nb in some ocean floor basaltic rocks. Earth and Planetary Science Letters 10, 7-11.

Cartwright, I, Valley, J.W., 1991. Low-^{18}O Scourie Dike Magmas from the Lewisian Complex, Northwestern Scotland. Geology 19, 578-581.

Cartwright, I, Valley, J.W., 1992. Oxygen-Isotope Geochemistry of the Scourian Complex, Northwest Scotland. Journal of Geological Society 149, 115-126.

Corfu, F., Heaman, L.M., Rogers, G., 1994. Polymetamorphic Evolution of the Lewisian Complex, NW Scotland, as Recorded by U-Pb Isotopic Compositions of Zircon, Titanite and Rutile. Contributions to Mineralogy and Petrology 117, 215–228.

Cribb, J.W., Barton, M., 1996. Geochemical Effects of Decoupled Fractional Crystallization and Crustal Assimilation. Lithos 37, 293-307.

Criss, R.E., and Taylor, H.P., 1986, Meteoric- hydrothermal systems: Reviews in Mineralogy, v. 16, p. 373–424.

DePaolo, D.J., 1981. Trace Element and Isotopic Effects of Combined Wallrock Assimilation and Fractional Crystallization. Earth and Planetary Science Letters 53, 189–202.

Dufek, J., Bergantz, G.W., 2005. Lower Crustal Magma Genesis and Preservation: a Stochastic Framework for the Evaluation of Basalt-Crust Interaction. Journal of Petrology 46, 2167–2195.

Ersoy, Y., Helvacı, C., 2010. FC–AFC–FCA and mixing modeler: A Microsoft® Excel spreadsheet program for modeling geochemical differentiation of magma by crystal fractionation, crustal assimilation and mixing. Computer and Geoscience 36, 383–390

Floyd, P.A., Winchester, J.A., 1978. Identification and discrimination of altered and metamorphosed volcanic rocks using immobile elements. Chemical Geology 21, 291-306.

Foley, S.F., Jackson, S.E., Fryer, B.J., Greenouch, J.D,, Jenner, G.A., 1996. Trace Element Partition

Coefficients for Clinopyroxene and Phlogopite in an Alkaline Lamprophyre from Newfoundland by LAM-ICP-MS. Geochimica et Cosmochimica Acta 60, 629–638.

Fujimaki, H., Tatsumoto, M., Aoki, K-I., 1984. Partition Coefficients of Hf, Zr, and Ree Between Phenocrysts and Groundmasses. Journal of Geophysical Research 89B, 662-762.

Goodenough, K.M., Park, R.G., Krabbendam, M., Myers, J.S., Wheeler, J., Loughlin, S.C., Crowley, Q.G., Friend, C.R.L., Beach, A., Kinny, P.D., Graham, R.H., 2010. The Laxford Shear Zone: an End-Archaean Terrane Boundary? In: Law, R.D., Butler, R.W.H., Holdsworth, R.E., Krabbendam, M., Strachan, R.A., (eds) Continental Tectonics and Mountain Building: The Legacy of Peach and Horne. Geological Society London Special Publications 335 103–120.

Green, T.H., Blundy, J.D., Adam, J., Yaxley, G.M., 2000. SIMS Determination of Trace Element Partition Coefficients Between Garnet, Clinopyroxene and Hydrous Basaltic Liquids at 2-7.5 GPa and 1080-1200 C. Lithos 53, 165–187.

Hattori, K., Muehlenbachs, K., 1982. Oxygen Isotope Ratios of the Icelandic Crust. Journal of Geophysical Research: Solid Earth 87B 6559-6565.

Heaman, L.M., Tarney, J., 1989. U Pb Baddeleyite Ages for the Scourie Dyke Swarm, Scotland: Evidence for Two Distinct Intrusion Events. Nature 340, 705–708.

Hofmann, A.W., Jochum, K.P, Seufert, M., White, W.M., 1986. Nb and Pb in oceanic basalts: new constraints on mantle evolution. Earth and Planetary Science Letters 79, 33-45.

Holland, T., Blundy, J. 1994. Non-Ideal Interactions in Calcic Amphiboles and Their Bearing on Amphibole-Plagioclase Thermometry. Contributions to Mineralogy and Petrology 116, 433–447.

Ketchum, K.Y., Heaman, L.M., Bennett, G., Hughes, D.J., 2013. Age, petrogenesis and tectonic setting of the Thessalon volcanic rocks, Huronian Supergroup, Canada. Precambrian Research 233, 114-172.

Kinny, P.D., Friend, C.R.L., Love, G.J., 2005. Proposal for a Terrane-Based Nomenclature for the Lewisian Gneiss Complex of NW Scotland. Journal of the Geological Society, London 162, 175–186. doi:10.1144/0016-764903-149.

Larsen, E.S., Gottfried, D., 1960. Uranium and Thorium in selected suites of igneous rocks. American Journal of Science, Bradley Volume 258A, 151-169.

Le Bas, M.J., Le Maitre, R.W., Streckeisen, A., Zanettin, Bruno., 1986. A Chemical Classification of Volcanic Rocks Based on the Total Alkali-Silica Diagram. Journal of Petrology 27, 745–750.

Mattey, D., Lowry, D., Macpherson, C., 1994. Oxygen Isotope Composition of Mantle Peridotite. Earth and Planetary Science Letters 128, 231–241.

McDonough, W.F., Sun, S.S., The composition of the Earth. Chemical Geology 120, 223-253.

McKenzie, D., O'Nions, R.K., 1991. Partial Melt Distributions From Inversion of Rare Earth Element Concentrations. Journal of Petrology 32, 1021–1091.

Nesbitt, H.W., Young, G.M., 1982. Early Proterozoic climates and plate motions inferred from major element chemistry of lutites. Nature 299, 715-717.

O'Hara, M.J., 1961. Petrology of the Scourie dyke, Sutherland. Mineralogical Magazine 32, 848-865.

O'Hara, M.J., 1962. Some Intrusions in the Lewisian Complex Near Badcall, Sutherland. Transactions of the Edinburgh Geological Society 19, 201-207.

Rollinson, H.R., 1996. Tonalite-Trondhjemite-Granodiorite Magmatism and the Genesis of Lewisian Crust During the Archaean. In: Brewer, T.S. (ed.), Precambrian Crustal Evolution in the North Atlantic Region, Geological Society London, Special Publication 112, 25-42.

Rollinson, H., 2012. Geochemical Constraints on the Composition of Archaean Lower Continental Crust Partial Melting in the Lewisian Granulites. Earth and Planetary Science Letters 351-352, 1–12.

Rubin, J.N., Henry, C.D., Price, J.G., 1993. The Mobility of Zirconium and Other 'Immobile' Elements During Hydrothermal Alteration. Chemical Geology 110, 29–47.

Sampson, J.P., 2009. A Reappraisal of the Paleomagnetism of the Lewisian Foreland, NW Scotland: the occurrence of primary magnetizations and their implication for a Baltica-Lewisian fit at 2.0 Ga. MSc Thesis, University of Alberta.

Tarney, J. 1963. Assynt Dykes and Their Metamorphism. Nature 199, 672–674.

Tarney J., 1973. The Scourie dyke suite and the nature of the Inverian event in Assynt. In: Park, R.G., Tarney, J. (eds) The early Precambrian of Scotland and related rocks of Greenland. pp 105-118

Tarney, J., Weaver, B.L., 1987a. Mineralogy, petrology and geochemistry of the Scourie dykes: petrogenesis and crystallization processes in dykes intruded at depth. In: Park, R.G. & Tarney, J., eds. Evolution of the Lewisian and comparable Precambrian high grade terrains. The Geological Society London, Special publications, 27, pp. 217-234.

Tarney, J., Weaver, B.L., 1987b. Geochemistry of the Scourian complex: petrogenesis and tectonic models. In: Park, R.G. & Tarney, J., eds. Evolution of the Lewisian and comparable Precambrian high grade terrains. The Geological Society London, Special publications, 27, pp. 45-56.

Waters, F.G., Cohen, A.S., O'Nions, R.K., O'Hara, M.J., 1990. Development of Archaean Lithosphere

Deduced From Chronology and Isotope Chemistry of Scourie Dykes. Earth and Planetary Science Letters 97, 241–255.

Weaver, B.L., Tarney, J., 1981a. The Scourie Dyke Suite: Petrogenesis and Geochemical Nature of the Proterozoic Sub-Continental Mantle. Contributions to Mineralogy and Petrology 78, 175–188.

Weaver, B.L., Tarney, J., 1981b. Lewisan gneiss geochemistry and Archaean crustal development models. Earth and Planetary Science Letters 55, 171-180.

Whitehouse, M.J., Kemp, A.I.S., 2010. On the Difficulty of Assigning Crustal Residence, Magmatic Protolith and Metamorphic Ages to Lewisian Granulites: Constraints From Combined in Situ U–Pb and Lu–Hf Isotopes. Geological Society London Special Publications 335, 81–101.

Zanetti, A., Tiepolo, M., Oberti, R., Vannucci, R,. 2004. Trace-Element Partitioning in Olivine: Modelling of a Complete Data Set From a Synthetic Hydrous Basanite Melt. Lithos 75, 39–54.

Conclusions

In this chapter, I summarize the major findings in Chapters 2-5 followed by concluding remarks regarding the thesis as a whole.

The age of the Scourie dykes

The new geochronology indicates that the majority of the dykes intruded over a ~40 Ma period between 2418-2375 Ma, and these early dykes are referred to as the 'Scourie dykes' to avoid confusion with the multiple dyke generations including dykes as young as 2.0 Ga that are present in the Lewisian. The composition of the magma changes over time with ultramafic dykes intruding between 2418-2395 Ma followed by mafic dykes from 2395-2375 Ma.

Recent tectonic interpretations of the Lewisian Gneiss Complex subdivide the area into several small terranes, which possibly amalgamated during the ca. ~1.9-1.7 Ga Laxfordian metamorphic event (Kinny and Friend, 1997). However, the majority of Scourie dykes intruded the Lewisian terranes shortly after a ~2.5 Ga (Inverian) amphibolite-grade metamorphic event, interpreted to be related to the collision of the Rhiconich and Assynt terranes (Goodenough et al. 2010). The timing and placement of the Scourie dykes indicates that they could have formed during a period of post-collisional extension. Scourie dykes located in the Tarbert terrane on the Isle of Lewis in the Outer Hebrides and the Assynt terrane of the Scottish mainland indicate that the two areas, along with the Rhiconich terrane, shared a common ancestry prior to dyke emplacement, rather than amalgamating during the Laxfordian orogeny.

The new geochronology, along with paleomagnetism, and geochemistry of the Scourie dykes allow the Lewisian Gneiss Complex to be placed in a broad paleogeo-

graphic context. Various Neoarchean supercontinents have been proposed based on broad similarities in the timing of major cratonic events. New dates from the Scourie dykes, combined with the regional geology of the NW Scottish Highlands, indicate that the Lewisian Gneiss Complex, and potentially the North Atlantic craton, were separate crustal entities from the proposed supercontinent Nunavutia during the Neoarchean and Paleoproterozoic.

Younger dykes are also present in the same orientation as the Scourie dykes. So far only two younger dykes have been dated using U-Pb techniques, one at ~1990 Ma (Heaman and Tarney, 1989) and the other at ~2045 Ma. There does not appear to be an obvious way to distinguish between the older and younger dyking events either in the field, or geochemically.

Zircon oxygen isotopes from the Scourie dykes

Some zircons from the Scourie dykes record extremely low $\delta^{18}O$ isotopic values. This finding corroborates the earlier work of Cartwright and Valley (1991) based on whole-rock and major O-isotope analyses that some of the Scourie dykes represent primary low $\delta^{18}O$ magmas. Zircon populations from the dykes have a range in $\delta^{18}O$ values from -3.7 to ~5 ‰ with no obvious relationship between oxygen isotopic composition and cathodoluminescence response of the analyzed parts of the zircon grains. Raman spectra from the zircons show evidence for fluid interaction in some areas of the grains due to partial recrystallization and movement away from the Raman spectroscopic radiation damage trend. Electron microprobe analysis in the same areas of the crystals that contain evidence for fluid interaction show elevated U and Ca contents. When the Raman and electron microprobe data are used to filter the oxygen isotopic data, the fluid altered areas of the grains produce consistently higher $\delta^{18}O$ values than the areas without evidence for fluid alteration. The low $\delta^{18}O$ values

are therefore closest to the original magmatic composition of the grains and indicate that the Scourie dyke magmas were very low in $\delta^{18}O$.

Using in-situ and non-destructive Raman and electron microprobe analysis on complex zircon populations provides important information on the areas of zircon grains that have experienced fluid interaction. This technique is shown to be particularly useful in interpreting zircon data with complex isotopic systematics.

Dyke Geochemistry

The dykes are split into mafic and ultramafic compositions similar to the original dyke groupings suggested by Weaver and Tarney (1981). All of the dykes are enriched in trace elements relative to primitive mantle although the ultramafic dykes have more fractionated trace element profiles. Previous interpretations of the origin of the dykes have suggested that they are not products of the same mantle source that has undergone different degrees of fractional crystallization or crustal contamination (Weaver and Tarney, 1981). In the present study I show that the trace-element profiles and selected trace element ratios from the dykes can be re-created by modeling melting of a primitive mantle source followed by an assimilation-fractional-crystallization process involving two different crustal contaminants. The crustal contaminants used to model the geochemistry are tonalites and amphibolites from the Gruinard terrane. The trace-element modeling is consistent with the oxygen isotopic compositions of the dykes, which require that the dyke magmas have assimilated rocks that were previously hydrothermally altered by meteoric water.

Baddeleyite oxygen isotope analysis by SIMS

Megacrysts of baddeleyite from Phalaborwa South Africa and Mogok Burma were tested for their suitability for use as ion microprobe oxygen isotope reference materi-

als. Neither of the baddeleyite crystals are homogeneous in regards to $\delta^{18}O$ and are therefore not ideal reference materials. It is shown that metamictization, orientation and composition do not cause significant bias in oxygen isotope ratios measured by SIMS. The dominant cause of uncertainty in ion microprobe baddeleyite oxygen isotope analysis is an unknown source of bias, which causes SIMS $\delta^{18}O$ values to be ~1.5 ‰ different to values measured by conventional laser fluorination techniques.

The oxygen isotopic composition of smaller more typical baddeleyites from the Duck Lake sill in the Northwest Territories, Canada indicates that baddeleyite may not be a robust recorder of the oxygen isotopic composition of a magma in the same way as zircon. This sill contains both baddeleyite and zircon and whereas the zircon record a highly consistent oxygen isotopic composition the baddeleyite are more variable with some values tending towards low $\delta^{18}O$ compositions suggesting that baddeleyite may exchange oxygen with surface waters more easily than zircon.

Overall conclusions

I laid out four goals in the introduction to this thesis: 1) understand the timing of dyke emplacement in the Scourie dykes using baddeleyite and zircon U-Pb geochronology, 2) discover if the anomalous $\delta^{18}O$ signatures shown in the dykes around Scourie are real, and if they are recorded elsewhere in the swarm, 3) create a geochemical model for the evolution of the dykes, 4) develop ion probe baddeleyite oxygen isotopic analysis and use this tool on the Scourie dykes.

Progress has been made to completing all four goals, although none of them have been fully completed. There are still many more dykes to date, and with most of the dykes dated so far have produced different ages, it is likely that the geochronological story is far from complete. The same is true for the oxygen isotopic record. Most

of the dykes record different oxygen isotopic compositions, most likely in response to different degrees of crustal contamination and hydrothermal alteration during the Caledonian. The low $\delta^{18}O$ signatures of the dykes originally reported by Cartwright and Valley (1991) have been confirmed and new low $\delta^{18}O$ values have been discovered. It is also likely that the oxygen isotopic story is not yet complete with many more dykes to analyze. The ultra mafic dykes have not been measured for oxygen isotopes yet, which is something that is required to test the geochemical model. Also, temporal relationship between the dykes and oxygen isotopes is not yet understood. The development of a new technique to determine which areas of zircon have experienced post crystallization hydrothermal alteration is an unforeseen positive outcome from the oxygen isotopic study. The geochemical model for the dykes would also benefit from tighter constraints on the assimilants. Hafnium isotope analysis from the zircons in the dykes is planned, which may provide more insight into the age and origin of the assimilants.

Although much progress has been made, oxygen isotope analysis of baddeleyite by SIMS has not yet been fully developed. Specifically, we systematically investigated possible analytical biases associated with orientation, metamictization and composition of baddeleyite and found these to be very minor. More work is required to understand the bias between the SIMS and laser fluorination results however, and to determine if the bias is systematic or not. However, it is a technique that could have great potential for understanding the origin of mafic rocks especially in Precambrian dyke swarms.

In general, this thesis documents a significant advance in the understanding of the age and origin of the Scourie dykes, their age and origin. The results have implications for the evolution of the Lewisian, and more generally for mafic dyke swarms

worldwide by indicating that dykes of similar orientation may not be all the same age. As with most research, this study answers a few questions regarding the origin of the Scourie dykes, but ultimately poses new questions and offers new interpretations which may be challenged by future researchers.

References

Cartwright I. Valley, J.W., 1991. Low 18O Scourie dike magmas from the Lewisian complex northwestern Scotland. Geology 19, 578-581.

Goodenough, K.M., Park, R.G., Krabbendam, M., Myers, J.S., Wheeler, J., Loughlin, S.C., Crowley, Q.G., Friend, C.R.L., Beach, A., Kinny, P.D., Graham, R.H., 2010. The Laxford Shear Zone: an End-Archaean Terrane Boundary?. Geological Society London Special Publications 335, 103–120.

Heaman, L.M., Tarney, J., 1989. U Pb Baddeleyite Ages for the Scourie Dyke Swarm, Scotland: Evidence for Two Distinct Intrusion Events. Nature 340, 705–708.

Kinny, P.D., Friend, C.R.L., 1997. U-Pb Isotopic Evidence for the Accretion of Different Crustal Blocks to Form the Lewisian Complex of Northwest Scotland. Contributions to Mineralogy and Petrology 129, 326–340.

Weaver, B.L., Tarney, J., 1981. The Scourie Dyke Suite: Petrogenesis and Geochemical Nature of the Proterozoic Sub-Continental Mantle. Contributions to Mineralogy and Petrology 78, 175–188.

Appendix A: Raman spectra fitting program

Raman analysis

Download data

Obtain the data from its specific location on the hard drive

In[1]:=
```
ClearAll["Global`*"]
DirectoryNAME = "/Users/Josh/Dropbox/Rojas file share (1)/Josh/Raman-data";
InputFILE = "badcall bay 3-1.txt";

SetDirectory[DirectoryNAME];
data = Import[InputFILE, "CSV"];
```

Select the frequencies of interest around the 1000 cm – 1 band

Select the line numbers of the file which contatain the frequencies between 850 cm and 1150 - we only use the data in this range

In[7]:=
```
l1 = Position[data[[All, 1]], 850.][[1, 1]];
l2 = Position[data[[All, 1]], 1150.][[1, 1]];

x1 = data[[l1]][[1]];
x2 = data[[l2]][[1]];
```

Plot the data

We plot the data to make sure we have the correct range

In[236]:=
```
lmin = Position[data[[All, 2]], Min[data[[l1 ;; l2, 2]]]][[1, 1]];
lmax = Position[data[[All, 2]], Max[data[[l1 ;; l2, 2]]]][[1, 1]];
ymin = data[[lmin]][[2]];
ymax = data[[lmax]][[2]];

ListPlot[data, PlotRange → {{x1, x2}, {ymin, 1.05 * ymax}},
 AxesOrigin → {x1, ymin}, LabelStyle → {FontSize → 14}, Frame → True,
 FrameLabel → {"Wave number (cm^-1)", "Intensity (a.u.)"},
 FrameStyle -> Directive[Black, FontSize → 16], LabelStyle → Directive[Black],
 PlotStyle → {{Black, Thick}, {Blue, Thick}}, PlotRangePadding → 0]
```

Out[240]=

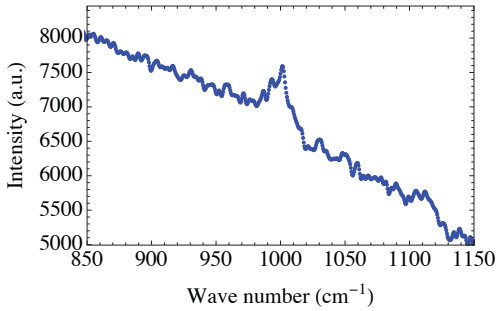

Background model

We fit a 3rd order polynomial function to the data between 850-965 and 1035-1150cm-1 and show the plot

In[250]:=
```
xBKG1 = Position[data[[All, 1]], 850.][[1, 1]];
xBKG2 = Position[data[[All, 1]], 965.][[1, 1]];
xBKG3 = Position[data[[All, 1]], 1035.][[1, 1]];
xBKG4 = Position[data[[All, 1]], 1150.][[1, 1]];

UnionBKG = Join[data[[xBKG1 ;; xBKG2, All]], data[[xBKG3 ;; xBKG4, All]]];
BKGFunc[A0_, A1_, A2_, A3_, x_] = A0 + A1 * x + A2 * x^2 + A3 * x^3;
BKGModel = BKGFunc[A0, A1, A2, A3, x];

fit = FindFit[UnionBKG, BKGModel, {{A0, ymin}, {A1, 1}, {A2, 1}, {A3, 1}},
    x, MaxIterations → 10 000, Gradient → "FiniteDifference"];

Show[{ListPlot[data, PlotRange → {{x1, x2}, {ymin, 1.05 * ymax}},
    AxesOrigin → {x1, ymin}, LabelStyle → {FontSize → 14}, Frame → True,
    FrameLabel → {"Wave number (cm^-1)", "Intensity (a.u.)"},
    FrameStyle -> Directive[Black, FontSize → 16], LabelStyle → Directive[Black],
    PlotStyle → {{Black, Thick}, {Blue, Thick}}, PlotRangePadding → 0],
  Plot[Evaluate[BKGModel /. fit], {x, x1, x2}]}]
```

Out[258]=

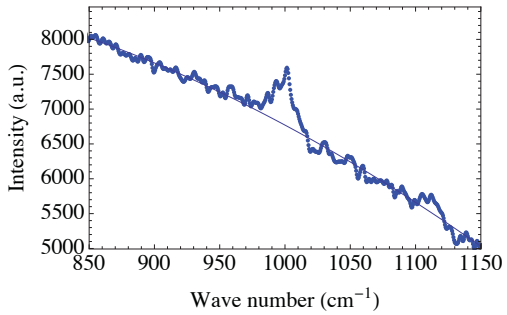

Background subtraction

we subtract the polynomial function from the data to remove the background and any low frequency modes associated with an amorphous component

In[281]:=
```
f[x_] = Evaluate[BKGModel /. fit];
data2 = data;
data2[[All, 2]] = data2[[All, 2]] - f[data2[[All, 1]]];

lmax = Position[data2[[All, 2]], Max[data2[[l1 ;; l2, 2]]]][[1, 1]];
lmin = Position[data2[[All, 2]], Min[data2[[l1 ;; l2, 2]]]][[1, 1]];
xmax = data2[[lmax]][[1]];
ymax = data2[[lmax]][[2]];
xmin = data2[[lmin]][[1]];
ymin = data2[[lmin]][[2]];

ListPlot[data2, PlotRange → {{x1, x2}, {-400, 1.1 * ymax}},
 LabelStyle → {FontSize → 14}, Frame → True,
 FrameLabel → {"Wave number (cm^-1)", "Intensity (a.u.)"},
 FrameStyle -> Directive[Black, FontSize → 16], LabelStyle → Directive[Black],
 PlotStyle → {{Black, Thick}, {Blue, Thick}}, PlotRangePadding → 0]
```

Out[290]=

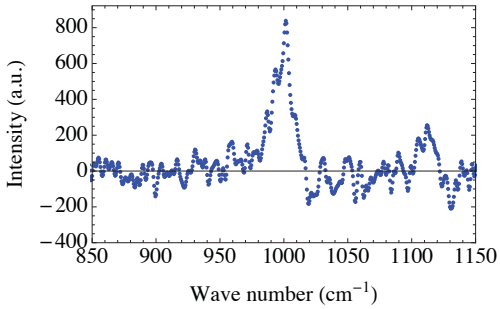

Definition of the fitting models for the peaks

We define the Voigt, Lorentzian and Gauss fitting function. First we define a 1-peak function and then a 2-peak function. We call them "voigtmodel", "lorentzianmodel" and "gaussianmodel" for simplicity in the rest of the code.

In[291]:=
```
VoigtFunc[δ_, σ_, A_, x0_, x_] = A * PDF[VoigtDistribution[δ, σ], (x - x0)];
Voigt2Func[A1_, δ1_, σ1_, x01_, A2_, δ2_, σ2_, x02_, x_] =
  A1 * PDF[VoigtDistribution[δ1, σ1], (x - x01)] +
   A2 * PDF[VoigtDistribution[δ2, σ2], (x - x02)];

LorentzianFunc[Y0_, A_, γ_, x0_, x_] = Y0 + (A / Pi) * (γ / ((x - x0) ^ 2 + γ ^ 2));
Lorentzian2Func[A1_, A2_, γ1_, γ2_, x01_, x02_, x_] =
  (A1 / Pi) * (γ1 / ((x - x01) ^ 2 + γ1 ^ 2)) + (A2 / Pi) * (γ2 / ((x - x02) ^ 2 + γ2 ^ 2));

GaussianFunc[A_, σ_, x0_, x_] = A / (σ * Sqrt[2 * Pi]) * Exp[-(x - x0) ^ 2 / (2 * σ ^ 2)];
Gaussian2Func[Y0_, A1_, σ1_, x01_, A2_, σ2_, x02_, x_] =
  Y0 + A1 / (σ1 * Sqrt[2 * Pi]) * Exp[-(x - x01) ^ 2 / (2 * σ1 ^ 2)] +
   A2 / (σ2 * Sqrt[2 * Pi]) * Exp[-(x - x02) ^ 2 / (2 * σ2 ^ 2)];

VoigtModel = VoigtFunc[δ, σ, A, x0, x];
Voigt2Model = Voigt2Func[A1, δ1, σ1, x01, A2, δ2, σ2, x02, x];
LorentzianModel = LorentzianFunc[Y0, A, γ, x0, x];
Lorentzian2Model = Lorentzian2Func[A1, A2, γ1, γ2, x01, x02, x];
GaussianModel = GaussianFunc[A, σ, x0, x];
Gaussian2Model = Gaussian2Func[Y0, A1, σ1, x01, A2, σ2, x02, x];
```

Fit the data with the 2 – peak Gaussian model

we specified the guess parameters iteratively offline.

In[303]:=
```
fitgaussian2 = FindFit[data2[[l1 ;; l2]], Gaussian2Model,
   {{Y0, 10}, {A1, 25 000}, {σ1, 5}, {x01, 965}, {A2, 25 000}, {σ2, 5}, {x02, 1000}},
   x, MaxIterations → 1000, Gradient → "FiniteDifference"];

Show[{Plot[Evaluate[Gaussian2Model /. fitgaussian2],
   {x, x1, x2}, PlotRange → {-400, 1.1 * ymax}, GridLines → {{}, {0}},
   GridLinesStyle → Directive[Black, Bold], LabelStyle → {FontSize → 14},
   Frame → True, FrameLabel → {"Wave number (cm^-1)", "Intensity (a.u.)"},
   FrameStyle -> Directive[Black, FontSize → 16], LabelStyle → Directive[Black],
   PlotStyle → {{Black, Thick}, {Blue, Thick}}, PlotRangePadding → 0],
  Graphics[{Red, PointSize[.005], Map[Point, data2]}]}]
```

```
fitgaussian2
```

Out[304]=

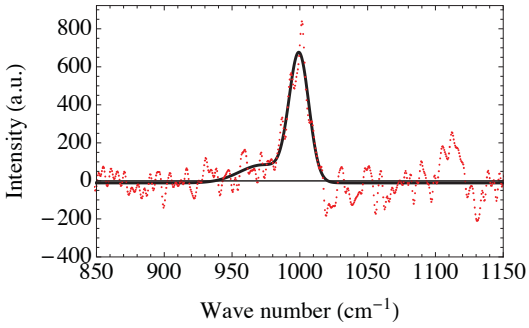

Out[305]=
```
{Y0 → -10.792, A1 → 4119.57, σ1 → 17.2922,
 x01 → 972.764, A2 → 11 975.3, σ2 → 7.25799, x02 → 999.414}
```

Fit the data with the 2 – peak Voigt model

We define a new range of frequencies: smaller because the otherwise the 2-peak Voigt model takes too long. We specified the guess parameters iteratively offline.

In[127]:=
```
ll1 = Position[data2[[All, 1]], 950.][[1, 1]];
ll2 = Position[data2[[All, 1]], 1050.][[1, 1]];

fitVoigt2 = FindFit[data2[[ll1 ;; ll2]], Voigt2Model,
    {{A1, 100 000}, {δ1, 3}, {σ1, 0.5}, {x01, 965}, {A2, 130 000}, {δ2, 3}, {σ2, 0.5},
     {x02, 1004}}, x, MaxIterations → 1000, Gradient → "FiniteDifference"];

Show[{Plot[Evaluate[Voigt2Model /. fitVoigt2],
    {x, x1, x2}, PlotRange → {-400, 1.1 * ymax}, GridLines → {{}, {0}},
    GridLinesStyle → Directive[Black, Bold], LabelStyle → {FontSize → 14},
    Frame → True, FrameLabel → {"Wave number (cm^-1)", "Intensity (a.u.)"},
    FrameStyle -> Directive[Black, FontSize → 16], LabelStyle → Directive[Black],
    PlotStyle → {{Black, Thick}, {Blue, Thick}}, PlotRangePadding → 0],
  Graphics[{Red, PointSize[.005], Map[Point, data2]}]}]

fitVoigt2
```

FindFit::sszero :
The step size in the search has become less than the tolerance prescribed by the PrecisionGoal option, but the gradient is larger than the tolerance specified by the AccuracyGoal option. There is a possibility that the method has stalled at a point that is not a local minimum. ≫

Out[130]=

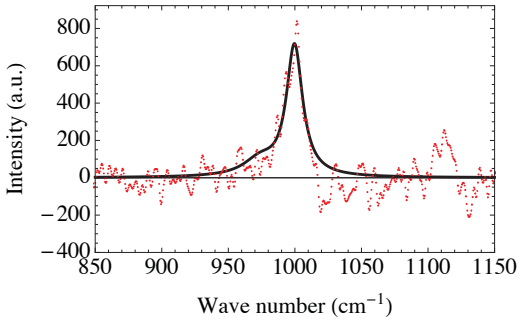

Out[131]=
```
{A1 → 4027.85, δ1 → 14.8464, σ1 → 1.20149, x01 → 973.857,
 A2 → 16 100.7, δ2 → 7.32168, σ2 → 0.431775, x02 → 999.711}
```

Fit the data with the 2 – peak Lorentzian

In[135]:=
```
fitLorentzian2 = FindFit[data2[[l1 ;; l2]], Lorentzian2Model,
    {{A1, 8559}, {A2, 48 653}, {γ1, 3.15}, {γ2, 3.837}, {x01, 971.1}, {x02, 1003.4}},
    x, MaxIterations → 10 000, Gradient → "FiniteDifference"];

Show[{Plot[Evaluate[Lorentzian2Model /. fitLorentzian2],
    {x, x1, x2}, PlotRange → {-400, 1.1 * ymax}, GridLines → {{}, {0}},
    GridLinesStyle → Directive[Black, Bold], LabelStyle → {FontSize → 14},
    Frame → True, FrameLabel → {"Wave number (cm^-1)", "Intensity (a.u.)"},
    FrameStyle -> Directive[Black, FontSize → 16], LabelStyle → Directive[Black],
    PlotStyle → {{Black, Thick}, {Blue, Thick}}, PlotRangePadding → 0],
  Graphics[{Red, PointSize[.005], Map[Point, data2]}]}]

fitLorentzian2
```

Out[136]=

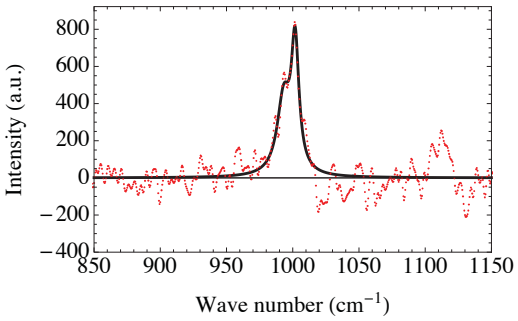

Out[137]= {A1 → 7732.23, A2 → 7418.91, γ1 → 6.00158, γ2 → 3.46521, x01 → 993.195, x02 → 1001.79}

Final figure and statistics

We define the function "G" which is the result of the fitting procedure - in this case we used the Lorentzian model. We calculate the residual which = Model - data, and also a Chi squared value for the fit. The error bar on the data points is defined as σ which in this case is 50. Freep is the number of free parameters in the model, and needs to be changed depending on the model used, for the Lorentzian it is 6, Gaussian it is 7 and the Voigt is is 8.

In[172]:=
```
G[x_] = Evaluate[Lorentzian2Model /. fitLorentzian2];
m1 = Position[data2[[All, 1]], 960.][[1, 1]];
m2 = Position[data2[[All, 1]], 1040.][[1, 1]];
σ = 50;
freep = 6;

Nlines = Dimensions[data2[[m1 ;; m2]]][[1]];
Res = Table[1, {k, 1, Nlines}];
Res = data2[[m1 ;; m2, 2]] - G[data2[[m1 ;; m2, 1]]];

χ2 = Sum[(Res[[i]] / σ) ^ 2, {i, 1, Nlines}] / (Nlines - freep - 1);

Res2 = Table[{data2[[m1 ;; m2, 1]][[i]], Res[[i]]}, {i, 1, Nlines}];
G2 =
  Table[{data2[[m1 ;; m2, 1]][[i]], G[data2[[m1 ;; m2, 1]]][[i]]}, {i, 1, Nlines}];

ploter =
 Show[{ListLinePlot[{Res2, G2}, PlotRange → {-400, 1.1 * ymax}, GridLines → {{}, {0}},
    GridLinesStyle → Directive[Black, Bold], LabelStyle → {FontSize → 14},
    Frame → True, FrameLabel → {"Wave number (cm^-1)", "Intensity (a.u.)"},
    FrameStyle -> Directive[Black, FontSize → 16], LabelStyle → Directive[Black],
    PlotStyle → {{Black, Thick}, {Blue, Thick}}, PlotRangePadding → 0],
   Graphics[{Red, PointSize[.008], Map[Point, data2[[m1 ;; m2]]]}]}]

Print["χ square = ", χ2]
```

Out[183]=

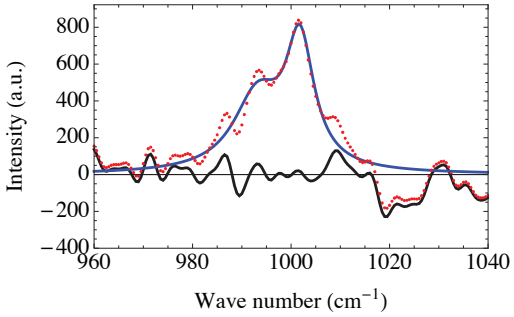


```
χ square = 2.79627
```

Extract the parameters of the peaks

we calculate the FWHM of the two peaks for each of the models. Some of the parameters have the same name for all the models e.g. A1 and so to extract the Lorenztian parameters, only the Lorentzian model can be run, if the Gaussian model is run, the parameter A1 will be Gaussian rather than Lorentzian. The peak parameters need to be turned on (uncommented) for the model that is being run. In this case the Lorentzian parameters will be printed.

Lorentzian parameters

In[206]:=
```
A1value = A1 /. fitLorentzian2;
A2value = A2 /. fitLorentzian2;
γ1value = γ1 /. fitLorentzian2;
γ2value = γ2 /. fitLorentzian2;
x01value = x01 /. fitLorentzian2;
x02value = x02 /. fitLorentzian2;
FWHM1 = 2 * γ1value;
FWHM2 = 2 * γ2value;
RESULTparamL = List[x01value, FWHM1, x02value, FWHM2, σ, Re[χ2]];
```

Gaussian parameters

```
(*A1value=A1/.fitGaussian2;
A2value=A2/.fitGaussian2;
σ1value=σ1/.fitGaussian2;
σ2value=σ2/.fitGaussian2;
x01value=x01/.fitGaussian2;
x02value=x02/.fitGaussian2;
FWHM1=2*Sqrt[2*Log[2]]*σ1value;
FWHM2=2*Sqrt[2*Log[2]]*σ2value;
RESULTparamG=List[x01value,FWHM1,x02value,FWHM2,σ,Re[χ2]];*)
```

Voigt parameters

```
(*A1value=A1/.fitVoigt2;
A2value=A2/.fitVoigt2;
δ1value=δ1/.fitVoigt2;
δ2value=δ2/.fitVoigt2;
σ1value=σ1/.fitVoigt2;
σ2value=σ2/.fitVoigt2;
x01value=x01/.fitVoigt2;
x02value=x02/.fitVoigt2;
FWHM1VG=2*Sqrt[2*Log[2]]*σ1value;
FWHM2VG=2*Sqrt[2*Log[2]]*σ2value;
FWHM1VL=2*δ1value;
FWHM2VL=2*δ2value;
FWHM1=0.5346*FWHM1VL+Sqrt[0.2166*FWHM1VL^2+FWHM1VG^2];
FWHM2=0.5346*FWHM2VL+Sqrt[0.2166*FWHM2VL^2+FWHM2VG^2];
RESULTparamV=List[x01value,FWHM1,x02value,FWHM2,σ,Re[χ2]];*)
```

Export results

We export the plot as a .pdf file and the peak parameters as a .txt file. The output directory needs to be specified, the result list - in this case "RESULTparamL" for Lorentzian needs to be changed if a Gauss/Voigt model is run, e.g. in the case of Gauss, the results list would be "RESULTparamG". The file name also needs to be changed to reflect the model run, in this case _paramL.txt, it should be changed to paramG.txt if a Gaussian model is run. The same thing applies to the plot.

```
OutputDIRECTORY = "/Users/Josh/Dropbox/Rojas file share (1)/Josh";
SetDirectory[OutputDIRECTORY];
Export[StringDrop[InputFILE, -4] <> "_paramL.txt", RESULTparamL, "CSV"]
Export[StringDrop[InputFILE, -4] <> "_plotL.pdf", ploter,
 "AllowRasterization" → True, ImageSize → 380, ImageResolution → 600]
```

Out[221]= badcall bay 3-1_param.txt

Out[222]= badcall bay 3-1_plot.pdf

Appendix B: Mineral Chemistry

Amphibole Name	ferro-pargasite	magnesio-horn-blende	magnesio-horn-blende	magnesio-horn-blende	magnesio-horn-blende	magnesio-horn-blende	magnesio-horn-blende	magnesio-horn-blende	magnesio-horn-blende
Sample ID	LH99-46 1-1	JD09-8 1-9	JD09-8 1-8	JD09-8 1-7	JD09-8 1-5	JD09-8 1-45	JD09-8 1-43	JD09-8 1-41	JD09-8 1-4
SiO2	40.4	45.13	44.81	44.28	44.77	44.89	44.62	47.03	43.91
TiO2	2.17	0.59	0.60	0.45	0.42	0.40	0.42	0.36	0.43
Al2O3	12.89	12.57	12.58	13.61	13.52	13.05	13.3	10.88	13.6
FeO*	21.31	14.8	14.81	14.97	14.77	14.45	15.02	13.76	15.11
MgO	7.03	11.08	11.17	10.62	10.78	10.98	10.77	12.28	10.63
MnO	0.25	0.26	0.22	0.27	0.24	0.27	0.24	0.23	0.23
CaO	10.99	11.72	11.73	11.79	11.71	11.65	11.65	11.94	11.76
Na2O	2.17	1.63	1.55	1.69	1.49	1.53	1.52	1.28	1.59
K2O	1.14	0.25	0.25	0.29	0.28	0.26	0.28	0.23	0.28
F			0.01	0.01		0.01	0.02		
Cl	0.04								
Sum	98.39	98.03	97.73	97.98	97.97	97.49	97.83	97.99	97.54
Plagioclase									
Albite %	0.54	0.97	0.97	0.97	0.97	0.97	0.97	0.97	0.97
Anorthite %	0.45	0.02	0.02	0.02	0.02	0.02	0.02	0.02	0.02
Results based on iteration using Anderson and Smith pressure at various thermometers									
T (C) HB2	818.0	459.0	462.4	465.6	452.1	449.4	457.6	422.1	470.1
P(Kb) HB2	4.6	7.2	7.3	8.5	8.1	7.7	8.0	4.7	8.5
HB 2 refers to Holland and Blundy Hbld-Plag thermometry calibration reaction edenite + albite = richterite + anorthite									
Anderson, J. L. & Smith, D. R. 1995. The effect of temperature and oxygen fugacity on Al-in-hornblende barometry. AM MINERAL 80, 549-59.									
Holland, T. & Blundy, J. 1994. Non-ideal interactions in calcic amphiboles and their bearing on amphibole-plagioclase thermometry. CONTRIB MINERAL PETROL 116, 433-47.									

Amphibole Name	magne-sio-horn-blende	magne-sio-horn-blende	magne-sio-horn-blende	magne-sio-horn-blende	magne-sio-horn-blende	magne-sio-horn-blende	magne-sio-horn-blende	magne-sio-horn-blende	magne-sio-horn-blende	magne-sio-horn-blende	magne-sio-horn-blende
Sample ID	JD09-8 1-39	JD09-8 1-38	JD09-8 1-37	JD09-8 1-35	JD09-8 1-34	JD09-8 1-32	JD09-8 1-31	JD09-8 1-30	JD09-8 1-3	JD09-8 1-29	JD09-8 1-28
SiO2	46.18	45.27	44.49	44.88	45.01	44.88	45.84	45.19	45.37	44.9	45.24
TiO2	0.32	0.43	0.41	0.48	0.41	0.41	0.45	0.47	0.38	0.48	0.56
Al2O3	11.53	12.61	12.64	12.98	12.67	12.69	12.04	12.56	12.41	12.98	12.33
FeO*	14.13	14.73	14.73	14.81	14.32	14.74	14.25	14.42	14.57	14.87	14.61
MgO	11.75	11.17	11.13	10.97	11.24	11.05	11.45	11.33	11.26	10.89	11.22
MnO	0.23	0.24	0.25	0.22	0.25	0.25	0.24	0.24	0.22	0.25	0.24
CaO	11.91	11.89	11.89	11.84	11.77	11.64	11.82	11.65	11.75	11.77	11.87
Na2O	1.32	1.51	1.53	1.48	1.52	1.46	1.44	1.48	1.4	1.56	1.46
K2O	0.22	0.25	0.27	0.26	0.26	0.26	0.22	0.24	0.25	0.27	0.25
F			0.01		0.01				0.01	0.01	
Cl											
Sum	97.59	98.09	97.34	97.92	97.46	97.37	97.75	97.59	97.62	97.98	97.79
Plagioclase											
Albite %	0.97	0.97	0.97	0.97	0.97	0.97	0.97	0.97	0.97	0.97	0.97
Anorthite %	0.02	0.02	0.02	0.02	0.02	0.02	0.02	0.02	0.02	0.02	0.02
T (C) HB2	426.7	448.3	461.1	451.9	449.1	451.1	436.0	451.0	441.6	454.8	448.4
P(Kb) HB2	5.6	7.1	7.4	7.6	7.3	7.3	6.3	7.1	6.8	7.6	6.9

Amphibole Name	magnesio-ferri-hornblende	magnesio-hornblende	magnesio-hornblende	magnesio-hornblende	magnesio-hornblende	magnesio-hornblende	magnesio-hornblende	magnesio-hornblende	magnesio-hornblende	magnesio-hornblende	magnesio-hornblende
Sample ID	JD09-8 1-27	JD09-8 1-26	JD09-8 1-25	JD09-8 1-24	JD09-8 1-23	JD09-8 1-22	JD09-8 1-21	JD09-8 1-20	JD09-8 1-2	JD09-8 1-18	JD09-8 1-17
SiO2	44.19	44.96	45.02	45.61	44.13	45.03	45.53	45.25	45.08	45.06	45.19
TiO2	0.50	0.44	0.42	1.34	0.89	0.43	0.41	0.40	0.45	0.55	0.63
Al2O3	12.66	13.16	12.28	12.45	12.51	12.57	12.35	12.31	12.77	12.41	12.5
FeO*	15.09	14.67	14.36	14.67	15.19	14.73	14.75	14.58	14.71	14.87	14.74
MgO	11.89	10.77	11.24	11.26	11.54	11.26	11.39	11.45	11.18	11.31	11.18
MnO	0.23	0.25	0.24	0.26	0.24	0.23	0.26	0.25	0.25	0.23	0.22
CaO	11.09	11.56	11.64	11.7	11.17	11.83	11.85	11.75	11.75	11.71	11.76
Na2O	1.4	1.49	1.55	1.51	1.4	1.4	1.45	1.42	1.48	1.56	1.59
K2O	0.23	0.25	0.25	0.24	0.25	0.24	0.25	0.26	0.28	0.25	0.25
F	0.01	0.01			0.03				0.01	0.01	0.02
Cl											
Sum	97.28	97.56	96.99	99.04	97.35	97.72	98.23	97.67	97.95	97.96	98.09
Plagioclase											
Albite %	0.97	0.97	0.97	0.97	0.97	0.97	0.97	0.97	0.97	0.97	0.97
Anorthite %	0.02	0.02	0.02	0.02	0.02	0.02	0.02	0.02	0.02	0.02	0.02
T (C) HB2	500.7	446.0	449.3	468.2	499.4	453.0	448.8	451.9	453.0	463.0	458.3
P(Kb) HB2	7.8	7.7	6.9	7.1	7.7	7.2	6.8	6.9	7.4	7.1	7.1

Amphibole Name	magne-sio-horn-blende	magne-sio-horn-blende	magne-sio-horn-blende	magne-sio-horn-blende	magne-sio-horn-blende	magne-sio-horn-blende	magne-sio-horn-blende	pargasite	pargasite	pargasite	pargasite
Sample ID	JD09-8 1-16	JD09-8 1-15	JD09-8 1-14	JD09-8 1-13	JD09-8 1-12	JD09-8 1-10	JD09-8 1-1	JD09-20 light 1-4	JD09-20 1-9	JD09-20 1-8	JD09-20 1-7
SiO2	45.3	45.21	44.91	45.27	44.88	44.28	45.84	42.24	41.74	42.53	42.76
TiO2	0.46	0.47	0.50	0.51	0.42	1.60	0.39	0.63	0.90	0.47	0.51
Al2O3	12.36	12.29	12.48	13.04	13.03	12.32	11.87	14.39	14.4	14.33	14.31
FeO*	14.7	14.68	14.55	14.68	15.11	15.27	14.32	17.58	17.67	17.47	17.27
MgO	11.21	11.35	11.42	11.15	10.99	11.04	11.64	9.13	8.99	9.18	9.44
MnO	0.25	0.23	0.27	0.27	0.23	0.26	0.24	0.27	0.29	0.27	0.27
CaO	11.83	11.88	11.88	11.69	11.66	11.5	11.63	11.51	11.5	11.43	11.49
Na2O	1.44	1.42	1.46	1.48	1.61	1.53	1.35	1.72	1.7	1.7	1.77
K2O	0.23	0.24	0.24	0.25	0.28	0.26	0.21	0.75	1.14	0.61	0.66
F	0.01		0.01		0.01		0.01				
Cl								0.08	0.07	0.06	0.07
Sum	97.80	97.76	97.71	98.33	98.21	98.06	97.50	98.30	98.39	98.04	98.56
Plagioclase											
Albite %	0.97	0.97	0.97	0.97	0.97	0.97	0.97	0.68	0.68	0.68	0.68
Anorthite %	0.02	0.02	0.02	0.02	0.02	0.02	0.02	0.31	0.31	0.31	0.31
T (C) HB2	446.1	451.2	460.3	453.0	462.8	497.2	438.7	694.2	703.4	686.7	689.9
P(Kb) HB2	6.9	6.8	7.2	7.6	7.8	7.4	6.2	8.6	8.5	8.7	8.5

Amphibole Name	pargasite	pargasite	pargasite	magne-sio-horn-blende	magne-sio-horn-blende	magne-sio-horn-blende	magne-sio-horn-blende	magne-sio-horn-blende	magne-sio-horn-blende	magne-sio-horn-blende	pargasite
Sample ID	JD09-20 1-6	JD09-20 1-5	JD09-20 1-4	JD09-20 1-3	JD09-20 1-2	JD09-20 1-19	JD09-20 1-14	JD09-20 1-13	JD09-20 1-12	JD09-20 1-11	JD09-20 1-10
SiO2	43.24	42.8	42.44	43.65	43.85	43.21	43.49	43.99	41.95	43.1	41.53
TiO2	0.43	0.48	0.50	0.34	0.31	0.41	0.44	0.38	1.45	0.56	0.44
Al2O3	13.84	13.78	13.9	13.72	13.8	13.63	13.44	12.7	13.22	13.25	15.1
FeO*	17.2	17.36	17.38	16.78	16.99	17.12	16.98	16.86	17.83	17.3	17.82
MgO	9.63	9.56	9.47	9.86	9.89	9.69	9.85	10.06	9.47	9.85	8.64
MnO	0.25	0.29	0.28	0.28	0.26	0.27	0.27	0.29	0.32	0.26	0.26
CaO	11.55	11.6	11.5	11.51	11.6	11.59	11.41	11.36	11.28	11.25	11.41
Na2O	1.81	1.7	1.73	1.66	1.69	1.7	1.76	1.63	1.66	1.5	1.76
K2O	0.59	0.70	0.68	0.47	0.48	0.51	0.52	0.49	0.62	0.81	0.68
F		0.02			0.02						
Cl	0.09	0.10	0.09	0.05	0.08	0.07	0.05	0.05	0.07	0.07	0.11
Sum	98.63	98.38	97.96	98.32	98.95	98.20	98.20	97.81	97.88	97.95	97.76
Plagioclase											
Albite %	0.68	0.68	0.68	0.68	0.68	0.68	0.68	0.68	0.68	0.68	0.68
Anorthite %	0.31	0.31	0.31	0.31	0.31	0.31	0.31	0.31	0.31	0.31	0.31
T (C) HB2	683.6	689.5	694.9	672.2	673.4	680.8	681.9	672.8	729.7	691.9	695.7
P(Kb) HB2	8.3	8.2	8.2	8.3	8.3	8.2	8.0	7.5	7.0	7.7	9.2

Amphibole Name	magne-sio-horn-blende	magne-sio-horn-blende	magne-sio-horn-blende	ferro-parg-asite	ferro-parg-asite	ferro-parg-asite	magnesio-fer-ri-hornblende	magne-sio-horn-blende	ferro-parg-asite	ferro-parg-asite	ferro-parg-asite
Sample ID	JD09-20 1-1	JD09-18a rim 1-5	JD09-18a rim 1-4	JD09-18a rim 1-3	JD09-18a rim 1-2	JD09-18a rim 1-12	JD09-18a rim 1-11	JD09-18a rim 1-1	JD09-17h 1-8	JD09-17h 1-4	JD09-17h 1-3
SiO2	43.15	44.01	42.39	42.02	41.9	41.29	42.24	43.67	42.4	42.35	42.53
TiO2	0.34	1.54	1.28	1.62	1.81	2.14	1.39	1.22	0.54	0.56	0.56
Al2O3	13.88	10.82	12.98	13.53	13.73	11.66	10.94	11.08	14.06	13.89	14.12
FeO*	17.2	18.86	18.91	18.9	18.87	19.09	18.68	19.85	20.06	20.2	19.96
MgO	9.59	9.94	9.15	8.37	8.32	8.75	9.75	9.08	7.87	7.85	7.82
MnO	0.28	0.23	0.27	0.25	0.26	0.29	0.30	0.26	0.28	0.30	0.27
CaO	11.39	10.62	10.75	11.02	11.01	10.36	10.56	10.69	11.44	11.21	11.27
Na2O	1.67	1.86	1.89	2.02	2.15	2.21	1.88	1.79	1.76	1.8	1.93
K2O	0.55	0.28	0.39	0.38	0.42	0.33	0.28	0.32	0.63	0.65	0.63
F	0.01	0.01			0.02		0.01		0.01		
Cl	0.07	0.65	0.54	0.58	0.55	0.62	0.61	0.67	0.15	0.17	0.15
Sum	98.14	98.82	98.55	98.68	99.04	96.74	96.65	98.63	99.20	98.98	99.25
Plagioclase											
Albite %	0.68	0.27	0.27	0.27	0.27	0.27	0.27	0.27	0.85	0.85	0.85
Anorthite %	0.31	0.73	0.73	0.73	0.73	0.73	0.73	0.73	0.15	0.15	0.15
T (C) HB2	681.4	897.3	872.6	857.7	867.3	930.1	918.9	874.9	633.7	639.1	634.9
P(Kb) HB2	8.3	0.3	2.6	3.5	3.2			1.3	9.2	9.0	9.2

Amphibole Name	ferro-parg-asite	ferro-parg-asite	ferro-parg-asite	ferro-horn-blende	magne-sio-horn-blende	magne-sio-horn-blende	magne-sio-horn-blende	magne-sio-horn-blende	magne-sio-horn-blende	actinolite	magne-sio-horn-blende
Sample ID	JD09-17h 1-24	JD09-17h 1-23	JD09-17h 1-22	JD09-17h 1-19	JD09-15 1-9	JD09-15 1-8	JD09-15 1-6	JD09-15 1-5	JD09-15 1-40	JD09-15 1-4	JD09-15 1-39
SiO2	42.21	41.91	41.92	43.85	53.02	53.28	52.67	49.63	52.5	54.14	51.89
TiO2	0.56	0.56	0.54	0.60	0.12	0.14	0.19	0.29	0.28	0.08	0.26
Al2O3	14.52	14.4	14.7	12.62	4.58	4.94	6.26	8.92	7.53	3.58	8.15
FeO*	20.19	20.01	20.24	19.5	8.74	8.81	9.61	11.6	10.12	8.31	10.43
MgO	7.51	7.47	7.44	8.66	17.57	17.43	16.57	14.88	14.94	18.32	14.8
MnO	0.25	0.28	0.27	0.26	0.16	0.17	0.17	0.19	0.16	0.14	0.15
CaO	11.28	11.54	11.35	11.46	11.97	11.89	11.78	11	11.3	11.97	11.44
Na2O	1.78	1.74	1.86	1.55	0.63	0.71	0.78	1.13	0.87	0.48	1.05
K2O	0.68	0.71	0.69	0.73	0.03	0.04	0.06	0.10	0.08	0.02	0.09
F	0.01	0.01					0.02	0.01		0.01	
Cl	0.19	0.21	0.23	0.12							
Sum	99.17	98.84	99.23	99.35	96.82	97.4	98.10	97.74	97.78	97.04	98.26
Plagioclase											
Albite %	0.85	0.85	0.85	0.85	0.60	0.60	0.60	0.60	0.60	0.60	0.60
Anorthite %	0.15	0.15	0.15	0.15	0.40	0.40	0.40	0.40	0.40	0.40	0.40
T (C) HB2	631.5	627.9	637.1	615.0	623.5	621.4	604.6	638.5	547.4	621.4	574.0
P(Kb) HB2	9.6	9.6	9.7	8.0	0.7	1.0	2.1	4.4	2.9		3.6

Amphibole Name	magne-sio-horn-blende	magne-sio-horn-blende	cumming-tonite	actinolite	cumming-tonite	actinolite	actinolite	actinolite	actinolite	actinolite	magne-sio-horn-blende
Sample ID	JD09-15 1-35	JD09-15 1-34	JD09-15 1-33	JD09-15 1-32	JD09-15 1-3	JD09-15 1-29	JD09-15 1-28	JD09-15 1-26	JD09-15 1-25	JD09-15 1-23	JD09-15 1-22
SiO2	51.25	52.61	54.87	53.57	53.75	53.39	54.07	53.6	54.62	53.78	44.4
TiO2	0.24	0.15	0.02	0.11	0.09	0.09	0.08	0.09	0.04	0.14	0.42
Al2O3	7.71	5.65	1.33	4.62	3.73	4.05	2.85	4	2.96	4.33	13.92
FeO*	10.37	9.24	17.92	8.61	14.9	9	11.61	8.79	8.2	8.95	13.43
MgO	15.37	16.8	20.5	17.48	18.7	17.7	18.9	17.6	18.53	17.6	11.71
MnO	0.14	0.17	0.59	0.16	0.41	0.16	0.29	0.16	0.17	0.16	0.15
CaO	11.68	11.87	2.31	11.76	6.14	11.61	8.6	11.81	11.75	11.97	11.38
Na2O	0.97	0.74	0.15	0.60	0.46	0.51	0.37	0.53	0.40	0.56	1.76
K2O	0.07	0.04	0.02	0.05	0.03	0.03	0.03	0.04	0.03	0.06	0.33
F			0.02						0.01	0.01	
Cl											
Sum	97.8	97.27	97.72	96.95	98.21	96.54	96.80	96.62	96.70	97.56	97.50
Plagioclase											
Albite %	0.60	0.60	0.60	0.60	0.60	0.60	0.60	0.60	0.60	0.60	0.60
Anorthite %	0.40	0.40	0.40	0.40	0.40	0.40	0.40	0.40	0.40	0.40	0.40
T (C) HB2	605.9	610.5	752.1	606.3	672.6	614.9	651.2	616.6	627.4	614.9	692.1
P(Kb) HB2	3.4	1.6		0.7	-0.0	0.3		0.2		0.5	8.0

Amphibole Name	magne-sio-horn-blende	magne-sio-horn-blende	magne-sio-horn-blende	magne-sio-horn-blende	actinolite	cumming-tonite	cumming-tonite	actinolite	magne-sio-horn-blende	actinolite	magne-sio-horn-blende
Sample ID	JD09-15 1-21	JD09-15 1-20	JD09-15 1-2	JD09-15 1-19	JD09-15 1-18	JD09-15 1-17	JD09-15 1-16	JD09-15 1-15	JD09-15 1-14	JD09-15 1-13	JD09-15 1-12
SiO2	52.02	52.3	52.85	51.32	53.58	54.02	54.58	53.53	52.56	53.87	53.11
TiO2	0.24	0.24	0.12	0.19	0.13	0.04	0.05	0.18	0.13	0.09	0.16
Al2O3	6.84	5.98	4.45	5.81	3.99	1.53	1.22	4.43	4.79	3.71	4.79
FeO*	12.24	9.67	8.8	9.44	8.67	17.85	18.44	8.88	9.04	9.15	9.16
MgO	15.91	16.7	17.34	16.84	17.71	20.27	20.61	17.6	17.14	18.13	17.32
MnO	0.26	0.17	0.15	0.16	0.17	0.55	0.54	0.15	0.15	0.16	0.16
CaO	9.2	11.65	11.86	11.78	11.6	2.46	1.76	11.93	11.7	11.43	11.9
Na2O	0.85	0.70	0.67	0.68	0.54	0.16	0.16	0.58	0.64	0.52	0.58
K2O	0.07	0.05	0.03	0.08	0.03	0.01	0.02	0.06	0.04	0.01	0.05
F	0.01	0.02		0.01	0.01					0.02	
Cl											
Sum	97.65	97.48	96.27	96.31	96.43	96.89	97.37	97.33	96.18	97.09	97.23
Plagioclase											
Albite %	0.60	0.60	0.60	0.60	0.60	0.60	0.60	0.60	0.60	0.60	0.60
Anorthite %	0.40	0.40	0.40	0.40	0.40	0.40	0.40	0.40	0.40	0.40	0.40
T (C) HB2	605.9	607.9	628.4	619.6	618.9	746.3	798.6	618.0	616.8	628.9	610.7
P(Kb) HB2	2.6	1.9	0.6	1.8	0.2			0.6	0.9	-0.0	0.9

Amphibole Name	cumming-tonite	actinolite	actinolite	ferro-parg-asite	ferro-parg-asite	ferro-parg-asite	ferro-parg-asite	ferro-parg-asite	ferro-parg-asite	ferro-fer-ri-tscher-makite	ferro-parg-asite
Sample ID	JD09-15 1-11	JD09-15 1-10	JD09-15 1-1	JD09-14b 1-9	JD09-14b 1-8	JD09-14b 1-6	JD09-14b 1-44	JD09-14b 1-43	JD09-14b 1-40	JD09-14b 1-4	JD09-14b 1-39
SiO2	53.02	52.71	54.08	40.77	42.11	40.34	41.5	42.58	41.61	40.93	40.09
TiO2	0.09	0.12	0.14	0.97	1.20	0.92	0.44	0.81	0.19	0.34	0.20
Al2O3	3.73	4.39	4.01	13.49	11.71	14.36	14.39	12.41	14.53	14.38	15.67
FeO*	15.81	13.74	8.65	24.99	24.76	23.87	22.08	21.99	21.93	23.79	21.7
MgO	18.42	18.16	17.9	4.8	5.01	4.84	6.34	7.01	6.47	6.03	6.12
MnO	0.42	0.34	0.15	0.25	0.37	0.28	0.43	0.41	0.40	0.28	0.39
CaO	5.28	7.26	11.93	11.08	11.02	11.15	11.15	11.01	11.24	10.42	11.2
Na2O	0.45	0.56	0.55	1.7	1.64	1.71	1.77	1.73	1.73	1.62	1.67
K2O	0.04	0.05	0.02	1.05	1.04	1.09	0.91	0.82	0.95	0.90	0.99
F			0.01	0.02		0.01					0.01
Cl											
Sum	97.27	97.33	97.44	99.12	98.87	98.57	99.01	98.76	99.04	98.70	98.04
Plagioclase											
Albite %	0.60	0.60	0.60	0.57	0.57	0.57	0.57	0.57	0.57	0.57	0.57
Anorthite %	0.40	0.40	0.40	0.41	0.41	0.41	0.41	0.41	0.41	0.41	0.41
T (C) HB2	683.2	662.8	620.6	748.8	739.6	735.8	731.0	738.3	724.6	759.9	736.3
P(Kb) HB2	-0.0	0.5	0.2	7.1	5.9	8.1	8.0	6.3	8.2	7.3	9.0

Amphibole Name	ferro-parg-asite	ferro-parg-asite	ferro-parg-asite	ferro-parg-asite	ferro-parg-asite	ferro-parg-asite	ferro-parg-asite	ferro-parg-asite	ferro-parg-asite	ferro-fer-ri-tscher-makite	ferro-parg-asite
Sample ID	JD09-14b 1-38	JD09-14b 1-37	JD09-14b 1-36	JD09-14b 1-35	JD09-14b 1-33	JD09-14b 1-32	JD09-14b 1-31	JD09-14b 1-3	JD09-14b 1-25	JD09-14b 1-23	JD09-14b 1-22
SiO2	41.76	41.72	41.42	40.64	42.22	43.28	40.79	42.54	41.46	40.93	41.63
TiO2	0.35	0.53	0.31	0.32	1.23	0.72	0.64	0.54	1.11	0.86	0.74
Al2O3	14.62	13.78	14.71	15.85	12.43	12.35	15.12	13.47	13.15	14.36	13.25
FeO*	21.79	21.83	21.22	21.34	23.32	21.82	22.73	22.46	24.03	25.15	23.97
MgO	6.35	6.56	6.63	6.14	5.9	7.14	5.5	5.99	5.24	5.28	5.4
MnO	0.39	0.41	0.41	0.41	0.41	0.39	0.41	0.35	0.35	0.32	0.35
CaO	11.25	11.22	11.31	11.29	11.08	11.06	11.24	11.22	11.03	9.8	11.04
Na2O	1.71	1.75	1.68	1.71	1.71	1.6	1.78	1.6	1.73	1.46	1.66
K2O	0.95	0.96	0.93	1.05	0.91	0.75	1.05	0.9	1.02	0.86	0.91
F	0.01										
Cl											
Sum	99.18	98.76	98.62	98.74	99.21	99.11	99.26	99.07	99.12	99.02	98.96
Plagioclase											
Albite %	0.57	0.57	0.57	0.57	0.57	0.57	0.57	0.57	0.57	0.57	0.57
Anorthite %	0.41	0.41	0.41	0.41	0.41	0.41	0.41	0.41	0.41	0.41	0.41
T (C) HB2	718.1	728.1	720.7	725.7	742.2	722.7	731.3	705.8	742.2	752.4	732.2
P(Kb) HB2	8.4	7.6	8.5	9.3	6.3	6.5	8.6	7.8	6.9	7.5	7.2

Amphibole Name	ferro-parg-asite	ferro-parg-asite	ferro-parg-asite	ferro-parg-asite	ferro-parg-asite	ferro-parg-asite	ferro-parg-asite	ferro-parg-asite	ferro-parg-asite	ferro-fer-ri-tscher-makite	ferro-parg-asite
Sample ID	JD09-14b 1-38	JD09-14b 1-37	JD09-14b 1-36	JD09-14b 1-35	JD09-14b 1-33	JD09-14b 1-32	JD09-14b 1-31	JD09-14b 1-3	JD09-14b 1-25	JD09-14b 1-23	JD09-14b 1-22
SiO2	41.76	41.72	41.42	40.64	42.22	43.28	40.79	42.54	41.46	40.93	41.63
TiO2	0.35	0.53	0.31	0.32	1.23	0.72	0.64	0.54	1.11	0.86	0.74
Al2O3	14.62	13.78	14.71	15.85	12.43	12.35	15.12	13.47	13.15	14.36	13.25
FeO*	21.79	21.83	21.22	21.34	23.32	21.82	22.73	22.46	24.03	25.15	23.97
MgO	6.35	6.56	6.63	6.14	5.9	7.14	5.5	5.99	5.24	5.28	5.4
MnO	0.39	0.41	0.41	0.41	0.41	0.39	0.41	0.35	0.35	0.32	0.35
CaO	11.25	11.22	11.31	11.29	11.08	11.06	11.24	11.22	11.03	9.8	11.04
Na2O	1.71	1.75	1.68	1.71	1.71	1.6	1.78	1.6	1.73	1.46	1.66
K2O	0.95	0.96	0.93	1.05	0.91	0.75	1.05	0.9	1.02	0.86	0.91
F	0.01										
Cl											
Sum	99.18	98.76	98.62	98.74	99.21	99.11	99.26	99.07	99.12	99.02	98.96
Plagioclase											
Albite %	0.57	0.57	0.57	0.57	0.57	0.57	0.57	0.57	0.57	0.57	0.57
Anorthite %	0.41	0.41	0.41	0.41	0.41	0.41	0.41	0.41	0.41	0.41	0.41
T (C) HB2	718.1	728.1	720.7	725.7	742.2	722.7	731.3	705.8	742.2	752.4	732.2
P(Kb) HB2	8.4	7.6	8.5	9.3	6.3	6.5	8.6	7.8	6.9	7.5	7.2

Appendix C: Dyke inventory

Scourie Dyke Inventory

Dyke	Lithology	Decimal lat	Decimal long	Orientation and width	Sample amount	Crush	Dyke Name	General location	Geochem	Tracer isotopes (Sr-Nd)	WR oxygen	U-Pb age	Zirc oxygen	Comments
LH86-20	Amphibolite				2	Yes		S. of Gairloch						
LH86-21A	Picrite	58.1868	-5.14		20	Yes	Beannoch dyke	Loch Beannoch				Yes		more differentiated portion of dyke on west margin
LH86-21B	Picrite				43	Yes	Beannoch dyke	Loch Beannoch				Yes		more differentiated portion of dyke on west margin
LH86-21C	Picrite				11	Yes	Beannoch dyke	Loch Beannoch				Yes		opx megacrysts, east side of dyke
LH86-23	Dolerite	58.1772	-5.1289					West of Loch Assynt						close to road; have a full 5 gal pail
LH86-24	Biotite Diorite	58.1317	-5.2609			Yes	Strathan	S. of Strathan				Yes		west of road (likely same dyke as LH07-11; just further north along strike)
LH86-25	Diorite	58.122	-5.2515					E. of Inverkirkaig						
LH86-26	Amphibolite							Achmelvich Bay						
LH86-35	Gabbro	58.1794	-5.1479					SE of Loch Beannoch						have a full 5 gal pail
LH86-36	Dolerite							SE of Loch Beannoch						fine grained, late dolerite
LH86-40	Norite	58.3254	-5.1677			Yes		Badcall Bay				Yes	Yes	discordant zircon, young rutile
LH86-41	Peridotite							Scourie More						
LH86-42	Garnet Peridotite							Scourie More						
LH99-31	Diorite	57.8344	-7.0293			Yes		South Harris Igneous Complex	Yes					
LH99-35	Norite	57.7534	-7.0015			Yes		South Harris Igneous Complex on the way to Strond	Yes			Yes		Lots of large baddeleyite
LH99-39	Gabbro	57.8403	-6.8344					South Harris Igneous Complex	Yes			Yes		
LH99-41A	Gabbro	57.0929	-6.6342						Yes					
LH99-42	Gabbro	58.2338	-6.6502			Yes	Cleitchean Lewis	Cleitchean Beag, Lewis	Yes			Yes		some nice baddeleyite, most with polycrystalline zircon overgrowths
LH99-43	Gabbro						Cleitchean Lewis	Cleitchean Beag, Lewis	Yes			Yes		some nice baddeleyite, most with polycrystalline zircon overgrowths
LH99-44	Gabbro	58.2374	-6.6551			Yes	Cleitchean Lewis	Cleitchean Beag, Lewis	Yes			Yes		some nice baddeleyite, most with polycrystalline zircon overgrowths
LH99-45	Coarse Granophyre	58.3524	-5.1667				Graveyard	Scourie				Yes	Yes	Graveyard Dyke, large long zircon in thin section
LH99-46	Gabbro					Yes	Graveyard	Scourie	Yes			Yes	Yes	Graveyard Dyke
LH99-47	Gabbro						Graveyard	Scourie	Yes			Yes	Yes	Graveyard Dyke
LH99-48	Gabbro						Graveyard	Scourie	Yes			Yes	Yes	Graveyard Dyke
LH99-49	Gabbro					Yes	Graveyard	Scourie	Yes			Yes	Yes	Graveyard Dyke
LH99-50	Charnockite	58.3462	-5.1627			Yes		Scourie					Yes	
LH99-51	Gabbro	58.3604	-5.1708		2 bags	Yes	Poll Eorna	Scourie	Yes			Yes		Poll Eorna Dyke; collected several fist size pieces from various parts of the dyke
LH07-10	Gabbro	58.1315	-5.2677				Badnaban	S. of Badnaban	Yes	Yes	Yes			collected several pieces along strike (070210-077205)
LH07-11	Gabbro	58.1317	-5.2592	110			Badnaban	S. of Badnaban	Yes	Yes	Yes			road outcrop just south of tiny bridge (likely the same dyke as LH86-24)
LH07-12	Gabbro	58.2502	-5.0109				Unapool	Unapool	Yes	Yes	Yes	Yes		Kylesku Dyke; collected several hand samples along west road exposure
LH07-14	Gabbro	58.3524	-5.1667	130			Kylesku	Scourie						Graveyard Dyke
LH07-15	Gabbro			130			Graveyard	Scourie				Yes	Yes	Graveyard Dyke
LH07-16	Gabbro			130			Graveyard	Scourie				Yes	Yes	Graveyard Dyke
LH07-17	Amphibolite	58.3255	-5.1643				Upper Badcall Bay	Upper Badcall Bay						LH07-17 and -19 are likely from the quartz tholeiite dyke (QT2) shown on the detailed sketch by Mike O'Hara in the 1986 Guidebook (area B)
LH07-18	Amphibolite	58.3237	-5.1675				Upper Badcall Bay	Upper Badcall Bay						
LH07-19	Meta-gabbro						Upper Badcall Bay	Upper Badcall Bay						

2009 Fieldwork														
Dyke	Lithology	Decimal lat	Decimal long	Orientation and width	Sample amount	Crushed	Dyke Name	General location	Geochem	Tracer isotopes (Sr-Nd)	WR oxygen	U-Pb age	Zirc oxygen	Comments
JD09-01	Diabase	58.3485	-5.1323		3 Pieces (A-C)	B	Loch a' Bhadaidh Dyke	Off Scourie road in Creag Gharbh	B	Yes				A = Eastern Contact, B = Centre of dyke, C = Western contact (C&V 1991 sample 1 and 8)
JD09-02	Diabase	58.364	-5.0873		1 Piece	Yes	Loch a' Bhagh Ghainmhich Dyke	Just South of Laxford bridge famous road cut	Yes	Yes	Yes	Yes	Yes	metamorphosed look for metamorphic minerals
JD09-03	Diabase	58.3641	-5.0873		1 Piece	Yes	Same as JD09-2	Just South of Laxford bridge famous road cut	Yes	Yes	Yes	Yes	Yes	metamorphosed look for metamorphic minerals
JD09-04	Gabbro			310/80NE	2 Pieces (A+B)	A		North coast of Scourie inlet	A	Yes	Yes			A = North contact with gneiss, B = Centre of dyke
JD09-05	Gabbro	58.3598	-5.1648	300/68NE	3 Pieces (A-C)		Poll Eorna	Poll Eorna	Yes	Yes	Yes	Yes	Yes	A = Centre of Dyke, B = Contact with wall rock, C = gneiss and dyke contact
JD09-06	Gabbro	58.361	-5.1607	ENE	1 Piece			North of Poll Eorna						May not be dyke…
JD09-07	Gabbro	58.36	-5.1528	046/80NE	1 Piece	Yes		NE of Poll Eorna	Yes	Yes	Yes			Different trend to usual
JD09-08	Gabbro	58.1778	-5.3057	ENE	1 Piece	Yes	Canisp Dyke	Achmelvich coast canisp shear zone	Yes	Yes	Yes			foliated by shearing
JD09-09	Picrite	58.181	-5.3152		1 Piece	Yes	north Achmelvich Coast Dyke	Achmelvich coast	Yes	Yes	Yes			
JD09-10	Dolerite/amphibolite	58.1715	-5.3062		3 Pieces (A-C)	A, B and C	Achmelvich Bay dyke	Achmelvich bay	A, B and C	Yes	Yes			A = Dyke Margin - poss archean, B = felsic pod, poss archean, C = dioritic centre of dyke
JD09-11	Dolerite/amphibolite	58.1702	-5.3113	NW	2 Pieces (A+B)	A	W Achmelvich	S of Achmelvich bay	A	Yes	Yes			A = Vein samples from centre of dyke - poss archean, B = fine to med grained sample from centre of dyke
JD09-12	Rhyolite?	58.164	-5.3023		1 Piece			SE of Achmelvich bay						Unsure..
JD09-13	Ledmorite	58.165	-5.2978		1 Piece	Yes	Loch Roe	SE of Achmelvich bay	Yes	Yes	Yes			Garnet for U-Pb
JD09-14	Diorite	58.1853	-5.1132		3 Pieces (A-C)	B	Loch na h-Innse Fraoich Dyke	N shore Loch Assynt	B	Yes	Yes	Yes	Yes	A = bag of chip samples for zircon U-Pb, B = diorite block, C = contact between diorite and gabbro
JD09-15	Gabbro	58.1863	-5.1093		1 Piece	Yes	Loch Leitir Easaidh Dyke	E of car park on A837	Yes	Yes	Yes			sample in bad shape (Same as JD09-14?)
JD09-16	Bronzite Picrite	58.183	-5.1142		5 Pieces (A-E)	D	Loch Torr an Lochain Dyke	N shore Loch Assynt	D	Yes	Yes			Samples A-D are a Transverse across dyke W to E, sample E = diorite block from above picrite
JD09-17	Gabbro with diorite lenses	58.1698	-5.1832	314/86NW	7 Pieces (A-H)	B, E + H	Lochan Fearna	Road cut North shore Loch Assynt	B, E+H	Yes	Yes	Yes	Yes	A = West margin, B = 1m East of West contact, C = mafic section close to centre, D = dioritic section close to centre, E = East contact, F = Granitic pod close to centre, H = dioritic lens and gabbro contact
JD09-18	Gabbro	58.1363	-5.262	306/78NE	3 Pieces (A-C)	A+B	Badnaban road	on road to Badnaban	A+B	Yes	Yes			A = dyke centre, B = Olivine rich dyke centre, C = SW margin of dyke for geochem
JD09-19	Gabbro	58.129	-5.26		1 Piece		Inverkirkaig road Dyke	S of road just past Badnaban						Fresh plag in sample
JD09-20	Gabbro	58.1912	-5.1003		1 Piece	Yes		N shore Loch Assynt (Maybe the same as JD09-22)	Yes	Yes	Yes			samples not in place
JD09-21	Norite	58.1783	-5.0453		1 Piece	Yes	N Assynt Dyke	opposite car pull in W margin of Loch assynt	Yes	Yes	Yes	Xenocryst	Yes	hand sample not in place
JD09-22	Gabbro	58.1782	-5.0403		3 Pieces (A-C)	B	N Assynt pull in	shore of loch assynt, S of car pull in	B	Yes	Yes	Yes	Yes	A = SW contact, B = coarse grained dyke centre, C = diabase close to centre
JD09-23	mafic pod?	58.1128	-5.2683		1 Piece	Yes	Loch an Arbhair Dyke	past badnaban at lookout over bay to south	Yes	Yes	Yes			poss look for metamorphic zircon
JD09-24	mafic pod?	58.1142	-5.2498		1 Piece	Yes	Loch a' Choin Dyke	S extent of loch inver pier	Yes	Yes	Yes	Xenocryst	Yes	
JD09-25	Amphibolite	58.1882	-5.0769		2 Pieces (A+B)	B		Loch assynt road	B					A = chilled margin on W contact, B = Centre of dyke
JD09-26	Picrite	58.1528	-5.1552		4 Pieces (A-D)	A	Loch an Leothaid Dyke	N shore Loch An Leothaid	A					A = huge felsic crystals - are olivines in equilibrium with opx? Or xenocrysts, B = close to N contact, C = samples throughout dyke, D = sand from loch shore
JD09-27	Meta Gabbro	58.1559	-5.1507		2 Pieces	Yes	Cnoc an Leothaid Dyke	N of Loch An Leothaid on south slope	Yes	Yes	Yes	Yes		2 samples
JD09-28	Meta dolerite	58.1656	-5.1507		2 Pieces	Yes	Poll a' Gharbh Bhair Dyke	N of Loch An Leothaid on North slope	Yes	Yes	Yes			2 samples
JD09-29	Meta dolerite	58.1705	-5.1452		1 Piece	Yes	Allt an Tiaghaich Dyke	500m north of previous sample - stepping stones	Yes	Yes	Yes			

2010 Fieldwork														
Dyke	Lithology	Decimal lat	Decimal long	Orientation and width	Sample amount	Crushed	Dyke Name	General location	Geochem	Tracer isotopes (Sr-Nd)	WR oxygen	U-Pb age	Zirc oxygen	Comments
JD10-01	Basalt	57.7266	-5.6898		1 piece			Northern tip of Gairloch in Loch Maree group						Fine grained schistose basalt with some minor quartz veining
JD10-02	Amphibolite	57.7498	-5.1363		1 piece			Road side N of Gairloch in Lewisian gneiss						amphibole rich dyke with some serpentinization and qtz veining
JD10-03	Mafic Pod	57.853	-5.4727		1 piece			Just south of Mungas dale						Highly amphibolatized mafic pod
JD10-04	Amphibolite	57.8569	-5.4479		1 piece			2 Km west of Badcaul						Amphibole rich dyke poss originally diabase
JD10-05	Pyroxenite - highly altered	58.1795	-5.2978	30m wide	6 pieces (A+F)		Poll Buidhe	Between Achmelvich and Clachtoll						A = Med grained use for geochem, B = felsic section for geochron, C = coarse grained pyroxenite from centre may contain ol, C = on S side of dyke, odd mafic section exposed, poss containing opx? Lots of biotite and is schistose, E = Gneiss from N contact, F = dyke with poss Ol (2 samples taken
JD10-06	Mafic Pod	58.186	-5.3234		1 piece		Maiden Loch	Just before Clachtoll						paleomag holes drilled in gneiss - amphibolite sample for geochem and titanite/rutile U-Pb
JD10-07	Gabbro	58.2445	-5.2048		6 pieces (A-C)		Drumbeg Dyke	Just behind Drumbeg toilets						A = fresh gabbroic dyke, B = felsic section of dyke (poss contains quartz) 4 pieces taken, C = felsic section found on ground out of place
JD10-08	Gabbro	58.2435	-5.2136		2 Pieces (A+B)		W Drumbeg Dyke	0.5Km W of Drumbeg on roadside						A = Most felsic portion for U-Pb, B = Finer grained portion for geochem
JD10-09	Pyroxenite	58.0968	-5.2543	30m wide	6 pieces (A+F)			S of Inverkerkaig along stream in river valley						Fresh dyke - samples taken from different areas, dyke exposed in grassy mound, may not be entirely inplace?
JD10-10	Tonalite	58.0824	-5.2374		2 Pieces			1.5 Km furthur S of Inverkerkaig						samples A and B taken - try rutile/titanite U-Pb and geochem
JD10-11	Dolerite	58.0849	-5.2387	30m wide	2 pieces (A+B)			W off road next to Loch in gully on top of hill						A = Dyke margin sample for geochem, B = poss dyke centre, sample out of place but coarse grained, no real exposure of dyke centre
JD10-12	Gabbro	58.2419	-5.0079	20m wide	2 Pieces A, 2 Pieces B		Newton Dyke	Newton Dyke (inbetween Newton and Unapool)						A = Heavily paleomag'ed coarse grained, B = finer grained close to S contact with gneiss
JD10-13	Gabbro	58.1562	-5.2367	30m wide	2 Pieces A, 2 Pieces B		Lochinver Dyke	Lochinver dyke just before bridge at entrance to Lochinver						A = coarse grained centre of the Dyke, B = close to S contact of dyke
JD10-14	Amphibolite	58.3691	-4.982	10m wide	2 Pieces	Yes		Richonich Terrane N of Laxford bridge in E hillside						Amph plag and garnet dominated, highly amphibolatized. Located due to abundance of lichen on dyke. Dykes heavily foliated but not banded
JD10-15	Amphibolite	58.3729	-4.9835	10m wide	1 piece	Yes		200m from previous locality						foliated but not banded, dyke cross cut by granitic sheets - laxfordian
JD10-16	Amphibolite/dolerite	58.3898	-5.0262		2 Pieces	Yes		Laxford brige famous locality						2 samples of dolerite from the supposed dykes in the famous road cut locality
JD10-17	Dolerite	58.1546	-5.2548	20m wide	2 Pieces	Yes		Glendarrach Dyke in hamlet next to Lochinver						contact not seen, doleritic dyke no observed felsic section
JD10-18	Dolerite	58.1536	-5.2533	20m wide	2 Pieces	Yes	Baddidarach Dyke	probably a continuation of Glendarrach dyke						A= dyke centre, B = close to margin - no real margin seen
JD10-19	Tonalite	57.867	-5.4382		6 Pieces (A-F)	Yes		Just before Inchina in southern area - roadside outcrop						amphibolite fascies tonalite, possibly used for goechron and geochem
JD10-20	Dolerite	57.8567	-5.4483	40m wide	3 Pieces taken (A-C)	Yes		Roadside outcrop 1km S of JD10-19, above lovely beach	B		Yes			A = geochron sample cose to centre, B = Geochem sample, close to S contact, C = sample of gniess right on contact (U-Pb titanite/rutile)
JD10-21	Tonalite/dyke ?	57.7496	-5.6033		2 Pieces	Yes		on Road to Gairloch, view over Loch Maree no name	yes		Yes			possibly mafic dyke/ possibly tonalite - some layering in parts, massive in others?
JD10-22	Dolerite	57.6888	-5.5891		1 piece	Yes		On road between Gairloch and Tarbert near cattle grid						Highly altered - epidote present, lots of fractures, no real fresh pieces
JD10-23	Amphibolite	58.159	-5.2333	12m width	1 piece	Yes		On junction between Lochinver and Achmelvich roads						could be mafic layer in gneiss, abundant fractures/veinlets, 1 sample for geochem
JD10-24	Amphibolite	58.16	-5.227		1 piece	Yes		just down road towards Assynt from JD10-23	yes		Yes			could be mafic layer in gneiss, abundant fractures/veinlets, 1 sample for geochem
JD10-25	Amphibole/pegmatite	58.1598	-5.2245		2 pieces (A+B)	Yes		Furthur down road towards loch Assynt from JD10-23	A		Yes			poss mafic layer? A = mafic rock same orientation as major banding in gneiss, B = pegmatite vein sample with gneiss attached - not inplace
JD10-26	Pyroxenite	58.1897	-5.3188		4 Pieces (2 A and 2 B)	Yes		Clachtoll dyke - in hill just behind village	A		Yes			A = pyroxenite sample - 2 pieces, B = mafic dyke sample which has intruded ultramafic, 2 pieces for geochron hopefully - med grained

Dyke	Lithology	Decimal lat	Decimal long	Orientation and width	Sample amount	Crush	Dyke Name	General location	Geochem	Tracer isotopes (Sr-Nd)	WR oxygen	U-Pb age	Zirc oxygen	Comments
JD10-27	altered dolerite	58.2252	-5.3027	15m width	7 Pieces (A-E)	Yes	N Clachnessy Dyke	Clachnessy Dyke, just outside hamlet	yes		Yes			A = sample of gneiss far away from contact with dyke, B = gneiss at dyke contact, C = relatively coarse grained sample from dyke centre, D = fragments from all over dyke (3 pieces), E = vein fragments from dyke
JD10-28	Amphibolite	58.2348	-5.1637		3 Pieces taken (A-C)	Yes	E Nedd Dyke	Nedd dyke, just outside hamlet	A		Yes			A = fine grained for geochem, B = gneiss sample with dyke contact, C = gneiss sample far from contact
JD10-29	norite?	58.253	-5.1153		1 piece	Yes	Ardvar Dyke	Fisheries road dyke (not marked on map)	yes					amphibolatized sample possibly previously a norite
JD10-30	Gneiss	58.2495	-5.1153		1 piece	Yes		gneiss over looking Unapool road						try to date rutile/titanite to see if metamorphic events other than the laxfordian can be ID'd - other metamorphic events appear to be affecting the Clachtoll area
JD10-31	Gabbro	58.2639	-5.0406	30m wide	6 Pieces taken (A-C)		Kylestrome Dyke	Kylestrome dyke						A = fresh gabbro (4 pieces) B =gniess sample from ~1m from contact, C = S contact chilled dyke w contact exposed
JD10-32	Picrite	58.165	-5.2086	40m wide	3 Pieces taken (A-C)		Loch a' Chiorrachain	Brockloch dyke						large fresh dyke - v different to those around Clachtoll area, A = sample around dyke, B = section close to margin - finer grain size, C = sample with large biotite rich nodule
JD10-33	Gabbro	58.1651	-5.1651		2 Pieces			located at loch just abover Brockloch dyke						older than brochloch dyke - the picrite cross cuts this gabbro, samples are relatively fresh hetrogenious in terms of plag content
JD10-34	Dolerite	58.1645	-5.2074	15m width	1 piece			next to road close to JD10 -34 and 33						fresh dolerite, possibly cross cuts 34 and 33 may be part of 1990 group? Appears coarse grained and fresh
JD10-35	Picrite	58.1624	-5.215	30m wide	2 Pieces		Loch nan Eun	Down road W of JD10-34						well preserved fresh picrite, samples for geochron and geochem
JD10-36	Olivine Gabbro	57.9964	-6.7603	40m wide	5 Pieces (A-E)			On Lewis N of Tarbert						Presence of biotite may indicate lower metamorphic grade, A = coarse grained section lots of biotite, B = dyke containing cross cutting veins, C = biotite rich section in centre of dyke, D = close to contact, finer grained, E = fresh part from centre of dyke - no biotite
JD10-37	Norite	57.9868	-6.747	100m wide	6 Pieces (3 A+3 B)			Folded dyke N of Tarbert						Coarse grained Norite comp thoughout, A = coarse grained norite from around dyke, B = poss second dyke N of pullout on side of road - metagabbro, look for zircon..
JD10-38	Gabbro	58.2412	-6.7615		3 Pieces taken (A-C)			W side of Lewis close to…						amphibolatized dyke with biotite and garnet, A = pieces of coarse grained dyke throughout outcrop, B = pegmatite vein crosscutting dyke, C = gneiss sample close to dyke
JD10-39	Gabbro	58.2937	-5.0945	25m wide	3 Pieces taken (A-B)		Loch a'Mhinidh Dyke	halfway between Karlstrom and Badnaban						metamorphosed outcrop, A = 2 pieces from across dyke, B = dyke centre more felsic
JD10-40	Gabbro	58.2996	-5.115	30m wide	4 Pieces			North of Karlstrom						Medium grained samples, numerous fractures are present, chlorite mineralized on fracture surfaces, appears competant away from fractures
JD10-41	Gabbro	58.3528	-5.1689	184/56W	5 Pieces (A-E)			Next to graveyard dyke but with a different strike						highly deformed area just S along coast from Graveyard dyke, lots of folding, may be layer in gneiss? A = dyke contact with gneiss, B = coarse grained sections from around dyke, C = Coarse grained sample with abundant mica, D = sample from other side of dyke, E = possible heavy mineral layer - garnet and amph rich
JD10-42	Amphibolite	58.3111	-5.1246		2 Pieces			Just south of Badcaul bay						coarse grained amphibolite with v large garnets maybe layer in gneiss?
JD10-43	Gabbro	58.144	-5.2493	30m wide	2 Pieces (A+B)	Yes		Loch Culag dyke on Anna's path in culag woods						Metagabbro in wooded area - unusual… appears relatively fresh with plag a little white. A = coarse grained section from close to centre, B = fine grained sample from close to S contact for geochem
JD10-44	Olivine Gabbro	58.0971	-5.2545		2 Pieces	Yes		Right next to JD10-09 on other side of the road						very fresh Ol gabbro - not seen dykes like this before, Fresh Ol visible, maybe same as 1990 dyke, 2 large samples taken
JD10-45	Gabbro	58.243	-5.2484	15m width	2 Pieces (A+B)	Yes		next to road far south of Inverkerkaig						Fresh dyke with unaltered plag present. A = coarse grained sample from dyke centre, B = Dyke margin sample for geochem
JD10-46	Gabbro	58.1833	-5.1511	20m wide	2 Pieces	Yes		on way towards Loch Beanoch						fresh and unmetamorphosed samples, centre of dyke appears to be very coarse and pegmatite like - v good for dating!
JD10-47	Gabbro	58.1883	-5.1511		2 Pieces (A+B)	Yes		closer towards Loch Beanoch may be same dyke ars JD10-46?						Fresh gabbro samples, no pegmatitic section though, A = coarse grained material for geochron, B = close to contact for geochem
JD10-48	Picrite	58.1894	-5.1657	30m wide	9 Pieces (A-G)	Yes		Loch Beanoch dyke						samples thoughout dyke to show variation, very large pyroxene crystals present in some samples.
JD10-49	Gabbro	57.859	-5.4469	30m wide	3 Pieces taken (A-C)	Yes		500m S of Inchina						highly metamorphosed dyke cross cut by granite intrusions, A = metagabbro/ampibolite dyke, B = cross cutting granite, C = sample containing both dyke and granite.
JD10-50	Amphibolite	57.6931	-5.7182		2 Pieces	Yes		500m E of Badachro						highly altered mafic body poss layer in gneiss? Lots of veins. 2 samples taken for geochem
JD10-51	Amphibolite	57.6924	-5.7103	20m wide	2 Pieces	Yes		close to W edge of loch W of Badachro						foliated mafic body with lots of garnet present samples for geochem
JD10-52	Amphibolite	57.6931	-5.701	10m wide	1 piece	Yes		Mikissok house dyke						strong fabric highly metamorphosed, suprising dyke is not marked as foliated on map - in similar condition to dykes around laxford bridge
JD10-53	Amphibolite	58.6249	-5.0052		2 Pieces (A+B)	Yes		Cape wrath lighthouse dyke						highly amphibolatized 'dyke' also highly deformed. Lots of granitic pegmatites cross cutting, A = coarse sample of mafic body. B = sample of gneiss for rutile/titanite U-Pb, prob overprinted by pegmatite but worth a go.
JD10-54	Amphibolite	58.549	-4.68	3m wide	2 Pieces (A+B)	Yes		3km E of Durness						Highly altered, amphibolite dyke, same foliation direction as gneiss, dyke is cut by granite pegmatite, A = amphibolite dyke close to centre, B = gneiss close to amphibolite contact.
JD10-55	Amphibolite	58.4564	-4.4353		6 pieces (A-C)			Ribigill Dyke						large mafic unit exposed in hillside, amphibolite grade with numerous epidote veins. A = 4 coarser pieces from aroung outcrop, B = Fine grained dyke with epidote vein present, C = tonalite gneiss from close to contact.